# CORRELATED ELECTRON SYSTEMS IN THE LIMIT OF INFINITE DIMENSIONS

BY MARCELO J. ROZENBERG

A dissertation submitted to the
Graduate School—New Brunswick
Rutgers, The State University of New Jersey
in partial fulfillment of the requirements
for the degree of
Doctor of Philosophy
Graduate Program in Physics and Astronomy
Written under the direction of
Professor Gabriel Kotliar
and approved by

New Brunswick, New Jersey October, 1994 ABSTRACT OF THE DISSERTATION

Correlated Electron Systems in the Limit of Infinite

**Dimensions** 

by Marcelo J. Rozenberg

Dissertation Director: Professor Gabriel Kotliar

The limit of large dimensionality is considered for the study of strongly correlated

electron systems. Different numerical techniques are developed, and applied to the

solution of model hamiltonians. The solution of the Hubbard model is presented in

detail. The results are discussed in regard to the experiments in transition metal oxide

and heavy fermion compounds.

ii

# Preface

This thesis is organized as follows: Chapter 1 contains a brief introduction to the subject. In Chapter 2 we derive the basic equations and introduce the numerical methods developed for the study of the model hamiltonians. In chapters 3 to 6 we present in detail the solution of the Hubbard model and discuss the results with respect to experimental data on transition metal oxides. Chapters 7 is devoted to the study of the optical conductivity in the Hubbard and Anderson lattice model. This issue is considered in regard of the experimental results on various correlated electron compounds. A certain amount of overlap between chapters has been allowed in order to make each of them essentially self-contained units.

# Acknowledgements

I would like to thank in first place my thesis advisor, Gaby Kotliar, for helping me to discover what science really is about. Working with him has been an intense, fruitful and truly enjoyable experience.

I would also like to thank my classmates and the postdocs from the Condensed Matter Theory group. Especially Xin-Yun Zhang, Qimiao Si and Goetz Moeller, with whom I have directly collaborated at different stages of my thesis, and Vlad Dobrosavljevic with whom I enjoyed endless discussions.

An acknowledgement also goes to my former classmates at the University of Buenos Aires, Bocha (who taught me Fortran one afternoon), Dario, Diego, Fabian, Fernando, Javier, Juan and especially Ruben. With them I not only learned to enjoy physics, but also built a beautiful friendship that has persisted after I left.

# Dedication

I want to dedicate this thesis to my parents and my brother, for giving me your love and unconditional support throughout these many years of study.

Is also dedicate it to my friends Diego, Sergio and Ruben, that remained always by my side, especially after I came to the States.

Finally, I dedicate this thesis to my wife, Florencia, for these exciting years together, and for being a limitless and endless source of joy, care, and over all, love.

# Table of Contents

Abstra	act		•	٠	 •	ii
Prefac	e					iii
Ackno	$\mathbf{w}$ ledge	${f ements}$		٠	 •	iv
Dedica	ation .		•		 ٠	v
List of	f Tables	es	•	•	 ě	ix
List of	fFigur	${f res}$	•	•	 •	X
1. Intr	oductio	ion			 •	1
1.1.	The p	problem of strong correlations			 •	1
Refere	ences .		•	•	 •	3
2. Met	hodolo	$\mathbf{ogy}$	•			4
2.1.	Deriva	vation of the Mean Field Equations	•	•		4
2.2.	Nume	$ m erical\ methods$				9
	2.2.1.	. Quantum Monte Carlo		٠	 •	9
	2.2.2.	. Second Order Perturbation Theory				12
	2.2.3.	. Exact Diagonalization		٠	 •	14
	2.2.4.	. Comparison of the methods				19
Refere	ences .		•	•	 •	22
3. The	Mott-	-Hubbard transition	•		 •	23
3.1.	$\operatorname{Introd}$	duction		•	 •	23
3.2.	The m	mean field equations			 •	24
3.3.	The m	metal-insulator transition				25

	3.4.	Discussion	31
	3.5.	Conclusions	32
R	e <b>fer</b> e	nces	34
4.	The	transition at zero temperature	35
	4.1.	Introduction	35
	4.2.	Methodology	37
	4.3.	Mott transition	40
	4.4.	Conclusion	46
R	e <b>fer</b> e	nces	48
5.	The	transition at finite temperature	49
	5.1.	Introduction	49
	5.2.	The self-consistent equations	52
	5.3.	Phase diagram and thermodynamics	57
		5.3.1. The breakdown of the metallic solution	65
		5.3.2. The breakdown of the insulating solution	69
	5.4.	$\mathbf{U_{c2}}$ The Brinkman Rice point	71
	5.5.	$\mathbf{U_{c1}}$ The Hubbard point	73
	5.6.	Susceptibilities and the Mott-Hubbard transition	73
	5.7.	The magnetic solution and frustration	82
	5.8.	The transition as a function of doping	93
	5.9.	Conclusion	94
Re	e <b>fer</b> e	nces	98
6.	The	coexistent solutions	100
	6.1.	Introduction	L00
	6.2.	Methodology	102
	6.3.	The two solutions	L05
	6.4	Conclusion	ınq

Refere	nces	11	LO
7. Opti	ical conductivity in correlated electron systems	11	11
7.1.	Introduction	11	11
7.2.	Methodology	11	12
	7.2.1. Mean field equations	11	12
	7.2.2. Optical conductivity	11	13
7.3.	Hubbard model	11	14
	7.3.1. The insulator state	11	15
	7.3.2. The metallic state	11	17
7.4.	Anderson lattice model	12	22
7.5.	Conclusions	12	27
Refere	nces	13	30
8. Con	clusions	13	32
Refere	$\mathbf{nces}$	13	36
Appen	dix A. Source codes	13	37
A.1.	Quantum Monte Carlo	13	37
A.2.	$2^{nd}$ Order Perturbation Theory (Matsubara space)	15	51
A.3.	$2^{nd}$ Order Perturbation Theory (Real space $T=0$ )	15	57
A.4.	Exact Diagonalization	16	32
<b>T</b> 7:1-		9.0	20

# List of Tables

	7.1.	Experimentally	determined	parameters for	the model.			115
--	------	----------------	------------	----------------	------------	--	--	-----

# List of Figures

2.1.	Bethe lattice (Cayley tree) with connectivity $d=2$ . The effective action	
	is obtained by integrating out the $d.o.f.$ of sites other than 0. When	
	this site is removed the Cayley trees branching from the $n.n.$ become	
	${\it decoupled.} \ldots \ldots \ldots \ldots \ldots \ldots$	6
2.2.	The only diagram that contributes to the self-energy $\Sigma$ to second order.	12
2.3.	The cluster hamiltonian with the impurity site (black), and the effective	
	bath represented by 2 chains of atomic sites (white). The site en-	
	ergies and hopping amplitudes are given by the parametrization of	
	$G_0$	16
2.4.	The metallic solution self-energy $\Sigma$ , as obtained from the different meth-	
	ods presented in the text	20
2.5.	The insulator solution self-energy $\Sigma$ , as obtained from the different meth-	
	ods presented in the text	21
3.1.	The imaginary part of the Weiss field $ ilde{G}_0^{-1}$ as a function of Matsubara	
	frequency for $U=2$ (solid line), $U=3$ (dotted line), and $U=3.6$	
	(dashed line), at $\beta=64$ . All energy scales are renormalized by the	
	half-bandwidth $D=1.$ For $U < U_c$ the Weiss field approaches its	
	unrenormalized zero frequency value $D/2$ . For $U>U_c$ it matches	
	the analytical solution of equation (11) in the text, $Im( ilde{G}_0^{-1})$ =	
	$-\omega_n,\omega_n o\infty,  ext{ and } Im( ilde{G}_0^{-1})=-rac{U^2}{U^2-D^2}\omega_n,\omega_n o0.$	29

3.2.	The self-energy $\hat{\Sigma}$ as a function of Matsubara frequency for $U=2$ (solid	
	line), $U=3$ (dotted line), and $U=3.6$ (dashed line), at $\beta=64$ .	
	For $U < U_c$ the self-energy is linear at low frequencies with a slope	
	increasing with U. The noise of the plot at $U=3$ is due to the	
	proximity to the critical U	30
3.3.	The particle occupation as a function of the chemical potential $\mu - \frac{U}{2}$ for	
	(top to bottom) $U=2,3,4,6$ at $eta=4.$	31
3.4.	Schematic representation of the fully connected lattice. The hopping	
	elements are scaled as $t_{ij} = \epsilon_{ij} rac{t}{d^{1/2}}$ with $\epsilon_{ij}$ independent Gaussian	
	${\rm random\ variables.} \ldots \ldots \ldots \ldots \ldots \ldots \ldots \ldots \ldots$	33
4.1.	Comparison of Matsubara self-energy obtained from Quantum Monte	
	Carlo (crosses) to that from perturbation calculation(dots). For	
	U=2 on the metallic side and $U=3.6$ on the insulating side at a	
	T=1/64. Note that on the insulating side the growing deviation at	
	low energies is purely due to the $\omega^{-1}$ divergency, the relative error	
	remains the same but the absolute error becomes bigger	39
4.2.	Density of states $-\mathrm{Im}G$ at zero temperature as a function of $U$ . From top	
	to bottom, $U=1,2,2.5,3,4.\ldots$	41
4.3.	a) Spin-spin correlation function obtained from Monte Carlo for $eta=32,$	
	and $U=1,2,2.3,2.4,2.5,3,4,6.2.$ The correlation length $\sim \Delta^{-1}$	
	diverges as we approach the insulating side. b) Local moment as a	
	function of $U$ for two temperatures: $eta=16({ m dots}),32({ m solid}).$	42
4.4.	Particle occupation number vs. noninteracting energy $\epsilon$ as a function	
	of $U=2,2.5,3,4,$ obtained from perturbative calculations. Inset:	
	$m/m^*$ vs. $U$ calculated from the slope of the real part of the self-	
	energy at the Fermi level	45

4.5.	The	temperature where the QMC solution changes from metallic-like	
		to insulating-like as a function of the interaction $U$ (bold line).	
		The low energy scale defined as the quasiparticle width obtained	
		from 2OPT (dotted line). A true transition occurs only at the	
		lowest temperatures where the change in the slope is observed in	
		the metal-insulator boundary line. The transition is driven by the	
		interaction $U$ instead of the temperature only below this scale. For	
		higher temperatures it becomes a crossover	47
5.1.	$\operatorname{Sch}\epsilon$	ematic representation of the two sublattice fully frustrated model	
		(TSFF). The fully-connected fully-frustrated sublattices $\boldsymbol{A}$ (white	
		dots) and $B$ (black dots) at the top of the figure, are combined into	
		a single lattice through the interlattice hopping elements $t_2$	54
5.2.	$\operatorname{Sch}\epsilon$	ematic representation of the Bethe lattice with next nearest neighbor	
		hopping. This model has the same mean field equation as the TSFF	
		but does not have randomness	55
5.3.	Pha	se diagram of the fully-frustrated model. It is possible to continu-	
		ously move from one phase to the other since at high $T$ the tran-	
		sition becomes a crossover. The dashed lines indicate the region	
		where the metallic and the insulating solutions coexist. The filled	
		square indicates the end of the first-order line in a second-order point.	58
5.4.	$\mathbf{The}$	density of states for the metallic (thin line) and insulating (bold line)	
		solution at $T=0$ and the same value of the interaction $U=2.9$ ,	
		obtained with the self-consistent perturbative calculation	60
5.5.	Con	parison of the insulating and metallic Green function obtained us-	
		ing the quantum Monte Carlo algorithm and the perturbative cal-	
		culation. The value of the interaction $U=2.8$ and the inverse	
		temperature $\beta=64.\dots\dots\dots\dots\dots$	61
5.6.	The	energy as a function of the temperature for a value of $U=2$ in	
		the metallic region (solid line), and $U=4$ in the insulating phase	
		(dotted line)	62

5.7. The	specific heat $C_v$ as a function of temperature. The solid line is for	
	U=2 and the dashed line corresponds to $U=4$ . In the metallic	
	case ( $U=2$ ) it is apparent the separation of energy scales. The	
	linear part, at low T, ends at $T\sim \Delta,$ and the thermal activation of	
	the incoherent features peaks at the bigger scale $T \sim U - 2D$ . This	
	last effect is the only one present in the insulating case	63
5.8. The	specific heat $C_v$ as function of temperature for several values of $U$ .	63
5.9. Ent	ropy $perspin$ as a function of temperature for two different values of	
	interaction $U=2,4.$	64
5.10. The	temperature value where the entropy reaches $\frac{\ln 2}{2}$ as function of the	
	distance to $U_{c2}$ . This temperature defines the region where the	
	Fermi liquid description is applicable.	64
5.11. The	kinetic, potential and internal energy as function of $U$ for $T=0.02$	
	(a) and $T=0.03$ (b). The hysteresis effect is clearly observed	65
5.12. The	low frequency part of the density of states $ ho(\omega)$ as function of the	
	frequency for values of the interaction $U=3,3.1,3.2,3.3$ (a). The	
	four curves of (a) collapse to one universal form after rescaling:	
	$f(rac{\omega}{\Delta})=t ho_l(\omega),  ext{ where } \Delta \propto U_c-U  ext{ (b)}. \;\; \ldots \;\; \ldots \;\; \ldots \;\; \ldots$	68
5.13. The	quasiparticle weight $z$ as a function of the interaction $U$ . The solid	
	bold line corresponds to ED results with 8 sites. The dotted line is	
	obtained from 20PT. For comparison we also plot the results using	
	the Gutzwiller variational method	72
5.14. Dou	ble occupation as a function of the interaction $U$ . The data cor-	
	responds to QMC simulations at $\beta=32$ (dots), 8 sites exact di-	
	agonalization (bold line) and 2OPT at $T=0$ (dotted line). For	
	comparison the results for the Gutzwiller variational wavefunction	
	is also plotted (thin line).	72
5.15. Para	amagnetic gap (solid) as function of the interaction $U$ obtained from	
	ED. For comparison, the corresponding results from 2OPT (dot-	
	ted), and $U_{c1}^{HIII} \approx 1.73$ (diamond)	74

5.16. Local magnetization $m_z$ as function of an external magnetic field, for	
different values of the interaction $U.$	76
5.17. Inverse of magnetic susceptibility at $\mathbf{q} = 0$ (solid dots) and the magnetic	
exchange $J=rac{2t^2}{U}$ (dashed line) as a function of the interaction $U.$ .	77
5.18. Wilson ratio as function of the interaction $U$	78
5.19. Comparison of an exact Green function away from half-filling obtained	
from QMC at $\beta=64$ , and the parametrization discussed in the	
text. The interaction $U=2.5$ and $\mu=0.3.$	80
5.20. The local antiferromagnetic Green function of spin $\sigma$ as a function of	
Matsubara frequency. The imaginary part is odd and the real part	
even. Obtained from QMC at $\beta=32$ (full line) and ED of 8	
sites (dotted line). The results can hardly be resolved due to the	
excellent agreement. The interaction $U=1.5$	84
5.21. The density of states for $\sigma$ and $-\sigma$ electrons (full and dotted line) ob-	
tained from ED of 8 sites for $U=1.5$ . The top plot corresponds to	
the bipartite Bethe lattice and the lower plot to the TSFF model	
with $t_1^2 = \frac{1}{4}t^2$ and $t_2^2 = \frac{3}{4}t^2$	84
5.22. Comparison of the Néel temperature of the bipartite Bethe lattice model	
obtained from QMC (bold line), 2OPT (dotted line), and Hartree-	
Fock (thin line).	85
5.23. Local staggered magnetic moment as function of temperature obtained	
from Hartree-Fock approximation. The interaction $U=0.5,1,2$	
(thin, dotted, and bold line). $\dots$	86
5.24. The gap in the density of states obtained from ED for the bipartite	
Bethe lattice (thin line), fully-frustrated lattice (dotted line), and	
TSFF model (bold line). The gap is defined as the distance between	
the lowest poles in the Green function. The curves correspond to	
the extrapolated results to an infinite size system from clusters of	
$N_{\text{corr}} = 3.5.7$ . A $1/N_{\text{corr}}$ scaling behavior is assumed.	87

5.25. The local staggered magnetization obtained from ED for the bipartite	
Bethe lattice (dotted line), and TSFF model (bold line). The curves	
correspond to the extrapolated results to an infinite size system	
from clusters of $N_{sites}=3,5,7.$ A $1/N_{sites}$ scaling behavior is as-	
$\mathbf{sumed.}  \dots $	88
5.26. The antiferromagnetic metallic solution of the TSFF model as a function	
of Matsubara frequency. The imaginary part is odd and the real	
part even. Obtained from QMC at $\beta=64$ (full line) and ED of 8	
sites (dotted line). The interaction $U=2$	89
5.27. The antiferromagnetic metallic solution of the TSFF model as a function	
of Matsubara frequency. Obtained from the Hartree-Fock approx-	
imation at $U=0.95$ and $T=0.05$ . The bold line corresponds to	
the imaginary part and the dotted line to the real part	89
5.28. Approximate phase diagram of the TSFF model. The solid lines indicate	
the first-oder lines separating the magnetic phases that correspond	
to parameters $t_1^2 = 0.25t^2$ , $t_2^2 = 0.75t^2$ . The square indicates a	
second order critical point. The shaded region corresponds to a	
crossover from a paramagnetic metal to an insulator state	92
5.29. Particle number $\delta = n - \frac{1}{2}$ as a function of the chemical potential $\mu$ .	
Data obtained from QMC at $\beta = 16$ , for different values of the	
interaction $U$	93
5.30. Specific heat (white dots) and spin susceptibility (black dots) as function	
of doping for $U=3$ and $\beta=32$ . The experimental results for the	
specific heat from ref. [31] are plotted for comparison (grey dots).	
The inset shows the renormalized mass $m^st/m=Z^{-1}$ as a function	
of doping.	95
5.31. The Wilson ratio as function of doping for $U=3\ldots\ldots\ldots$	96

6.1.	Comparison of the metallic and insulating Matsubara Green functions	
	for $U = 2.7$ , as obtained from the two variations of the algorithm.	
	Full line "star geometry" and dotted line "two chain geometry" (10	
	sites for the metallic case and 8 sites for the insulating) 1	106
6.2.	Kinetic, potential and total energy for the metallic and insulating solu-	
	tions in the coexistence region. Difference between the metallic and	
	insulating solution (inset). From the "two chain geometry" 1	.08
7.1.	The optical conductivity $\sigma(\omega)$ in $[\Omega^{-1}cm^{-1}]$ for $V_{2-y}O_3$ . The top curve	
	corresponds to $y=0.013, T=10K,$ and the lower curve to $y=$	
	0,T=70K	16
7.2.	The optical gap $\Delta$ as a function of the interaction $U$ , for both the antifer-	
	romagnetic (dotted) and paramagnetic (solid) insulator solutions.	
	The points show the experimental gap in units of the experimental	
	half-bandwidth1	.17
7.3.	The optical conductivity from ED at $T=0$ . Results for the paramagnetic	
	insulator solution with a value of the interaction $U=2.15D$ (top)	
	and $U=4D$ (bottom). For comparison, the results from 2OPT at	
	U=4D are also shown (dotted)	.18
7.4.	The kinetic energy as a function of the interaction $U$ , for both the antifer-	
	romagnetic (dotted) and paramagnetic insulator (thin) and metal-	
	lic (thick) solutions. The points show the experimental integrated	
	spectral weight in units of $\frac{\pi\epsilon^2}{2\hbar^2a}$	.18
7.5.	The higher figure contains the optical conductivity $\sigma(\omega)$ in $[\Omega^{-1}cm^{-1}]$ of	
	$V_2O_3$ for $T=170K$ (top) and $T=300K$ (bottom). In the lower	
	figure we plot the difference $\Delta\sigma(\omega)$ of the two spectra. $$	.19
7.6.	The optical conductivity from 2OPT for $U=2.1D, { m and} \ T=0.05D \ { m (top)}$	
	and $0.083D$ (bottom). This values correspond to $T\approx 170K$ and	
	$300  K$ by setting the half-bandwidth $D \approx 0.3 eV$ . A small $\Gamma$ was	
	included in the calculation to mimic a finite amount of disorder 1	20

7.7.	The	optical conductivity spectra of the Anderson lattice for values of the
		interaction $U=0.5,1,2,3$ (right to left), keeping the hybridization
		$V=0.25$ fixed. The inset shows the gap $\Delta_cpprox V^*$ and the indirect
		gap from the local density of states $\sim T_K$ for $V=0.6$ . The slopes
		of these curves give ${V^*}^2/D  lpha  T_K$ in the strong correlation region 123
7.8.	The	optical conductivity spectra $\sigma(\omega)$ in $[\Omega^{-1}cm^{-1}]$ for the Kondo in-
		sulators $Ce_3Bi_4Pt_3$ and $FeSi$ . The higher figure corresponds to
		$Ce_3Bi_4Pt_3$ at $T=25,50,75,100,300K$ (from below). The lower
		figure corresponds to $FeSi$ at $T=20,100,150,200,250K$ (from
		below)
7.9.	The	optical conductivity for the Anderson model at $T=0.001$ (bold),
		0.005, 0.01, 0.02 (dotted), $0.03$ (thin). The interaction $U=3$ and
		$V=0.25.$ Inset: The same quantity at $T=0.001(\mathrm{bold}), 0.005, 0.01, 0.02$
		(dotted), 0.03 (thin) with lorentzian random site disorder of width
		$\Gamma=0.005.$
7.10	The	local spin-spin (bold) and density-density (thin) susceptibility from
		8 sites ED. The optical conductivity from 2OPT (dotted). The
		parameters are $U = 1$ and $V = 0.2$ . The inset shows the direct
		gap as obtained form 2OPT (upper dotted line), the indirect gap
		(lower dotted line) and the spin gap (solid line) from 8 sites ED.
		The hybridization is $V=0.2.$

## Chapter 1

#### Introduction

### 1.1 The problem of strong correlations

The discovery of exciting new materials like the high temperature superconductors and heavy fermion systems has revived the interest in the strong correlation problem in condensed matter physics.

At the heart of this problem lies the interplay between the localized and itinerant character of the d and f-electrons in the transition metal oxide compounds. This fascinating issue has been actively studied and debated since the late forties with the early ideas of Mott on the metal-insulator transition [1].

The model hamiltonians that we consider here for the study of the effect of correlations, are variations of the one originally introduced by Hubbard in a series of three papers in the sixties [2]. Their solution and the extent to which they are able to account for the rich phenomena that are experimentally observed, mostly remains a standing challenge to theoretical solid state physicists.

A crucial aspect of this class of problems is that perturbation theory cannot be applied straightforwardly. It is usually the relevant physical case the one where the interaction term is not small. We are thus in a situation where we lack of a natural small parameter for a controlled expansion, and the validity of the procedure becomes unclear.

One can attempt different alternatives to go beyond the traditional perturbative approaches [3]. The underlying idea is to modify the formulation of the model in such a manner that, although a priori may seem unjustified, will allow us to get new physical insights and possibly obtain a solution that can shed some light on realistic situations.

These alternatives include the change of the representation of the spin group, from the fundamental two dimensional representation to a larger one, but keeping the symmetry group to be SU(2). In particular the case where the size goes to infinity can be studied and corresponds to a semi-classical limit. Another possibility is to modify the symmetry of the group. For instance, one can extend the spin SU(2) symmetry to SU(N), and consider the limit where N is large.

A third option is to modify the dimensionality. Actually, most of the exact results that are available for the kind of models that we are considering, were obtained from their one dimensional formulation. The Bethe Ansatz technique is very successful in the consideration of this class of problems. Although relevant to real physical systems such as one dimensional organic compounds, the results do not seem to be particularly enlightening for the case of the regular three dimensional systems, or even the high  $T_c$  superconductors whose basic physics is generally considered to be two dimensional.

On the other hand, one can consider the opposite limit, i.e., the one where the dimensionality goes to infinity, which was originally proposed by Metzner and Vollhardt [4]. The interest in the formulation of the many body problem in this limit, has consequently led to a novel mean field theory of the strong correlation problem [5, 6, 7, 8]. This theory is similar in spirit to the familiar Weiss mean field theory of spin systems.

The subject of this thesis is a detailed investigation of the results of this last approach to the study of the Hubbard model and some of its variations. We will see that a full solution of the model is possible in this limit, and in the latter chapters we will address the question of its relevance in the light of recent experimental results.

# References

- [1] N. F. Mott, Phil. Mag. 6, 287 (1961).
- [2] J. Hubbard, Proc. Roy. Soc. (London) A281, 401 (1964).
- [3] Correlated Electron Systems. Jerusalem Winter School for Theoretical Physics, edited by V. J. Emery (World Scientific, 1992).
- [4] W. Metzner and D. Vollhardt Phys. Rev. Lett. 62, 324 (1989).
- [5] A. Georges and G. Kotliar, Phys. Rev. B 45, 6479 (1992).
- [6] V. Janis, Z. Phys. B 83, 227 (1991)
- [7] V. Janis and D. Vollhardt, Int. Journ. Mod. Phys. B 6, Nos 5 & 6, 731 (1992).
- [8] A. Georges, G. Kotliar and Q. Si Int. J. Mod. Phys. B 6, 705 (1992).

## Chapter 2

# Methodology

### 2.1 Derivation of the Mean Field Equations

Here, we derive the set of self-consistent equations that define the mean field theory that results from the  $\infty - d$  formulation of the model. They follow from the mapping of the lattice model onto an impurity problem (i.e. a 0+1 dimensional model), supplemented by a self-consistency condition. For definiteness we consider here the Hubbard model. Generalization of the mapping procedure to other models is straightforward [4].

The Hubbard hamiltonian reads,

$$H = -\sum_{\langle i,j \rangle} (t_{ij} + \mu) c^{\dagger}_{i\sigma} c_{j\sigma} + U \sum_{i} (n_{i\uparrow} - \frac{1}{2}) (n_{i\downarrow} - \frac{1}{2})$$
 (2.1)

where  $c_i^{\dagger}$  is the creation operator on the site  $i, \langle i, j \rangle$  means summation over nearest neighboring sites, and summation over repeated spin indices is understood. The parameter  $t_{i,j}$  corresponds to the hopping between sites i and j, U is the local repulsion between electrons on the same site, and  $\mu$  is the chemical potential ( $\mu = 0$  in the particle-hole symmetric case). In the limit of large dimensionality ( $d \to \infty$ ), as was first noticed by Metzner and Vollhardt, the hopping parameter t is rescaled as  $t \to \frac{t}{\sqrt{d}}$  for the kinetic and potential energy to be of the same order and obtain a non-trivial limit [1].

The mapping procedure is most conveniently carried out in the Path Integral formalism. We begin by writing the partition function of the lattice model and singling out a particular site that we call 0.

$$Z = \int D[c_0,c_i]e^{-\int Ld au}$$

$$L = c_{0\sigma}^{\dagger}(\partial_{\tau} - \mu)c_{0\sigma} + U(n_{0\uparrow} - \frac{1}{2})(n_{0\downarrow} - \frac{1}{2}) +$$

$$+ \sum_{i\neq 0} \{t_{0i}c_{0\sigma}^{\dagger}c_{i\sigma} + t_{i0}c_{i\sigma}^{\dagger}c_{0\sigma} + c_{i\sigma}^{\dagger}(\partial_{\tau} - \mu)c_{i\sigma} + U(n_{i\uparrow} - \frac{1}{2})(n_{i\downarrow} - \frac{1}{2})\} +$$

$$+ \sum_{\langle i\neq 0, j\neq 0 \rangle} t_{ij}c_{i\sigma}^{\dagger}c_{j\sigma}$$

$$(2.2)$$

Now, we have to integrate out all the degrees of freedom of the sites other than 0. The partition function can then be factorized and the formal integration can be performed to obtain,

$$Z_{0} = \int D[c_{0}] e^{-S_{0}}$$

$$S_{0} = -\sum_{\sigma} \int \int d\tau d\tau' c_{0}^{\dagger} \left\{ \partial_{\tau} - \mu + \sum_{(i \neq 0, j \neq 0)} t_{0i} \tilde{G}_{ij} t_{j0} \right\} c_{0} + U \int d\tau (n_{0\uparrow} - \frac{1}{2}) (n_{0\downarrow} - \frac{1}{2})$$

$$(2.3)$$

 $\tilde{G}$  is generated in this process and corresponds to the Green function of the lattice model with site 0 removed ("cavity" Green function). We can relate  $\tilde{G}_{ij}$  to the full  $G_{ij}$  by subtracting those paths that visit the origin,

$$\tilde{G}_{ij} = G_{ij} - \frac{G_{i0}G_{0j}}{G_{00}},\tag{2.4}$$

where  $G_{00}$  is the local Green function of the site 0, and its presence in the denominator avoids double counting. This expression is similar to one derived in Hubbard-III, establishing an interesting connection to that work [3].

To proceed further we should now define the particular type of lattice where the model is defined. A natural choice would be, perhaps, a hyper-cubic lattice which is the natural extension of a cubic lattice to the case of high number of dimensions. The free density of states that corresponds to that lattice is of gaussian form [1]. This has the implication of the presence of arbitrary high energy states in the exponential tails of the density of states, which is obviously unphysical. Another possible choice is the Bethe lattice of connectivity d. A schematic representation of this lattice is shown in figure 2.1. In this case, the free density of states results a semicircle, which not only is bounded but also correctly captures the square root edges of the free density of states of the realistic three-dimensional cubic lattice [2]. This density of states is also the

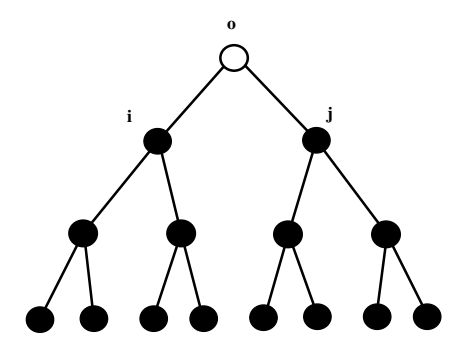


Figure 2.1: Bethe lattice (Cayley tree) with connectivity d = 2. The effective action is obtained by integrating out the d.o.f. of sites other than 0. When this site is removed the Cayley trees branching from the n.n. become decoupled.

same one considered in Hubbard's classical works [3]. Here, we will consider this type of lattice, which we believe can better capture important features of finite dimensional situation.

Therefore, we immediately realize that in a Bethe lattice the Green function between the sites i, j with the site 0 removed  $\tilde{G}_{ij}$ , becomes diagonal and consequently identical to  $G_{00}$ . This is because removing the site 0, has the effect of decoupling the Cayley trees that branch out from sites i and j (see figure 2.1).

Thus,

$$\tilde{G}_{ij} = \tilde{G}_{ij}\delta_{ij} = G_{ii}\delta_{ij} = G_{00}\delta_{ij}. \tag{2.5}$$

Replacing (2.5) into (2.3) and taking  $t_{0i} = t$ , we finally obtain the effective action at the site 0,

$$Z_{0} = \int D[c_{0}] e^{-S_{0}}$$

$$S_{0} = \sum_{\sigma} \int_{0}^{\beta} \int_{0}^{\beta} d\tau d\tau' c_{0}^{\dagger}(\tau) G_{0}^{-1}(\tau - \tau') c_{0}(\tau') + U \int_{0}^{\beta} d\tau (n_{0\uparrow}(\tau) - \frac{1}{2}) (n_{0\downarrow}(\tau) - \frac{1}{2})$$
(2.6)

with,

$$G_0^{-1}(i\omega_n) = i\omega_n - \mu + t^2 G(i\omega_n). \tag{2.7}$$

These last two expressions represent the mapping of our original lattice model,

onto an single impurity problem (2.6) with a self-consistency condition (2.7) (note the to simplied notation  $G_0 \equiv G_{00}$ ). In the derivation, we have implicitly assumed a magnetically disordered state and accordingly the spin indices were dropped. The extension of these equations to state with magnetic long range order is straightforward and will be considered in later chapters.

Notice that the central object in the present scheme is a quantity  $G_0$  which plays the role of the effective field in an analogy to mean field theories of magnetic systems [5]. Another important point to note is the similarity of the local effective action to the corresponding one for the f-electrons in the Anderson single impurity model. In particular it is interesting to see that the role of the hybridization function that describes the conduction band in that model, is played in this case by the local Green function itself. This analogy will be essential for the development of practical methods for the solution of the problem. Also, and equally important, the vast preexistent knowledge of the physics of impurity models will be a continuous source of physical insights.

The system of equations (2.6-2.7) has to be solved for the unknown  $G_0$  iteratively. As we demonstrate below, the Green function of the impurity model  $G(i\omega_n) = -\int_0^\beta e^{i\omega_n\tau} \langle T_\tau c(\tau)c^\dagger(0)\rangle_{S_{eff}}$  becomes the local Green function of the Hubbard model only once self-consistency is attained. We should think of the local Green function G as a functional of  $G_0$ . Therefore, one has to look for of an infinite number of self-consistent solutions, one for each of the frequencies (modes) of  $G_0$ .

From the impurity problem (2.6), an impurity self-energy can be defined through the Dyson's equation

$$\Sigma_{imp} = G_0^{-1} - G^{-1}. \tag{2.8}$$

Combining this expression with the self-consistency condition (2.7) gives,

$$G(i\omega_n) = \frac{2}{i\omega_n - \Sigma_{imp} + i \, sgn(\omega_n) \sqrt{D^2 + (\omega_n + i\Sigma_{imp})^2}}.$$
 (2.9)

where D=t/2 is the half-bandwidth of the semicircular free density of states of the lattice.

We can easily check that at the self-consistent point, the *impurity* self-energy coincides with the Hubbard model self-energy [5]. This follows from the *locality* of the

self-energy in the limit of  $d \to \infty$  [1].

By definition, the k dependent Green function reads,

$$G(k, i\omega_n) = \frac{1}{i\omega_n - \epsilon_k - \Sigma_{local}(i\omega_n)}.$$
 (2.10)

We can obtain the local Green function performing the integration over momenta. This is easy to do in the limit of infinite dimensionality. The multidimensional integration becomes the one-dimensional integral over the variable  $\epsilon$  [1],

$$G_{local}(i\omega_n) = \int_{-\infty}^{\infty} \frac{\rho^0(\epsilon)}{i\omega_n - \epsilon - \Sigma_{local}(i\omega_n)} d\epsilon.$$
 (2.11)

Using the Bethe lattice free density of states  $\rho^0(\epsilon) = \frac{2}{\pi D} \sqrt{1 - (\frac{\epsilon}{D})^2}$  we obtain,

$$G_{local}(i\omega_n) = rac{2}{i\omega_n - \Sigma_{local} + i \, sg \, n(\omega_n) \sqrt{D^2 + (\omega_n + i\Sigma_{local})^2}}.$$
 (2.12)

Comparing (2.12) with (2.9), it follows that at the self-consistent point,

$$\Sigma_{local} = \Sigma_{imp}, \qquad (2.13)$$

and,

$$G_{local} = G_{imp}. (2.14)$$

We can now solve for  $G_0$  to obtain,

$$G_0(i\omega_n) = \frac{2}{i\omega_n + \Sigma(G_0) + i \, sgn(\omega_n)\sqrt{D^2 + (\omega_n + i\Sigma(G_0))^2}}$$
(2.15)

which can be used as an alternative self-consistency equation that relates  $G_0$  with  $\Sigma$  and does not require the explicit calculation of the Green function during the iteration process.

In the the next section we will present various schemes for the solution of the mean field equations. Depending on the particular one, we will need to consider equation (2.7) or (2.15).

It should be clear that the problem is composed of two parts: an easy one — the self-consistency condition—, and a harder one —the impurity problem—. Dealing with the first is mostly straight forward. For the second, we will introduce in what follows three different numerical procedures. Lets emphasize here that there is no single

"most appropriate" method. Each one, as it turns out, is more suitable for the study of different aspects of the problem and, more importantly, provide different physical insights.

The methods we use to solve the impurity problem are quantum Monte Carlo (QMC), second order perturbation theory (20PT), and a novel algorithm based in the exact diagonalization of an effective cluster hamiltonian that is defined from a parametrization of the Green function  $G_0$ .

#### 2.2 Numerical methods

In this section we describe the numerical procedures. We will consider here the algorithms at a formal level, indicating where the technical difficulties are. The source codes can be found in the appendix.

#### 2.2.1 Quantum Monte Carlo

This method for the solution of the impurity problem basically follows the work of Hirsch and Fye [6]. It is implemented in the subroutine *impurity* in the code in the appendix. This is a finite temperature calculation with the Green functions being antiperiodic functions of the imaginary time  $\tau$ 

$$G(\tau + \beta) = -G(\tau) \tag{2.16}$$

with  $\beta$  being the inverse temperature  $(k_B = 1)$ .

The starting point is the Functional Integral formulation of the problem. The partition function reads,

$$Z = \int D[c, c^{\dagger}] e^{-\sum_{\tau \tau'} c^{\dagger}_{\sigma}(\tau) G_0^{-1}(\tau, \tau') c_{\sigma}(\tau') + U \sum_{\tau} n_{\uparrow}(\tau) n_{\downarrow}(\tau)}$$

$$(2.17)$$

where the imaginary time is discretized in L "slices" of size  $\Delta \tau$ , and the inverse temperature is  $\beta = L \Delta \tau$ .

To deal with the quartic term, we use a discrete Hubbard-Stratanovich transformation [7]

$$e^{-\Delta \tau U n_{\uparrow} n_{\downarrow} + (\Delta \tau U/2)(n_{\uparrow} + n_{\downarrow})} = \frac{1}{2} \sum_{S=\pm 1} e^{\lambda S(n_{\uparrow} - n_{\downarrow})}$$
 (2.18)

where  $\lambda = \operatorname{arccosh}(e^{\Delta \tau U 2})$ . Performing this transformation at every time-slice, we are led to a quadratic action, and the partition function becomes

$$Z = \sum_{S=\pm 1} \int D[c, c^{\dagger}] e^{-\sum_{\tau \tau'} c_{\sigma}^{\dagger}(\tau) G_{0}^{-1}(\tau, \tau') c_{\sigma}(\tau') + \lambda \sum_{\tau} S(\tau) (n_{\dagger}(\tau) - n_{\downarrow}(\tau))}$$
(2.19)

with

$$G_{\sigma}^{-1}(\tau, \tau') = G_{0\sigma}^{-1}(\tau, \tau') + \sigma \lambda S(\tau) \delta_{\tau, \tau'+1}$$
(2.20)

being the inverse propagator for a particular realization of the pseudo-spin field  $s = (S(\tau_1), ..., S(\tau_L))$ . The origin of the  $\delta_{\tau,\tau'+1}$  is in the proper time ordering of the creation and destruction operators [8, 9]. The process of discretization involves the introduction of systematic errors of order  $\Delta \tau^2 U$  due to the Trotter break-up. As a working rule, one should keep  $\Delta \tau^2 U < 1$  to maintain their effect under control.

The trade of a quartic term for an extra summation on the auxiliary field s, makes the action quadratic and allow us to apply Wick's theorem at each time slice. We can now perform the gaussian integration of the Grassman variables, to obtain

$$Z = \sum_{\{s\}} \det[G_{\uparrow}^{-1}(s)] \det[G_{\downarrow}^{-1}(s)]$$
 (2.21)

were  $\{s\}$  denotes the set of all possible field configurations.

In principle, the trace over the auxiliary field, would give the full interacting Green function

$$G_{\sigma} = \sum_{\{s\}} G_{\sigma}(s) \tag{2.22}$$

in practice, this involves a sum over  $2^L$  configurations, and more importantly each term involves the inversion of an  $L \times L$  matrix as follows from expression (2.20).

We can deal with the first problem by performing the sum over a smaller set  $N << 2^L$  of configurations, chosen with a probability distribution given by the Metropolis algorithm.

$$\langle G_{\sigma} \rangle = \sum_{s:.i=1}^{N} G_{\sigma}(s_i)$$
 (2.23)

The set of  $s_i$  is obtained by starting with a randomly chosen configuration, and attempting successive flips of the auxiliary field. The probability of accepting a new

configuration is obtained from the change in the action produced by the flip of a single pseudo-spin. We attempt a change

$$s = (S(\tau_1), ..., S(\tau_j), ..., S(\tau_L)) \rightarrow s' = (S(\tau_1), ..., -S(\tau_j), ..., S(\tau_L))$$
 (2.24)

and accept the new configuration with a probability R, given by

$$R = e^{-\Delta S} = \frac{\det[G_{\uparrow}(s)G_{\downarrow}(s)]}{\det[G_{\uparrow}(s')G_{\downarrow}(s')]}$$
(2.25)

The remaining problem is now the calculation of both a determinant and the inverse of a matrix that differs in one element from a matrix for which these quantities are known (c.f. eq. (2.20)). Following references [6, 8], we take the difference in the inverse propagator produced by a single spin flip at time slice j to be  $1 - e^{\lambda(S'(j) - S(j))}$ . This expression differs from the one that would follow from (2.20) in terms of order  $\Delta \tau^2$ , and we check that decreases the errors introduced by the Trotter break-up.

It is not difficult to see that the new determinant is obtained in terms of the old one as

$$\det[G_{\sigma}(s')] = \{1 + (1 - G(j,j))(e^{\lambda(S'(j) - S(j))} - 1)\} \det[G_{\sigma}(s)]. \tag{2.26}$$

The calculation of the inverse of a matrix, which regularly demands  $O(L^3)$  operations, can be efficiently obtained using the Shermann-Morrison formula [10]. The new inverse can be thus calculated in  $O(L^2)$  operations by

$$G'(j,k) = G(j,k) + \sum_{l} \frac{(G(j,l) - \delta_{j,l})(e^{\lambda(S'(l) - S(l))} - 1)}{1 + (1 - G(l,l))(e^{\lambda(S'(l) - S(l))} - 1)} G(l,k)$$
(2.27)

The obvious change of notation  $\tau_j \equiv j$  is used to simplify the expression. This fast matrix inversion is implemented in the subroutine gnew.

We typically perform 5,000 sweeps to the set of L spins, and store measurements every other sweep to avoid auto-correlation. It is necessary to consider a number of "warm-up" sweeps at the beginning of the procedure to thermalize the initial randomly chosen spin configuration. We regularly make 500 warm-up sweeps. To prevent numerical instabilities produced by the error build-up, a regular matrix inversion  $(O(L^3)$  operations) has to be performed about every hundred fast inversions. This regular inversion is implemented in the subroutine gnewclean.

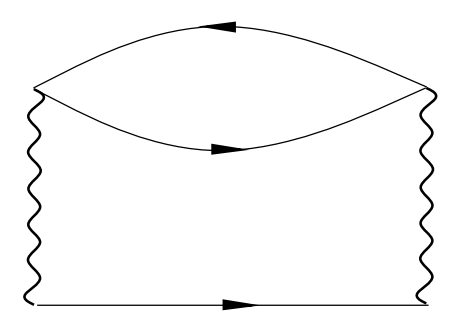


Figure 2.2: The only diagram that contributes to the self-energy  $\Sigma$  to second order.

Finally, the spin-spin correlation functions can be easily obtained from the auxiliary fields by means of the identity [7]

$$\langle S_z( au)S_z(0)
angle = \langle (n_\uparrow( au)-n_\downarrow( au))(n_\uparrow(0)-n_\downarrow(0))
angle = rac{1}{1-e^{-\Delta au U}}\langle S( au)S(0)
angle \qquad (2.28)$$

which is valid for  $\tau \neq 0$ .

#### 2.2.2 Second Order Perturbation Theory

This method basically follows the work of Yamada and Yosida [11]. The perturbation expansion is generated by  $H_I = U(n_{\uparrow} - 1/2)(n_{\downarrow} - 1/2)$ , which causes all the contributions from "tadpole" diagrams to vanish. Therefore, to second-order, only the bubble diagram survives for the evaluation of the self-energy (figure 2.2). This diagram involves the convolution of three  $G_0$  in Matsubara frequency representation

$$\Sigma(\omega) = -U^2 \sum_{\omega'} \sum_{\omega''} G_0(\omega - \omega') G_0(\omega' + \omega'') G_0(\omega'')$$
 (2.29)

therefore, is numerically most convenient to perform a Fourier transformation of this expression. We are, thus, left with a simple multiplication of three  $G_0$  expressed in imaginary time representation.

$$\Sigma(\tau) = -U^2 G_0(\tau) G_0(\tau) G_0(-\tau) \tag{2.30}$$

It is worth noting here that the same expressions for the self-energy hold both in the Matsubara and in the real frequency, T = 0, formalism (with sums turning to integrals).

We typically need to consider 32,000 points for the frequency discretization of the Green functions. This follows from the requirement of a high frequency cut-off of at least a few times U, and the need to deal at the same time with the small energy scales that are characteristic of the impurity problem. The emergence of small energy scales is characteristic of impurity problems. Nevertheless, the change of representation (from time to frequency and vice versa) can be very efficiently implemented using a Fast Fourier Transform algorithm. In practice the computational limitation is not given by the speed, but by the memory capacity of the platform.

A relevant point is the choice of an appropriate seed to start the iterative procedure. A regular  $G_0$  should be used to flow to the metallic solution. On the other hand, a singular  $G_0 \sim \frac{1}{i\omega}$  (atomic limit solution) is an appropriate choice for the insulating case. An other technical detail arises from the unavoidable need to use equation (2.15), since in the perturbative approach the self-energy  $\Sigma$  is a central quantity. A careful consideration of the branch cut of the square root is essential. This is especially relevant in the real frequency calculation. We were able to successfully overcome this problem by requiring the numerical continuity of the first derivative of the  $G_0$  obtained from equation (2.15). In the Matsubara frequency case, it was enough to require the imaginary part of the square root to have the same sign as imaginary part of the other term in the denominator.

Another issue worth mentioning is that in the real time representation, the function  $G_0(t)$  decays, for long times, as  $t^{-1}$ . Therefore,  $\Sigma(t)$  has long tails. Müller-Hartmann has proposed a clever procedure to avoid this problem. We have also implemented it finding that the results remain basically unchanged respect to calculation with the familiar causal Green function representation, that is implemented in the appendix, provided a large number of points in time/frequency are used. In general, when the Fourier transformation of functions with long tails are involved, a more precise implementation can be made with the consideration of "attenuation coefficients" [10]. However, since their use will not produce any fundamental change in the results, we have chosen not

to include it in our codes, to avoid any loss of performance.

The zero temperature (real frequency) calculation can be extended to finite temperature by the Keldysh formalism. The implementation is straight forward, it merely involves the consideration of an extended class of diagrams. Therefore, here, we just give a useful reference [13].

The source codes for the real and Matsubara frequency perturbative calculation can be found in the appendix.

#### 2.2.3 Exact Diagonalization

Let us now finally turn to the novel exact diagonalization algorithm. We will consider it in greater detail since it has especially been developed for application to models in the limit of large dimensionality.

The basic idea is as follows. The initial insight is that the Green function  $G_0$  can be well represented by a finite number of parameters in a continued fraction representation. We can then think of the parametrization of  $G_0$  as the definition of an effective non-interacting hamiltonian  $H^0$ . This hamiltonian consists basically of an impurity site connected to an effective bath with hopping amplitudes given by the elements of the parametrization. The iteration now proceeds by switching on the local repulsion  $U n_{\uparrow} n_{\downarrow}$  and then the interacting Green function G is calculated as as a continued fraction expansion. As a result we obtained a parametrization of G that can be easily related to a new parametrization of  $G_0$  through the self-consistency condition (2.7). The procedure is iterated until convergence is attained.

Let us now consider the algorithm in more detail. A local Green function G(z), at T=0, of a cluster Hamiltonian can be obtained as a continued fraction expansion. To do this, we first decompose G(z) into "particle" and "hole" contributions

$$G(z) = G^{>}(z) + G^{<}(z)$$
 (2.31)

with,

$$G^{>}(z) = \langle gs|crac{1}{z-(H-E_0)}c^{\dagger}|gs
angle$$

$$G^{<}(z) = \langle gs|c^{\dagger} \frac{1}{z + (H - E_0)}c|gs\rangle. \tag{2.32}$$

where H is the Hamiltonian,  $E_0$  is its ground state energy, and c and  $c^{\dagger}$  are the destruction and creation operators at the local site.

The respective contributions can be obtained as the continued fraction expansions

$$\langle f_0^{>} | \frac{1}{z - (H - E_0)} | f_0^{>} \rangle = \frac{\langle f_0^{>} | f_0^{>} \rangle}{z + E_0 - a_0^{>} - \frac{b_1^{>2}}{z + E_0 - a_1^{>} - \frac{b_2^{>2}}{z + E_0 - a_2^{>} - \frac{b_2^{>2}}{z + E_0 - a_2^{>} - \frac{b_2^{>2}}{z + E_0 - a_2^{>} - \frac{b_2^{>2}}{z - E_0 - a_1^{<} - \frac{b_2^{<2}}{z - E_0 - a_2^{<} - \frac{b_1^{<2}}{z - E_0 - a_2^{<} - \frac{b_2^{<2}}{z - E_0 - a_2^{<}}}$$

$$(2.33)$$

where

$$|f_0^{>}
angle = c^{\dagger}|gs
angle, \hspace{0.5cm} |f_0^{<}
angle = c|gs
angle \hspace{0.5cm} (2.34)$$

and the coefficients are determined recursively by

$$|f_{n+1}\rangle = H|f_n\rangle - a_n|f_n\rangle - b_n^2|f_{n-1}\rangle,$$

$$a_n = \langle f_n|H|f_n\rangle,$$

$$b_n^2 = \frac{\langle f_n|f_n\rangle}{\langle f_{n-1}|f_{n-1}\rangle}, \quad b_0 = 0.$$
(2.35)

This procedure is implemented in the subroutines *getfn* and *getab* in the code "exact diagonalization" that is included in the appendix.

We combine this representation of the local Green function, with the self-consistency condition (2.7) to obtain,

$$G_0 = \frac{1}{z - t^2 G^{>}(z) - t^2 G^{<}(z)}. (2.36)$$

Therefore, we can think of the  $G_0$ , as the impurity Green function of the Hamiltonian of an impurity site in an effective bath  $H^0_{eff}$  (figure 2.3). The bath is composed of two chains of fictitious atomic sites with energies given by the  $a'_is$ , and hopping elements given by the  $b'_is$ . Explicitly, the effective hamiltonian reads

$$H_{eff}^{0} = \sum_{\sigma} \sum_{\rho = >, <} \sum_{i=1}^{N_{C}} a_{i}^{\rho} c_{i\sigma}^{\rho\dagger} c_{i\sigma}^{\rho} + (b_{i-1}^{\rho} c_{i-1\sigma}^{\rho\dagger} c_{i\sigma}^{\rho} + h.c.)$$
 (2.37)

with  $\{c_0, c_0^{\dagger}\} \equiv \{c, c^{\dagger}\}$  the destruction and creation operators at the impurity site,  $b_0 = \frac{t}{2}$ , and  $N_C$  the number of atomic sites on each chain. The construction of the hamiltonian matrix is implemented in the subroutine geth.

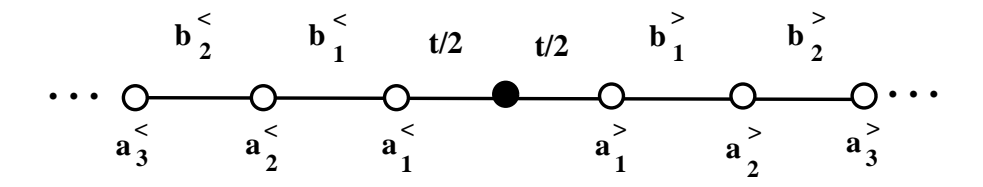


Figure 2.3: The cluster hamiltonian with the impurity site (black), and the effective bath represented by 2 chains of atomic sites (white). The site energies and hopping amplitudes are given by the parametrization of  $G_0$ .

The next step, is to switch on the local interaction term at the impurity site of the hamiltonian

$$H_{eff} = H_{eff}^{0} + H_{I}$$

$$H_{I} = U(n_{\uparrow} - \frac{1}{2})(n_{\downarrow} - \frac{1}{2}) \qquad (2.38)$$

and calculate a new interacting Green function at the impurity site. This Green function, of course, will be obtained as a new continued fraction expansion, and the whole process is then iterated. As should be clear from (2.35), this procedure only requires to compute the ground state and ground state energy from the hamiltonian (2.38). Since  $H_{eff}$  is a large sparse matrix, we have implemented a modified Lanczos procedure for the calculation of the ground state and ground state energy [14]. This can be found in the subroutine lanczos in the code in the appendix. It is possible that there is more than a single ground state. In that case, some knowledge about the effective impurity model is of great help. For instance in the case of an impurity in an insulating bath, there will be two degenerate ground states in the sectors with spin  $\pm 1$ . Therefore we have to performed the Lanczos procedure twice, and then take the linear combination of the degenerate ground states according to the symmetries of the particular model.

In general the ground state or states that are obtained from it by the action of operators such as  $c^{\dagger}$ , c,  $c^{\dagger}c$ , and H, will belong to a sector with a particular number of particles and spin projection. Therefore, it is numerically advantageous to restrict the corresponding matrix operations to the block that correspond to that particular sector of the Hilbert space. The restriction to a specific sector is conveniently implemented

by the construction of "pointers" that define the reordering of the basis within the different sectors and "masks" that allow to restrict the matrix operation to only the components that belong to the sector of interest. An implementation can be found in the subroutine sector that defines the sub-basis within the sectors, the subroutine mask that creates a "mask" given a particular sector and the subroutine hxvm which applies the hamiltonian to a state using the corresponding "mask".

We thus see that this numerical algorithm consists in the solution of the mean field equations (2.6-2.7), through the self-consistent iteration of a set of parameters  $\{a_i^>, b_i^>, a_i^<, b_i^>\}$  that define an effective hamiltonian  $H_{eff}$  or, equivalently, the parametrization of  $G_0$ .

At this point it is worth noting the following remarks. The kinetic and potential of energies can be easily and accurately obtained. To obtain their corresponding expressions, we first note that the effective hamiltonian is formally similar to the one for the Anderson impurity model. Using relations valid for that model in combination with equation (2.7), we can obtain the energy of the Hubbard model directly without frequency summations. The kinetic energy per site of the Hubbard model is given as

$$T = \frac{2t}{\beta N} \sum_{\langle j,k \rangle} \sum_{i\omega_n} G_{jk}(i\omega_n) e^{i\omega_n 0^+}. \tag{2.39}$$

Taking the limit of infinite coordination number this reduces to

$$T = \frac{2t^2}{\beta} \sum_{i\omega_n} G(i\omega_n)^2 e^{i\omega_n 0^+}.$$
 (2.40)

Using the self-consistency condition and the fact that in the Anderson model

$$\frac{2}{\beta} \sum_{i\omega_n} \sum_{\alpha} \frac{b_{\alpha}^2}{i\omega_n - \epsilon_{\alpha}} \langle c_{\sigma}(i\omega_n) c_{\sigma}^{\dagger}(i\omega_n) \rangle = \sum_{\alpha} b_{\alpha} \langle c_{\sigma}^{\dagger} c_{\alpha\sigma} + h.c. \rangle \tag{2.41}$$

where  $c^{\dagger}$  creates a particle at the impurity site and  $c_{\alpha}^{\dagger}$  creates a particle on a site neighbor to the impurity. We can finally express the kinetic energy in terms of an expectation value on the ground state

$$T = \sum_{lpha\sigma} b_{lpha} Re \langle gs| c_{\sigma}^{\dagger} c_{lpha\sigma} |gs
angle, \hspace{1.5cm} (2.42)$$

The potential energy of the Hubbard model is simply obtained as

$$V = U \langle gs | n_{\uparrow} n_{\downarrow} | gs \rangle \tag{2.43}$$

which also amounts to calculate an expectation value on the groundstate.

The local correlation functions can be easily obtained. One just has to construct the corresponding  $|f_0\rangle$  similar to equation (2.34), and follow the same procedure as for the Green functions (2.35). For example the local spin-spin correlation function is obtained by acting on the ground state with the local spin operator

$$|f_0
angle = (n_\uparrow - n_\downarrow)|gs
angle \qquad (2.44)$$

and obtaining the corresponding continued fraction expansion for the correlation function, analogous to equation (2.33). The implementation of this calculation can be found in subroutine getcorr.

Let us now make some final remarks. The number of poles in the calculated Green function is in general larger than the number of sites in the chains of the effective hamiltonian  $(N_C + N_C)$ . Therefore, in order to close the self-consistency, we make the approximation of truncating the continued fraction expansion to length  $N_C$ . That is, only the set  $\{a_i^>, b_i^>, a_i^<, b_i^>\}$  with  $i = 1, ..., N_C$  of parameters is iterated. This approximation turns out to be well behaved, and the extrapolation to an infinite system is possible, as will be shown in latter chapters. The numerical algorithm relies on the fact that the continued fraction representation captures exactly the moments of the energy of the hamiltonian, up to the order retained in the continued fraction (equal to the length of the chains  $N_C$ ). It can thus be thought of as a "moment by moment" fitting procedure. The scheme has the advantage, respect to a similar one introduced independently [15], that avoids the need for a multidimensional fit of the Green function on the imaginary axis (see chapter 6). On the other hand, it presents the disadvantage that it can be implemented practically only in the case of a semi-circular density of states (Bethe lattice).

From a numerical point of view, a basic problem is to efficiently deal with large sparse matrices, a compressed matrix storage procedure is needed. The particular implementation used here consists in simply compressing the rows of a matrix in the following form: we take, for instance, a row of the hamiltonian that is composed of mostly zeros except for a few entries, and construct a new shorter row that will only

consist of the non-zero entries in the same order as they appear. To keep note of the actual position of the elements we also construct a "pointer matrix", that is, a matrix of integers that will have in each row, the original row index of the corresponding elements. In the last component of the rows of the "pointer matrix" we write the number of non-zero stored entries of the row. With this information, we are then able to perform fast matrix multiplications, and equally important we save memory space. This procedure is directly implemented in the construction of the hamiltonian in the subroutine geth, getcp and getcd. The matrix multiplications are performed by the subroutines cxv, hxvl and hxvm.

As mentioned before, the problem of the calculation of the ground state energy (lowest eigenvalue) and the ground state (corresponding eigenvector) of a large sparse matrix, can be effectively solved by the modified Lanczos technique [14]. The computational limitation is not speed, but the memory capacity of the particular platform. Clusters of up to 10 sites can be considered in a workstation.

## 2.2.4 Comparison of the methods

To end this chapter, we illustrate how the solutions that are obtained from the different methods compare. In figure 2.4, we plot the self-energy  $\Sigma(i\omega)$  calculated at the value of the interaction U=2.4D, that places the system in its metallic state (chapter 3). Figure 2.5 shows similar results for U=3.6D, in the insulator state. A more thorough comparison will emerge from the following chapters were the results of the model will be presented in detail.

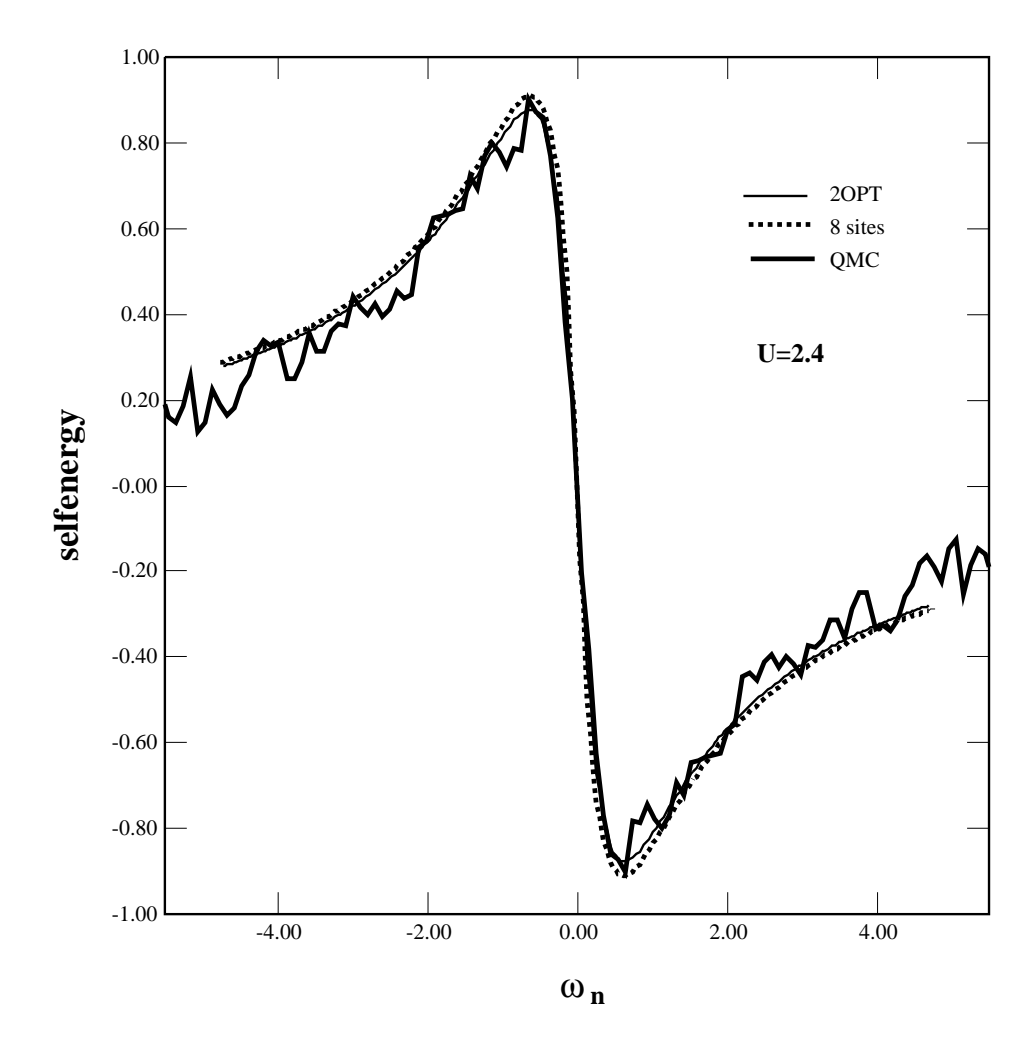


Figure 2.4: The metallic solution self-energy  $\Sigma$ , as obtained from the different methods presented in the text.

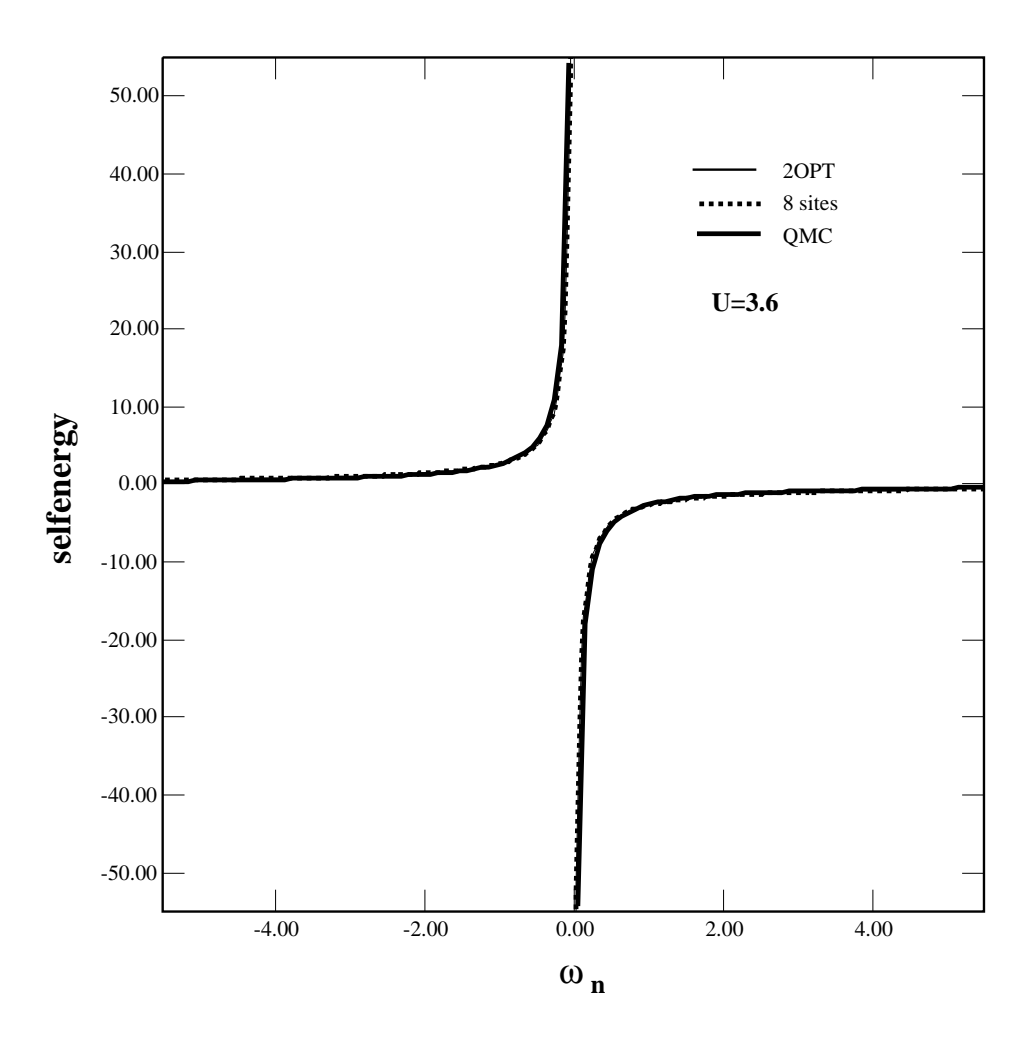


Figure 2.5: The insulator solution self-energy  $\Sigma$ , as obtained from the different methods presented in the text.

# References

- [1] W. Metzner and D. Vollhardt Phys. Rev. Lett. 62, 324 (1989).
- [2] E. N. Economou, Green's functions in quantum physics, (Springer-Verlag, 1983).
- [3] J. Hubbard, Proc. Roy. Soc. (London) A281, 401 (1964).
- [4] A. Georges, G. Kotliar and Q. Si Int. J. Mod. Phys. B 6, 705 (1992).
- [5] A. Georges and G. Kotliar, Phys. Rev. B 45, 6479 (1992).
- [6] J. Hirsch and R. Fye, Phys. Rev. Lett. 56, 2521 (1986).
- [7] J. Hirsch, Phys. Rev. B 28, 4059 (1983).
- [8] R. Blankenbecler, D. J. Scalapino, and R. L. Sugar, Phys. Rev. D24, 2278 (1981).
- [9] D. Soper, Phys. Rev. D18, 4596 (1978).
- [10] W. Press, S. Teukolsky, W. Vetterling and B. Flannery, Numerical Recipes (Cambridge University Press 1994).
- [11] K. Yamada, Prog. Theor. Phys. 53, 4, 970, (1975). K. Yosida and K. Yamada, ibid. 1286
- [12] E. Müller-Hartmann, Z Phys. B 74, 507-512 (1989), and Z. Phys. B 76, 211-217 (1989).
- [13] L. D. Landau and E. M. Lifshitz, Course of Theoretical Physics.
- [14] E. Dagotto and A. Moreo, Phys. Rev. D31, 865 (1985), and E. R. Gagliano and C. A. Balseiro, Phys. Rev. Lett.59, 2999 (1987).
- [15] M. Caffarel and W. Krauth Phys. Rev. Lett. 72, 1545 (1994).

## Chapter 3

## The Mott-Hubbard transition

## 3.1 Introduction

Strongly correlated Fermi systems in infinite dimensions were introduced by Metzner and Vollhardt [1]. They have received intensive recent attention because they are simple enough that are amenable to exact treatment and at the same time retain some of the essential features of finite dimensional models [2]. In this paper we will focus on the Hubbard model:

$$H = -\sum_{ij\sigma} t_{ij} c_{i\sigma}^{\dagger} c_{j\sigma} + \sum_{i} U n_{i\uparrow} n_{i\downarrow} - \mu \sum_{i\sigma} n_{i\sigma}$$
 (3.1)

 $-\sum_{ij} t_{ij} e^{i\vec{k}(i-j)} - \mu = \epsilon_k$  is the unperturbed one particle energy and  $\mu$  is the chemical potential which at half filling equals  $\frac{U}{2}$ .

In ref. [3], Georges and Kotliar constructed a mean field theory of the Hubbard model which becomes exact in the limit of infinite dimensionality. Independently Janis and Vollhardt [4] arrived at the same mean field equations using a very different approach. Georges and Kotliar also analyzed qualitatively a class of solutions of these equations which describe the Fermi liquid regime of this model using a mapping onto the single impurity Anderson model. These ideas have been extended to other strongly correlated electron systems [5].

In this chapter we introduce a different class of solutions which describe a Mott insulating phase. We then discuss how the transition between the Fermi liquid and the Mott insulating phase takes place within the mean field theory. We will show that one can obtain substantial analytic insights from the mean field equations. In addition we have obtained an exact, numerical solution of these equations, which we use to check our considerations.

## 3.2 The mean field equations

A basic observation in ref. [3] is that for the purpose of calculating local quantities the information about all intersite processes is contained in a single function of frequency  $G_0(i\omega_n)$  which plays the role of the Weiss field in conventional mean field theories. Given the Weiss field, the local Green's function  $G_L(i\omega_n) = -\langle c_{\sigma}(i\omega_n)c_{\sigma}^+(i\omega_n)\rangle_{S(G_0)}$  is calculated from the single site action

$$S[G_0] = \sum_{\sigma} - \int_0^{eta} \int_0^{eta} d au d au' \; c_{\sigma}^+ G_0^{-1} c_{\sigma} \;\; + \;\; U \int_0^{eta} d au \; n_{\uparrow}( au) n_{\downarrow}( au). \hspace{1cm} (3.2)$$

 $G_L$  is related to the Green's function of the Hubbard model in infinite dimension via

$$-\left\langle c_K(i\omega_n)c_K^+(i\omega_n) 
ight
angle = rac{1}{i\omega_n - \epsilon_K - \Sigma(i\omega_n)}, \hspace{1.5cm} (3.3)$$

so that,

$$G_L(i\omega_n) = \sum_K \frac{1}{i\omega_n - \epsilon_K - \Sigma(i\omega_n)}.$$
 (3.4)

To solve the model we have to compute the Weiss field  $G_0(i\omega_n)$  from the self-consistency condition equation

$$[G_0^{-1}(i\omega_n) - \Sigma(G_0, i\omega_n)]^{-1} = \int \frac{\rho(\epsilon)d\epsilon}{i\omega_n - \epsilon - \Sigma(G_0, i\omega_n)}$$
(3.5)

where,

$$\Sigma(G_0, i\omega_n) \equiv G_0^{-1} - \langle c^+ c \rangle_{S[G_0]}^{-1}$$
 (3.6)

is the self-energy of the impurity model (3.2). After solving for  $G_0$ , the self-energy of the Hubbard model is obtained by evaluating  $\Sigma$  at the self-consistent  $G_0$ .

The only place where the precise nature of the lattice enters the mean field equations is in the density of states  $\rho(\epsilon) \equiv \sum_K \delta(\epsilon - \epsilon_K)$ . We view  $\rho(\epsilon)$  as a parameter in the mean field equations. The hypercubic lattice in infinite dimensions gives a Gaussian density of states [6]. We use a bounded density of states, which captures an essential features of the band structures in *finite* dimensions. At half filling the model is particle hole symmetric and it is convenient to define quantities which are odd functions of Matsubara frequency:  $\tilde{G}_0^{-1} = G_0^{-1} - \frac{U}{2}$  and  $\tilde{\Sigma}(G_0) = \Sigma(G_0) - \frac{U}{2}$ .

## 3.3 The metal-insulator transition

In ref. [3] Georges and Kotliar analyzed the qualitative behavior of the solutions of (3.2) under the assumption that  $G_0$  is finite at zero frequency and  $ImG_0(i\omega_n = \Omega + i\delta) \neq 0$ , which they showed, implies Fermi liquid behavior. Here we would like to point out that the system of equations (3.2)-(3.5) can have a different class of solutions which describe a Mott Hubbard insulator. They are characterized by a  $G_0$  which diverges at zero Matsubara frequency. This behavior is very natural if we think in terms of the mapping onto the Anderson model proposed in ref. [3]. In that picture the original electron is split into a local degree of freedom which captures the localized aspect and a conduction band which reflects the itinerant aspect of the strong correlation problem. The local degree of freedom hybridizes with the conduction band.  $\tilde{G}_0$  is parametrized by the hybridization function  $\Delta(\epsilon)$  of the Anderson model [3],

$$\tilde{G}_0^{-1} = i\omega_n + (\mu - \frac{U}{2}) - \frac{1}{\pi} \int \frac{\Delta(\epsilon)d\epsilon}{(i\omega_n - \epsilon)}.$$
 (3.7)

The Fermi liquid regime has  $\Delta(0) \neq 0$  which binds the conduction electrons and the local moment to form quasiparticles. The insulating behavior that we find at half filling,  $\mu = \frac{U}{2}$ , corresponds to a hybridization function which vanishes as we approach zero energy, i.e.  $\Delta(0) = 0$ .

When the hybridization function vanishes at zero frequency the Kondo model obtained from the Anderson model by eliminating the charge degree of freedom scales to weak coupling as shown by Whittoff and Fradkin [7]. We then have a realization of the paramagnetic insulating solution, the charge degrees of freedom are frozen while the spin degrees of freedom are free to fluctuate.

To exhibit our new type of solution analytically we take a semi-circular density of states  $\rho(\epsilon) = \frac{2}{\pi D^2} \sqrt{D^2 - \epsilon^2}$ . We work in the limit  $U \gg D$ , and start with the assumption (which we will show is self-consistent) that  $\tilde{G}_0^{-1}(i\omega_n) \sim i\omega_n$  that is  $\Delta(i\omega_n) \to 0$  as  $i\omega_n \to 0$ . Substituting this into (3.2), one finds that the action becomes almost local (in imaginary time) at low energies, or in the language of the Anderson model, it reaches the atomic limit. The local Green's function and  $\Sigma(G_0, i\omega_n)$  are then evaluated

by taking an average of the two magnetic Hartree Fock solutions,

$$G_L(i\omega) = \frac{1/2}{G_0^{-1}(i\omega_n) - U} + \frac{1/2}{G_0^{-1}(i\omega_n)}$$
(3.8)

which gives,

$$ilde{\Sigma} = \left(rac{U}{2}
ight)^2 ilde{G}_0(i\omega_n). ag{3.9}$$

Once more we emphasize that while the magnetic HF solution of the Anderson model is invalid when  $\Delta(0) \neq 0$ , the results of ref. [7] imply that the magnetic Hartree Fock solution is qualitatively correct for large U, since  $\Delta(0) = 0$ , and in this case the Kondo coupling renormalizes to zero at low energies.

Now we show that the Ansatz  $\Delta(i\omega_n) \to 0$  as  $i\omega_n \to 0$  is indeed self-consistent. The Hilbert transform of the semi-circular density of states  $\int \frac{\rho(\epsilon)d\epsilon}{(Z-\epsilon)}$ , is given by  $\frac{2}{z+\sqrt{z^2-D^2}}$  and the self-consistency equation becomes

$$[\tilde{G}_0^{-1} - \tilde{\Sigma}(G_0)]^{-1} = \frac{2}{i\omega_n - \tilde{\Sigma}(G_0) + isgn(\omega_n)\sqrt{D^2 + (\omega_n + i\tilde{\Sigma}(G_0))^2}}$$
(3.10)

which, in combination with (3.9), leads to

$$4g_0^{-2} - U^2g_0x - 4g_0^{-1}x + (U^2 - D^2) = 0 (3.11)$$

where for convenience, we define  $x=\omega_n$  and,  $\tilde{G}_0=-ig_0$   $\tilde{\Sigma}=-i\sigma$  so that  $g_0$  and  $\sigma$  are positive when  $\omega_n>0$ . This is a cubic equation in  $g_0^{-1}$  which can be solved in closed form. Only one of the three roots corresponds to the physical solution. For small frequencies, the solution has a simple form  $g_0^{-1}=\frac{U^2}{U^2-D^2}x$ , (which requires U>D), for large frequencies  $g_0^{-1}=x$ . When  $U\gg D$  which is the region where the expansion around the atomic limit is valid, it is possible to approximate the solution of the equation (analytically continued to real frequencies) as

$$\tilde{G}_{0}^{-1} = \omega - \omega \frac{4\omega^{2} - U^{2} - \sqrt{(4\omega^{2} - U^{2})^{2} - 4(4\omega^{2} + U^{2})D^{2}}}{2(4\omega^{2} + U^{2})}$$
(3.12)

The spectral function consists of two features centered around  $\omega=\pm U/2$  with width 2D, arising from the finite imaginary part of the square root. The hybridization function can be estimated,

$$\Delta(i\omega_n) = \tilde{G}_0^{-1}(i\omega_n) - i\omega_n \simeq i\omega_n \frac{D^2}{U^2 - D^2},$$
 (3.13)

as  $\omega_n \to 0$ .

Thus we have shown that  $\tilde{G} \to i\omega$ ,  $\tilde{G}_0 \to (i\omega)^{-1}$  and  $\tilde{\Sigma} \to (i\omega)^{-1}$  in the low frequency limit is a solution of the infinite dimensional Hubbard model. This solution describes a Mott-Hubbard insulator characterized by a divergent self-energy and a gap in the single particle spectrum of order U-2D.

A crucial question is how one goes from the Fermi liquid solutions characterized by Fermi liquid low frequency behavior,  $\tilde{\Sigma}(i\omega_n) \sim -i\omega_n$  to the Mott-Hubbard insulator regime described in this chapter. To answer this question, we go back to the metallic solution and gradually increase the interaction U. As described in ref. [5], the Fermi liquid regime at half filling corresponds to the formation of the Abrikosov-Suhl Kondo resonance in Anderson model. Equations (3.2)-(3.5) constitutes a system of functional equations for the Weiss field  $G_0^{-1}(i\omega_n)$  which cannot be solved analytically, (we will turn to its numerical solution below).

To gain insight into the mechanism that destroys the Fermi liquid resonance peak one would like to project the functional equation on a small space of "relevant variables". Here we present a simple argument for the vanishing of the resonance, in a later chapter this issue will be revisited in greater detail. Since  $\Delta(0)$  is unrenormalized in the Fermi liquid regime, we focus on a variable W, which describes the region over which the effective hybridization is nonzero at low energies. In the Anderson model analogy it is the effective bandwidth of the conduction electrons. We envision an approximate parametrization of the exact solution of the system, at low frequencies, of the form  $\tilde{G}_0^{-1} = -isgn(\omega_n)D/2 + O(i\omega_n)$  for  $|\omega_n| < W$ , and  $G_0^{-1} \approx i\omega_n$  for  $|\omega_n| > W$ . Imagine solving the system (3.2)-(3.10) by iteration. At the  $n^{th}$  step we have some finite value of  $W = W^{(n)}$ , and obtain from the impurity model a self-energy,  $\tilde{\Sigma} = (1 - \frac{1}{Z(G_0)})\omega + O(\omega^2)$ . For a large U/D, Z is just the inverse of the Kondo temperature,  $Z(G_0) = 4\frac{W^{(n)}}{D} \exp \frac{-\pi U}{4D}$ . The next step in the iteration, is to solve equation (3.10), which gives,

$$W^{(n+1)} = 4W^{(n)} \exp \frac{-\pi U}{4D}.$$
 (3.14)

It is clear that for large U the effective bandwidth iterates to zero, reaching the insulating regime. For small  $\frac{U}{D}$ , solving the impurity model gives a Z of order unity.

The iteration step then gives  $W \approx D$ . This is the Fermi liquid regime. Separating these two regimes, is the critical  $U_c$ . In this scenario the Mott transition is driven by the shrinking of the dynamical range of the Fermi-liquid regime, the height of the quasi-particle peak remains unrenormalized. Related ideas have been put forward by Khurana [8].

To confirm these qualitative arguments, we solve equations (3.2)-(3.5) numerically using quantum Monte Carlo simulations. The procedure to compute  $\Sigma(G_0)$  is based on the algorithm of Hirsch and Fye, and of Gubernatis, Hirsch and Scalapino [9] who studied the single impurity Anderson model. The functional equation is solved using an iterative procedure. The technical details of the simulations are discussed in the previous chapter. The Mott-Hubbard transition with the semi-circular density of states is found at  $U \approx 3.1$  for D=1 (all energy scales are renormalized by D), which is slightly lower than the result obtained from the Gutzwiller approximation, where  $U_c$  is calculated to be  $32D/3\pi$  [10, 11]. In figure 3.1 we show plots of  $(Im\tilde{G}_0)^{-1}$  vs  $\omega_n$  for U=2, U=3 and U=3.6.

Figure 3.2 shows the self-energy for the same values of the interaction. Below  $U_c$ , we distinguish two Fermi liquid sub-regimes characterized by small and large slopes of the self-energies respectively. The plot for U=2 is characteristic of the weakly correlated Fermi liquid regime where the Weiss field  $\tilde{G}_0^{-1}$  decreases monotonically with frequency. The plot for U=3.0 is representative of the strongly correlated Fermi liquid regime characterized by a small dip in  $\tilde{G}_0^{-1}$ , making it to increase towards its zero frequency value  $\frac{D}{2}$  as we reduce the frequency. The behavior for  $U>U_c$  is completely consistent with our analytic arguments. The numerical results are obtained at an inverse temperature  $\beta=64$ . The agreement of the numerical data with our analytic arguments gives us confidence that no new features will appear as we take the  $\beta\to\infty$  limit.

To further confirm the opening of a gap, we also measured the discontinuity in the chemical potential vs. occupation number as shown in figure 3.3. At finite temperatures the metal insulator transition we obtained, becomes a crossover. However this crossover is quite sharp. For example, at finite temperatures for  $U > U_c$  the  $\mu$  vs n curve should be continuous because there is always activation from the lower to the upper Hubbard

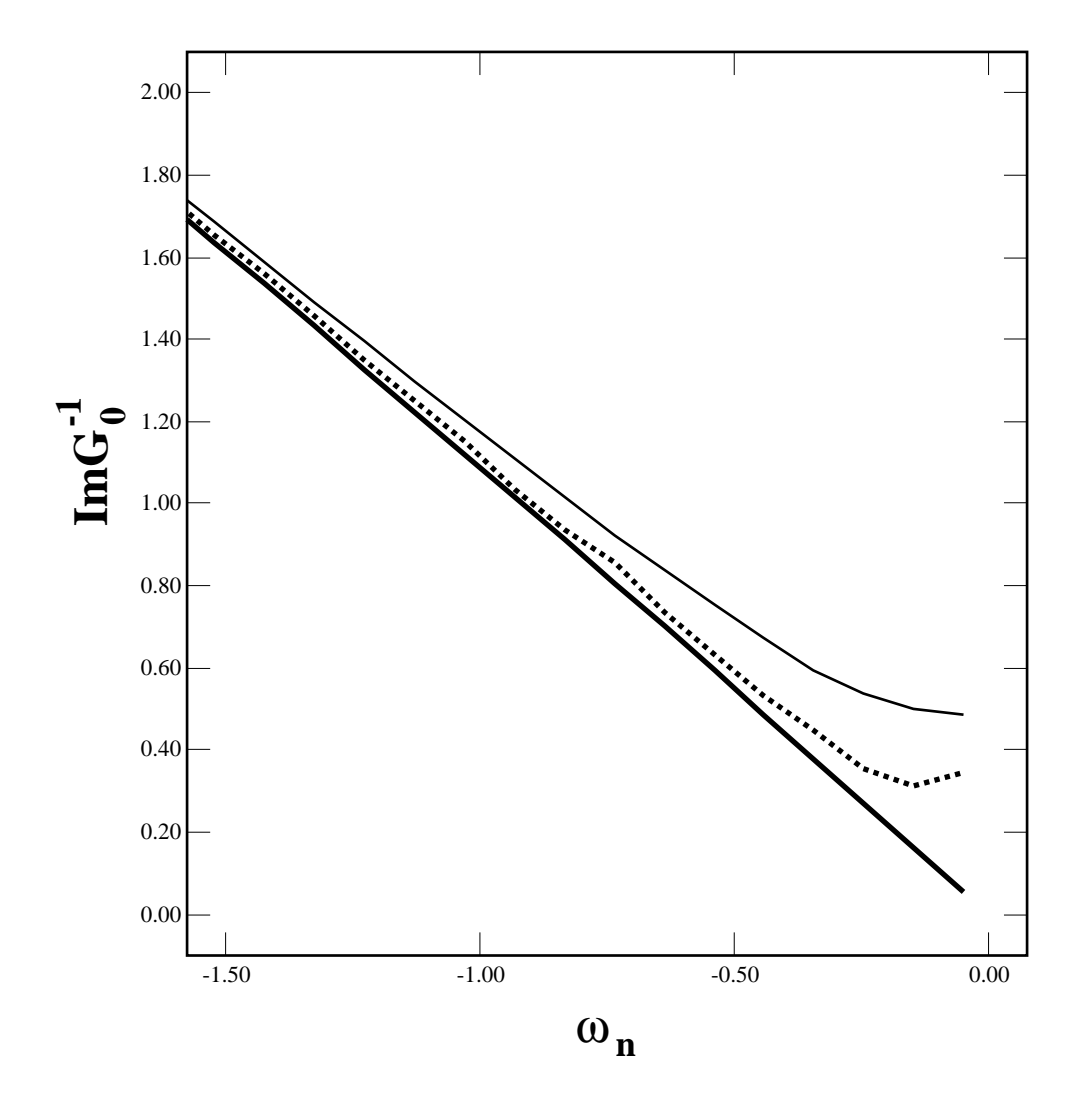


Figure 3.1: The imaginary part of the Weiss field  $\tilde{G}_0^{-1}$  as a function of Matsubara frequency for U=2 (solid line), U=3 (dotted line), and U=3.6 (dashed line), at  $\beta=64$ . All energy scales are renormalized by the half-bandwidth D=1. For  $U< U_c$  the Weiss field approaches its unrenormalized zero frequency value D/2. For  $U>U_c$  it matches the analytical solution of equation (11) in the text,  $Im(\tilde{G}_0^{-1})=-\omega_n,\,\omega_n\to\infty,$  and  $Im(\tilde{G}_0^{-1})=-\frac{U^2}{U^2-D^2}\omega_n,\,\omega_n\to0.$ 

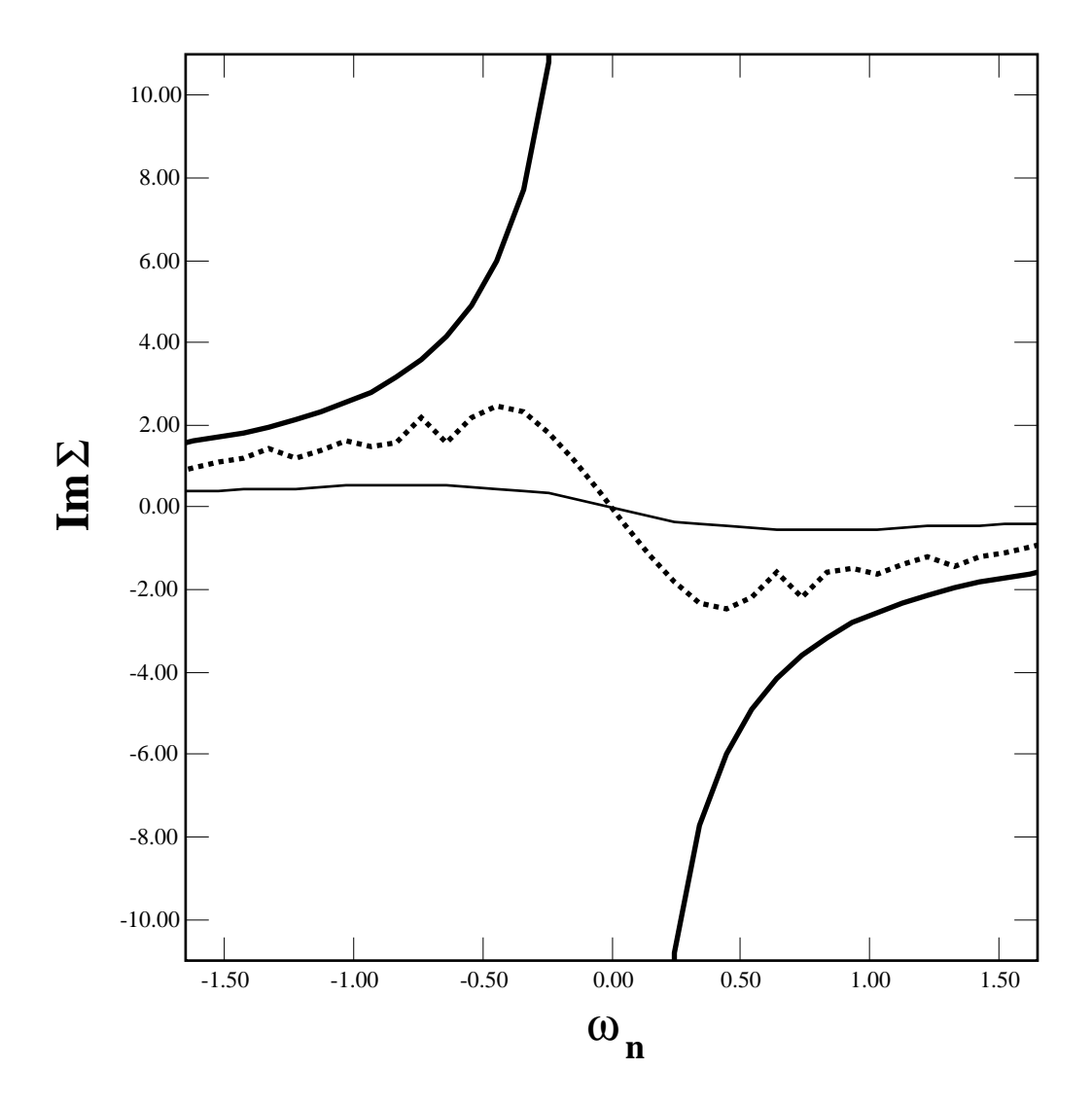


Figure 3.2: The self-energy  $\tilde{\Sigma}$  as a function of Matsubara frequency for U=2 (solid line), U=3 (dotted line), and U=3.6 (dashed line), at  $\beta=64$ . For  $U<U_c$  the self-energy is linear at low frequencies with a slope increasing with U. The noise of the plot at U=3 is due to the proximity to the critical U.

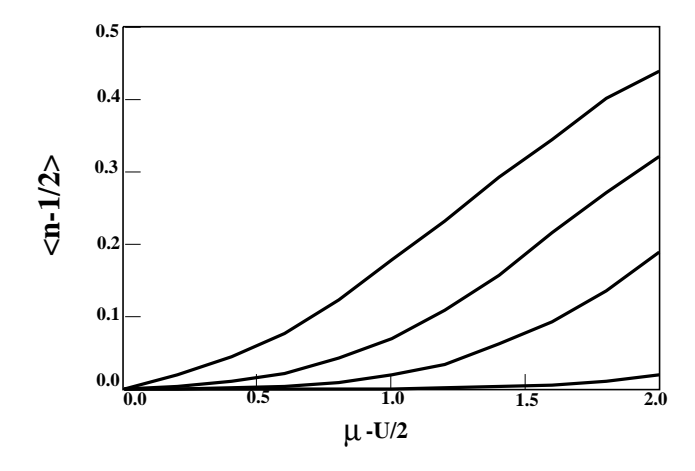


Figure 3.3: The particle occupation as a function of the chemical potential  $\mu - \frac{U}{2}$  for (top to bottom) U = 2, 3, 4, 6 at  $\beta = 4$ .

band. Nevertheless the curves in figure 3.3, obtained at finite temperatures are nearly discontinuous because the temperature is much smaller than the Mott Hubbard gap.

We also measured the local spin spin autocorrelation function of the Hubbard model, in imaginary time. It is given by the spin spin correlator of the impurity model. Our measurements are consistent with the following behavior: on the insulating side of the transition there is long range order in imaginary time  $lim_{\tau \to \infty} \langle m(\tau)m(0) \rangle = m > 0$  for  $U > U_c$  and it decays to zero on the metallic side. m = 0, for  $U < U_c$ .

## 3.4 Discussion

In this chapter we have focused on the paramagnetic one particle Green's function of lattice models in infinite dimensions with a bounded density of states. We also studied the unbounded Gaussian density of states. In this case the numerical results for  $G_0$  and the self-energy are very similar to that of unbounded ones. However, analytically can be seen that there is a qualitative difference in the spectral function of the local Green's function G: in the unbounded case, above  $U_c$  the one particle spectral function has a pseudogap at the Fermi level. The rate at which the density of states decays at zero energy is simply related to the decay of the Hilbert transform of the density of states

at infinity.  $Im(G(\omega)) \sim \rho(\omega-1/\omega), \, \omega \to 0.$ 

We concentrate on the paramagnetic solution in order to bring out the physics of the charge degrees of freedom. The physics of this phase depends only on the density of states. Müller-Hartmann [6] has shown that in infinite dimensions several lattice dispersions, (some which correspond to non-nested lattices) share the same density of states. The question on the nature of the magnetic order and the magnetic transition temperature will be considered in later chapters. It requires to specify more information on the form of the dispersion than just the density of states. Nonfrustrated lattices have antiferromagnetic transition temperatures which are exponentially small for small U, and of order  $\frac{t^2}{U}$  for large U, with a maximum transition temperature at U of order t. Frustrated lattices can have much lower transition temperatures. The semi-circular density of states used in our calculations can be realized in a Cayley tree with infinite coordination number [12]. This lattice is not frustrated and bipartite. As a result, at zero temperature it has antiferromagnetic long range order for an arbitrary value of U. The semi-circular density of states is also realized in a lattice where every site is connected to every other site, and the hopping matrix elements are independent Gaussian random variables suitably scaled as the inverse square root of the number of lattice sites to have a good thermodynamic limit. While this model has randomness, the one particle Green's function is non random, i.e., it is self averaging. This model is very frustrated and it does not order magnetically. A schematic representation of this fully-connected lattice is shon in figure 3.4.

#### 3.5 Conclusions

To conclude, we have found a new regime for the infinite dimensional Hubbard model at half filling. We showed that the large U narrow quasiparticle feature [3] disappears above a critical value of U. This is due to a divergence in the inverse of the self-consistent Weiss field  $G_0$ , which allows our  $d=\infty$  model to map onto an Anderson model with vanishing effective hybridization at the Fermi level  $(\Delta(0)=0)$ . The Kondo model obtained from the Anderson model via the Schrieffer-Wolff transformation then flows to zero coupling at low energies. In this case the self-energy  $\Sigma$  has a pole singularity

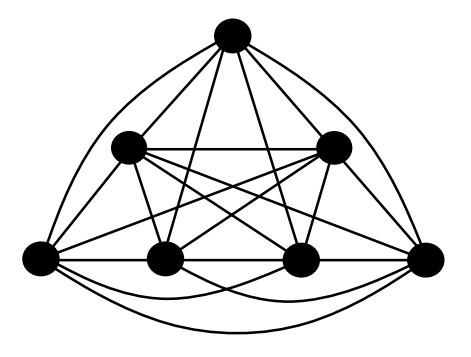


Figure 3.4: Schematic representation of the fully connected lattice. The hopping elements are scaled as  $t_{ij}=\epsilon_{ij}\frac{t}{d^{1/2}}$  with  $\epsilon_{ij}$  independent Gaussian random variables.

at zero frequency which reflects the opening of a Mott-Hubbard gap in the one particle spectrum. Our solution for the case of very large U is essentially the same as that in Hubbard III [13]. What has been accomplished in this chapter is: (1) to show how Hubbard-like physics emerge in the limit of large d and large U, (2) to obtain a true Fermi liquid solution on the metallic side of the transition, and (3) to show how a transition between the two regimes takes place as we change the value of U.

# References

- [1] W. Metzner and D. Vollhardt Phys. Rev. Lett. 62, 324 (1989).
- [2] For a recent review and a list of references see D. Vollhardt, *Physica B* **169**, 227 (1991).
- [3] A. Georges and G. Kotliar, Phys. Rev. B 45, 6479 (1992).
- [4] V. Janis and D. Vollhardt, Int. Journ. Mod. Phys. B, 6, Nos 5 & 6, 731 (1992).
- [5] A. Georges, G. Kotliar and Q. Si Int. J. Mod. Phys. B 6, 705 (1992).
- [6] E. Müller-Hartmann, Z. Phys. B, 74 507-512 (1989), and E. Müller-Hartmann, Z. Phys. B, 76 211-217 (1989).
- [7] D. Whittoff and E. Fradkin, Phys. Rev. Lett. 64, 1835 (1990).
- [8] Anil Khurana, Phys. Rev. B 4316 (1989).
- [9] J. Hirsch and R. Fye, Phys. Rev. Lett. 56, 2521 (1986), and J. E. Gubernatis, J. E. Hirsch, and D. J. Scalapino, Phys. Rev. B35, 8478 (1987).
- [10] For a brief review see D. Vollhardt, P. G. J. van Dongen, F. Gebhard and W. Metzner, Mod. Phys. Lett. B4, 499 (1990).
- [11] W. F. Brinkman and T. M. Rice, Phys. Rev. B 2, 4302 (1970).
- [12] P. G. J. van Dongen, Mod. Phys. Lett. B5, 861 (1991).
- [13] J. Hubbard, Proc. Roy. Soc. (London) A281, 401 (1964).

# Chapter 4

# The transition at zero temperature

function and the local spin spin correlation function

### 4.1 Introduction

In his pioneer work on the metal-insulator transition (MIT) [1], Mott envisioned that in transition metals, as the Coulomb interaction among the charged carriers increases, the system will undergo a first order transition from a metal to an insulator. The first serious attempt using many-body theory to produce this effect is due to Hubbard [2]. He based his calculation on the atomic limit which naturally leads to a two-band picture, the lower and upper Hubbard bands separated by the interaction U. He concluded that the MIT happens at  $U_c \approx D$  the bandwidth, and a gap opens gradually as a function of U. Although this treatment provides a good insulating solution for large U, it fails to capture correctly the low energy physics in the metallic side: the Fermi liquid quasiparticles are absent [3]. Brinkman and Rice (BR) [4] attacked the problem from the opposite limit by using a Gutzwiller variational wave function, and found the MIT at a much higher  $U_c$ . The Gutzwiller wave function gives a good Fermi liquid description for the metallic side, but misses the insulating side completely and lacks the high energy excitations which are the precursors, in the metal, of the upper and lower Hubbard bands of the insulating solution.

Until now, it is still not clear what the right picture of the transition is: How is Hubbard's solution related to BR's? Does the gap open continuously or does it jump at the transition? Behind these questions lies the far more interesting issue, How does Fermi liquid theory break down when the interactions become strong?

Recently Metzner and Vollhardt [5], recognized a simple but nontrivial limit of the

Hubbard model: large dimensionality. In that limit, the Gutzwiller approximation used by BR becomes exact, and a major assumption made in Hubbard-III, the self-energy being site diagonal, also becomes exact. In fact, a set of self-consistent equations that describe the paramagnetic phase of the Hubbard model for  $d \to \infty$  [6, 7] is reminiscent of the Hubbard-III treatment. Therefore, it is natural that a solution in the  $d = \infty$  limit should provide a bridge between the Hubbard-III and the BR treatments and a clear picture of the Mott transition.

We have seen in the previous chapter how Quantum Monte Carlo (QMC) simulations were used for solving these equations. They were also independently studied by two other groups [8]. All found the existence of a metallic-like solution for small U and insulating-like state for large U, thus providing strong evidence that a metalinsulator transition indeed exists. But, due to the limitations of QMC, the picture of the transition is still unclear.

Our strategy here is to combine QMC with a more conventional tool: the perturbation expansion. QMC, been essentially exact, is used as a benchmark to select among the various perturbative schemes the one that works. Perturbation is then used in the low temperature region that QMC fails to reach, to obtain important information like the density of states. The result is a complete numerical solution of the self-consistent equations at half-filling and T=0. The metallic side exhibits aspects of the BR's solution, particularly, the divergence of the effective mass of quasi-particles as  $U \to U_c$ . On the other hand, the insulating side is very similar to that of the Hubbard III. The emergence of a three band picture close to the transition: the two well separated upper and lower Hubbard bands, and a central narrow quasi-particle band at the Fermi level provides a bridge between the two approaches. The continuous narrowing of the quasi-particle peak drives the MIT. Right above the transition, a full gap is already opened, as predicted by Mott for a different reason. This is valid as long as the density of states is bounded. We focus in this type of DOS, because we believe it provides the correct scenario to understand the physics in finite dimensions.

The central object in the self-consistent scheme [6] is a quantity  $G_0$  which plays the role of the effective field in magnetic systems.  $G_0$  is defined in an effective local action

S obtained by integrating out all the degrees of freedom except for a single site 0,

$$S[G_0] = -\int \int d au d au' \; c_{0\sigma}^+ G_0^{-1} c_{0\sigma} \; + \; U \int d au \; (n_\uparrow - 1/2) (n_\downarrow - 1/2).$$

The self-consistent equations for the Weiss field  $G_0$  are written in terms of an impurity self-energy  $\Sigma_{imp}(G_0) = \langle c^+c^- \rangle_{S(G_0)}^{-1} - G_0^{-1}$  and the lattice density of states  $\rho(\epsilon) = \sum_k \delta(\epsilon_k - \epsilon)$ 

$$[G_0^{-1} - \Sigma_{imp}(G_0)]^{-1} = \int rac{
ho(\epsilon)d\epsilon}{i\omega + \mu - \epsilon - \Sigma_{imp}(i\omega)}.$$
 (4.2)

The impurity self-energy evaluated at the self-consistent  $G_0$  [6] gives the self-energy of the Hubbard model in infinite dimensions.

We use a semi-circle density of states as in Hubbard-III,  $\rho(\epsilon) = \frac{2}{\pi D} \sqrt{1 - (\frac{\epsilon}{D})^2}$ , which corresponds to a Bethe lattice in infinite-d, where Hubbard's hopping parameter t = D/2 [9]. The set of self-consistent equations then becomes:

$$G_0^{-1} = i\omega_n + \mu - t^2 G(i\omega_n), \quad G = \langle c^+ c \rangle_{S(G_0)}$$
 (4.3)

 $G(\omega_n)$  being the local Green function of the Hubbard model. The spin index has been removed because paramagnetic phase is assumed. Throughout the calculation the bandwidth D is set to unity.

#### 4.2 Methodology

The key part in solving the above equation is to obtain the self-energy  $\Sigma$ , given  $G_0$ . This is equivalent to solving the Anderson impurity model with an arbitrary hybridization function [6]. Although QMC is exact, it has severe limitations: the data collected are on the imaginary axis and the analytic continuation cannot be always reliably carried out; a more essential difficulty is that the method does not allow to investigate the zero temperature limit. In the previous chapter, we have found evidence that at low temperatures there is a value of the interaction  $U_c$  where a metal insulator transition takes place.  $U_c$  was then determined by the sudden development of a divergence in the Matsubara self-energy at low frequencies. This is a strong indication for a metal-insulator transition that is driven by correlation effects. Nevertheless, it is no conclusive,

since the divergence of the self-energy is cut-off by the finite temperature (or the lowest Matsubara frequency). In this chapter with the aid of insights obtained from a very accurate perturbative scheme, we will be able to unambiguously establish the existance of a metal-insulator transition from the exact QMC data.

As mentioned in the introduction, we will try to find a perturbative calculation that enable us to investigate the metal insulator transition in the zero temperature limit. The perturbative approaches fall into four categories. (a) fully self-consistent perturbation in  $G_{ii}$  [10]; (b) noncrossing approximation (NCA) [11]; (c) analytic expansion in U as in Yamada and Yosida [12] (YY); and (d) a fourth approach proposed by Metzner [13] who systematized the expansion in the kinetic energy. It is discussed in [6] that (a) does not produce the correct high-energy features, while it is well known that the NCA becomes inaccurate at low temperatures. We will show below, that approach (c) can successfully reproduce the QMC data, and argue why it does so.

Figure 4.1 shows a comparison of QMC with perturbation calculations using (c) for values of U on the metallic side and the insulating side.

With almost point by point fit on the metallic side and the insulating side, a posteriori one can rationalize the success of the perturbative calculation as follows: (1) the transition happens at an intermediate value of U, around which it is known that perturbation to second order captures all the important features of the Anderson impurity model as was shown by YY; (2)the essential ingredient that drives the transition is not in the self-energy calculation, but rather in the process of enforcing self-consistency. Higher order corrections to  $\Sigma$  will only change the exact value of  $U_c$ , but not the nature of the transition. (3) From the pioneer work of YY and Zlatic, Horvatic, and Sokcevic [14] we know that the impurity problem is analytic in U. Therefore it is natural to treat the analytic parts of the problem using a power series expansion while the non-analytic aspects of the problem are addressed using a self-consistent scheme. (4) It can produce the atomic solution exactly (see below). Therefore this approximation becomes at least an interpolation between the two extreme limits (free case U = 0, and atomic t = 0). The latter is purely accidental, and unfortunately does not apply to the asymmetric case.

Figure 4.1: Comparison of Matsubara self-energy obtained from Quantum Monte Carlo (crosses) to that from perturbation calculation(dots). For U=2 on the metallic side and U=3.6 on the insulating side at a T=1/64. Note that on the insulating side the growing deviation at low energies is purely due to the  $\omega^{-1}$  divergency, the relative error remains the same but the absolute error becomes bigger.

We calculate the self-energy to second order following [6] and [12]. The perturbation expansion is generated by  $H_I = U(n_{\uparrow} - 1/2)(n_{\downarrow} - 1/2)$ . To second order, only the bubble diagram survives,

$$\Sigma(t) = U^2 G_0(t)^2 G_0(-t). \tag{4.4}$$

It is worth noting here that the same expression for the self-energy holds both in the zero temperature and in the Matsubara formalism. The zero temperature causal Green function is then used to obtain the density of states and other quantities.

### 4.3 Mott transition

An observable that signals the MIT is the density of states (DOS) at the Fermi surface. Figure 4.2 shows the zero temperature DOS as a function of interaction U. As pointed out by Müller Hartmann [10], the height of the peak at zero frequency is unrenormalized by the interactions in a theory with a k independent self-energy, as long as one is in the Fermi liquid regime. Therefore the value of the one particle spectral function jumps discontinuously to zero at the Mott transition. Right after the transition, the structure of a full gap is already in place.

Since  $\mathrm{Im} G_0^{-1} = -\frac{D^2}{4} \mathrm{Im} G$ , the width  $\Delta$  of the quasi-particle at the Fermi level is also the width of the coherent hybridization  $\Delta(\omega)$  in the Anderson model analogy. As U approaches  $U_c$ , this scale vanishes in the following way:  $G_0$  develops a singularity at an energy  $\omega_0 = \sqrt{\Delta D}$ , very near the real axis ( $\sim \Delta^2$ ), which then leads to a similar singularity in the self-energy. The Mott transition happens when the pole collapses to zero, and  $\Sigma$  becomes divergent.

A different view of the transition is obtained by measuring the local spin-spin correlator using QMC. On the metallic side,  $\langle m(\tau)m(0)\rangle\approx e^{-\Delta\tau}$ . Long range order sets in as  $\Delta\to 0$  as shown in figure 4.3. A spin mode whose energy is independent of momentum (local paramagnon) is softening as  $U\to U_c$ .

We now proceed to provide an analytical description of the transition, focusing on the most important quantity  $\Delta$ . Using the relation (4.3), we rewrite  $G_0$  as,

$$G_0^{-1}(z) = z - \frac{D^2}{4} \int \frac{\bar{\rho}(\epsilon)d\epsilon}{z - \epsilon},$$
 (4.5)

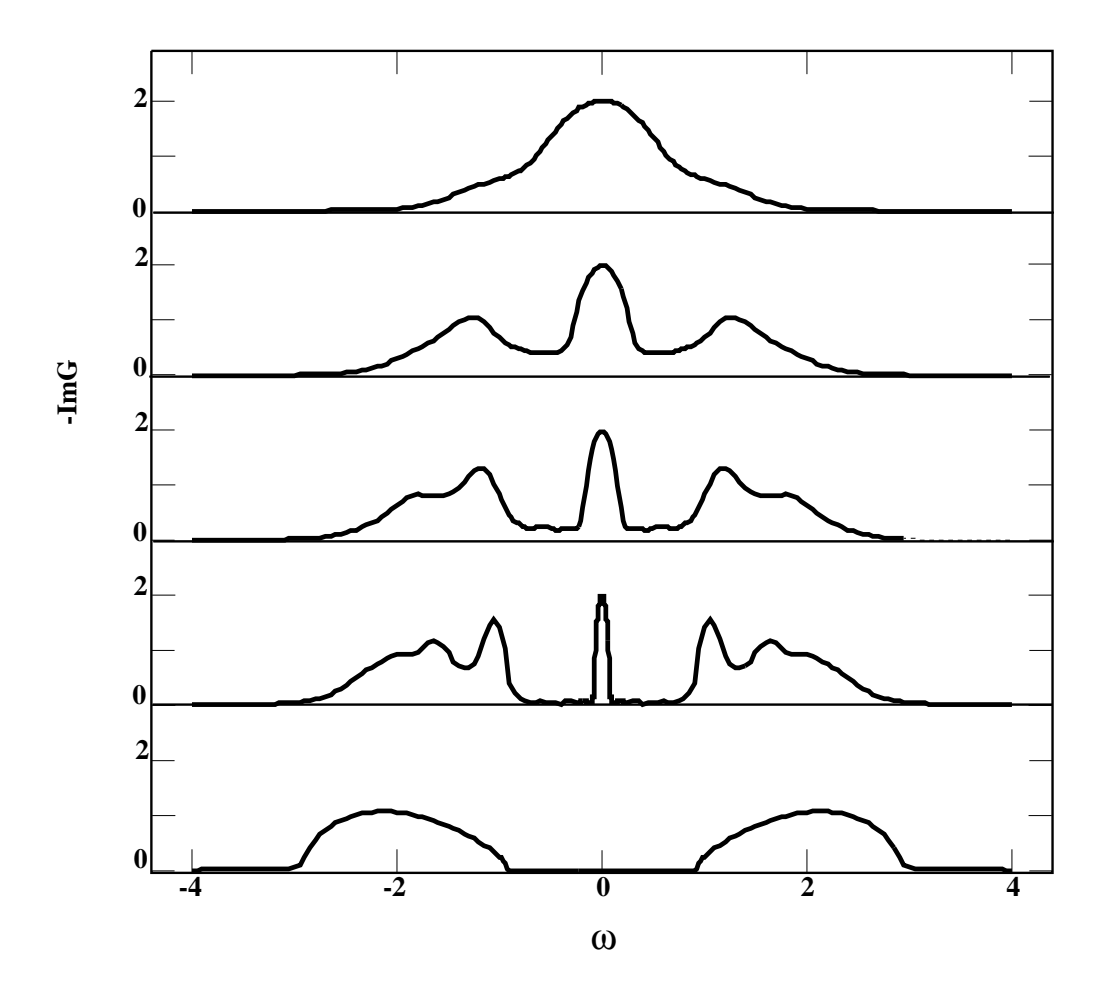


Figure 4.2: Density of states -ImG at zero temperature as a function of U. From top to bottom, U=1,2,2.5,3,4.

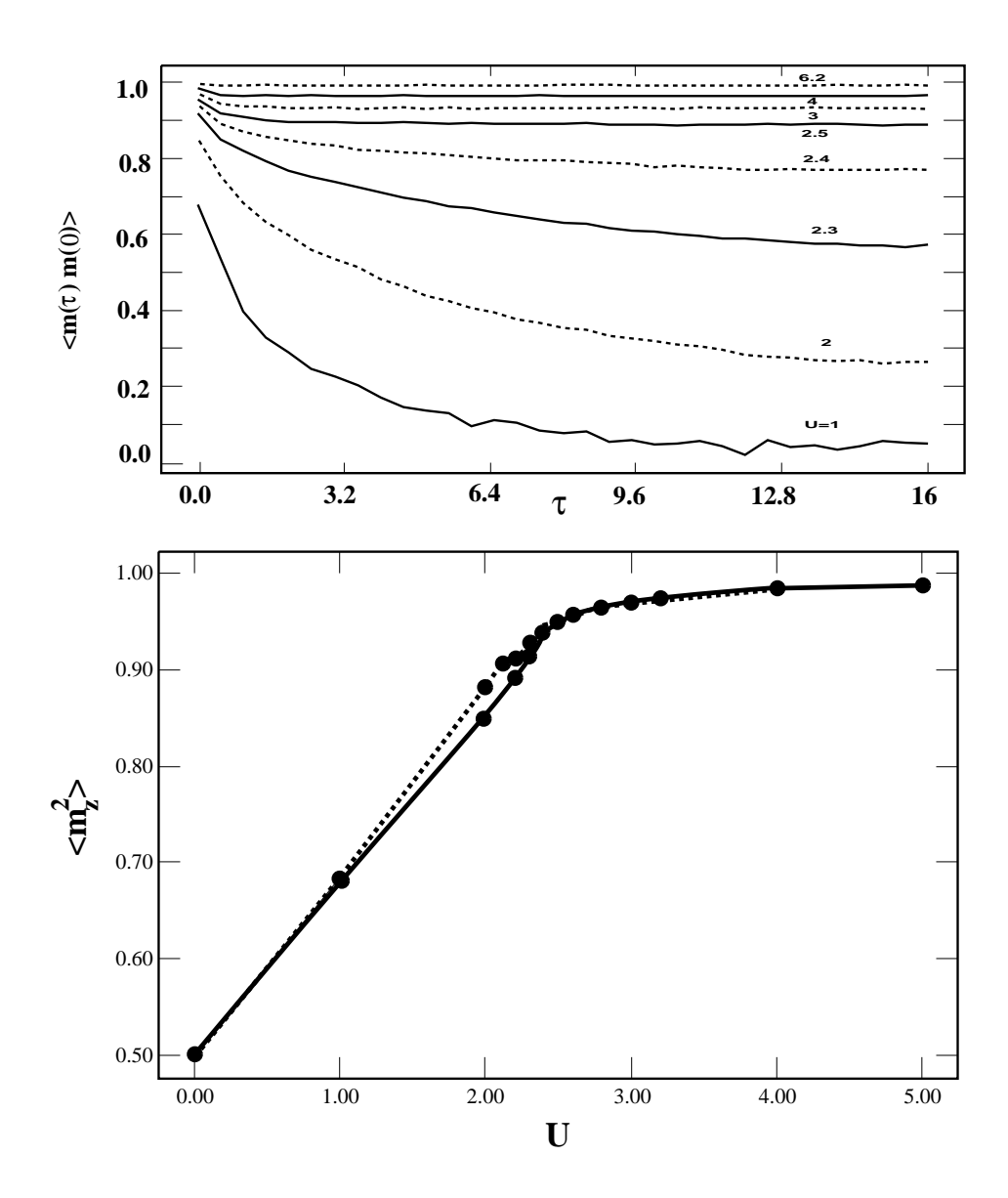


Figure 4.3: a) Spin-spin correlation function obtained from Monte Carlo for  $\beta=32$ , and U=1,2,2.3,2.4,2.5,3,4,6.2. The correlation length  $\sim \Delta^{-1}$  diverges as we approach the insulating side. b) Local moment as a function of U for two temperatures:  $\beta=16(\text{dots}),32(\text{solid})$ .

where  $\bar{\rho}(\epsilon)$  is the DOS of the fully interacting system shown in figure 4.3. Its three peak feature can be represented by a Lorentzian at the center with width  $\Delta$ , and two semi-circles centered at  $\pm U/2$ , with half-width D. The weight of the center Lorentzian is determined by demanding that  $\text{Im}G_0^{-1}(0) = D/2$ . A simple and good approximation for  $G_0$ , close to the transition can be then obtained:

$$G_0^{-1}(z,\Delta) = \frac{1}{2}\left(z - \frac{D\Delta}{z + i\Delta sanz}\right). \tag{4.6}$$

We checked numerically, that the parametrized  $G_0$  and the self-energy calculated from it are in good agreement with the actual  $G_0$  and  $\Sigma$ . The impurity self-energy has an explicit  $\Delta$  dependence when calculated from the parametrized  $G_0$ .

$$\Sigma(\omega, \Delta) = U^2 \int F^3(\lambda) e^{-|\lambda|\omega} d\omega,$$
 (4.7)

where

$$F(\lambda) = \int_0^\infty \rho(\epsilon) e^{-i\lambda \epsilon} d\epsilon, \tag{4.8}$$

and,

$$\pi 
ho(\omega) = -\mathrm{Im}G_0 = rac{2D\Delta^2}{(\omega^2 - D\Delta)^2 + \Delta^2\omega^2}.$$
 (4.9)

As  $\Delta \to 0$ ,  $\rho(\omega)$  peaks sharply at  $\omega_0^2 = D\Delta - \Delta^2/2$ , approaching a  $\delta$  function with unit weight. Thus, for low frequencies, we find the real part of the self-energy,

$$\Sigma(\omega, \Delta) = \frac{-U^2 \omega}{9(D\Delta - \Delta^2/2)}.$$
 (4.10)

On the other hand, the self-consistency equation for  $G_0$  in equation (4.2),

$$G_0^{-1}(\omega, \Delta) = \frac{1}{2}(\omega + \Sigma(\omega, \Delta) + \sqrt{(\omega - \Sigma(\omega, \Delta))^2 - D^2}), \tag{4.11}$$

requires that to linear order in  $\omega$ ,  $\Sigma = \frac{D}{\Delta}\omega$ . Since the self-consistency is an iterative procedure, we can equate the above two expressions for the self-energy iteratively:

$$\Delta_{n+1} = \frac{9D}{U^2} (D\Delta_n - \Delta_n^2/2)$$
 (4.12)

There are two fixed points of the iteration,  $\Delta^* = 2D(1 - \frac{U^2}{U_c^2})$  which is stable for  $U < U_c = 3D$ , and  $\Delta^* = 0$ . The first one is the Fermi liquid fixed point discussed in [6], the second one is the insulating fixed point. We focus here on the fate of the

metallic solution. The destruction of the  $\Delta=0$  (insulating) solution will be discussed in a latter chapter. When  $U=U_c$  the two fixed points merge into one: the unstable Mott point. We note here that  $\Delta=0$  is the exact atomic solution, because from the parametrized  $G_0$  we have  $G_0(\tau)=\theta(\tau)-\frac{1}{2}$ , and consequently,  $\Sigma(\tau)=\frac{U^2}{4}[\theta(\tau)-\frac{1}{2}]$ , or  $\Sigma=\frac{U^2}{4}G_0$  (see previous chapter).

Since  $\Delta/D \approx m/m^*$ , the fixed point solution also provides the critical behavior of the effective mass close to the transition,  $m^*/m \propto (1-(U/U_c)^2)^{-1}$  which is the same as BR. The numerical results are plotted in figure 4.5. The transition occurs at  $U_c = 3.37D \approx 8\bar{\epsilon}$ , as in BR. However, above the transition in the insulating side, the two band-features are not quite symmetric around  $\pm U/2$ , meaning there are still some residual kinetic energies gained from local hoppings [15]. The fact that virtual double occupancy is present in the insulating side which gives a finite exchange constant is also clear from QMC measurements of the local spin-spin correlation function, which shows a reduced moment on the insulating side,  $\langle m_z^2 \rangle = 1 - 2 \langle n_{i\uparrow} n_{i\downarrow} \rangle$  figure 4.3. QMC also indicates that the paramagnetic spin susceptibility does not diverge as the effective mass does [16]. These are the crucial differences between the exact solution in  $d = \infty$  and that of BR.

Another important quantity is the occupation number  $n_k$ . Since  $\Sigma$  is independent of k, it is more convenient to label n with the non-interacting energy  $\epsilon$ ,

$$n_{\epsilon} = -rac{1}{\pi} {
m Im} \int_{-\infty}^{0} rac{d\omega}{\omega - \epsilon - \Sigma(\omega)}.$$
 (4.13)

Figure 4.4 shows, in accordance with the divergence of  $m^*$ , the jump at the Fermi level Z continuously shrinking to zero. The monotonic behavior found here should be contrasted with the results using Gutzwiller wave function in 1-d [17].

With the new insights obtained from the present perturbative approach, it is worth revisiting the *exact* finite temperature QMC results. In particular we consider the question of the existance of a true correlation induced transition at low enough temperatures. This issue is relevant since the perturbative approach being an approximation, cannot demonstrate the existence of the transition. The low energy scale of the problem, as the correlations become important, is set by the width of the central quasiparticle peak in

Figure 4.4: Particle occupation number vs. noninteracting energy  $\epsilon$  as a function of U=2,2.5,3,4, obtained from perturbative calculations. Inset:  $m/m^*$  vs. U calculated from the slope of the real part of the self-energy at the Fermi level.

the density of states. It is clear that if the temperature is bigger than this energy scale, for a fixed value of U, the low frequency quasiparticle states cannot be sustained. At those temperatures we should see a crossover from a metallic-like solution at low U, to an insulating-like solution as the interaction is increased. This solutions could be characterized by a Green function with an imaginary part that extapolated to zero frequency results non-zero or zero respectively. Also we should observe that this crossover takes place at higher values of the temperature as the interaction U is increased, since the Hubbard bands become more widely separated. On the other hand, if the temperature of the system is lower than the characteristic low energy scale, the correlated quasiparticle state is realized. In this case, we should see, unlike in the previous situation, that as we lower the temperature, the metallic state can be mantained for increasingly bigger values of the interaction, and eventually sharply disappear into an insulating one, as a critical value  $U_c$  is reached. In figure 4.5 we see this whole scenario being realized. We plot the temperature where the QMC solution changes from metallic-like to insulating-like as a function of the interaction U. We also plot the value of the quasiparticle width obtained from the perturbative approach, as a definition of the low energy scale given a value of U. This is of course justified by the excellent agreement that we already discussed before. We observe that the results illustrate our previous discussion, as the change in the slope in the MIT curve changes when the temperature is smaller than the low energy scale. This is a definite signature of the existence of a true transition between a metallic and insulating state driven by correlation effects. We will revisit this issue in later chapters to a greater detail. It will turn out that there is a whole region where two soloutions, one metallic and the other insulating, are allowed to coexist. This will lead to the result that the transition is indeed first order at low enough temperature.

### 4.4 Conclusion

We have shown in this chapter a simple and reliable perturbative scheme to treat the impurity model. It enables us to provide a detail analysis of the Mott transition in the  $\infty - d$  limit. Our solution connects two very different approaches, the BR and

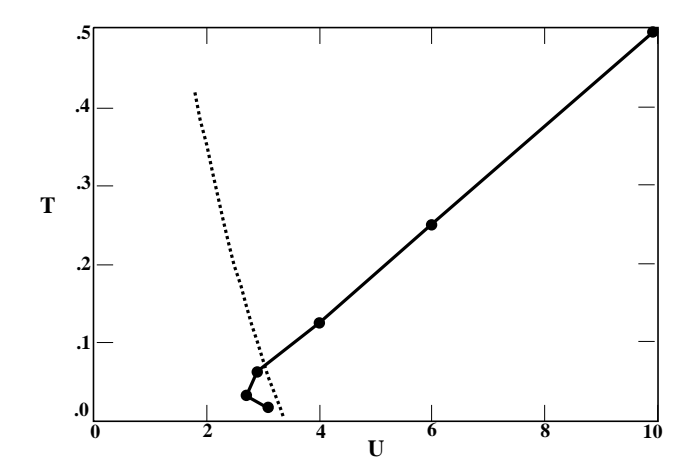


Figure 4.5: The temperature where the QMC solution changes from metallic-like to insulating-like as a function of the interaction U (bold line). The low energy scale defined as the quasiparticle width obtained from 2OPT (dotted line). A true transition occurs only at the lowest temperatures where the change in the slope is observed in the metal-insulator boundary line. The transition is driven by the interaction U instead of the temperature only below this scale. For higher temperatures it becomes a crossover.

the Hubbard-III. In particular it shows a continuous increase of the effective mass as  $U \to U_c$  from below, and contrary to one's intuition, this is followed by the discontinuous opening of a gap in the one particle spectrum at  $U_c$ . On the insulating side, there is an unsaturated local moment with long range order in the imaginary time indicating a nonzero double occupancy, and consequently, a finite magnetic exchange and a nondivergent magnetic susceptibility.

## References

- [1] N. F. Mott, Phil. Mag. 6, 287 (1961).
- [2] J. Hubbard, Proc. Roy. Soc. (London) A281, 401 (1964). This paper is commonly known as the Hubbard-III.
- [3] D. M. Edwards and A. C. Hansen, Rev. Mod. Phys. 40, 810 (1968).
- [4] W. F. Brinkman and T. M. Rice, Phys. Rev. B 2, 4302 (1970).
- [5] W. Metzner and D. Vollhardt, Phys. Rev. Lett. 62, 324 (1989).
- [6] A. Georges and G. Kotliar, Phys. Rev. B 45, 6479 (1992).
- [7] V. Janis, Z. Phys. B 83, 227 (1991), Phys. Rev. B40 11331 (1989), and V. Janis and D. Vollhardt, Int. Journ. Mod. Phys. B, Vol. 6, Nos 5 & 6, 731 (1992).
- [8] M. Jarrell, Phys. Rev. Lett. 69, 168 (1992). M. Rozenberg, X. Y. Zhang and G. Kotliar, Phys. Rev. Lett. 69, 1236 (1992). A. Georges and W. Krauth, Phys. Rev. Lett. 69, 1240 (1992).
- [9] P. G. J. van Dongen, Mod. Phys. Lett. B5, 861 (1991).
- [10] E. Müller-Hartmann, Z Phys. B 74, 507-512 (1989), and Z. Phys. B 76, 211-217 (1989).
- [11] Th. Pruschke, D. L. Cox and M. Jarrell, Euro Phys. Letts. 21, 5 (1993).
- [12] K. Yamada, Prog. Theor. Phys. 53, 4, 970, (1975). K. Yosida and K. Yamada, ibid. 1286
- [13] W. Metzner, Phys. Rev. B 43, 8549 (1991).
- [14] V. Zlatic, B. Horvatic and D. Sokcevic, Z. Phys. B59, 151(1985).
- [15] This observation was made by Florian Gebhard.
- [16] Th. Pruschke, D. L. Cox and M. Jarrell, Phys. Rev. B 48, (1993).
- [17] H. Yokoyama and H. Shiba, J. Phys. Soc. Jpn.56, 1490 (1987), and C. Gros, R. Joynt, and T. M. Rice, Phys. Rev. B36, 381 (1987).

# Chapter 5

# The transition at finite temperature

### 5.1 Introduction

The Mott transition, that is the metal insulator transition induced by the electron electron interactions in a periodic system, has been investigated theoretically and experimentally for many years [1]. Experimentally it seems to be realized in three dimensional transition metal oxides such as  $V_2O_3$  and can be driven by varying pressure, temperature, and composition.

From a theoretical point of view, several ideas have been put forward. Hubbard first introduced the notion of Hubbard bands, which are formed by the states that describe propagating empty and doubly occupied sites. For large U these bands split, and as U is reduced, there is a critical value where the two bands merge again [2]. This is the Hubbard picture of the metal-insulating transition.

Brinkman and Rice, building on the work of Gutzwiller, started from the metallic phase which they described as a strongly renormalized Fermi liquid with a characteristic Fermi energy scale gradually collapsing as the transition is approached [3]. The metal insulator transition in this view is driven by the disappearance of the Fermi liquid quasiparticles.

Slater pointed out that the metal insulator transition is always accompanied by long range antiferromagnetic order, and viewed the doubling of the unit cell which makes the band structure of the system that of a band-insulator, as the driving force behind the metal insulator transition [4].

Building on earlier ideas [5, 6, 7, 8, 9], a new mean field theory of strongly correlated electron systems has been developed. It is based on a mapping of the models of strongly

correlated electrons onto impurity models supplemented by a self-consistent condition [10, 11]. This approach becomes exact in the limit of infinite dimensions [5] and can be investigated using a variety of techniques. In this chapter, we continue our study of the Mott transition in the Hubbard model in large dimension, expanding on the results of previous chapters, and those of ref. [12, 13, 14]. In particular, we make comparisons of our solutions to experimental observations, and find good agreement considering the relative simplicity of the model. Related work on this problem has been carried out independently by other groups [15, 16, 17, 18].

The chapter is organized as follows: In section 5.2, we start by briefly reviewing the general framework of [11] to present the set of self-consistent equations that describe the Hubbard model in infinite dimensions. We concentrate on the semi-circular density of states which can be realized on a Bethe lattice, and on other lattices having various amounts of magnetic frustration. The mean field equations are functional equations that determine a Weiss field function  $G_0$  and involve a mapping of the problem onto an Anderson impurity model. Two realizations of the Hubbard model, which share the same density of states but have very different magnetic properties, are introduced later to shed light into the issue of magnetic ordering. We close the section with a discussion of the methods used to analyze this problem.

To study the mean field equations we use a combination of exact methods such as quantum Monte Carlo, exact diagonalization, and analytic arguments exploiting the well understood structure of the Anderson impurity model. We also rely on an approximate method, which was proposed by Georges and Kotliar, to extract low temperature information. We stress that, while at high temperature this method [13] gives results in very good agreement with the quantum Monte Carlo, in principle is only an approximate scheme and we point out some of its limitations. The results obtained with this method are useful because they provide a concrete analytic realization of the functional  $\Sigma_{imp}[G_0]$  defined in section 5.2, and illustrates in a simple example the important role played by the self-consistency condition [9].

In section 5.3 we describe the thermodynamics and present the finite temperature phase diagram of the system of the magnetically disordered state. In frustrated lattices,

where magnetic order is not possible, the phase diagram features a region bounded by two values of the interaction  $U_{c1}$  and  $U_{c2}$ , where a metallic and an insulating solutions coexist. We demonstrate that at finite T, the actual transition takes place at an intermediate value  $U_c$  where the free energy of the two solutions cross. We further show that  $U_{c1} < U_c < U_{c2}$ , and the metal-insulator transition is of first-order like a liquid-gas transition. While the region of stability of the two phases are model dependent and will vary upon changing the density of states or adding more general interactions to the Hamiltonian, there are some general lessons that can be drawn by studying the disappearance of the metallic and the insulating solution. These are general scenarios for describing a strongly correlated metal and a Mott insulator.

In section 5.4 we study the behavior of the system close to the critical value of the interaction  $U_{c2}$ , where the metallic state disappears. We consider the results in relation to the Brinkman Rice scenario for the metal-insulator transition.

In section 5.5 we analyze the disappearance of the insulating solution, and relate it to Hubbard's early ideas.

Section 5.6 is devoted to the study of the correlation functions. In particular, we address the question of how they behave as the transition takes place. We relay on a combination of analytical arguments and QMC simulations to discuss these points.

In section 5.7, we address the important question of solutions with magnetic long range order. We verify that in a bipartite lattice, Slater's ideas for the metal-insulator transition become relevant. On the other hand, when a partial degree of magnetic frustration in allowed, a rich phase diagram is obtained. The results are considered in regard to the experimental phase diagram of  $V_2O_3$ .

Finally, in section 5.8, we study the transition as a function of doping. On the way, we make qualitative comparisons to existing experimental data, in  $La_{1-x}Sr_xTiO_3$ .

We conclude by arguing that the Hubbard model and its extended version is at least a qualitatively correct model for the description of some basic features of these systems. We also present various theoretical questions raised by our work.

## 5.2 The self-consistent equations

Our starting point is the Hubbard Model:

$$H = -\sum_{\langle i,j \rangle} (t_{ij} + \mu) c_{i\sigma}^{\dagger} c_{j\sigma} + U \sum_{i} (n_{i\uparrow} - \frac{1}{2}) (n_{i\downarrow} - \frac{1}{2}), \tag{5.1}$$

where summation over repeated spin indices is assumed.

In the limit of the coordination number d going to infinity, the hopping matrix elements can be chosen to give a semi-circular density of states of width 4t, and are scaled as  $t_{ij} \sim \frac{t}{\sqrt{d}}$  [5] to provide a well defined and non trivial limit. This density of states is realized on lattices with different amounts of magnetic frustration such as the Bethe lattice (no frustration), the fully-connected fully-frustrated lattice (FF) [13], and the two sublattice fully-frustrated model (TSFF), which allows to mimic a varying degree of frustration [14].

Now we proceed to briefly review the the self-consistent equations which give the paramagnetic solution in large d following the scheme of [9]. The central object in this approach is a quantity  $G_0$  which plays the role of the effective field in magnetic systems.  $G_0$  is defined in an effective local action  $S_{eff}$  obtained by integrating out all the degrees of freedom except for a single site 0,

$$S_{eff}[c,c^{\dagger}] = \sum_{\sigma} \int d au d au' c_{\sigma}^{\dagger}( au) G_0^{-1}( au- au') c_{\sigma}( au') + U \int_0^{eta} d au (n_{i\uparrow}( au) - rac{1}{2}) (n_{i\downarrow}( au) - rac{1}{2}). ~~(5.2)$$

This action is identical to the one of an Anderson impurity model with arbitrary hybridization. The self-consistent equations for the Weiss field  $G_0$  are written in terms of an impurity self-energy  $\Sigma_{imp}(G_0) = \langle c^{\dagger}c \rangle_{S(G_0)}^{-1} + G_0^{-1}$  and the lattice density of states  $\rho(\epsilon) = \sum_k \delta(\epsilon_k - \epsilon)$ 

$$[G_0^{-1} - \Sigma_{imp}(G_0)]^{-1} = \int \frac{\rho(\epsilon)d\epsilon}{i\omega - \epsilon - \Sigma_{imp}(G_0)}.$$
 (5.3)

The impurity self-energy evaluated at the self-consistent  $G_0$  gives the self-energy of the Hubbard model in infinite dimensions [9].

We use a semi-circle density of states,  $\rho(\epsilon) = \frac{2}{\pi D} \sqrt{1 - (\frac{\epsilon}{D})^2}$ . The set of self-consistent equations then becomes

$$G_0^{-1} = i\omega_n - t^2 G(i\omega_n), \quad G = -\langle c^{\dagger} c \rangle_{S(G_0)}$$
 (5.4)

 $G(i\omega_n)$  being the local Green function of the Hubbard model. The spin index has been removed, since magnetic disorder is implicitly assumed. This last equation, which does not require the explicit calculation of  $\Sigma_{imp}$ , and can be used as an alternative to (5.3). The semi-circular density of states is realized in the Bethe lattice with coordination d, in the limit that d becomes infinite, and with Hubbard's hopping parameter equal to  $\frac{t}{\sqrt{d}}$ . In this case t = D/2. This lattice with nearest neighbor hopping, if not frustrated, will strongly favor a Néel ordered state at low temperatures.

The semi-circular density of states is also realized in the fully-frustrated model [12] [19].

$$H_{FF} = -t \sum_{i,j=1,d} \epsilon_{ij} c_{i\sigma}^{\dagger} c_{j\sigma} + U \sum_{i} (n_{i\uparrow} - \frac{1}{2})(n_{i\downarrow} - \frac{1}{2}). \tag{5.5}$$

Summation over repeated spin indices is assumed. Here  $\epsilon_{ij}$  are quenched independently distributed Gaussian random variables with zero mean and a variance  $\langle \epsilon_{ij}^2 \rangle = \frac{1}{d}$ . This model has a semi-circular density of states with a half-bandwidth equal to 2t and therefore shares the same *local* properties as the Bethe lattice but of course is not expected to display Néel order at any finite temperature. Finally, we can vary the degree of frustration by studying a two sublattice version of the fully-frustrated model (TSFF). The Hamiltonian is given by

$$H_{TSFF} = -t_1 \sum_{i,j \in Aor\, B} \epsilon_{ij} c_{i\sigma}^{\dagger} c_{j\sigma} - t_2 \sum_{i \in Aj \in B} \epsilon_{ij} c_{i\sigma}^{\dagger} c_{j\sigma} + U \sum_{i \in A \cup B} (n_{i\uparrow} - \frac{1}{2})(n_{i\downarrow} - \frac{1}{2}). \ (5.6)$$

This model interpolates between the fully-frustrated lattice and the Bethe lattice in the antiferromagnetic phase while still sharing a semi-circular local density of states. In this case  $D = \frac{\sqrt{t_1^2 + t_2^2}}{2}$ . Figure 5.1 contains a schematic representation of the TSFF model. Notice that while the hamiltonians (5.5) and (5.6) contain randomness, the single particle properties are self-averageing. The single particle Green functions are the same for any typical realization of the random variables  $\epsilon_{ij}$ .

Let us mention in passing that there are other lattices that lead to the same mean field theory in the limit of large dimensionality. One is obtained from the TSFF model by considering the interlattice hopping parameter  $t_2$  as a gaussian variable (in the same manner as  $t_1$  was defined). This model is fully random and has a variable degree of frustration. Another possibility is a lattice with n.n. constant hopping parameter  $t_1$ ,

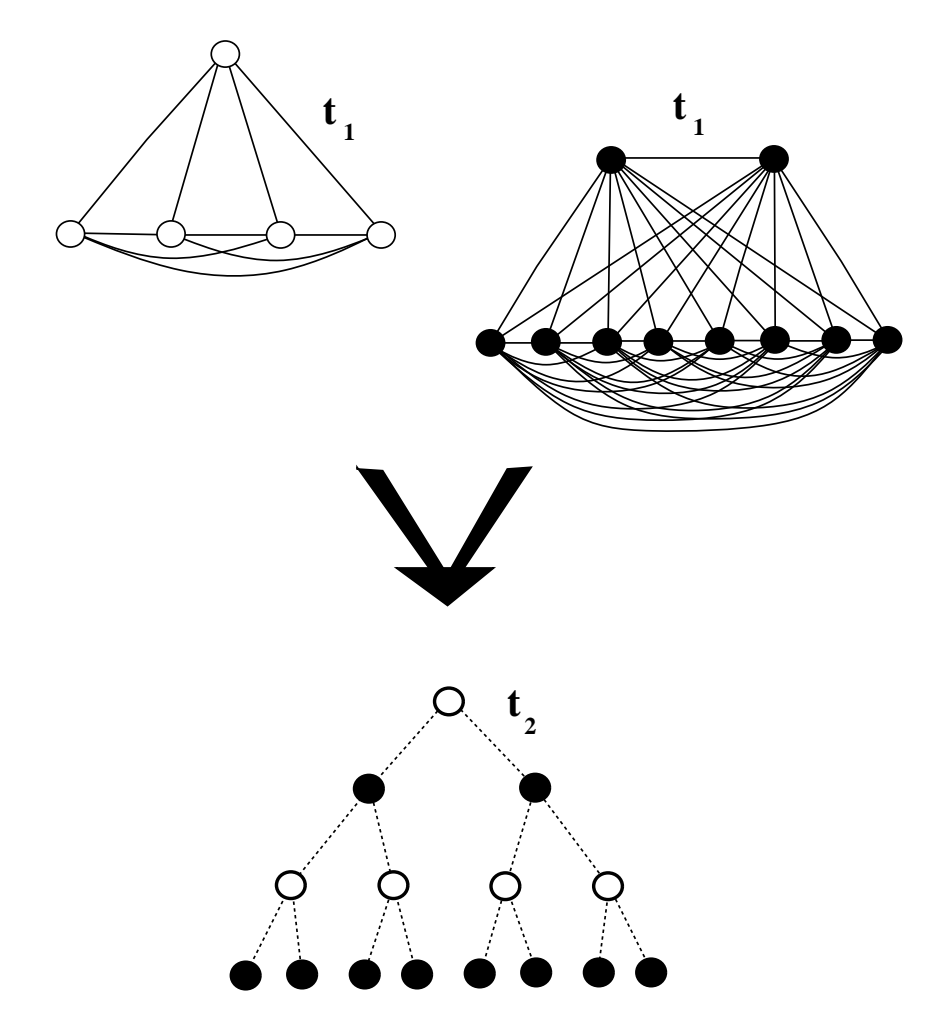


Figure 5.1: Schematic representation of the two sublattice fully frustrated model (TSFF). The fully-connected fully-frustrated sublattices A (white dots) and B (black dots) at the top of the figure, are combined into a single lattice through the interlattice hopping elements  $t_2$ .

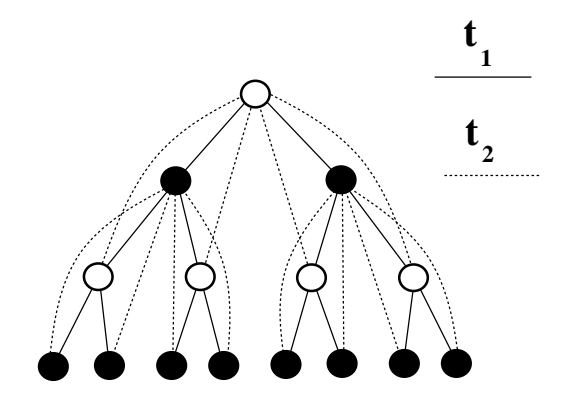


Figure 5.2: Schematic representation of the Bethe lattice with next nearest neighbor hopping. This model has the same mean field equation as the TSFF but does not have randomness.

and n.n.n. constant hopping parameter  $t_2$ . This model does not contain randomness and is schematically shown in figure 5.2.

As in a previous chapter we have studied the semi-circular density of states instead of the Gaussian density of states which is realized in the large dimension limit of a hypercubic lattice, because the latter has long tails which prevent the development of a true Hubbard gap. For a study of the hypercubic lattice see [15, 16].

When antiferromagnetism sets in, the Weiss field depends on the sublattice and the spin. For a general bipartite lattice in the Néel phase  $G_{A\sigma} = G_{B-\sigma}$  the equations were derived in [11]. For the Bethe lattice, the equations are simplified to

$$G_{0A\sigma}^{-1} = i\omega - t^2 G_{B\sigma}$$

$$G_{0B\sigma}^{-1} = i\omega - t^2 G_{A\sigma}$$
(5.7)

where A denotes one sublattice and B the other. The two impurity Green functions  $G_A$  and  $G_B$  are evaluated independently given  $G_{0A\sigma}$  and  $G_{0B\sigma}$  and the single site action,  $S_{eff}$  defined at the beginning of the section.

Finally in the two sublattice fully-frustrated model, which mimics an intermediate degree of frustration, the mean field equations in a phase where the A and B sublattices

magnetize in opposite directions are given by

$$G_{0A\sigma}^{-1} = i\omega - t_1^2 G_{A\sigma} - t_2^2 G_{B\sigma}$$

$$G_{0B\sigma}^{-1} = i\omega - t_1^2 G_{B\sigma} - t_2^2 G_{A\sigma}$$
(5.8)

In a previous chapter we have discussed that the exact treatment of the problem by a quantum Monte Carlo solution of the impurity can be reproduced, remarkably well, by the second-order perturbative calculation proposed in [20]. The perturbative calculation allows us to investigate the low temperature behavior of the system, including T=0, which is unattainable by the QMC approach. To second order in perturbation,

$$\Sigma[G_0](\tau) = -U^2 G_0^3(\tau). \tag{5.9}$$

We can understand the success of this approximation for the following reasons: 1) It is good for weak couplings (U << t) by construction, since the expansion is around U=0. As shown by Yamada and Yosida (YY), it is able to produce not only the Abrikosov-Suhl resonance, but also the upper and lower incoherent bands as well. YY showed that the  $4^{th}$  order correction is two orders of magnitude smaller that the  $2^{nd}$  order contribution for the range of the interaction where the MIT occurs. 2) The atomic limit is exactly captured. When U is very large, and the system is deep in insulating side,  $G_0^{-1} \approx i\omega_n$ , the non-magnetic Hartree-Fock solution of the Green function becomes exact,

$$G_L(i\omega) = \frac{1/2}{G_0^{-1}(i\omega_n) - U/2} + \frac{1/2}{G_0^{-1}(i\omega_n) + U/2}$$
 (5.10)

therefore, the self-energy reads,

$$\Sigma = \frac{U^2}{4} G_0(i\omega_n) \tag{5.11}$$

which is identical to the self-energy that results from inserting  $G_0$  in Equation (5.9) and Fourier transforming. Thus, the second order approximation is at least an interpolation scheme which becomes exact for both the  $U \to 0$  and  $U \to \infty$  limits.

A third numerical technique that we developed for the study of the present type of models is an exact diagonalization algorithm. It is based on a parametrization of the function  $G_0$ , with a finite set of parameters that are then used as input for an

effective Anderson hamiltonian. This technique allows for a non perturbative solution of the model in all parameter range. It is particularly effective for the investigation of the insulating phases with and without magnetic order. A detailed description of this procedure can be found in the second chapter.

The mean field equations are coupled functional equations to be solved for the Weiss field  $G_0$  and the local Green function. The most difficult aspect of the mean field theory is the solution of the Anderson impurity model in an arbitrary bath. The essential insight is to use reliable approximations to calculate  $G[G_0]$  in eq. (5.2), this step captures the local aspects of the problem. The self-consistency condition (5.3-5.4) then brings back the lattice aspect. Several techniques are used in the analysis of the mean field equations. They range from qualitative arguments and analytic perturbative schemes to numerical methods based on quantum Monte Carlo (QMC) [12] [15, 16], exact diagonalization (ED) [21, 22] and second order perturbative calculations (2OPT) [13, 14]. To obtain details of the low energy behavior we have developed the projective self-consistent method which is the lattice equivalent for large d problems of the Wilson renormalization group method [23]. An important point here is that no single technique can be pointed out as the most suitable, but the insights obtained on the Mott transition problem rely on a combined use of these techniques to elucidate the different aspects of the physics. We will illustrate the capabilities and the range of applicability of the different approaches in the following sections where we present the results for the model.

## 5.3 Phase diagram and thermodynamics

The schematic phase diagram of the Hubbard model at half filling in a fully-frustrated lattice is shown in figure 5.3 (from 2OPT). To determine the phase diagram we proceed in three steps: a) We first determine the region where the two paramagnetic solutions coexist. b) We then compare their free energy, their crossing determines the phase boundary. The study of the magnetically ordered phase and the calculation of the Néel temperature; along with a discussion on whether the metal insulator transition found in step b) is preempted by a magnetic ordering transition, will be considered in detail in a later section.

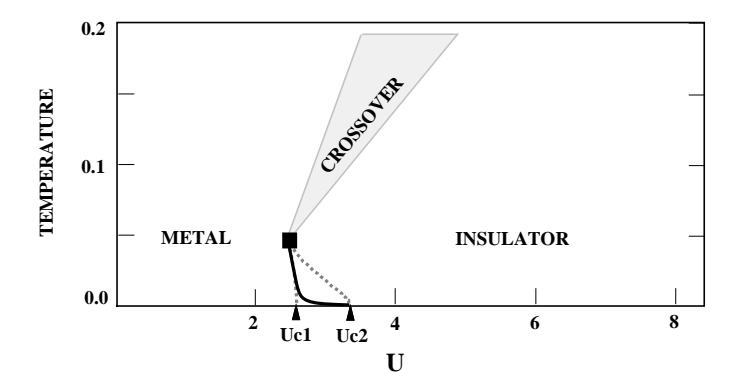


Figure 5.3: Phase diagram of the fully-frustrated model. It is possible to continuously move from one phase to the other since at high T the transition becomes a crossover. The dashed lines indicate the region where the metallic and the insulating solutions coexist. The filled square indicates the end of the first-order line in a second-order point.

At low temperature there are two phases a Fermi liquid metal characterized by a non zero density of states at zero energy and paramagnetic insulator with a gap in the one particle excitation spectra. The metallic solution disappears at the dotted line ending at  $U_{c2}$ , while the insulating solution persist down to the dotted line ending at  $U_{c1}$ . There is a region enclosed by the lines  $U_{c1}(T)$  and  $U_{c2}(T)$ , where both the metallic and the insulating solutions are allowed. Within this region, there is a first order boundary where the two very different solutions cross in free energy, and several quantities experience a jump: the specific heat, the susceptibility, the number of doubly occupied sites, etc. The first order line has a negative slope indicating that the paramagnetic insulating phase has a higher entropy than the metallic phase. This line ends in a second order point at  $T_{MIT} \approx 0.05$ . Above this temperature one can go continuously from the metal to the insulator via a crossover region which is shaded in the phase diagram. The first order line has a negative slope indicating that the paramagnetic insulating phase has a higher entropy than the metallic phase.

At T=0, the metallic state is lower in energy than the paramagnetic insulator and therefore the first order line ends in a T=0 second order quantum critical point, denoted  $U_{c2}$  in the figure (this point is discussed in detail in the next chapter). In this region is where the Brinkman Rice scenario for a metal insulator transition becomes relevant. In fact, the mean field theory has confirmed the essentials of the Brinkman Rice picture as applied to the vicinity  $U_{c2}$  and allowed us to obtain non critical corrections to this picture. We also notice that the paramagnetic insulating solution and the metallic solution are very close in energy and therefore departures from full frustration will stabilize the insulating state.

The ED and QMC methods confirmed that the qualitative phase diagram obtained from 2OPT is correct, with only the values of  $U_{c1}$  and  $U_{c2}$  slightly reduced. With ED we obtained  $U_{c1}\approx 2.15$  and  $U_{c2}\approx 3$ . For comparison notice that the Hubbard III approximation gives  $U_c^{HIII}=\sqrt{3}\approx 1.732$ , and the Brinkman Rice approach gives  $U_c^{BR}=8\bar{\epsilon}\approx 3.37$ . The metallic state of the system can be well described by a narrow central quasiparticle peak characterized by an effective Fermi energy  $\Delta\equiv zD$  where z is the quasi-particle weight,  $z=(1-\frac{d\Sigma}{d\omega})^{-1}$ , plus two high energy incoherent features at  $\pm \frac{U}{2}$  corresponding to the upper and lower Hubbard bands. The effective Fermi energy  $\Delta$  is found to go to vanish as  $U_{c2}-U$ . The insulator state consists of incoherent features only. Notice however that the shapes of the incoherent features of the metallic and the insulating phase are very different.

At the point  $U_{c1}$  the gap between these bands closes continuously realizing the essential ideas of the Hubbard scenario. While this solution is not the lowest energy one in the fully-frustrated lattice, as mentioned above, we expect it to be stabilized in any lattice having finite frustration. If the magnetic frustration is large we expect the spectral function of the paramagnetic insulator to be rather close to the frustrated magnetic solution.

To illustrate the nature of the two coexistent solutions, we plot the zero temperature spectral function of the metallic and the insulating state in figure 5.4, as obtained from 2OPT.

We also show in figure 5.5 a metallic and an insulating Green function obtained for the same value of the parameters U = 2.8 and T = 1/64, as is obtained from both QMC and the perturbative calculation. This demonstrates that the coexistent solutions is a genuine feature of the model, and that it is also correctly captured by the approximate

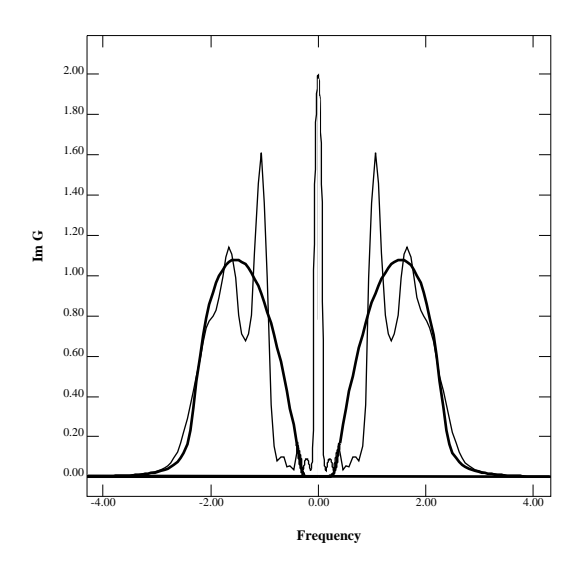


Figure 5.4: The density of states for the metallic (thin line) and insulating (bold line) solution at T=0 and the same value of the interaction U=2.9, obtained with the self-consistent perturbative calculation.

calculation. In order to select an insulating or a metallic solution one has to choose  $G_0$  obeying  $G_0(i\omega) = \frac{1}{i\omega}$  or  $G_0(0) \neq 0$  respectively as the initial guess in the substitution procedure for solving the mean field equations.

The energy is computed from the Green function by

$$E = \frac{T}{2} \sum_{n,k} (i\omega_n + \epsilon_k) G_k(i\omega_n)$$
 (5.12)

The entropy is given by

$$S(T) = \int_0^T \frac{C_v}{T'} dT' + S(0)$$
 (5.13)

where  $C_v$  is evaluated numerically by differentiating the energy. S(0) is zero for the metallic side and ln2 for the insulating side reflecting the double degeneracy of the paramagnetic insulating phase.

The physical critical line where the first order phase transition takes place is determined by equating the free energies of the two states,

$$F_M - F_I = E_M - E_I - (S_M - S_I)T. (5.14)$$

Figure 5.6 shows the calculated internal energy as a function of the temperature for two values of the interaction U. For the smaller value of U the temperature dependence

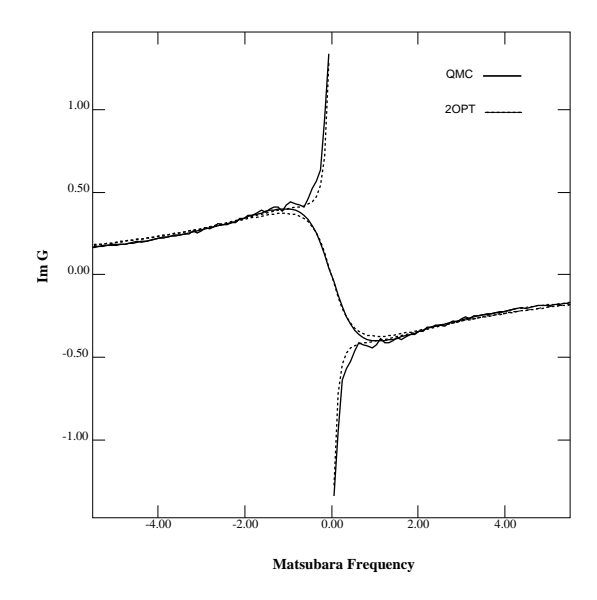


Figure 5.5: Comparison of the insulating and metallic Green function obtained using the quantum Monte Carlo algorithm and the perturbative calculation. The value of the interaction U=2.8 and the inverse temperature  $\beta=64$ .

of the internal energy of the metal displays a characteristic Fermi liquid  $T^2$  behavior in the low temperature region. The characteristic energy scale in this regime is set by the renormalized Fermi energy. At higher temperatures we see a thermal activation of the incoherent features. In the case of the insulator we just observe only this last effect at an energy scale U-2D.

In figure 5.7 we plot the specific heat  $C_v$  as a function of the temperature. The curves are obtained through numerical differentiation of E(T). In the strongly correlated metallic phase we find a separation of scales since  $\Delta$  is much smaller than U-2D. At higher T a thermal activation peak appears at a scale U-2D in both the metallic and insulating case. As shown in figure 5.8, the linear in T Fermi liquid behavior is observed in the low temperature region, with the slope  $\gamma$  proportional to  $m^* \sim (U_{c2} - U)^{-1}$  (see also section 5.4).

The integral (5.13) gives the entropy as a function of temperature. As expected the integral over the quasi-particle peak is equal to ln2 as shown in figure 5.9. As can be

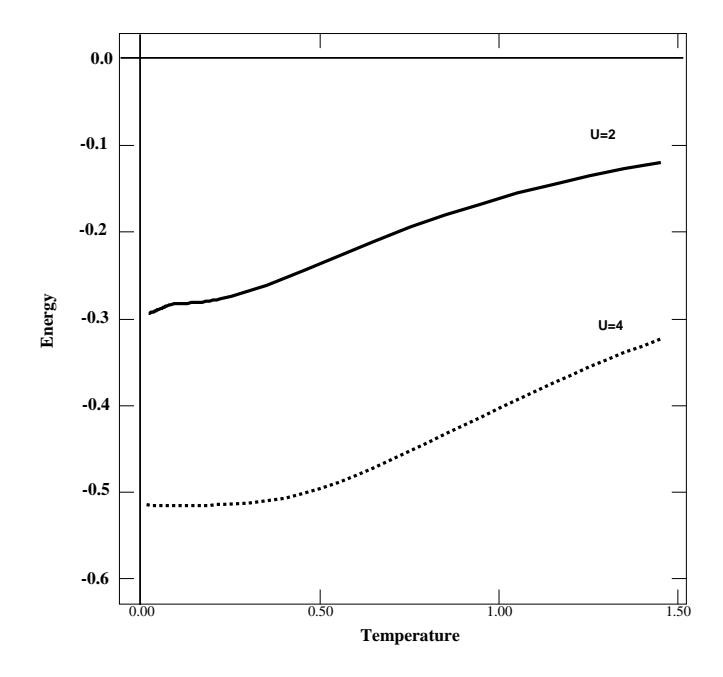


Figure 5.6: The energy as a function of the temperature for a value of U=2 in the metallic region (solid line), and U=4 in the insulating phase (dotted line).

seen in figure 5.8, for larger values of U but with  $U < U_{c2}$  the metallic solution disappears discontinuously before the entropy reaches ln2. Therefore, we define a coherence temperature  $T_s$  as the temperature where the entropy reaches the value of  $\frac{ln2}{2}$ . The physical relevance of  $T_s$  is that it delineates the temperature range where Fermi liquid theory is valid; see figure 5.10.

The comparison of the kinetic energy  $T = \langle \sum_k \epsilon_k c_k^+ c_k \rangle = \sum_{nk} \epsilon_k G_k(i\omega_n)$  and the potential energy  $V = U \sum \langle n_\uparrow n_\downarrow \rangle$  of the two solutions, is shown in figure 5.11. We find that the difference in the internal energy of the two states is much smaller than the corresponding difference in the kinetic and potential energy. The gain in kinetic energy by delocalization is almost perfectly cancelled by the loss in potential energy due to the Coulomb repulsion in doubly occupied sites. This makes the higher order corrections from higher order terms in the Yamada Yoshida perturbation theory important for resolving the relative stability of the metallic and the insulating solution at zero temperature. The small energy difference between the two states, however, is a general

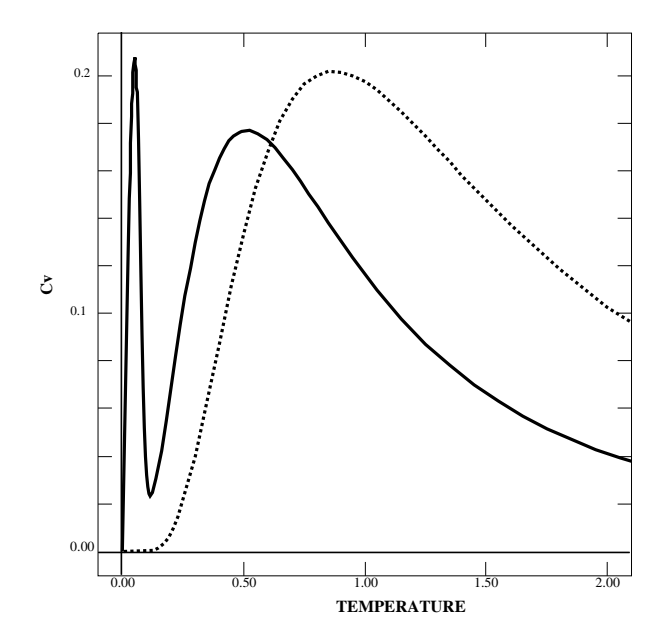


Figure 5.7: The specific heat  $C_v$  as a function of temperature. The solid line is for U=2 and the dashed line corresponds to U=4. In the metallic case (U=2) it is apparent the separation of energy scales. The linear part, at low T, ends at  $T\sim\Delta$ , and the thermal activation of the incoherent features peaks at the bigger scale  $T\sim U-2D$ . This last effect is the only one present in the insulating case.

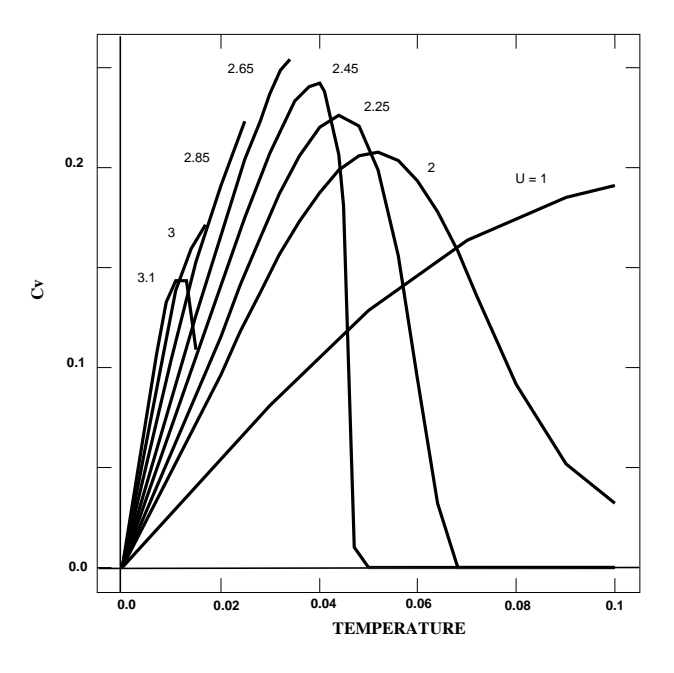


Figure 5.8: The specific heat  $C_v$  as function of temperature for several values of U.

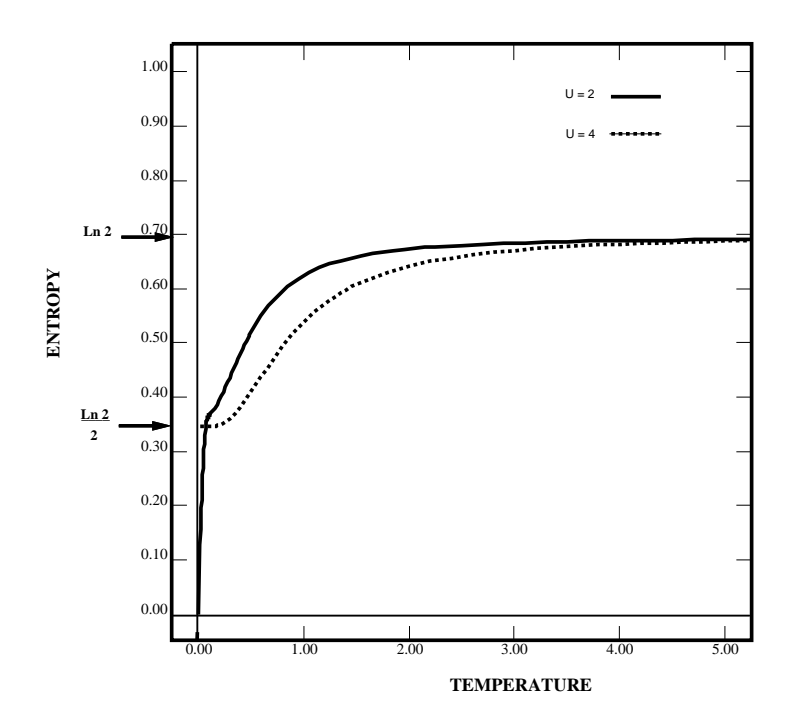


Figure 5.9: Entropy perspin as a function of temperature for two different values of interaction U=2,4.

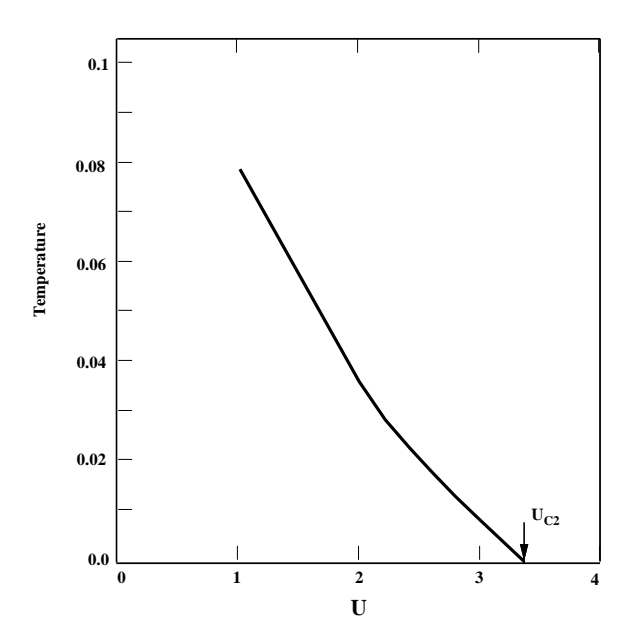


Figure 5.10: The temperature value where the entropy reaches  $\frac{\ln 2}{2}$  as function of the distance to  $U_{c2}$ . This temperature defines the region where the Fermi liquid description is applicable.

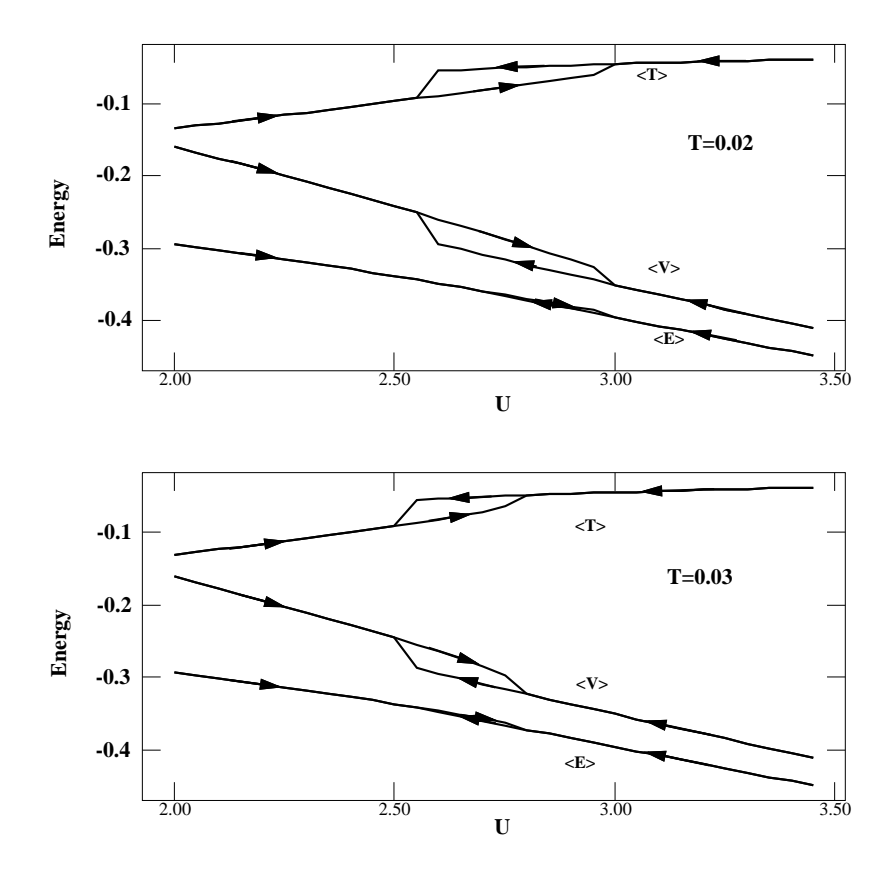


Figure 5.11: The kinetic, potential and internal energy as function of U for T=0.02 (a) and T=0.03 (b). The hysteresis effect is clearly observed.

feature of the problem. In fact the near degeneracy of the metallic and the insulating state near  $U_{c2}$  follows from the bifurcation of two stationary points of the free energy energy functional at  $U_{c2}$ . This issue will be revisited in the next chapter.

# 5.3.1 The breakdown of the metallic solution

In this section we investigate the fate of the metallic solution. The destruction of the metallic state is driven by the collapse of the renormalized Fermi energy scale  $\Delta$  which we showed is proportional to  $U_{c2}-U$  (see also section 5.4). From the mean field equation (5.4), we realize that this scale is also the bandwidth of the conduction electron bath which hybridizes with the local impurity in the Anderson model picture. It is easy to understand then, that for sufficiently large U this scale vanishes. Imagine solving the

system of equations (5.2), (5.3), and (5.4), by iteration. Consider a conduction electron bandwidth  $\Delta^n$ , ( $W^n$  in the notation of chapter 4) at the  $n^{th}$  iteration step. For large U, solving the Kondo problem produces a new bandwidth  $\Delta^{n+1} \approx e^{-U/t}\Delta^n$ . Therefore, this energy scale iterates to zero for  $n \to \infty$ .

In what follows we will make this argument more precise by introducing a parametrization for the local Green function. Close to  $U_{c2}$ , there is a clear separation of energy scales and the Green function can be written as a sum of a low energy and a high energy parts:  $G_l$  and  $G_h$ . The high energy part resembles the solution of an atomic problem while the low energy part obeys a scaling form.

In terms of a spectral representation:

$$G_{l} = \int_{-\infty}^{\infty} \frac{\rho_{l}(\epsilon)}{i\omega - \epsilon} d\epsilon$$

$$G_{h} = \int_{-\infty}^{\infty} \frac{\rho_{h}(\epsilon)}{i\omega - \epsilon} d\epsilon$$

$$(5.15)$$

with  $\rho_l(\epsilon) = \frac{1}{t} f(\frac{\epsilon}{\Delta})$  exhibiting a scaling form as  $\Delta \propto U_{c2} - U$  goes to zero.  $\rho_h(\epsilon)$  describes the high energy non scaling parts (Hubbard bands) centered around  $\pm U/2$ . A somewhat oversimplified but transparent picture of the spectral function is obtained by taking  $\rho_h$  to be two semi-circles with overall weight  $1 - \Delta/D$ , t = D/2. The calculation of the scaling function f is an open problem, in the exact solution of the large d Hubbard model. Here we determine it within the second order perturbation theory scheme outlined in section 5.2.

Approaching the transition,  $G_0$  develops a pole at a scale  $\sqrt{\Delta t} >> \Delta$ . The pole can be determined exactly from the relation  $G_0^{-1} = i\omega - t^2G$ . In the frequency range of  $\Delta << \omega << U/2$ , the Green function can be simplified to:

$$G=rac{2}{\omega}\int_{0}^{\infty}
ho_{l}(\epsilon)d\epsilon-2\omega\int_{0}^{\infty}rac{
ho_{h}(\epsilon)}{\epsilon^{2}}d\epsilon+i\pi
ho(\omega)$$
 (5.16)

where particle-hole symmetry  $\rho(-\epsilon) = \rho(\epsilon)$  has been used to change the integration limit. In the energy region we are considering, the imaginary part is negligibly small and we will ignore it in the following calculations.

$$G_0^{-1} = (1 + 2t^2C)\omega - \frac{2t^2\Delta F}{\omega}$$
 (5.17)

where,  $F=rac{1}{t}\int_0^\infty f(x)dx$  and  $C=\int_0^\infty rac{
ho_h(\epsilon)}{\epsilon^2}d\epsilon$ . The pole results at  $\omega_0=\sqrt{\Delta}(rac{2t^2F}{1+2t^2C})^{1/2}$ .

Notice that the existence of this pole follows from the general scaling argument. Now, combining this with the second order expression for the self-energy, one can make further progress and determine the value of  $U_{c2}$  analytically.

The self-energy is given by,  $\Sigma = -U^2 G_0^3(\tau)$ , which can be conveniently expressed in terms of the density of states of the  $G_0$ ,

$$\Sigma = -2\omega U^2 \int_0^\infty \int_0^\infty \int_0^\infty \frac{\rho_0(\epsilon_1)\rho_0(\epsilon_2)\rho_0(\epsilon_3)d\epsilon_1d\epsilon_2d\epsilon_3}{(\epsilon_1 + \epsilon_2 + \epsilon_3)^2 - \omega^2}$$
 (5.18)

where  $\rho_0(\omega) = -\frac{1}{\pi} Im G_0(\omega)$ . As  $\Delta \to 0$ ,  $\rho_0$  develops a  $\delta$  like peak positioned at  $\omega_0$  with a weight of  $\frac{1}{2(1+2t^2C)}$ . Therefore, the integrals can be performed in closed form to obtain,

$$\Sigma = -\frac{U^2 \omega}{4(1+2t^2C)^3(9\omega_0^2 - \omega^2)}$$
 (5.19)

as  $\Delta \to 0$ .

Comparing this expression with the one given by its definition,  $\Sigma = G_0^{-1} - G^{-1} = -\frac{D\omega}{\Delta}$ , where only the most singular term at small  $\omega$  is kept, at  $U = U_{c2}$  (i.e.  $\Delta = 0$ ), we have

$$U_{c2} = 3D(1 + D^2/U_{c2}^2) (5.20)$$

where D=2t, and the approximations  $F\approx \frac{1}{2D}$  and  $C\approx \frac{2}{U_{c2}^2}$  that follow from the parametrization discussed before are used. The value at which the metallic solution disappears is then  $U_{c2}=3.28D$  which is very close to the numerically determined value  $U_{c2}^{2OPT}=3.37D$ . From equation (5.19) it is clear that the scaling part of  $\Sigma$  is proportional to  $\frac{\omega}{\Delta}$  and that the scaling function f in this approximation is a semi-circle. Figure 5.12(a) and (b) contain the numerical solution for the density of states  $\rho_l$  and its scaling form f, as obtained from the second order perturbation theory near  $U_{c2}$ . It demonstrates that the region where scaling holds is actually quite large.

In principle equation (5.18) can be expanded to next order in  $\Delta$ , but the coefficient depends on the scaling function and the high energy part of the Green function and cannot be calculated analytically. However, it can be determined numerically that close to the critical point,  $\Delta = k(U_{c2} - U)$  with  $k \approx 0.21$ . Recalling the definition of  $\Delta = zD$  and that  $\frac{m^*}{m} = z^{-1}$ , this last result implies that within this approximation we find the

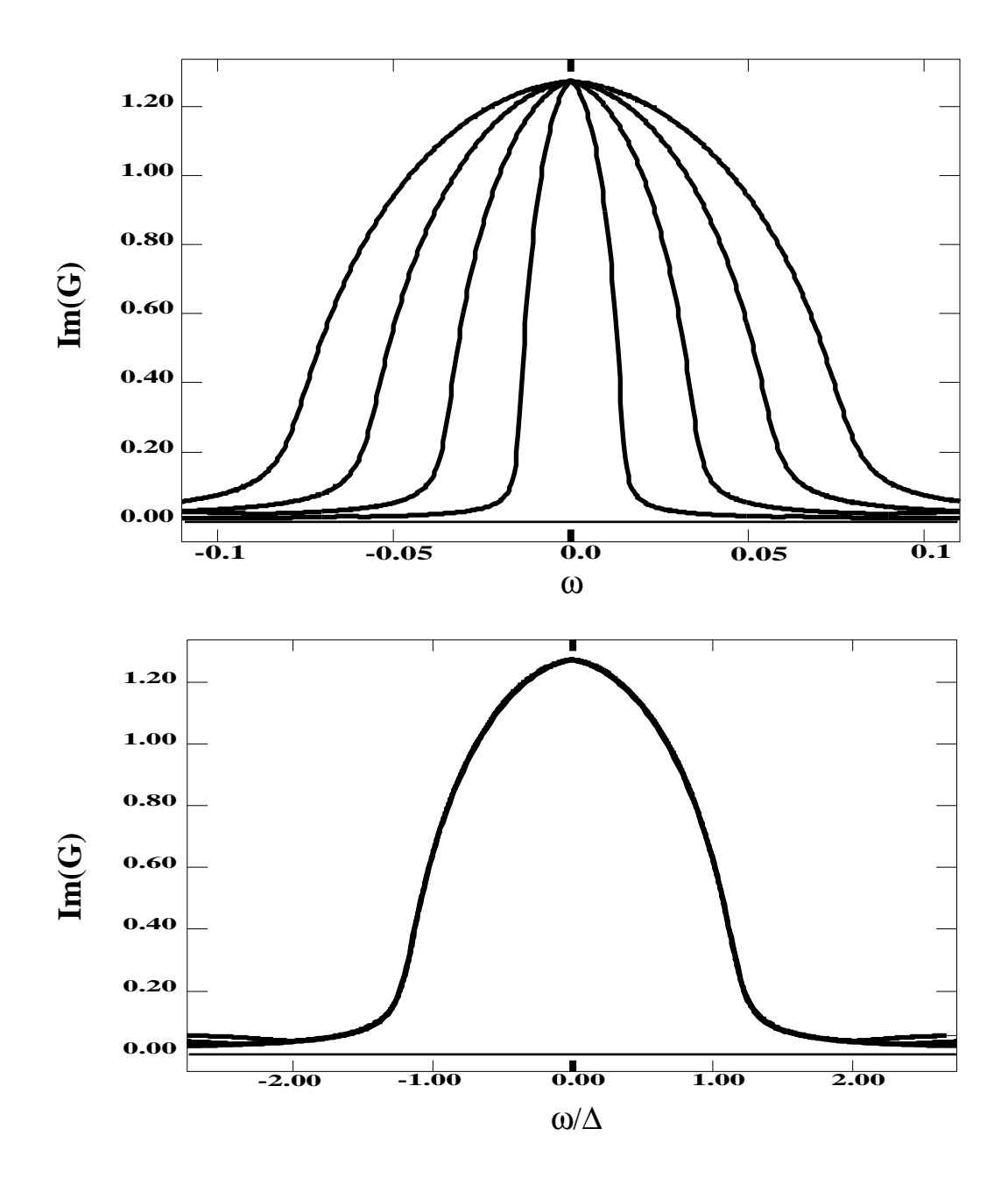


Figure 5.12: The low frequency part of the density of states  $\rho(\omega)$  as function of the frequency for values of the interaction U=3,3.1,3.2,3.3 (a). The four curves of (a) collapse to one universal form after rescaling:  $f(\frac{\omega}{\Delta})=t\rho_l(\omega)$ , where  $\Delta \propto U_c-U$  (b).

same critical behavior for the divergence of the renormalized mass as in the work of Brinkman and Rice [3]. Notice that within second order perturbation theory  $\frac{\partial^2 \Sigma}{\partial \omega^2}$  is not divergent as one would expect on general grounds. This is due to the fact that in this approach the vertex U is not renormalized.

#### 5.3.2 The breakdown of the insulating solution

In this section we study how the insulating solution disappears as we reduce the value of U. Our calculations determined that there indeed exists a new boundary  $U_{c1}(T) < U_{c2}(T)$ ,  $U_{c1}(T=0) \approx 2.6D$  associated with the break down of the insulating solution [24].

To understand the destruction of the insulating state, we proceed to parametrize the Green function once more,

$$G_0(\tau) = \alpha(\theta(\tau) - 1/2) + G_0^{inc}(\tau)$$
 (5.21)

with  $\theta(\tau)$  being the step function. The first term represents an insulating solution at the atomic limit (t=0).  $G_0^{inc}$  is the "incoherent part" of the insulating solution, which decays to zero as  $\tau \to \infty$  at zero temperature. Physically, this decomposition is motivated by viewing the self-consistent equations as describing a Kondo spin in an insulator. The spin operator S has a low energy part which is responsible for a Curie type of local spin susceptibility and a high frequency part. We write  $S = \sqrt{\alpha} S_{low} + S_{high}$ ,  $\alpha$  is a quantity similar to the "quasi-particle weight", it describes the weight of a pure free spin in an interacting system, the impurity + the insulating host. In frequency space,  $G_0^{inc}$  is only responsible for the details of the shape of the Hubbard bands which are high frequency features. The step function part gives rise to a divergency in  $G_0(i\omega_n) \sim 1/i\omega_n$  and is solely responsible for the existence of a gap. In the atomic limit  $\alpha$  approaches to unity, while on the contrary, the vanishing of  $\alpha$  signals the complete screening (or Kondo quenching) of the spin and the destruction of the insulating phase.

Using the parametrized form of  $G_0$ , we can relate  $\alpha$  to the density of states  $\rho(\epsilon)$  of the local Green function. At half-filling, because of the particle-hole symmetry,

$$G = 2i\omega_n \int_0^\infty \frac{\rho(\epsilon)d\epsilon}{(i\omega_n)^2 - \epsilon^2}$$
 (5.22)

Therefore, using (5.4) and comparing linear terms in  $i\omega$ ,

$$\alpha^{-1} = 1 + 2t^2 \int_0^\infty \frac{\rho(\epsilon)d\epsilon}{\epsilon^2}$$
 (5.23)

If the Mott-Hubbard gap collapses, i.e.,  $\rho(\epsilon)$  becomes finite at  $\epsilon \to 0$ ,  $\alpha^{-1}$  diverges. Alternatively, a finite  $\alpha$  at the transition indicates a finite Mott-Hubbard gap. Within the second order perturbation scheme, we can obtain a closed equation for  $\alpha$ . Inserting the parametrized  $G_0$  into the self-energy expression we obtain:

$$\Sigma(\tau) = \alpha^3 \frac{U^2}{4} (\theta(\tau) - 1/2) + \Sigma_{inc}.$$
 (5.24)

which determines the low frequency behavior of the local Green function:

$$G = \frac{2}{i\omega_n + \Sigma(G_0) + isgn(\omega_n)\sqrt{D^2 + (\omega_n + i\Sigma(G_0))^2}}$$
 (5.25)

Considering the most singular terms in the self-consistency condition (5.3) and (5.4), for small  $\omega$  we have

$$G_0^{-1} = i\omega_n + \frac{D^2}{4\Sigma},\tag{5.26}$$

and therefore,

$$\alpha = \left(1 + \frac{D^2}{U^2 \alpha^3}\right)^{-1} \tag{5.27}$$

There are two solutions for  $\alpha^*$  for  $U > U_{c1}$ . The one with a smaller  $\alpha^*$  is always unstable and unphysical since it is not connected continuously to  $\alpha = 1$  as U tends to infinity. At the transition  $U_{c1}$ , the unstable fixed point collides with the stable one, and the fixed point solution disappears.  $U_{c1} = 3\sqrt{3}/2D \approx 2.6D$  which is the same as the numerically obtained. Since  $\alpha$  is finite at the transition, the Mott-Hubbard gap, within this approximation, is finite. As was previously noted in section 5.2, we observed using QMC, that in the exact finite temperature solution the  $U_{c1}$  vs. T line is shifted to lower values of U, indicating a further reduction of the minimum gap. In fact, we will later show using the ED calculation (which is non-perturbative) how the gap indeed collapses to zero as in Hubbard's original scenario.

# 5.4 U<sub>c2</sub> The Brinkman Rice point

We now turn to the description of the neighborhood of  $U_{c2}$ . The quasiparticle residue z (inverse mass enhancement) as a function of U from the exact diagonalization method and the 2OPT is shown in figure 5.13. For a small value of U the latter becomes exact, at an intermediate range they coincide and as the critical point is approached the exact diagonalization method, that treats the interaction non-perturbatively, becomes more accurate. Using the projective self-consistent method we obtained  $U_c \approx 3$ . Notice that the z vs. U line extrapolates towards that value. It is noticeable that a straight line from  $U_c$  can be obtained for a big range of the interaction. The mass renormalization in the limit of infinite dimensionality is identical to the quasiparticle weight. The critical behavior of the renormalized mass is thus  $\frac{m*}{m} = z^{-1} \approx 0.92(1 - \frac{U}{U_c})^{-1}$ . These results can be compared to the Brinkman Rice picture for the transition [3] [25]. Using the Gutzwiller wavefunction, that variational approach gives  $U_c^{BR}=8\bar{\epsilon}\approx 3.37$ , and z= $(1-(\frac{U}{U_c^{BR}})^2)$ . This last result, close to the critical point reduces to  $z^{-1}=0.5(1-\frac{U}{U_c^{BR}})^{-1}$ , which is similar to the ones of the present treatment. It is interesting to note that the value for  $U_{c2}$  obtained with 2OPT is virtually identical to the Brinkman Rice calculation.

To gain further insight on the nature of the transition, we investigated the behavior of other quantities as a function of U. We plot in figure 5.14 the double occupation  $\langle D \rangle$  as a function of U as obtained from the different methods.

There are two branches, corresponding to the metallic and insulating solutions at T=0, which merge at  $U_c\approx 3$ . They show the excellent agreement of the exact diagonalization algorithm and the 2OPT in all parameter range, except very close to the MIT point. The QMC data being at an inverse temperature  $\beta=32$ , shows that the effect of the temperature is to reduce the double occupation on the metallic side. In the insulating side, the effect is negligible since in this case there are no small energy scales. At this temperature the coexistence region is very small, and the data shows a jump in  $\langle D \rangle$  at  $U\approx 2.4$ . Notice that this result indicates that the Brinkman-Rice approach captures the singular part of  $\langle D \rangle$ , but in addition we observe that this quantity does not

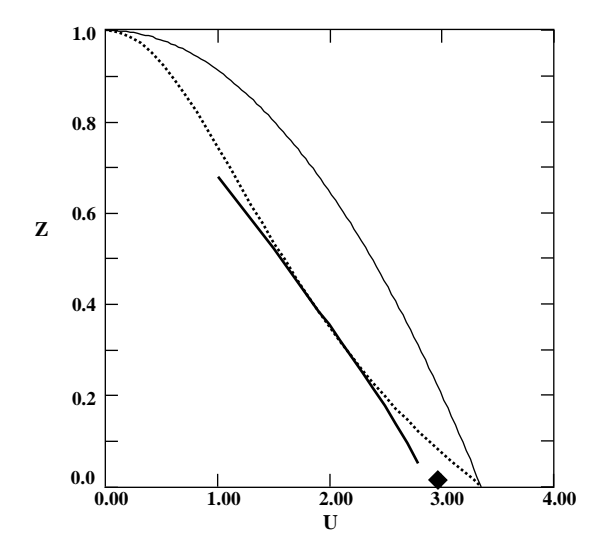


Figure 5.13: The quasiparticle weight z as a function of the interaction U. The solid bold line corresponds to ED results with 8 sites. The dotted line is obtained from 2OPT. For comparison we also plot the results using the Gutzwiller variational method.

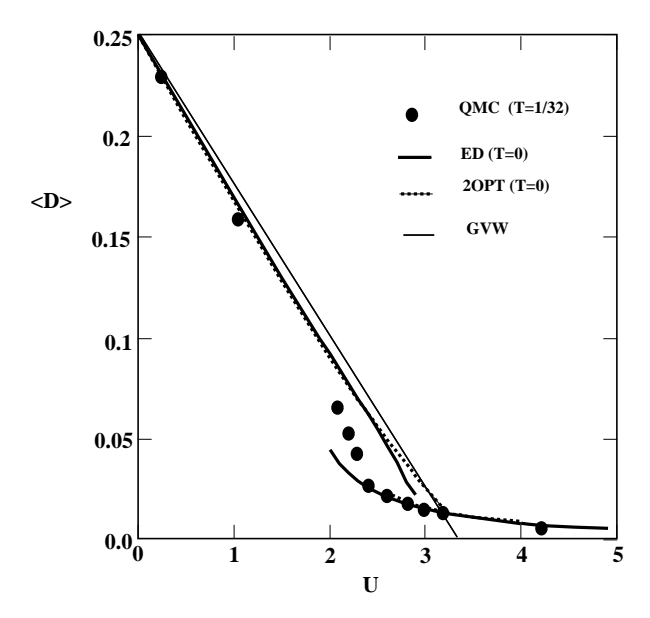


Figure 5.14: Double occupation as a function of the interaction U. The data corresponds to QMC simulations at  $\beta=32$  (dots), 8 sites exact diagonalization (bold line) and 2OPT at T=0 (dotted line). For comparison the results for the Gutzwiller variational wavefunction is also plotted (thin line).

vanish at the transition due to an additive non-singular part. We can thus parametrize  $\langle D \rangle = 0.235(\frac{U_c-U}{U_c}) + 0.015$  Also note that the magnetic moment is obtained from the double occupation through the identity  $\langle m_z^2 \rangle = 1 - 2\langle D \rangle$ . Therefore, we find that the magnetic moment is not saturated at the transition.

# 5.5 U<sub>c1</sub> The Hubbard point

We have just discussed how in the region of the phase diagram around  $U_{c2}$  the Brinkman Rice scenario for the destruction of the metal is realized. Surprisingly in the region around  $U_{c1}$  Hubbard's ideas regarding the closure of the Hubbard bands come to life. In figure 5.15 we plot the value of the Hubbard gap as a function of U in the paramagnetic phase. As a definition for the magnitude of the gap we take twice the energy of the lowest energy pole of the Green function obtained from the exact diagonalization method. We show data extrapolated for finite size effects from systems of 3,5 and 7 sites. A  $1/N_{sites}$  scaling behavior is assumed. The results indicate that, following the insulating solution, the gap closes at a value  $U_{c1} \approx 2.15$ , and that  $\Delta_{gap} \sim (U - U_{c1})$ . For comparison, we also plot the same quantity from the 2OPT calculation that gives  $U_{c1}^{2OPT} \approx 2.6$ . These results can be compared to the corresponding from Hubbard-III. In that case the critical value for the destruction of the insulating state is  $U_{c1}^{HIII} \approx 1.73$ , and  $\Delta^{HIII} \sim (U - U_{c1}^{HIII})^{3/2}$ .

Even though the paramagnetic insulating phase is strictly unstable at zero temperature, it is relevant to very frustrated magnetic insulators. Since the energy difference between the metal and the paramagnetic insulator is very small in the full coexistence region at T=0, departures from full frustration will stabilize a magnetic solution that will resemble the paramagnetic insulator solution.

## 5.6 Susceptibilities and the Mott-Hubbard transition

In what follows we are going to present a combination of theoretical arguments and numerical results, in order to discuss the behavior of the susceptibilities in the vicinity of the transition. Unfortunately, we cannot take further advantage of the perturbative approach. The vanishing of higher order corrections in the self-energy in the atomic

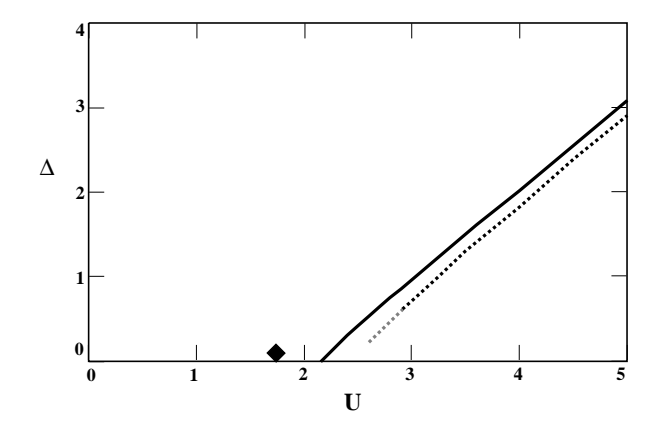


Figure 5.15: Paramagnetic gap (solid) as function of the interaction U obtained from ED. For comparison, the corresponding results from 2OPT (dotted), and  $U_{c1}^{HIII} \approx 1.73$  (diamond).

limit does not necessary imply that this will be also true for the calculation of other quantities. For example, negative compressibilities are obtained for intermediate and high values of U. Therefore, all the numerical results in this section were obtained with the QMC method. Although the present computational power does not allow a detailed quantitative analysis of higher correlation functions at very low temperatures, our results are sufficient to give support to the theoretical discussion.

Much theoretical insight about the behavior of the spin and charge susceptibilities can be gained by the fact that the impurity model describing the Hubbard model is an Anderson impurity model.

In chapter 4 we have already discussed that when the Mott point is approached, magnetic order of the local spin sets in [13]. In principle  $\chi_L^s$  can be determined in NMR experiments. However it is the  $\mathbf{q} = \mathbf{0}$  susceptibility that is easily accessible to experimental probes. The  $\mathbf{q} = \mathbf{0}$  quantities differ from the local ones because of the polarization of the Weiss field due to the external perturbation. We will illustrate how this effect, which is at the heart of the Fermi liquid theory, modifies the low energy responses near  $U_{c2}$ .

In the presence of a small chemical potential  $\mu$ , away from the particle-hole symmetric point, and a small magnetic field h, the mean field equations are

$$G_{0\sigma}^{-1} = i\omega_n + \mu + \sigma h - t^2 G_{\sigma}$$
 (5.28)

To proceed, we extend the simplified form of the parametrization discussed in section 5.3.1 to account for the magnetic properties. The high frequency part of the Green function is polarized like a local moment which can be described as a superposition of Hartree-Fock solutions. It has been demonstrated that when  $U \sim U_c$  the upper and lower Hubbard bands are well developed, so that for low frequencies and fields, a good approximation for  $G_{\sigma}$  is

$$G_{\sigma} = \frac{n_{\sigma}}{i\omega_{n} - \frac{U}{2}} + \frac{n_{-\sigma}}{i\omega_{n} + \frac{U}{2}} + \frac{2\Delta/D}{i\omega_{n} + i\Delta(sgn\omega_{n})}$$
(5.29)

with D = 2t. Inserting (5.29) in (5.28), we have for small frequencies,

$$G_{0\sigma}^{-1} = i\omega_n + \mu + h\sigma + 2\frac{t^2 m_\sigma}{U}\sigma \tag{5.30}$$

where  $m_{\sigma}=n_{\sigma}-n_{\bar{\sigma}}$ . Equation (5.30) describes an impurity problem in the presence of an external field  $h_{eff}=h-2\frac{t^2}{U}m_{\sigma}$ . We can compute the magnetization from the theory of the Anderson impurity model in an effective field  $h_{eff}$ . We know that  $m=\chi_o h_{eff}$ , with  $\chi_o\sim\frac{1}{\alpha T_k}$ , and  $T_k$  being the effective Kondo energy of the problem which in our case corresponds to  $\Delta$ .  $\alpha$  is a numerical coefficient of order unity. Solving for m we find

$$\chi_s = \left[\frac{dm}{dh}\right]_{h=0} = \frac{1}{\chi_o^{-1} + 2\frac{t^2}{II}} = \frac{1}{\alpha\Delta + J}$$
(5.31)

where we have defined the magnetic exchange energy  $J=2rac{t^2}{U}=rac{D^2}{2U}.$ 

The physical interpretation of this equation is transparent: the exchange arises from high energy processes which are largely unaffected by the Mott transition. As a result the susceptibility varies continuously, as U passes through  $U_c$ . Remarkably equation (5.31) was also obtained in the large N limit [26]. This findings are consistent with the QMC results displayed in figures 5.16 and 5.17. For smaller U, an initial fast increase in  $\chi_s$  is observed as  $\Delta$  rapidly decreases. However, unlike the Brinkman-Rice approach, this quantity remains finite at the transition due to the existence of a

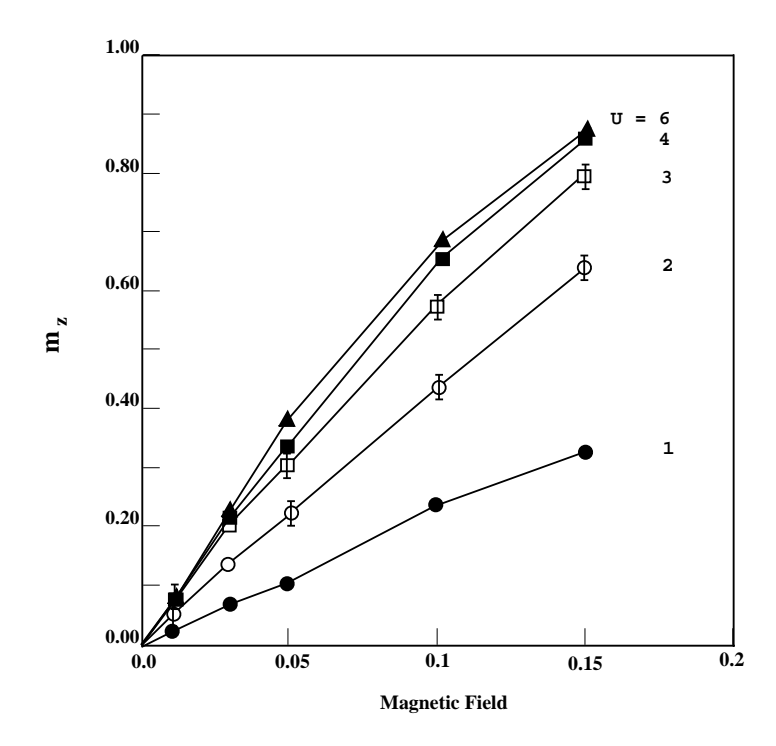


Figure 5.16: Local magnetization  $m_z$  as function of an external magnetic field, for different values of the interaction U.

non zero superexchange constant in the uniform response. The numerical result can be parametrize according to the analytic expression obtained above. We find  $\chi^{-1} \approx 0.7(1-\frac{U}{U_c})$  for the metallic phase, and  $\chi^{-1} \approx J$  in the insulator phase (J is plotted for comparison). It is intersting to note that this result (metallic case) compares very well with the Gutzwiller variational approach that gives for the spin susceptibility [25]

$$\chi_s = \mu_B^2 N(0)^2 \left( 1 - \frac{U^2}{U_c^2} \right)^{-1} \left( 1 - \frac{N(0)U}{2} \, \frac{1 + U/2U_c}{1 + U/U_c} \right)^{-1} \tag{5.32}$$

where N(0) denotes the density of states at the Fermi level. Close to the critical point reduces to  $\chi_{BR}^{-1} \approx 0.74(1-\frac{U}{U_c})$ , in agreement with our results as long as the critical point is not approached too close. This is because the variational scheme fails to capture the cut-off in the magnetic response.

We finally also obtained the Wilson ratio as a function of interaction U. This quantity is displayed in figure 5.18 and is derived from figures 5.13 and 5.17. It is found to vanish at the critical point since while the specific heat diverges as  $\frac{1}{\Delta}$ , the magnetic

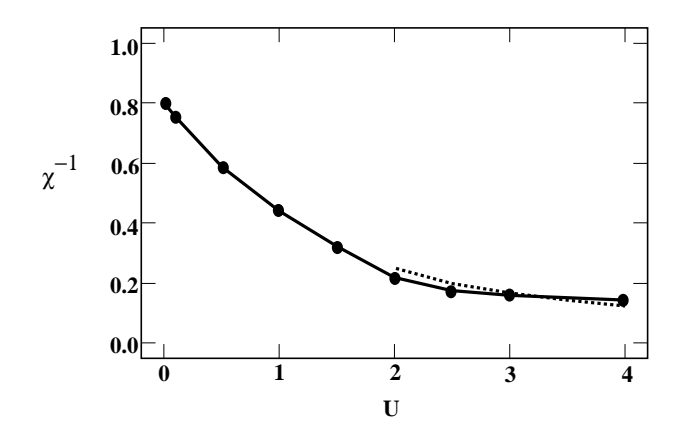


Figure 5.17: Inverse of magnetic susceptibility at  $\mathbf{q} = \mathbf{0}$  (solid dots) and the magnetic exchange  $J = \frac{2t^2}{U}$  (dashed line) as a function of the interaction U.

susceptibility is cut-off by  $min\{T^{-1}, J^{-1} = 2U/D^2\}$ .

Similar considerations apply to the charge susceptibility. Applying a chemical potential does not cause a change (to order  $\delta n$ ) in the distribution of integrated spectral weight between the upper and lower Hubbard bands. This can be readily understood by extending the observation of chapter 4 that the high energy features are correctly reproduced by an expansion around the atomic limit. In this limit a small particle hole asymmetry shifts the energies of the atomic levels but does not transfer spectral weight. The change in the low energy part of the Green function is easily estimated using Fermi liquid theorems. The change in G(0) as a result of a change in chemical potential is given by the phase shift, which in turn is given by the shift of the location of the center of the resonance. Its width does not change to order  $\Delta/D$  because of particle hole-symmetry. Assuming that at low frequencies the result of applying  $\mu$  is to shift the center of the resonance by  $\epsilon_f$ , the local Green function can be then approximated by

$$G(i\omega_n) = \frac{2\Delta/D}{(i\omega_n + \epsilon_f + i\Delta sgn\omega_n)}$$
 (5.33)

with  $\delta n \approx \frac{\epsilon f}{\Delta}$ . We thus find  $\delta G(0) \approx \frac{\delta n}{\Delta}$ , and therefore, from (5.28), the effective chemical potential of the impurity model becomes  $\delta \mu_{eff} \approx \delta \mu - \frac{t^2}{\Delta} \delta n$ . The response of the impurity to this shift in the chemical potential is  $\delta n = \chi_{imp} \delta \mu_{eff}$ , with  $\chi_{imp} \approx \frac{1}{U}$ 

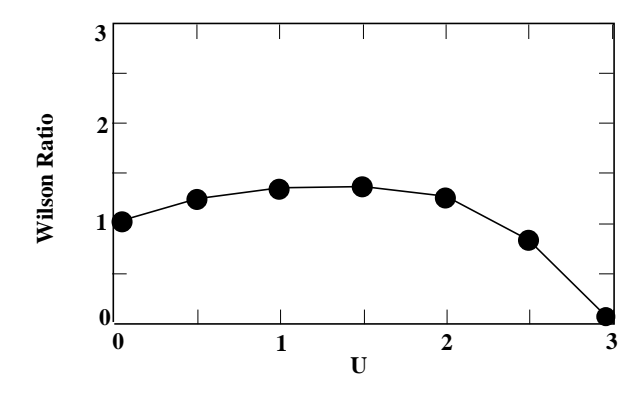


Figure 5.18: Wilson ratio as function of the interaction U.

the charge susceptibility of the impurity. Combining these results we obtain

$$\frac{\delta n}{\delta \mu} = \frac{\chi_c^0}{1 + \frac{\chi_c^0 t^2}{\Lambda}} \tag{5.34}$$

that implies that the charge susceptibility vanishes as  $(U_c-U)$  as we approach the Mott transition. This result is consistent with the Monte Carlo simulations that give  $\frac{\delta n}{\delta \mu} \approx 0.52(1-\frac{U}{U_c})/D \approx 0.6\Delta/D^2$ , with  $U_c \approx 2.75$  at an inverse temperature  $\beta=16$ . Thus, the compressibility goes to zero as  $\Delta$ , when U approaches  $U_c$ . It is intersting to note that this result compares well with corresponding one obtained from the Gutzwiller variational approach [25]. In that case the compressibility is obtained as

$$\kappa = \frac{1}{n_0} \frac{\delta n}{\delta \mu} = \frac{4}{U_c} \frac{1 - U/U_c}{1 + U/U_c}$$
 (5.35)

where  $n_0$  denotes the particle density. Close to the critical point it reduces to  $\frac{\delta n}{\delta \mu}_{BR} \approx 0.59(1-\frac{U}{U_c})/D$  in close agreement with our results.

On the other hand, we have seen in section 5.4, that the doubly occupancy does not saturates as the transition is crossed. This is consistent with the *local* charge susceptibility being finite. In fact, the *impurity* charge compressibility equals minus the kinetic energy by virtue of the mean field equations.

Before proceeding with our discussion we illustrate in figure 5.19 the quality of the fit that is obtained from the parametrization for the local Green functions introduced above. The data shows a comparison of a Green function obtained at  $\beta = 64$  from

QMC simulations and the fitting function

$$G_{\sigma} = \frac{n_{\sigma}}{i\omega_{n} + \mu - \frac{U}{2}} + \frac{n_{-\sigma}}{i\omega_{n} + mu + \frac{U}{2}} + \frac{2\Delta/D}{(i\omega_{n} + \epsilon_{f} + i\Delta sgn\omega_{n})}$$
(5.36)

As is clear from the plot this simple parametrization is able to capture the exact results in great detail as can be particularly noted from the low frequency behavior of the real and imaginary parts of the Green functions. The parametrization has three free parameters: the width  $\Delta$ , the position of the low frequency quasiparticle peak  $\epsilon_f$  and the number of particles in the Hubbard bands  $n_{\sigma}$  ( $n_{-\sigma}$  becomes fixed by the normalization condition). The value for the interaction is set to U=2.5 and the chemical potential is chosen  $\mu=0.3$ . This values are consistent with the made assumptions for the validity of the parametrization, that is, proximity to the critical point where the Hubbard bands are well developed and small doping. Note that in principle one may use a smaller number of free parameters by considering available information such as the expectation value of the particle number operator and the particle number sum rule. However, here our aim is not to produce the least free parameter fit, but rather to justify the validity of the parametrization scheme.

We argued before that the local spin susceptibility diverges at the Mott transition as  $\frac{1}{\Delta}$  while the  $\mathbf{q} = \mathbf{0}$  spin susceptibilty stays finite at the transition. This and an independent estimate of the exchange constant J can be obtained by approaching the transition from the insulating side by analyzing the fully-frustrated model.

For large U, the fully-frustrated model in equation (5.5) reduces at half filling to

$$H_J = \sum_{ij} J_{ij} S_i \cdot S_j \tag{5.37}$$

where  $J_{ij}$  are independent random variables with an exponential distribution  $P\{J\} = \frac{\Theta(J)}{\sqrt{J}} exp - (JN/J_o)$  with  $\theta(x) = 1$  for x > 0 and  $\theta(x) = 0$  for x < 0.

An important observation is that  $\bar{J}_{ij} = \frac{J}{N}$  while the variance  $\bar{J}_{ij}^2 - \bar{J}_{ij}^2 = \frac{J^2}{N^2}$  so the randomness is irrelevant in the thermodynamical limit. The solution of Hamiltonian (5.37) with  $J_{ij} = \frac{J}{N}$  is elementary.

We exhibit the solution to confirm and interpret the finite susceptibility in the insulating phase. The eigenstates of equation (5.37) are labeled by the total spin  $\epsilon_s$  =

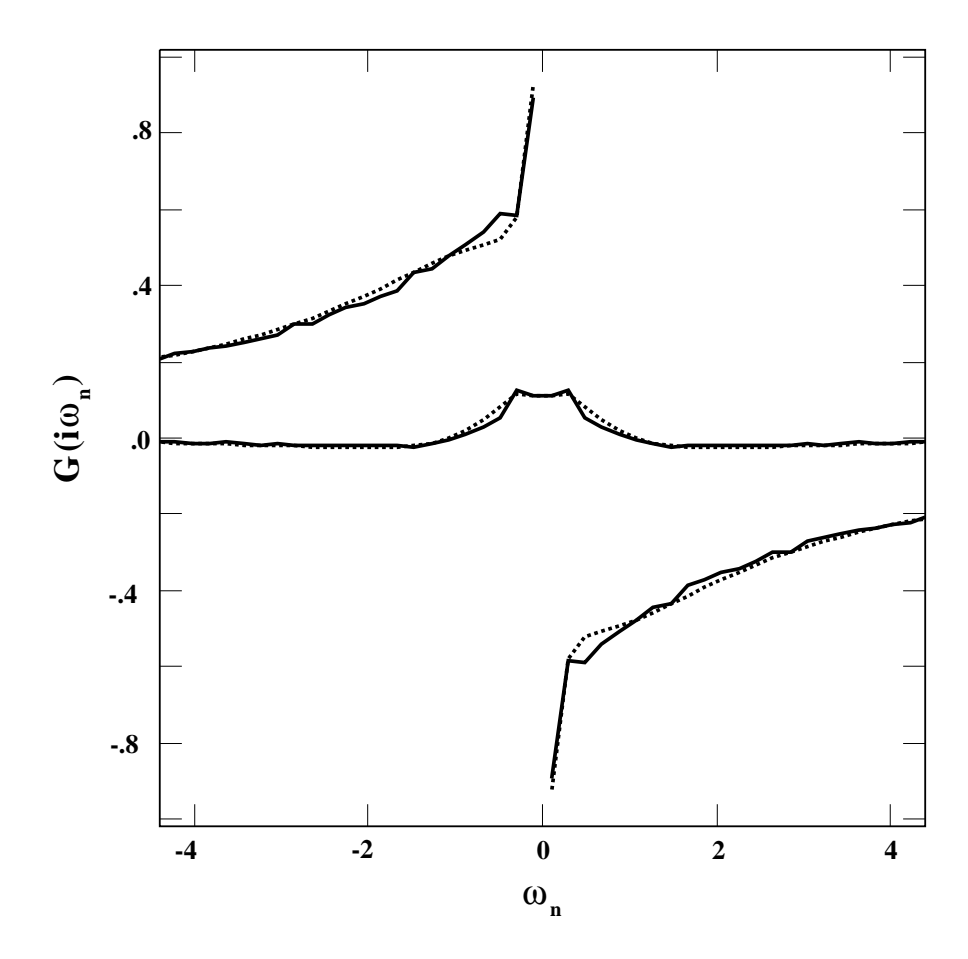


Figure 5.19: Comparison of an exact Green function away from half-filling obtained from QMC at  $\beta=64$ , and the parametrization discussed in the text. The interaction U=2.5 and  $\mu=0.3$ .

 $\frac{J_o}{N}[S(S+1)]$ . For simplicity we will take N to be even  $N\equiv 2N_o$ . For a given value of the spin the degeneracy of a state with a given value of total spin S and projection  $S_Z$  is  $d_S=\binom{2N_o}{N_o-S}-\binom{2N_o}{N_o-S-1}$ . The partition function in the presence of a uniform field reduces to

$$Z = \sum_{S=0}^{N_o} d_S \ e^{-\beta \frac{J_o}{2N_o} S(S+1)} \ \frac{\sinh(\beta h(S+\frac{1}{2}))}{\sinh(\frac{\beta h}{2})}$$
 (5.38)

In the thermodynamical limit  $N_o \to \infty$  it is convenient to introduce the variable  $x=S/N_o$  and equation (5.38) reduces to

$$Z = N_o \left\{ \int_0^1 dx \ e^{N_o g(x)} e^{-\frac{\beta J_o N_o x^2}{4}} \left[ \frac{e^{h\beta N_o x} - e^{-h\beta N_o x}}{2 sinh(\frac{h\beta}{2})} \right] + O(\frac{1}{N_o}) \right\}$$
 (5.39)

with  $g(x) \equiv ln \frac{4}{(1+x)(1-x)} + x ln [\frac{1-x}{1+x}]$  being the density of states. This system is peculiar in that the number of states decreases as the energy (or the spin) increases.  $g(x) = 2ln2 - x^2$  as  $x \to 0$ , therefore it has negative temperature. Equation (5.39) is easily evaluated when  $N_o$  is large and we obtain the free energy per particle

$$\frac{F(h,\beta)}{N} = -\frac{h^2 \beta}{8 + 2\beta J_o} - \frac{1}{\beta} ln2$$
 (5.40)

and the susceptibility

$$\chi^{s}(\mathbf{q}=\mathbf{0}) = -\frac{\partial^{2} f}{\partial h^{2}} = \frac{1}{4T + J_{o}}$$
 (5.41)

which displays Curie law for  $T>>J_o$  but saturates at the magnetic energy  $J_o$  at low temperatures in complete agreement with the discussion of the paramagnetic phase. From the free energy and the energy  $E=-\frac{\partial lnZ}{\partial\beta}$ , we can obtain the entropy  $S=\frac{E-F}{T}$ . Notice that when h=0, E=0 and  $S=2N_oln2$ . This is the result of the large degeneracy of the singlet sector. In fact the number of states per particle in the singlet sector can be estimated directly from equation (5.40).

The prediction that  $\chi^s$  remains finite as  $U \to U_{c2}$  is physically sensible and probably persists in finite dimensions. It reflects the fact that the magnetic energy is finite when  $d \to \infty$ . The same is true in the limit of large N of the model studied in [27] in any dimension, provided we identify the Mott transition with the metal charge transfer insulator transition. This physics is missed by the Gutzwiller approximation

which ignores the high energy processes thus the magnetic exchange completely. The divergence of  $\gamma$  (cf. section 5.3) as  $U \to U_c$  is consistent with the fact that the entropy is  $\ln 2$  in the insulator. In the metallic phases  $S(T) = \int_0^T \frac{C_v(T')}{T'} dT'$ . Since this quantity vanishes as  $T \to 0$  in the insulating phase  $\frac{C_v(T)}{T}$  diverges at the transition. This is the result of a large spin ground state degeneracy. It is rooted in the fact that since  $J_{ij} \sim \frac{1}{d}$  one needs long range order to gain finite magnetic energy. This is clearly unrealistic and will not persist in any finite dimension. In fact, in the large N limit in finite dimensions the specific heat remains finite when the metal insulator transition drives the system into a resonating valence bond state [28]. It would be interesting to construct a loop expansion around the  $d=\infty$  solution to remedy this problem.

# 5.7 The magnetic solution and frustration

In this section we will consider the solution of the model with magnetic order. In the absence of magnetic frustration, on a bipartite lattice, one expects to find an antiferromagnetically ordered state as the local moments develop when the interaction U is increased from zero and the temperature is low. This is indicated by finite dimensional Hartree-Fock and variational calculations [29, 30].

On the other hand, at big values of the interaction, the magnetic moments become fully developed and the model maps onto the Heisenberg model. It will consequently also display an antiferromagnetically order state with a Néel temperature that is inversely proportional to U.

The low temperature solution of the model, on a bipartite lattice, is therefore expected to be that of an antiferromagnetic insulating state due to the effective doubling of the lattice parameter.

We find that this scenario is fully realized in the limit of large dimensions. We solve the self-consistent equations (5.7) that define the model on a Bethe lattice without magnetic frustration. As usual in the case of antiferromagnetic order, two sublattices A and B are introduced. Even though we are at half filling and in the particle-hole symmetric case, the Matsubara Green functions acquire a non-zero real part as the occupation becomes different for the up and down spin functions on either sublattice.

$$G_{\sigma}^{A} = [-G_{\sigma}^{B}]^{*}$$

$$G_{\sigma}^{A,B} = [-G_{-\sigma}^{A,B}]^{*}$$
(5.42)

and,

$$n_{\sigma}^{A,B} = 1 - n_{-\sigma}^{A,B}$$
 $n_{\sigma}^{A} = n_{-\sigma}^{B}$  (5.43)

In figure 5.20 we show the local Green function of spin  $\sigma$  as a function of Matsubara frequency. The figure shows the results obtained by QMC simulations at  $\beta=32$  and the ED calculation with 8 sites. The value of the interaction is U=1.5. The solutions are insulating since the imaginary part goes to zero at the origin. On the other hand, the large real part signals the opening of a gap. Although QMC is at  $T\neq 0$ , the agreement is excellent since the gap is much bigger than T. In figure 5.21 we present the corresponding results for the density of states at the same value of the interaction. The difference in the occupation of the up and down spin Green functions is apparent. The gap in the density of states is obtained from the distance between the lowest energy poles.

To study the behavior of the system at the low temperatures where the QMC approach becomes inapplicable, we implemented both a Hartree-Fock calculation and the generalization of the second order perturbation approximation that we introduced before. To test the reliability of these approaches, we obtained the Néel temperature for the model. The results are displayed in figure 5.22. We find that none of them in good agreement with the QMC simulations.

The failure of the perturbative approach, which underestimates the value of the Néel temperature, can be understood from the following argument.

The local magnetization is defined as  $m_z=\langle n_\uparrow-n_\downarrow\rangle$ , and from particle-hole symmetry,  $m_z=2(\langle n_\uparrow\rangle-\frac{1}{2})=-2(\langle n_\downarrow\rangle-\frac{1}{2})$ . On the other hand, the local Green function for, say the up spin electrons, with the self-energy considered to second order reads,

$$G_{\uparrow} = rac{1}{G_{ ext{of}}^{-1} + \mu - U \langle n_{\perp} 
angle - \Sigma_{\uparrow}^{(2)}}$$
 (5.44)

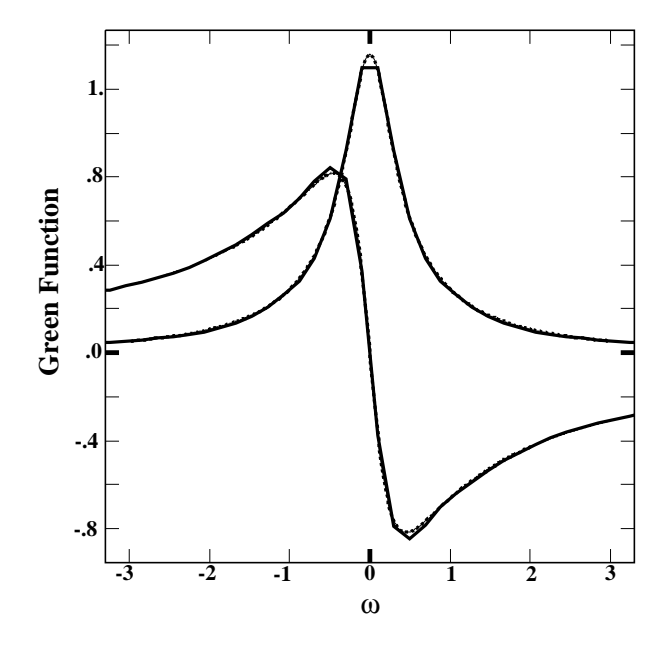


Figure 5.20: The local antiferromagnetic Green function of spin  $\sigma$  as a function of Matsubara frequency. The imaginary part is odd and the real part even. Obtained from QMC at  $\beta=32$  (full line) and ED of 8 sites (dotted line). The results can hardly be resolved due to the excellent agreement. The interaction U=1.5

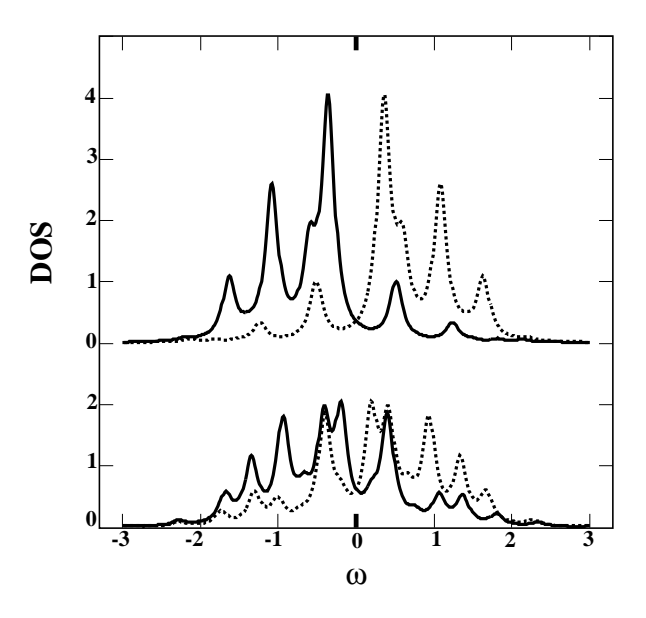


Figure 5.21: The density of states for  $\sigma$  and  $-\sigma$  electrons (full and dotted line) obtained from ED of 8 sites for U=1.5. The top plot corresponds to the bipartite Bethe lattice and the lower plot to the TSFF model with  $t_1^2 = \frac{1}{4}t^2$  and  $t_2^2 = \frac{3}{4}t^2$ .

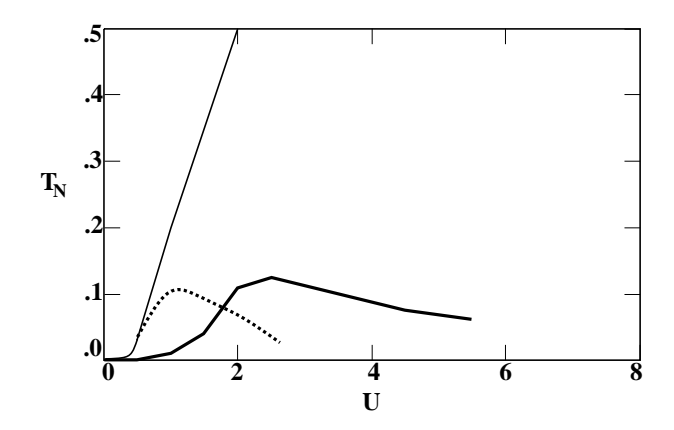


Figure 5.22: Comparison of the Néel temperature of the bipartite Bethe lattice model obtained from QMC (bold line), 2OPT (dotted line), and Hartree-Fock (thin line).

At particle-hole symmetry, we set  $\mu = \frac{U}{2}$ , and the Green function now becomes

$$G_{\uparrow} = rac{1}{G_{0\uparrow}^{-1} - U(\langle n_{\downarrow} 
angle - rac{1}{2}) - \Sigma_{\uparrow}^{(2)}}$$
 (5.45)

Now lets imagine that we produce a small magnetization or, equivalently, an increase of the up spin occupation. Then  $\langle n_{\uparrow} \rangle - \frac{1}{2} > 0$ , and  $\langle n_{\downarrow} \rangle - \frac{1}{2} < 0$ . Therefore the up spin electrons will experience an *increase* in their effective chemical potential whose rol is played by the second term in the denominator of equation (5.45). As was noted in a previous section, one of the failures of 2OPT away from half filling is that it produces negative compressibilities when the interaction becomes of the order of the bandwidth. Therefore, in the present case this effect is translated into an effective diamagnetic response to the original magnetization. This has the consequence of reducing the tendency of the system to develop a magnetization, and ultimately to reduce the Néel temperature. We have also check that the region of parameter U where the Néel temperature is fully suppressed, indeed coincides with the region where the negative compressibility becomes more pronounced.

Regarding the Hartree-Fock calculation, we find that it fails to accurately reproduce the Green function obtained by QMC, however, it correctly predicts the existence of the antiferromagnetic phase.

It is also worthy to note the very close agreement of the Hartree-Fock results with

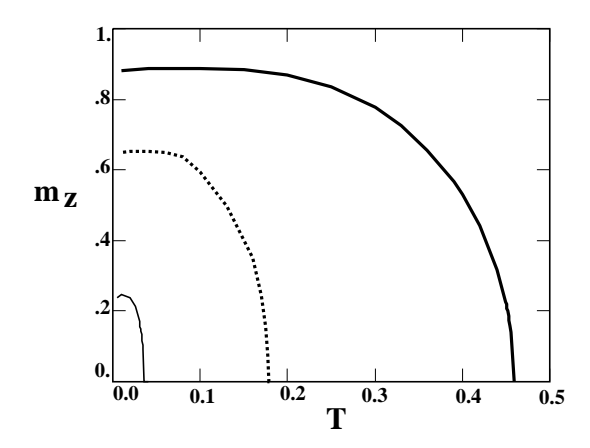


Figure 5.23: Local staggered magnetic moment as function of temperature obtained from Hartree-Fock approximation. The interaction U=0.5,1,2 (thin, dotted, and bold line).

the similar obtained for a three dimensional cubic lattice [29]. The agreement is very good not only for the Néel temperature, but also for the local magnetic moment as a function of U that we show in figure 5.23.

We want to turn now to the intersting case of adding frustration to the model. This question may be of relevance in the description of the  $V_2O_3$  compound. Although this system is found to be antiferromagnetic at low temperatures, experiments show that the magnetic interaction between neighboring variation sites is frustrated [31].

In this case we solve equations (5.8) that apply to the TSFF model introduced before. Many results are affected when a partial degree of frustration is added to the model. We see in figure 5.21 that the density of states is modified in a dramatic way. With the interaction U = 1.5 and the parameters  $t_1^2 = \frac{1}{4}t^2$  and  $t_2^2 = \frac{3}{4}t^2$ , we find that the frustration not only clearly reduces the magnetic moment, but more importantly, is able to close the gap, driving the system to a novel antiferromagnetic metallic phase. The possibility for this type of solutions has been previously considered by Cyrot [32], and it has been experimentally observed in  $V_2O_3$  by Carter et al. [33].

In figure 5.24 we show the results for the gap in the density of states as obtained from the ED calculation. It is clear from the plot how the TSFF represents an interpolation

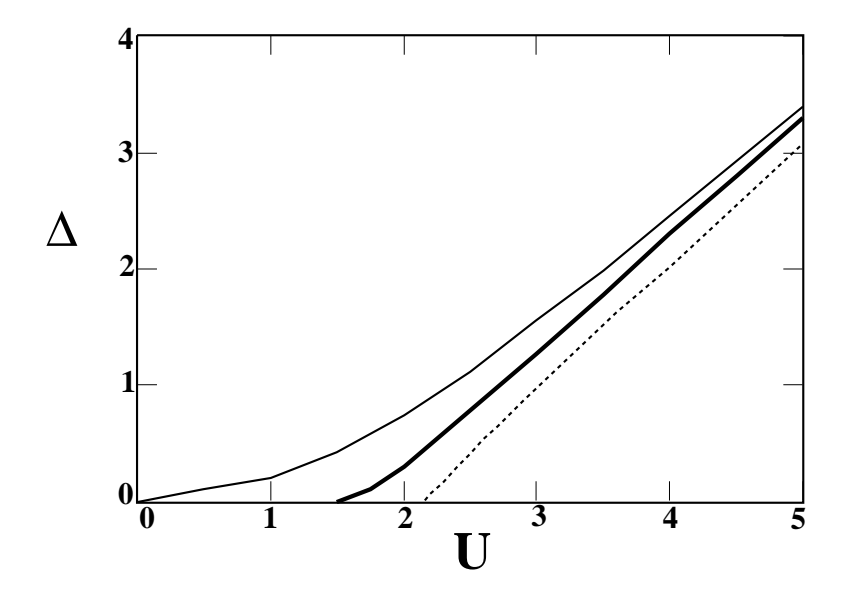


Figure 5.24: The gap in the density of states obtained from ED for the bipartite Bethe lattice (thin line), fully-frustrated lattice (dotted line), and TSFF model (bold line). The gap is defined as the distance between the lowest poles in the Green function. The curves correspond to the extrapolated results to an infinite size system from clusters of  $N_{sites} = 3, 5, 7$ . A  $1/N_{sites}$  scaling behavior is assumed.

between the fully frustrated case where no magnetic order is possible and the case of a bipartite lattice. It is interesting to note that the frustration lowers the value where the insulator disappears  $U_{AF2}$  respect to  $U_{c1}$  introduced before. We find that it is non-zero (unlike the bipartite case) and its value results  $U_{AF2} \approx 1.5$  for the above choice of parameters.

The local staggered magnetization shown in figure 5.25 remains continuous as a function of U as the antiferromagnetic gap closes. However, its value is decreased by the frustration. In particular it is driven to zero for a value of the interaction  $U_{AF1} \approx 0.5$ , in contrast to the bipartite lattice case where it remains non-zero when  $U \neq 0$ .

We have, therefore, a situation at T=0 where the solution is a paramagnetic metal until a value  $U_{AF1}$  is reached where the local staggered moment starts to develop and the system becomes an antiferromagnetic metal. When the interaction U is further increased, a gap in the density of states eventually opens as  $U_{AF2}$  is reached. From

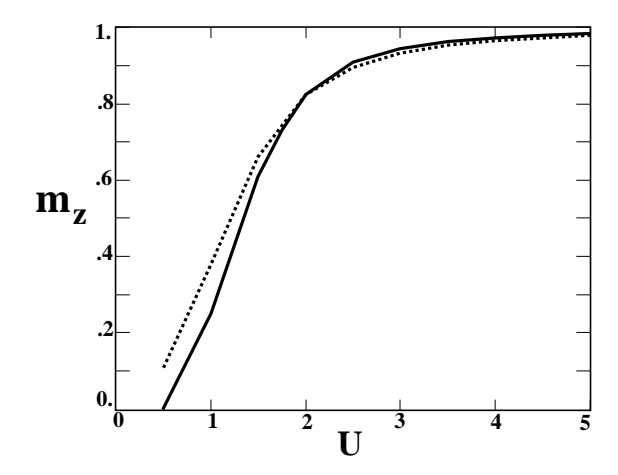


Figure 5.25: The local staggered magnetization obtained from ED for the bipartite Bethe lattice (dotted line), and TSFF model (bold line). The curves correspond to the extrapolated results to an infinite size system from clusters of  $N_{sites}=3,5,7$ . A  $1/N_{sites}$  scaling behavior is assumed.

there on an antiferromagnetic insulating state sets in.

As we increased the temperature with a value of the interaction slightly above  $U_{AF2}$ , we observe that the gap closes and we obtain an antiferromagnetic metallic state at finite temperature. The magnetization of this state rapidly disappears as T is further increased. This can be observed in figure 5.26 where we show results for the real and imaginary parts of the local Green function obtained from ED at T=0 and QMC simulations at T=1/64. It can be seen clearly how the imaginary part becomes non-zero at zero frequency in the finite temperature results, while the real part remains non-zero which signals an antiferromagnetic state.

It is interesting to note that the existence of an antiferromagnetic metallic phase is also obtained within the Hartree-Fock approximation. This is illustrated by the results of figure 5.27 that display the Green function obtained at U=0.95 and T=0.05. The imaginary part accordingly goes to a finite value at small frequency, while the real part is non-zero.

Within this approximation, it is possible to solve analytically for  $U_{AF1}$ , which is the value of the interaction where the solution acquires a staggered magnetic moment but

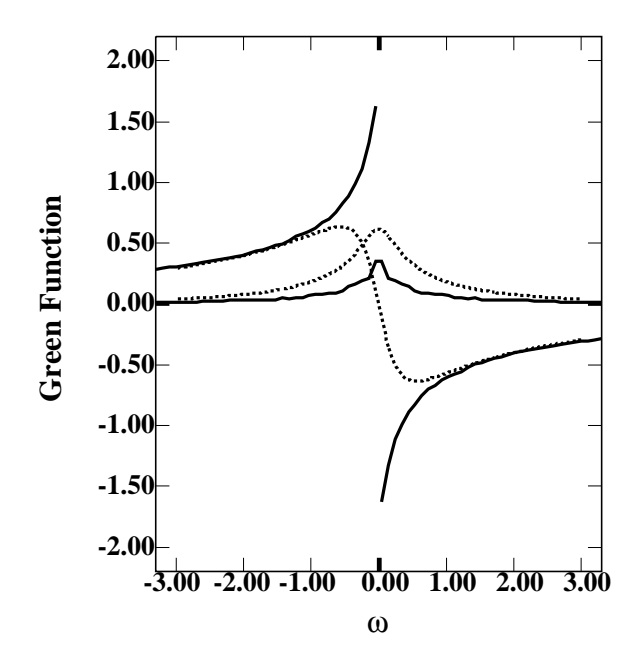


Figure 5.26: The antiferromagnetic metallic solution of the TSFF model as a function of Matsubara frequency. The imaginary part is odd and the real part even. Obtained from QMC at  $\beta = 64$  (full line) and ED of 8 sites (dotted line). The interaction U = 2

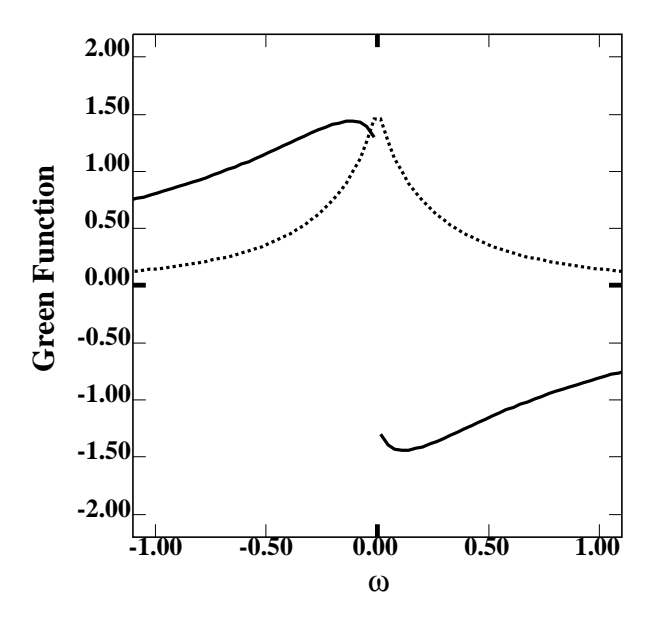


Figure 5.27: The antiferromagnetic metallic solution of the TSFF model as a function of Matsubara frequency. Obtained from the Hartree-Fock approximation at U=0.95 and T=0.05. The bold line corresponds to the imaginary part and the dotted line to the real part.

remains metallic.

The self-consistent equations for the TSFF model (5.8) that mimics a partial degree of frustration in the Hartree-Fock approximation read,

$$G_{\sigma} = \frac{1}{G_{0\sigma}^{-1} + \sigma \frac{U}{2} m_z} \tag{5.46}$$

$$G_{0\sigma}^{-1} = i\omega - t_1^2 G_{\sigma} - t_2^2 G_{-\sigma}$$
 (5.47)

where  $\sigma = 1, -1$  for the up and down spin Green function respectively.

We now expand the Green functions arround the non-interacting and non-magnetic  $G_0$  that corresponds to a semi-circular density of states of half-width 2t=D,

$$G_0(i\omega) = \frac{2}{i\omega + \sqrt{(i\omega)^2 - 4t^2}}$$
 (5.48)

Writing  $G_{\sigma} = G_0 + \delta G_{\sigma}$  and replacing in the self-consistency equations we obtain,

$$G_0^{-1} - \delta G_{\uparrow} G_0^{-2} = i\omega + \frac{U}{2} m_z - t^2 G_0 - t_1^2 \delta G_{\uparrow} - t_2^2 \delta G_{\downarrow}$$

$$G_0^{-1} - \delta G_{\downarrow} G_0^{-2} = i\omega - \frac{U}{2} m_z - t^2 G_0 - t_1^2 \delta G_{\downarrow} - t_2^2 \delta G_{\uparrow}.$$
(5.49)

Defining  $\delta G \uparrow -\delta G \downarrow = \delta G$ , we subtract the last equations to get

$$G_0^{-2}\delta G = -Um_z + (t_1^2 - t_2^2)\delta G$$
 (5.50)

and solving for  $\delta G$ ,

$$\delta G = \frac{Um_z}{-G_0^{-2} + (t_1^2 - t_2^2)} \tag{5.51}$$

which is the variation of  $G_{\uparrow} - G_{\downarrow}$  when U is small.

We can combine this result with the self-consistent condition for the magnetization that reads,

$$m_z = -\frac{1}{\pi} \int_{-\infty}^0 Im[\delta G] \tag{5.52}$$

Inserting the expression for  $G_0$  on the real axis

$$G_0^{-1}(\omega) = rac{\omega}{2} + irac{sgn(\omega)}{2}\sqrt{4t^2 - \omega^2}, \qquad -D < \omega < D \qquad (5.53)$$

into  $\delta G$ , we obtain, after a few steps of tedious algebra, the following expression for the critical value of  $U_{AF1}$  where a non-zero magnetization appears

$$U_{AF1}^{HF} = \frac{3\pi}{2} \left( \int_0^1 \frac{\sqrt{1-x}}{x^2 + x\frac{1}{3}(1-8\alpha) + \frac{4\alpha^2}{3}} dx \right)^{-1}$$
 (5.54)

where  $\alpha$  is defined from  $t_1^2 - t_2^2 = t^2 \alpha - t^2 (1 - \alpha) = -t^2 (1 - 2\alpha)$ . Examining equation (5.54) we realize that for  $\alpha \neq 0$  the integral converges and a finite  $U_{AF1}$  is obtained. For  $\alpha = 0.25$  we numerically solve the integral to obtain  $U_{AF1}^{HF} \approx 0.71$  which is consistent with the value obtained previously from the ED calculation.

For the case  $\alpha=0$  which corresponds to the bipartite Bethe lattice, i. e., without frustration, the integral has a logarithmic divergency. This is signals that the original assumption that the Green function can be expanded arround the non-interacting non-magnetic  $G_0$  breaks down. This is because in this case  $U_{AF2}=0$ , since an infinitesimal U immediately drives the system to the antiferromagnetic insulating state.

Let us now consider the large U region. The modification of the Néel temperature cannot be obtained with QMC in this case since U is large and T is low. However, it can be analytically determined. We have seen in figure 5.25 that even in the presence of partial frustration, the magnetic moment becomes rapidly saturated for intermediate values of U. We therefore consider, as we did in the previous section, the extension to the TSFF model of the spin hamiltonian that we introduced before. The solution is straightforward and the Néel temperature is found to be reduced as  $T_N = J_2 - J_1 = 2(t_2^2 - t_1^2)/U$ .

Finally, we combine all the present results with the earlier ones for the fully frustrated model, to obtain a new phase diagram for the model with a partial degree of magnetic frustration. The results are summarized in figure 5.28. It is very intersting to note that most of the main features experimentally observed in  $V_2O_3$  are realized in this model [34, 35, 33]. In particular if we associate decreasing pressure with increasing interaction U, we find the correct tilting of the first order line that separates the paramagnetic metallic to the paramagnetic insulating state. This line ends both, in the our case and in the experiment, in a second order critical point where a crossover region starts and which is tilted in the opposite way. The topology of the phase diagram is also captured in detail, even the small antiferromagnetic metallic region recently found by Carter et al. [33]. As a last remark, is notable that also the temperature scales are consistent with the experiments if we set the bandwidth  $D \approx 0.5 eV$ .

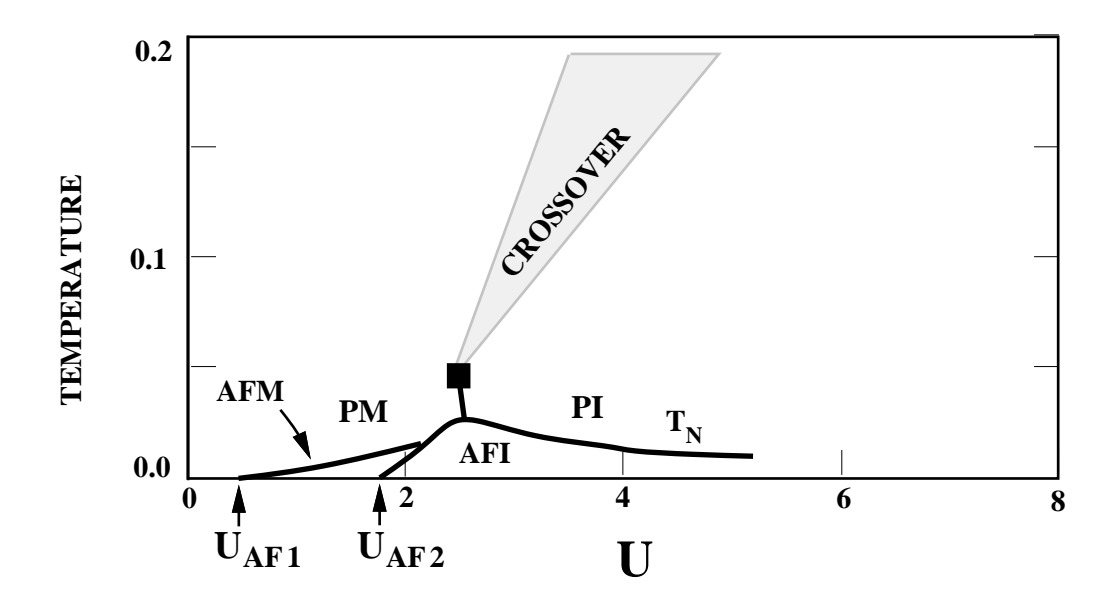


Figure 5.28: Approximate phase diagram of the TSFF model. The solid lines indicate the first-oder lines separating the magnetic phases that correspond to parameters  $t_1^2 = 0.25t^2$ ,  $t_2^2 = 0.75t^2$ . The square indicates a second order critical point. The shaded region corresponds to a crossover from a paramagnetic metal to an insulator state.

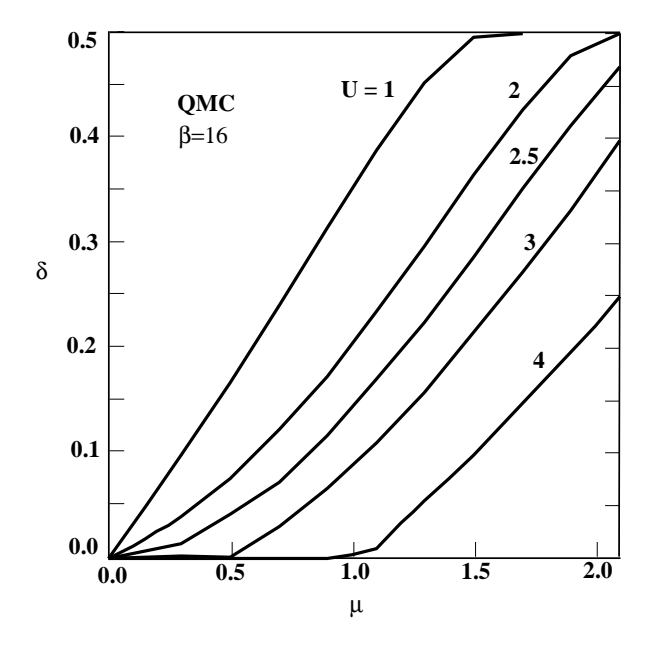


Figure 5.29: Particle number  $\delta = n - \frac{1}{2}$  as a function of the chemical potential  $\mu$ . Data obtained from QMC at  $\beta = 16$ , for different values of the interaction U.

### 5.8 The transition as a function of doping

It is interesting to investigate the Mott transition as a function of doping in the Hubbard model. We believe that away from half filling and in the paramagnetic phase there is only one solution, and then we can investigate the behavior of various quantities as a function of filling factor.

We first show in figure 5.29, the particle occupation as a function of the chemical potential as obtained from QMC at  $\beta=16$ . We note that the slope of the curve, i.e. the compressibility, goes to zero at  $\mu=0$  as  $U_c$  is approached. For bigger values of U, we have a vanishing compressibility characteristic of an insulating state. It displays a gap approximately equal to U-2D which compares very well with the results for the size of the gap from the exact diagonalization method (figure 5.15). Notice that for  $U>U_c$  the  $\delta$  vs.  $\mu$  curves approach half filling ( $\delta=0$ ) with a finite slope.

We also calculated the specific heat and spin susceptibility as a function of doping for the case U=3. This places the system close to the Mott point, as it seems to be the

case for compounds as  $La_xSr_{1-x}TiO_3$  and the high  $T_C$  cuprates [36]. The specific heat  $\gamma = \frac{\pi^2 k_B^2}{3} \rho^0(\epsilon_F) \frac{m^*}{m}$ , and the spin susceptibility  $\chi_S = \mu_B^2 \left[\frac{dm}{dh}\right]_{h=0}^{m}$ , with  $m = n_\uparrow - n_\downarrow$ , are displayed in figure 5.30. The plot is in units of  $\gamma^0 = \frac{\pi^2 k_B^2}{3} \rho^0(0) = \frac{4}{3} \frac{\pi k_B^2}{D}$  and  $\chi_S^0 = \frac{\mu_B^2}{D}$  respectively, and corresponds to QMC simulations at  $\beta = 32$ . This compares rather well with the experiments of Tokura et al. on  $La_xSr_{1-x}TiO_3$  [37]. The specific heat is consistent with the parametrization  $\gamma \approx 0.28 \frac{\gamma^0}{\delta}$ . Notice also that for small doping the renormalized mass behaves as  $\frac{m^*}{m} \propto z^{-1} \propto \gamma \propto \delta^{-1}$ . This quantity is shown in the inset of the figure.

The Wilson ratio  $(\chi_S/\gamma)/(\chi_S^0/\gamma^0)$ , plotted as function of doping in figure 5.31, is derived from these quantities. We note that its value is consistently lower than the experimental value  $R\approx 2$  that is found in the compound mentioned above. Whether this is due to a shortcoming of the mean field theory, or it is some interesting effect of the many orbital character of the experimental system, remains an interesting open problem.

#### 5.9 Conclusion

The solution of the Hubbard model in the limit of large dimensions has provided a limit where various early ideas can be put in perspective.

One issue is whether a metal insulator transition can take place in the absence of magnetic order. The phase diagram presented in figure 5.3 and figure 5.28 answers this question in the affirmative for a frustrated lattice.

There is a region enclosed by two lines  $U_{c1}(T)$  and  $U_{c2}(T)$ , where both the metallic and the insulating solutions are allowed. Within this region, there is a first order boundary where the two very different solutions cross in free energy, and several quantities experience a jump: the specific heat, the susceptibility, the number of doubly occupied sites, etc. The first order line has a negative slope indicating that the paramagnetic insulating phase has a higher entropy than the metallic phase. The line ends in an interesting second order critical point, above it there is a smooth crossover between a metallic and an insulating regime.

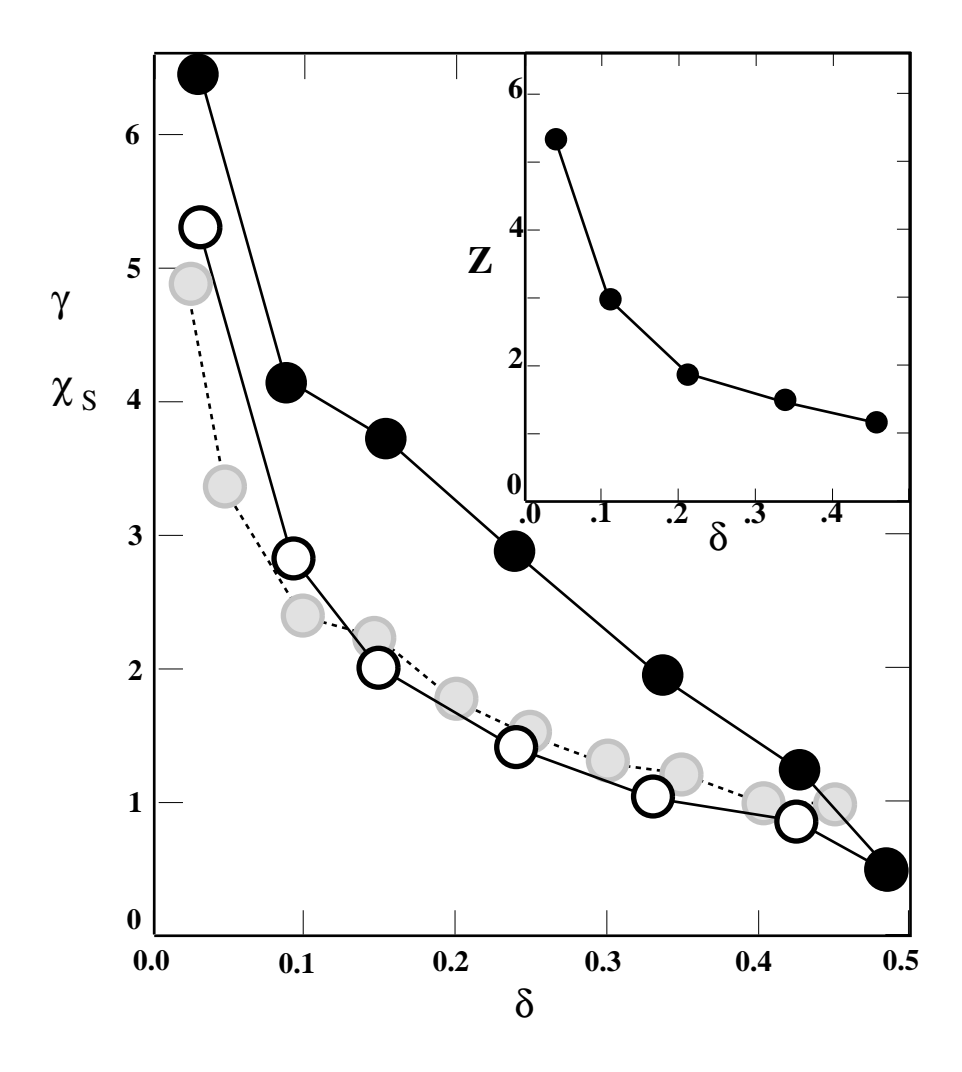


Figure 5.30: Specific heat (white dots) and spin susceptibility (black dots) as function of doping for U=3 and  $\beta=32$ . The experimental results for the specific heat from ref. [31] are plotted for comparison (grey dots). The inset shows the renormalized mass  $m^*/m=Z^{-1}$  as a function of doping.

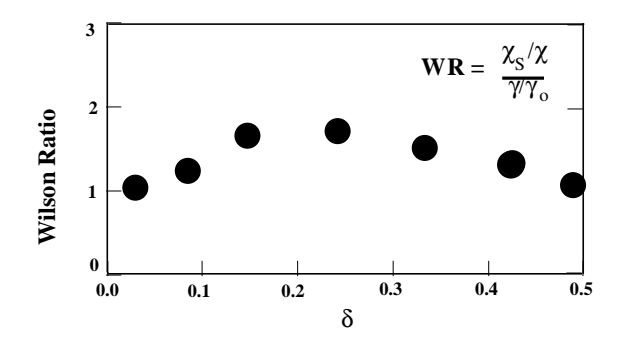


Figure 5.31: The Wilson ratio as function of doping for U = 3.

We also demonstrated that for  $U < U_{c2}$ , the one particle Green function of the model captures some aspects of the Brinkman-Rice scenario. In particular, the mass renormalization diverges as  $(U_{c2} - U)^{-1}$  [13]. At the same time, the solution of the Hubbard model in infinite dimension also allowed us to perform calculations of physical quantities at finite temperatures, and eliminated some of the shortcomings of the Brinkman Rice description of the Mott transition. In the actual solution, the number of doubly occupied sites is finite and changes smoothly at the metal-insulator transition resulting in a finite exchange constant which gives rise to a finite susceptibility. We also observed that at  $U_{c2}$ , the single particle gap opens discontinuously, which is different from the predictions of the slave boson method [38], but is not inconsistent with the experimental observations of Fujimori *et al.* [36].

We found a natural scenario for the destruction of the insulating solution with the continuous narrowing of the gap of the insulator. This is a realization of the original Hubbard scenario for the MIT driven by the closing of the upper and lower Hubbard bands. In this case,  $U_{c1}$  corresponds to the value of the interaction where the gap in the one particle spectra vanishes, or equivalently, where the divergence of the dielectric constant is observed. This was demonstrated by the exact diagonalization results. Although the same was not the case within the second order approximation to the impurity self-energy, this calculation, nevertheless, provided valuable insights on the nature of the destruction of the insulating solution.

On non-frustrated, bipartite lattices, however, we find that the Néel temperature is much higher than the metal insulator transition temperature, making the transition between small and large U continuous. In this case, the physics can be understood in terms of the magnetic long range order and a smooth crossover within the broken symmetry phase. The Mott transition is irrelevant, vindicating Slater's point of view.

When a partial degree of frustration is considered, in addition, at low temperatures there is a first order line between an antiferromagnetic metal and an antiferromagnetic insulating phase. This is possibly relevant to the experimental results of Carter *et al.* [33]. In this case, the phase diagram has the same topology and even the same scale as the experimentally observed phase diagram of  $V_2O_3$ . We therefore conclude, that the Hubbard model in large dimensions at half filling on a frustrated lattice can account for the basic experimental features observed in the  $V_2O_3$  system vindicating Mott's point of view.

The experimentally observed phase diagrams of transition metal oxides display incommensurate metallic magnetism. This can in principle be studied by extending the mean field theory to account for incommensurate phases as done by Freericks for the Falikov Kimball model [39]. For this calculation to be meaningful, however, one should include the details of a realistic band structure of the transition metal oxide, which is beyond the scope of our work.

An important open question is what happens to the transition at finite dimensions? We expect that the Mott transition and the metal charge transfer insulator transition are in the same universality class. The large N expansion results of [27] indicate that for N=2,  $U_{c1}$  and  $U_{c2}$  coincide and that the Mott transition is second order with continuous disappearance of the Kondo resonance and a gradual closing of the Mott gap. Similar results were obtained with the slave boson approach to the Hubbard model. Whether the large N expansion is missing crucial 1/N terms which would split the two transitions, or whether the 1/d corrections would bring the two transitions to one, remains an interesting open problem.

## References

- [1] N. F. Mott, Phil. Mag. 6, 287 (1961).
- [2] J. Hubbard, Proc. Roy. Soc. (London) A281, 401 (1964).
- [3] W. F. Brinkman and T. M. Rice, Phys. Rev. B 2, 4302 (1970).
- [4] J. C. Slater, Phys. Rev. 82, 538 (1951).
- [5] W. Metzner and D. Vollhardt, Phys. Rev. Lett. 62, 324 (1989).
- [6] U. Brandt and C. Mielsch, Z. Phys. 75, 365 (1989), 79, 295 (1990), and 82, 37 (1991).
- [7] V. Janis, Z. Phys. B 83, 227 (1991)
- [8] E. Müller-Hartmann, Z Phys. B **74** 507-512 (1989), and Z. Phys. B **76** 211-217 (1989).
- [9] A. Georges and G. Kotliar, Phys. Rev. B 45, 6479 (1992).
- [10] V. Janis and D. Vollhardt, Int. Journ. Mod. Phys. B, Vol. 6, Nos 5 & 6, 731 (1992).
- [11] A. Georges, G. Kotliar and Q. Si, Int. J. Mod. Phys. B 6, 705 (1992).
- [12] M. Rozenberg, X. Y. Zhang and G. Kotliar, Phys. Rev. Lett. 69, 1236 (1992).
- [13] X. Y. Zhang, M. J. Rozenberg and G. Kotliar, Phys. Rev. Lett. 70, 1666 (1993).
- [14] M. J. Rozenberg, G. Kotliar and X. Y. Zhang, Phys. Rev. B 49, 10181, (1994).
- [15] M. Jarrell, Phys. Rev. Lett. 69, 168 (1992). Th. Pruschke, D. L. Cox and M. Jarrell, Euro Phys. Letts. 21, 5 (1993), and Phys. Rev. B 48, (1993).
- [16] A. Georges and W. Krauth, Phys. Rev. Lett. 69, 1240 (1992).
- [17] A. Georges and W. Krauth, Phys. Rev. B 48, 7167 (1993).
- [18] V. Janis, M. Ulmke and D. Vollhardt, (preprint 1993).
- [19] A. Georges and S. Sachdev, (in preparation).
- [20] K. Yamada, Prog. Theor. Phys. 53, 4 (1975)970, and K. Yosida and K. Yamada, ibid., 1286.
- [21] M. Caffarel and W. Krauth, Phys. Rev. Lett. 72, 1545 (1994).
- [22] M. J. Rozenberg, G. Moeller and G. Kotliar, Mod. Phys. Lett. B (to appear 1994).
- [23] G. Moeller, Q. Si, G. Kotliar, M. J. Rozenberg and D. Fisher, (preprint).

- [24] This possibility was suggested to us by D. Fisher as a way of reconciling the numerical results of our group and those of the ENS group.
- [25] D. Vollhardt, Rev. Mod. Phys. 56, 99 (1984).
- [26] G. Kotliar, Int. Journ. Mod. Phys. B 1, 711 (1988).
- [27] C. Castellani, G. Kotliar, R. Raimondi, M. Grilli, Z. Wang, and M. Rozenberg, Phys. Rev. Lett. 28, 2009 (1992).
- [28] M. Grilli and G. Kotliar, Phys. Rev. Lett. 64, 1170 (1990).
- [29] W. Langer, M. Plischke, and D. Mattis, Phys. Rev. Lett. 23, 1448 (1969).
- [30] H. Yokoyama and H. Shiba, J. Phys. Soc. Jpn. 56, 3582 (1987).
- [31] R. M. Moon, Phys. Rev. Lett. 25, 527 (1970).
- [32] M. Cyrot, J. Physique 33, 125 (1972).
- [33] S. A. Carter, T. F. Rosenbaum, J. M. Honig, and J. Spalek, Phys. Rev. Lett. 67, 3440 (1992).
- [34] D. B. McWhan, A. Menth, J. P. Remeika, W. F. Brinkman, and T. M. Rice Phys. Rev. B 7, 1920 (1973).
- [35] H. Kuwamoto, J. M. Honig, and J. Appel Phys. Rev. B 22, 2626 (1980).
- [36] A. Fujimori, I. Hase, H. Namatame, Y. Fujishima, Y. Tokura, H. Eisaki, S. Uchida, K. Takegahara, and F. M. F. de Groot, Phys. Rev. Lett. 69, 1796 (1992).
- [37] Y. Tokura, Y. Taguchi, Y. Okada, Y. Fujishima and T. Arima, K. Kumagai, Y. Iye Phys. Rev. Lett. 70, 2126 (1993).
- [38] G. Kotliar, Int. J. Mod. Phys. B, 711 (1988).
- [39] J. Freericks, Phys. Rev. B 47,9263 (1993).

# Chapter 6

### The coexistent solutions

### 6.1 Introduction

The correlation induced metal-insulator transition (Mott-Hubbard transition) is one of the prime examples in which strong correlations dominate the low-energy behavior of a physical system. A theoretical treatment of the problem requires an approach which is non-perturbative in the interaction. Recently, new insights into the problem were gained using the limit of infinite dimensionality [1, 2]. It allows for a mapping of a variety of lattice models onto impurity problems in a self-consistently determined bath [3, 4] and is therefore a natural way to formulate a mean-field theory of itinerant systems. While being simpler than the original problem, the resulting mean-field theory remains a formidable many-body problem which has to be solved using numerical methods. Recently the Hubbard model has been investigated by several groups using Quantum Monte Carlo (QMC) simulations and self-consistent perturbation theory (PT) [5, 6, 7, 8]. While a combination of both methods established the existence of a Mott-Hubbard transition at a finite value of the interaction U in the paramagnetic phase of the Hubbard model at half-filling, important questions regarding the nature of the transition remain unsolved.

In the previous chapter, the coexistence of metallic and insulating solutions over a finite range of values of U has been demonstrated [9]. While the metallic solution disappears continuously at a value  $U_{c2}$ , the insulating solution disappears abruptly at a value  $U_{c1} < U_{c2}$ . At finite temperature, the difference between the free energy of the solutions is dominated by the entropy term. The large entropy, which is a result of the degeneracy of the ground state in the insulating case, made it possible to unambiguously determine the existence of a first order transition line close to  $U_{c1}(T)$ . As the temperature is reduced, the free energy approaches the energy, therefore an accurate evaluation of the energy is necessary. Depending on which solution is lower in energy two very different scenarios may take place: If  $E_{Ins} < E_{Met}$ , the transition will be close to  $U_{c1}$  and the sudden destruction of the metallic state implies a first-order transition even at T=0. On the other hand, in the case  $E_{Met} < E_{Ins}$ , the metallic solution continuously merges with the insulating one at  $U_{c2}$ , and the quasiparticles display a diverging renormalized mass [9].

While the limit T=0 cannot be attained by QMC simulations, within the secondorder perturbative approach the energies of the two solutions are almost degenerate, making the consideration of higher-order corrections necessary. An alternative numerical approach to the problem was introduced recently: While the large d mean field equations are functional equations for the Green function  $G(i\omega_n)$ , an approximation can be obtain by modeling  $G(i\omega_n)$  using a finite number N of parameters, which reduces the functional equations to non-linear algebraic equations in N unknowns. Following this idea, two different parameterizations were introduced [10, 11]. Both take advantage of a mapping of the lattice problem onto an Anderson impurity model with a self-consistently determined bath. The N parameters that model  $G(i\omega_n)$  define the hopping amplitudes and energies of the effective electron orbitals of the bath, as will be discussed in detail in next section. The resulting problem can then be solved at T=0by exact diagonalization of the effective Hamiltonian. This is followed by the new determination of the set of parameters, and the procedure is iterated until convergence is attained. The method is thus non-perturbative in nature and overcomes the problems of both QMC and PT, allowing for an accurate evaluation of the energies at T=0.

In this paper we apply this approach to the study of the Hubbard model. We establish the coexistence of metallic and insulating solutions over a finite range of the interaction parameter U and show that at T=0 the metallic solution has lower energy than the insulating one, implying that the metal-insulator transition in the Hubbard model with semicircular density of states is of second order. This justifies a posteriori the relevance of the earlier studies [8] of this quantum critical point which captures the essence of the Brinkman-Rice transition.

### 6.2 Methodology

In the limit of infinite dimensionality the Hubbard model, described by the Hamiltonian

$$H = -\sum_{\langle i,j \rangle} (t_{ij} + \mu) c_{i,\sigma}^{\dagger} c_{j,\sigma} + U \sum_{i} (n_{i\uparrow} - \frac{1}{2}) (n_{i\downarrow} - \frac{1}{2}), \tag{6.1}$$

can be reduced to an effective impurity problem, supplemented by a self-consistency condition [4]. As in the previous work we focus on a Bethe lattice of infinite connectivity d, which in the non-interacting limit corresponds to a semicircular density of states of width 4t, where the hopping parameter t is rescaled in the usual way as  $t \to \frac{t}{\sqrt{d}}$ . Integrating out the degrees of freedom other than the origin, one obtains an effective local action of the form

$$S_{eff}[c,c^{\dagger}] = \sum_{\sigma} \int d au d au' c_{\sigma}^{\dagger}( au) G_0^{-1}( au- au') c_{\sigma}( au') + U \int_0^{eta} d au (n_{i\uparrow}( au) - rac{1}{2}) (n_{i\downarrow}( au) - rac{1}{2}) (6.2)$$

In the following we focus on the paramagnetic solution at half filling ( $\mu = 0$ ). The self-consistency condition then reads  $G_0^{-1}(i\omega_n)=i\omega_n-t^2G(i\omega_n)$  where  $G(i\omega_n)=i\omega_n-t^2G(i\omega_n)$  $-\int_0^eta {
m e}^{i\omega_n au} < T_ au c( au)c^\dagger(0)>_{S_{eff}} {
m is \ the} \ local \ {
m Green \ function \ of \ the \ Hubbard \ model}$  once self-consistency is attained. As shown in previous chapters an action of the same form can be obtained from an Anderson impurity model by integrating out the conduction electrons [4]. Note that the self-consistency condition implies that the role of the hybridization function is played by the local Green function itself. The iterative solution now proceeds as follows:  $G(i\omega_n)$  is modeled by a finite set of parameters. In terms of the impurity problem, this represents an effective bath for the impurity with a finite number of poles. This effective impurity model is then solved by exact diagonalization and a new  $G(i\omega_n)$  is calculated. A new set of parameters is then obtained from  $G(i\omega_n)$ by approximating it by a function with a number of poles equal to the number of sites in the bath (this number is in general smaller than the number of poles of  $G(i\omega_n)$ ). Note that this represents a further approximation of the method (beyond the effective Hamiltonian being finite). The whole process is iterated until convergence of the parameters is achieved.

Exploiting these features, two new similar algorithms were proposed recently [10, 11], differing basically in the way the new set of parameters is obtained, that is, how the  $G(i\omega_n)$  is parametrized by a smaller number of poles. We will consider both schemes and comment on their respective advantages and limitations.

As mentioned, the number of poles of  $G(i\omega_n)$  is in general larger that the number of sites in the bath, therefore this approximation is an essential ingredient of the scheme. Caffarel and Krauth [10] proposed to obtain the new parameters by a  $\chi^2$  fit of  $G(i\omega_n)$ . Starting with an Anderson Hamiltonian of the form

$$H = \sum_{lpha,\sigma} \epsilon_{lpha} a^{\dagger}_{lpha\sigma} a_{lpha\sigma} + \sum_{lpha,\sigma} (V_{lpha} a^{\dagger}_{lpha\sigma} c_{\sigma} + h.c.) + U(n_{\uparrow} - rac{1}{2})(n_{\downarrow} - rac{1}{2})$$
 (6.3)

the self-consistency condition becomes  $t^2G(i\omega)=\sum_{\alpha=1}^{N_s}\frac{V_{\alpha}^2}{i\omega_n-\epsilon_{\alpha}}$ . We thus have to minimize

$$\chi^2 = \sum_{i\omega_n}^{N_\Omega} |G(i\omega_n) - \sum_{\alpha=1}^{N_{site}} \frac{V_\alpha^2}{i\omega_n - \epsilon_\alpha}|^2$$
 (6.4)

where we sum over frequencies  $\omega_n=(2n+1)\pi T$  with small fictitious temperature (T=.001) and large cutoff  $N_\Omega\Delta\omega\approx 2U$ , to obtain the new set of parameters  $V_\alpha$  and  $\epsilon_\alpha$ . Note that this Hamiltonian effectively describes an impurity surrounded by a "star" of bath electrons.

An alternative route was introduced in the context of an extended Hubbard model [11]. This procedure takes advantage of the fact that the Green function G(z) can be decomposed into "particle" and "hole" contributions as  $G(z)=G^>(z)+G^<(z)$  with  $G^>(z)=\langle gs|c\frac{1}{z-(H-E_0)}c^\dagger|gs>$  and  $G^<(z)=\langle gs|c^\dagger\frac{1}{z+(H-E_0)}c|gs>$ .

The respective contributions can be obtained from a continued fraction expansion as

$$\langle f_0^{>/<} | \frac{1}{z \mp (H - E_0)} | f_0^{>/<} \rangle = \frac{\langle f_0^{>/<} | f_0^{>/<} \rangle}{z \pm E_0 - a_0^{>/<} - \frac{b_1^{>/<2}}{z \pm E_0 - a_1^{>/<} - \frac{b_2^{>/<2}}{z \pm E_0 - a_2^{>/<} - \dots}}}$$
(6.5)

where  $|f_0^>>=c^\dagger|gs>$ ,  $|f_0^<>=c|gs>$  and  $|f_{n+1}>=H|f_n>-a_n|f_n>-b_n^2|f_{n-1}>$ ,  $a_n=<f_n|H|f_n>$ ,  $b_n^2=\frac{\langle f_n|f_n>}{\langle f_{n-1}|f_{n-1}>}$ ,  $b_0=0$ . This implies that  $G^>$  and  $G^<$  can be regarded as resulting from a Hamiltonian describing an impurity coupled to two chains

with site energies  $a_n^{>/<}$  and hopping amplitudes  $b_n^{>/<}$ . Again the number of poles in the Green function is in general larger than the number of sites of the Hamiltonian and in order to close the self-consistency, the continued fraction expansion has to be truncated. The approximation in this scheme relies on the fact that the continued fraction representation captures exactly the moments of the energy of the Hamiltonian, up to the order retained in the continued fraction. It can thus be thought of as a moment by moment fitting. This scheme has the numerical advantage that it avoids the multidimensional fit of the Green function, but the disadvantage that it can be implemented practically only in the case of a semi-circular density of states. In the metallic case an explicit extra site at the Fermi energy is introduced in order to better represent the low frequency region and, more importantly, to allow us to feed-back a metallic bath. The hopping parameter to this extra site is calculated by a single parameter minimization of the expression

$$\chi^2(\alpha) = \sum_{i\omega_{nL}}^{i\omega_{nH}} |G_A(i\omega_n, \alpha) - G(i\omega)|^2$$
 (6.6)

where now  $G_A(i\omega_n,\alpha)=\frac{\alpha}{i\omega_n}+(1-\alpha)G_{N_C}(i\omega_n)$ .  $G_{N_C}$  is the truncated Green function to length  $N_C=N_{Site}/2$  and  $\omega_L$  and  $\omega_H$  are low and high energy cut-offs defined by the lowest poles of G and  $G_{N_C}$ , respectively. In this case the moments will be modified by a small factor  $(\alpha)$  which decreases as the system size is increased.

The effective Anderson model therefore reads

$$H = \sum_{\sigma} \sum_{\rho = >, <} \left( \sum_{\alpha = 1}^{N_C - 1} a_{\alpha}^{\rho} c_{\alpha\sigma}^{\rho\dagger} c_{\alpha\sigma}^{\rho} + \sum_{\alpha = 1}^{N_C - 2} (b_{\alpha}^{\rho} c_{\alpha\sigma}^{\rho\dagger} c_{\alpha+1\sigma}^{\rho} + h.c.) \right) + \sum_{\sigma} b_0 (c_{\sigma}^{\dagger} c_{0\sigma} + h.c.) + U(n_{\uparrow} - \frac{1}{2})(n_{\downarrow} - \frac{1}{2})$$

$$(6.7)$$

with  $c_{\sigma}$  being the destruction operator at the impurity site,  $c_{0\sigma}$  being the destruction operator at the effective bath site with zero enemergy, and  $c_{\alpha\sigma}^{\rho}$  being the destruction operator at the chain sites of the effective bath.

In both schemes, ground-state wavefunction and ground-state energy of the Anderson Hamiltonian are determined by exact diagonalization (up to six sites) and the modified Lanczos technique [12]. Systems of up to ten sites can be handled on a work-station. The zero temperature Green function of the local site is finally obtained from

a continued fraction expansion using the recursion method discussed above.

As mentioned in the introduction, a further advantage of the formulation of the problem in terms of an Anderson impurity model is the fact that the energy of the Hubbard model can be obtained directly without frequency summations using Anderson model relations. The kinetic energy per site of the Hubbard model is given as  $T=\frac{2}{\beta N}\sum_{\langle j,k\rangle}\sum_{i\omega_n}tG_{jk}(i\omega_n)e^{i\omega_n0^+}$ . Taking the limit of infinite coordination number this reduces to  $T=\frac{2t^2}{\beta}\sum_{i\omega_n}G(i\omega_n)^2e^{i\omega_n0^+}$ . Using the self-consistency condition as well as the the fact that in the Anderson model  $\frac{2}{\beta}\sum_{i\omega_n}\sum_{\alpha\sigma}\frac{V_{\alpha}^2}{i\omega_n-\epsilon_{\alpha}} < c_{\sigma}(i\omega_n)c_{\sigma}^{\dagger}(i\omega_n) >$   $=\sum_{\alpha\sigma}V_{\alpha}< c_{\sigma}^{\dagger}c_{\alpha\sigma}+h.c.> \text{ we obtain}$ 

$$T = \sum_{lpha\sigma} V_{lpha} Re < gs | c_{\sigma}^{\dagger} c_{lpha\sigma} | gs >,$$
 (6.8)

where  $\alpha$  labels the sites neighboring the impurity. The potential energy of the Hubbard model is obtained as

$$V = U < gs|n_{\uparrow}n_{\downarrow}|gs>. \tag{6.9}$$

### 6.3 The two solutions

In our analysis we have focused on two major aspects: the determination of a region where two solutions are allowed, and the resolution of controversy regarding the lowest energy solution. The two approaches considered yield a consistent picture of the transition. We are able to obtain converged metallic and insulating solutions for a finite range of the interaction U within both schemes. We further demonstrate that the metallic solution is lower in energy in the whole coexistence region. The energy difference between the solutions goes to zero as  $U_{c2}$  is approached, implying that the transition can be classified as second order. This should be contrasted with the results from second-order perturbation theory, where the two solutions were found to cross in energy at an intermediate value of the interaction U. A point worth noticing (as was already observed within the perturbative approach) is that the energy difference between the solutions is much smaller than any energy scale of the problem. This is due to an almost perfect compensation of the gain in delocalization (kinetic) energy, by the loss of energy through double occupancy (potential energy), in the metallic state

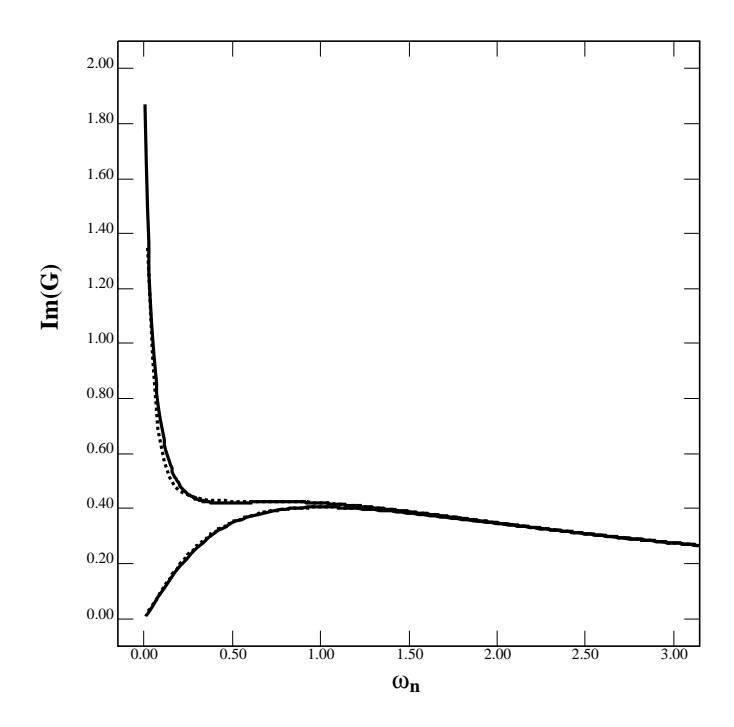


Figure 6.1: Comparison of the metallic and insulating Matsubara Green functions for U=2.7, as obtained from the two variations of the algorithm. Full line "star geometry" and dotted line "two chain geometry" (10 sites for the metallic case and 8 sites for the insulating).

compared to the insulator.

Metallic and insulating solutions for U=2.7 inside the coexistence region are shown in figure 6.1 (the half-bandwidth 2t is set equal to unity). In the first case the Green function displays a narrow resonance at low frequency (note that the pinning condition at  $\omega=0$  is fulfilled [13]), while the insulator in the second case merely consists of high energy features (upper and lower Hubbard bands). The figures also illustrate the consistency of the two schemes considered here. In both, the metallic and insulating, cases the agreement is very good. We also find that the results of both methods for the single particle Green function on the imaginary axis compare very well with the second-order perturbative calculation [8] and QMC [6, 7] (the latter is discussed in reference [10]).

The kinetic, potential and total energies for the two solutions in the coexistence

region are displayed in figure 6.2. An interesting feature is the already mentioned almost perfect cancellation of delocalization and double occupancy energy. Another important observation is that while a finite size effect is apparent in the results for the kinetic and potential energy, the convergence of the total energy is much faster [14]. A few runs for a ten site system show almost no difference to the results for eight sites.

The energy difference of the two solutions is shown in the inset of figure 6.2. As the critical point  $U_{c2}$  is approached from below, the finite size effects become relevant for  $U \approx 2.8$ . This limitation of the scheme is due to the fact that as the low energy scale associated with the quasiparticle peak goes to zero close to the transition, the discrete nature of the approximation starts playing an important role and the Kondo resonance is represented by only a single pole.

The smallness of the difference in energy between the metal and the insulator can be understood from the picture of a second-order critical point where the metallic and insulating solutions merge with a vanishing scale  $\Delta \sim U_{c2} - U$ . The problem can be formulated from a variational point of view, with the free energy F becoming an extremum at the metallic and insulating solutions, i.e.,  $\frac{\delta F}{\delta G_M} = \frac{\delta F}{\delta G_I} = 0$ . Since the two solutions merge at the point  $U_{C2}$ , F can be expanded in power series of  $G_M - G_I$  as

$$F_M - F_I = \frac{\delta^2 F}{\delta G^2} (G_M - G_I)^2. \tag{6.10}$$

As the difference between the metallic and the insulating solution is parameterized by  $\Delta$ , and the second derivative vanishes at the critical point as  $\Delta$ , it follows that the energy difference goes to zero as  $\Delta^3$ . The critical region cannot be accessed by the present method. In order to capture the vanishing energy scale, a higher resolution (i.e. an effective bath with more sites) is needed.

Finally, we would like to comment on the disappearance of the insulating solution at  $U_{c1}$ . From the "two chain" scheme, the insulating solution is found to persist all the way down until the gap closes. This differs from the results of perturbation theory and resembles the Hubbard III scenario for the destruction of the insulating state [17, 18]. In the case of the "star configuration", while a converged insulating solution can be obtained at values of the interaction U well below  $U_{c2}$ , the question of the closing of

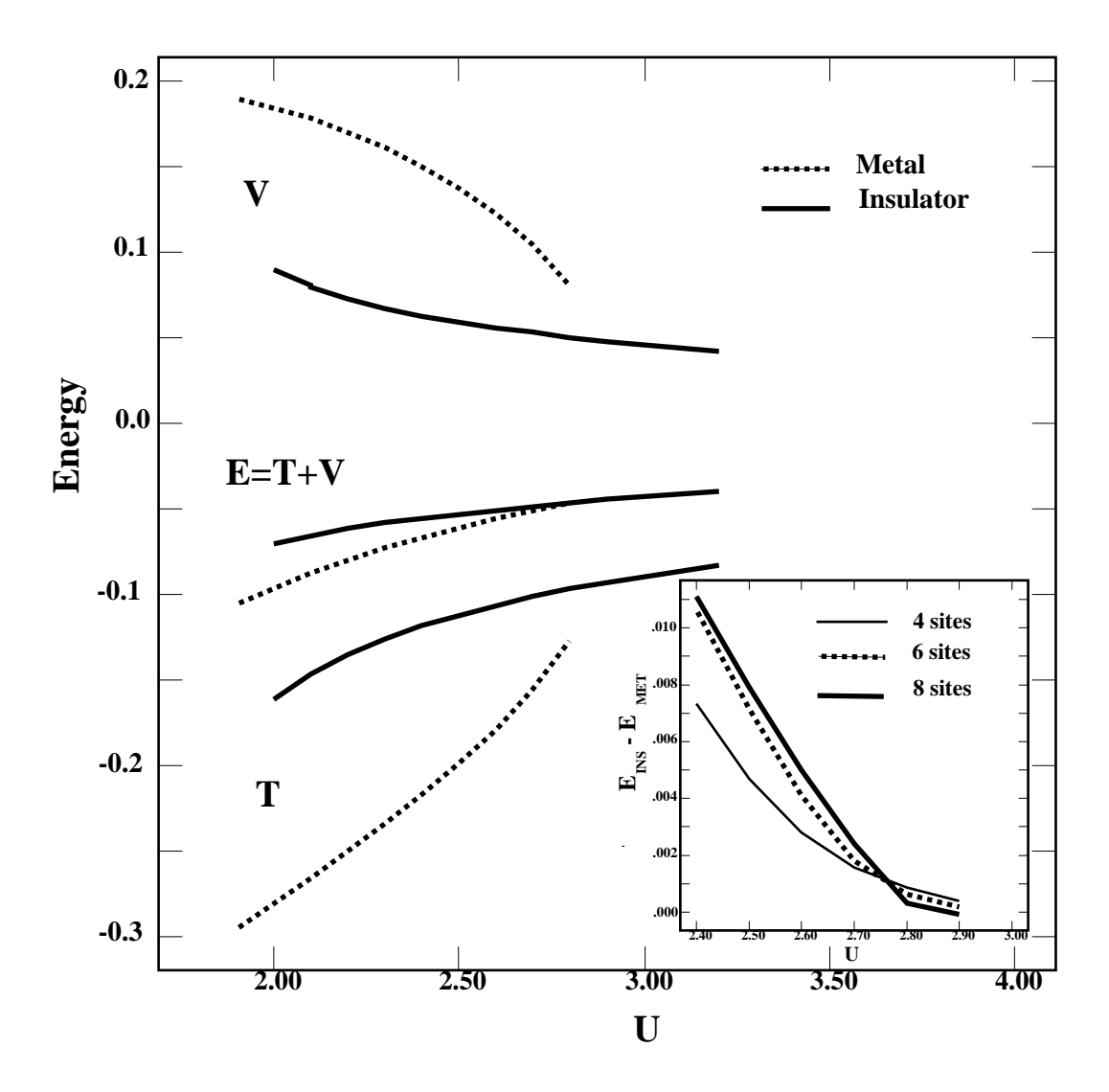


Figure 6.2: Kinetic, potential and total energy for the metallic and insulating solutions in the coexistence region. Difference between the metallic and insulating solution (inset). From the "two chain geometry".

the gap cannot be answered conclusively.

### 6.4 Conclusion

We have resolved the standing questions regarding the metal-to-insulator transition in the Hubbard model in infinite dimensions, using a powerful algorithm to obtain Green functions at zero temperature [15]. We were able to demonstrate the existence of a region in which metallic and insulating solutions coexist, which is in agreement with previous results, and showed that the metallic solution is always lower in energy. This implies that while at finite temperature the transition is first order, it becomes second-order at T=0, similar to the work of Brinkman and Rice in the context of the Gutzwiller approximation [16] [8]. Since the method presented is very general as well as simple, especially when compared to Monte Carlo simulations, it is an appealing approach to the study of strongly correlated electron systems.

## References

- [1] For a recent review, see D. Vollhardt, in Correlated Electron Systems, ed. V. Emery (World Scientific, Singapore, 1993).
- [2] W. Metzner and D. Vollhardt Phys. Rev. Lett. 62, 324 (1989).
- [3] A. Georges, G. Kotliar and Q. Si, Int. J. Mod. Phys. B 6, 705 (1992).
- [4] A. Georges and G. Kotliar, Phys. Rev. B 45, 6479 (1992).
- [5] M. Jarrell, Phys. Rev. Lett. 69, 168 (1992). Th. Pruschke, D. L. Cox and M. Jarrell, Euro Phys. Letts. 21, 5 (1993), and Phys. Rev. B 48, (1993).
- [6] M. Rozenberg, X. Y. Zhang and G. Kotliar, Phys. Rev. Lett. 69, 1236 (1992).
- [7] A. Georges and W. Krauth, Phys. Rev. Lett. 69, 1240 (1992), and Phys. Rev. B 48, 7167 (1993).
- [8] X. Y. Zhang, M. J. Rozenberg and G. Kotliar, Phys. Rev. Lett. 70, 1666 (1993).
- [9] M. J. Rozenberg, G. Kotliar and X. Y. Zhang Phys. Rev. B 49, 10181 (1994).
- [10] M. Caffarel and W. Krauth, Phys. Rev. Lett. 72, 1545 (1994).
- [11] Q. Si, M.J. Rozenberg, G. Kotliar and A. Ruckenstein, *Phys. Rev. Lett.* **72**,2761 (1994).
- [12] E. Gagliano et al., Phys. Rev. B 34, 1677 (1986).
- [13] E. Müller-Hartmann, Z. Phys. B 74 507 (1989), and Z. Phys. B 76, 211 (1989).
- [14] R. Haydock. The Recursion Method and Its Applications, (Springer-Verlag, Heidelberg 1985).
- [15] Note that this can also be used to obtain dynamical correlation functions like the spin-spin correlation function.
- [16] W. F. Brinkman and T. M. Rice, Phys. Rev. B 2, 4302 (1970).
- [17] J. Hubbard, Proc. Roy. Soc. (London) A 281, 401 (1964).
- [18] In a recent preprint, Gros et al. (SISSA # cond-mat/9312031) studied the insulating solution at zero temperature using a finite-size cluster method and obtained similar results on the issue of the disappearance of the insulator.

# Chapter 7

# Optical conductivity in correlated electron systems

### 7.1 Introduction

The question of the transfer of spectral weight in the optical conductivity of correlated electron systems is a long standing problem. The interest in this issue has been revived by the improvement of the quality of the experimental data in various strongly correlated systems.

From a theoretical perspective, the calculation of the optical conductivity in models where the interactions are strong proved to be a difficult task. It has only been studied by exact diagonalization of very small clusters, by approximate diagrammatic schemes where the reliability of the results is difficult to determine and by large N methods. All these treatments have been restricted to zero temperature and have been unable to account for the interesting transfer of spectral weight that occurs as a function of temperature in strongly correlated electron systems.

Recently, following the interest in the study of the many body problem in the limit of infinite dimensions [1], a new mean field theory of the strong correlation problem was developed [2, 3, 4]. This theory is similar in spirit to the Weiss mean field theory in classical statistical mechanics. It has provided new insights into the physics of Mott transition [5, 6, 7], a classical problem of strongly correlated systems.

At the heart of the mean field approach is the exact mapping of the many body system onto a single site problem (impurity model) in an effective medium which is solved for self-consistency [2, 3]. The remaining impurity problem can be efficiently solved by numerical techniques, and a great variety of physical observables of the original model can be then easily obtained [8, 9].

In this chapter we address, in the framework of this mean field theory, the question of the optical conductivity in the the light of the recent experiments on  $V_2O_3$  a system with a Mott transition [10], and  $Ce_3Bi_4Pt_3$  and FeSi which are considered to be Kondo insulators [11, 12].

### 7.2 Methodology

As model hamiltonians for these systems we consider respectively, the Hubbard model and the Anderson lattice.

$$H_{H} = -\sum_{\langle i,j \rangle} (t_{ij} + \mu) c_{i\sigma}^{\dagger} c_{j\sigma} + \sum_{i} U(n_{i\uparrow} - \frac{1}{2}) (n_{i\downarrow} - \frac{1}{2}), \tag{7.1}$$

$$H_{AL} = \sum_{k} (\epsilon_{k} - \mu) c_{k\sigma}^{\dagger} c_{k\sigma} + \sum_{i} (\epsilon_{d}^{o} - \mu) d_{i\sigma}^{\dagger} d_{i\sigma} + \sum_{i} V(d_{i\sigma}^{\dagger} c_{i\sigma} + h.c.) + \sum_{i} U(n_{i\uparrow} - \frac{1}{2}) (n_{i\downarrow} - \frac{1}{2})$$

$$(7.2)$$

where summation over repeated spin indices is assumed.

### 7.2.1 Mean field equations

Here we will consider the symmetrical case of the models  $\mu = 0$ ,  $\epsilon_d^o = 0$ . For simplicity, a semi-circular bare density of states for the conduction electrons is assumed,  $\rho^o(\epsilon) = \sum_{\mathbf{k}} \delta(\epsilon - \epsilon_{\mathbf{k}})/N_{site} = (2/\pi D)\sqrt{1 - (\epsilon/D)^2}$ , with  $t = \frac{D}{2}$ . This density of states can be realized in a Bethe lattice and also on a fully connected fully frustrated version of the model [13]. In the following we set the half-bandwidth D = 1.

The corresponding impurity problem is defined by an effective action. It follows from formulating the problem in the Functional Integral formalism, and integrating out the degrees of freedom of all sites but the one at the origin. We thus obtain for the Hubbard model [2]:

$$S_{eff}[c,c^{\dagger}] = \int_{0}^{\beta} \int_{0}^{\beta} d\tau d\tau' \ c_{\sigma}^{\dagger}(\tau) G_{0}^{-1}(\tau-\tau') c_{\sigma}(\tau') + \int_{0}^{\beta} d\tau \ U(n_{i\uparrow}(\tau) - \frac{1}{2})(n_{i\downarrow}(\tau) - \frac{1}{2}), \tag{7.3}$$

the self-consistency conditions reads,

$$G_0^{-1}(i\omega_n) = i\omega_n + \mu - t^2 G(i\omega_n)$$
(7.4)

The corresponding expressions for the Anderson lattice model are [3, 14]:

$$S_{eff}[\psi,\psi^{\dagger}] = \int_0^{eta} \int_0^{eta} d au d au' \; \psi^{\dagger}_{\sigma}( au) G_0^{-1}( au - au') \psi_{\sigma}( au') + \int_0^{eta} d au \; U(n_{di\uparrow}( au) - rac{1}{2})(n_{di\downarrow}( au) - rac{1}{2}), \eqno(7.5)$$

and,

$$[G_0^{-1}(i\omega_n)]_{cc} = i\omega_n + \mu - t^2[G(i\omega_n)]_{cc}$$
 (7.6)

with  $\psi^\dagger = \{c^\dagger, d^\dagger\}.$ 

The equations are solved by iteration. At the self-consistent point, the impurity Green function coincides with the local Green function of the lattice problem. Due to independence of momenta, the same applies to the self-energy. It obeys the Dyson equation  $\Sigma = G_{loc}^{-1} - G_0^{-1}$ .

We use an exact diagonalization algorithm (ED) [15, 16] and an extension of the second order perturbative (2OPT) calculation around the non-magnetic hamiltonian to solve the impurity problem [13, 17]. We have already discussed in previous chapters the remarkable success of this simple approximation to reproduce, for all parameter range, the essentially exact results that are obtained for these models by use of ED and quantum Monte Carlo simulations [9, 13]. We consider here the 2OPT calculation in the Keldysh formalism, that allows to obtain finite temperature results directly on the real axis, with no need of analytic continuation.

### 7.2.2 Optical conductivity

The optical conductivity is defined as

$$\sigma(\omega) = -rac{1}{\omega} {
m Im} < [j,j] >$$
 (7.7)

after a few steps of algebra one obtains the expression for the frequency dependent real part of  $\sigma$  in the limit of large dimensions

$$\sigma(\omega) = rac{1}{\omega} rac{e^2 t^2 a^2}{
u h} \int_{-\infty}^{\infty} d\epsilon \; 
ho^o(\epsilon) \int_{-\infty}^{\infty} rac{d\omega}{2\pi} \; A_\epsilon(\omega') A_\epsilon(\omega' + \omega) (n_f(\omega') - n_f(\omega' + \omega)) \quad (7.8)$$

with,  $A_{\epsilon}(\omega) = -2\text{Im}(G_k(\omega))$  being the spectral representation of the lattice conduction electrons Green function, e is the electron charge, and a the lattice constant. At T = 0, the optical conductivity of a correlated electron system can be parametrized by [18]

$$\sigma(\omega) = \frac{{\omega_P^*}^2}{4\pi} \delta(\omega) + \sigma_{reg}(\omega) \tag{7.9}$$

where the coefficient in front of the  $\delta$ -function is the Drude weight and  $\omega_P^*$  is the renormalized plasma frequency. In the presence of disorder  $\delta(\omega)$  is replaced by a lorentzian of width  $\Gamma$ .

The kinetic energy is related to the conductivity by the sum rule

$$\int_0^\infty \sigma(\omega) d\omega = -rac{\pi e^2}{2\hbar^2 a} < T> = rac{\omega_P^2}{4\pi}$$
 (7.10)

The Drude part can be directly obtained in terms of the quasiparticle weight z in the limit of  $d \to \infty$ . It can be shown that

$$\frac{{\omega_P^*}^2}{4\pi} = \frac{2e^2}{3\hbar^2 a} Dz. \tag{7.11}$$

### 7.3 Hubbard model

To apply the Hubbard model to  $V_2O_3$  one has to remember that in this compound, in a range of 2eV from the Fermi level, there are three d-orbitals per vanadium which are filled with two electrons. However, photoemission spectroscopy indicates that mainly one band is involved in the metal-insulator transition. This band extends to approximately 0.4eV. Using this value for the bandwidth we find that our model exhibits a phase diagram with a  $T_{MIT}\approx 240\,K$ , which is within a factor of two of the experimental result [19]. Therefore, we will consider the results for the optical conductivity, in the low frequency range of  $\omega < 1eV$ , within the framework of a single band model. One should keep in mind, however, that at high frequencies contributions from other bands will appear, but these are outside the scope of the present treatment.

Phase	Parameter			
	D [eV]	$\mathrm{U}\;\left[\mathrm{eV} ight]$	$\Delta \ [{ m eV}]$	$\omega_P^2/4\pi  [{ m eV}/\Omega{ m cm}]$
Insulator (stoich.)	0.33	1.3	0.32	175
Insulator (y=.013)	0.48	0.98	0.063	820
Metal (stoich. 170K)	pprox0.3	$\approx 0.6$	_	1400

Table 7.1: Experimentally determined parameters for the model.

To make contact with the experiments, we take the lattice constant  $a \approx 3 \text{ Å}$  the average vanadium-vanadium distance, and extract the parameters U and D from the main features of the experimental optical spectra. We then use these as input parameters to the Hubbard model to calculate the lineshape and its temperature dependence. We also compare interesting information such as the distribution of spectral weight,  $\omega_P^*$ ,  $\omega_P$ , and the optical gap. Experimentally one can vary the the parameters U and D, by modifying the oxigen content u. The parameters extracted for different situations are summarized in table 7.1. It is not surprising that U and D are very different in the metal and the insulator, since the lattice parameter and the screening length change rapidly across the phase diagram. We consider that the role of magnetic frustration is relevant in the insulating phase of  $V_2O_3$ , so we use our two sublattice model in the limit of strong frustration. This is consistent with the fact that the Néel temperature is much lower than the  $T_{MIT}$ , and with neutron scattering experiments.

### 7.3.1 The insulator state

We first discuss the insulating state. The experimental optical spectrum of the insulator is characterized by an excitation gap at low energies, followed by an incoherent feature that corresponds to charge excitations of mainly vanadium character. In figure 7.1, we reproduce the experimental results obtained recently by Thomas *et al.* for the optical conductivity of  $V_2O_3$  in the insulator phase [10].

In figure 7.2, we plot the optical gap  $\Delta$  as a function of the interaction U, for both the antiferromagnetic and paramagnetic insulator solutions. The gap is defined as twice the distance to the lowest energy pole obtained from the ED. The curve corresponds

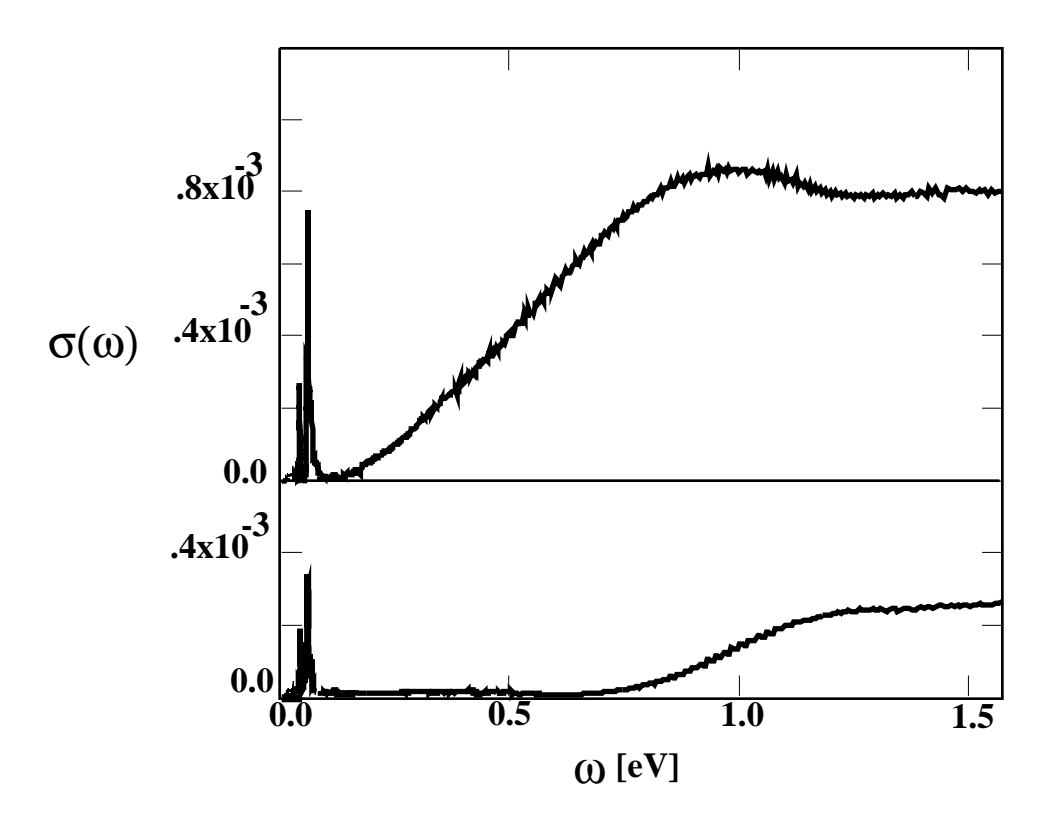


Figure 7.1: The optical conductivity  $\sigma(\omega)$  in  $[\Omega^{-1}cm^{-1}]$  for  $V_{2-y}O_3$ . The top curve corresponds to y=0.013, T=10K, and the lower curve to y=0, T=70K.

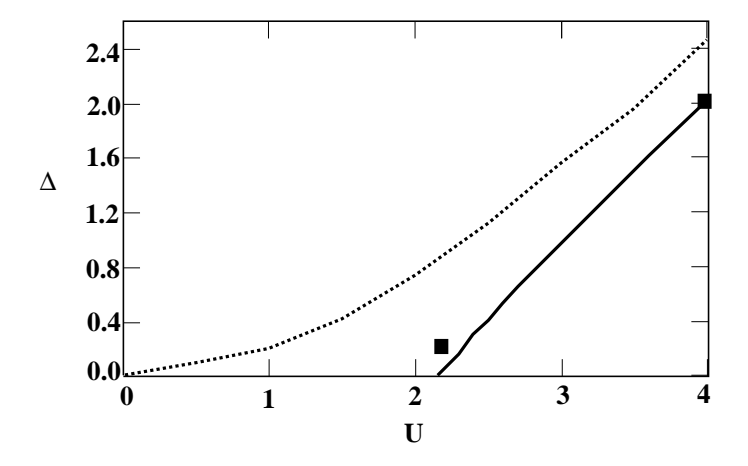


Figure 7.2: The optical gap  $\Delta$  as a function of the interaction U, for both the antiferromagnetic (dotted) and paramagnetic (solid) insulator solutions. The points show the experimental gap in units of the experimental half-bandwidth.

to the extrapolated data from clusters of 3, 5 and 7 sites. A  $\frac{1}{N_{sites}}$  scaling behavior is assumed.

In figure 7.3 we show the corresponding results for the optical spectrum that is obtained from the 2OPT at T=0. The shape of the spectrum is found to be in good agreement with the experimental results [10].

Another quantity that can be compared to the experiment is the integrated spectral weight. It is related to the kinetic energy by the sum rule in equation (7.10). In figure 7.4 we plot the results for the kinetic energy that are obtained from the ED. The curves show both the insulator and metallic paramagnetic results along with the antiferromagnetic insulator. We also include for comparison the experimentally determined spectral weight. The experimental points are plotted in units of  $\frac{\pi e^2}{2\hbar^2 a}$ .

### 7.3.2 The metallic state

We now turn to the discussion of the metallic state. Experimental data were obtained for T=170K and T=300K, on stoichiometric samples of  $V_2O_3$  that become insulating at  $T_c\approx 150K$ . In figure 7.5, we reproduce the experimental results obtained recently by Thomas *et al.* for the optical conductivity of  $V_2O_3$  in the metallic phase [10].

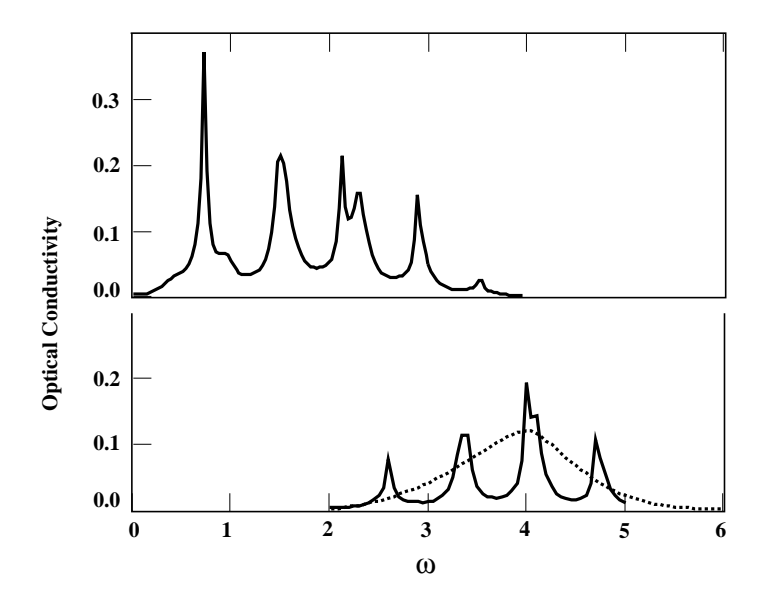


Figure 7.3: The optical conductivity from ED at T=0. Results for the paramagnetic insulator solution with a value of the interaction U=2.15D (top) and U=4D (bottom). For comparison, the results from 2OPT at U=4D are also shown (dotted).

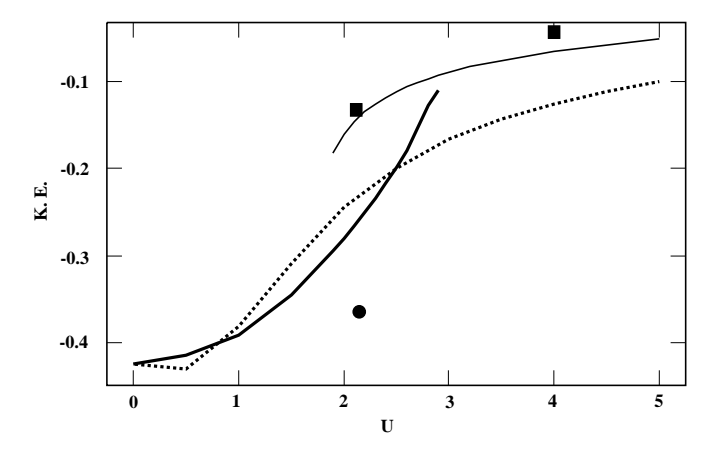


Figure 7.4: The kinetic energy as a function of the interaction U, for both the antiferromagnetic (dotted) and paramagnetic insulator (thin) and metallic (thick) solutions. The points show the experimental integrated spectral weight in units of  $\frac{\pi \epsilon^2}{2\hbar^2 a}$ .

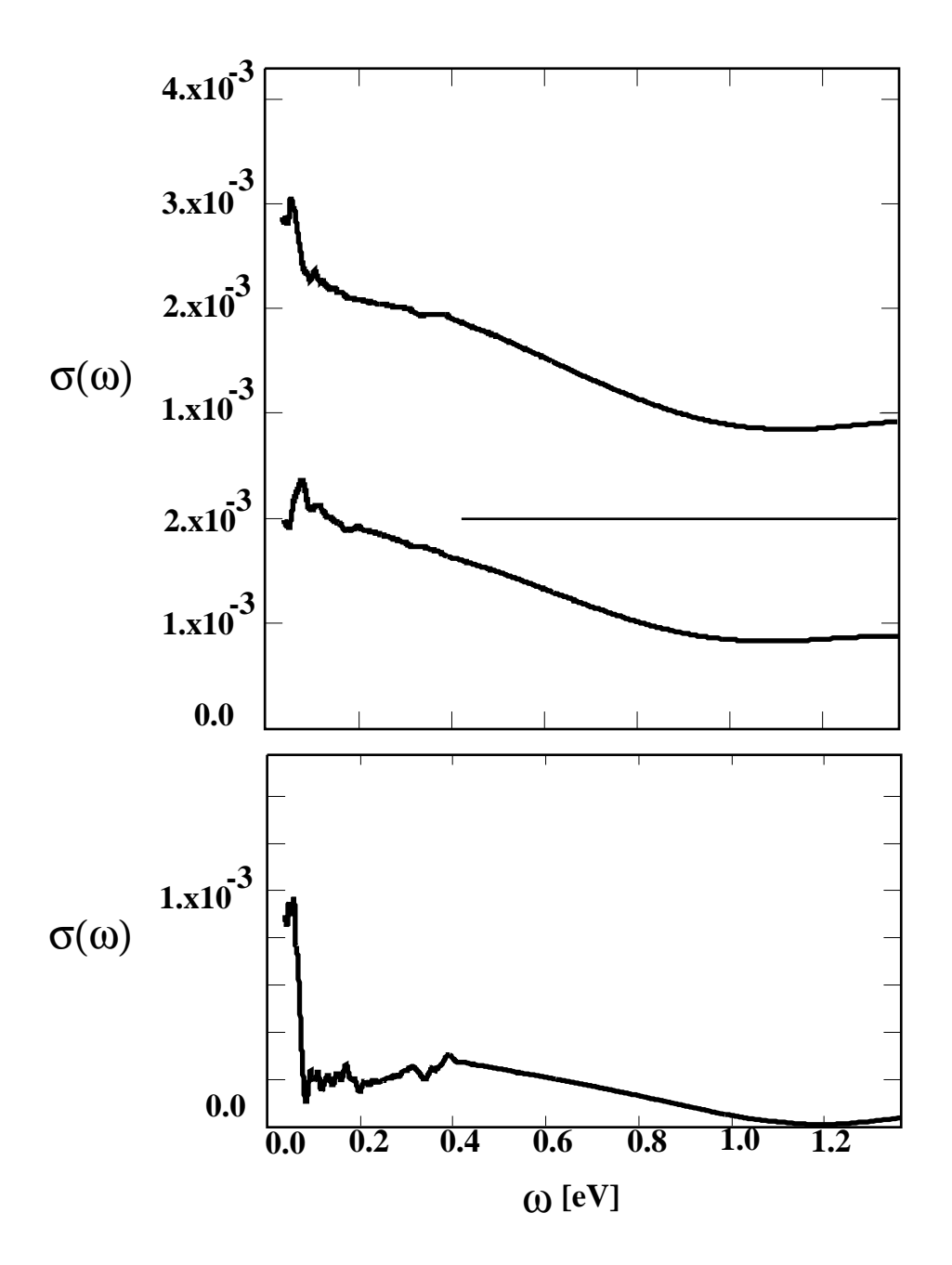


Figure 7.5: The higher figure contains the optical conductivity  $\sigma(\omega)$  in  $[\Omega^{-1}cm^{-1}]$  of  $V_2O_3$  for T=170K (top) and T=300K (bottom). In the lower figure we plot the difference  $\Delta\sigma(\omega)$  of the two spectra.

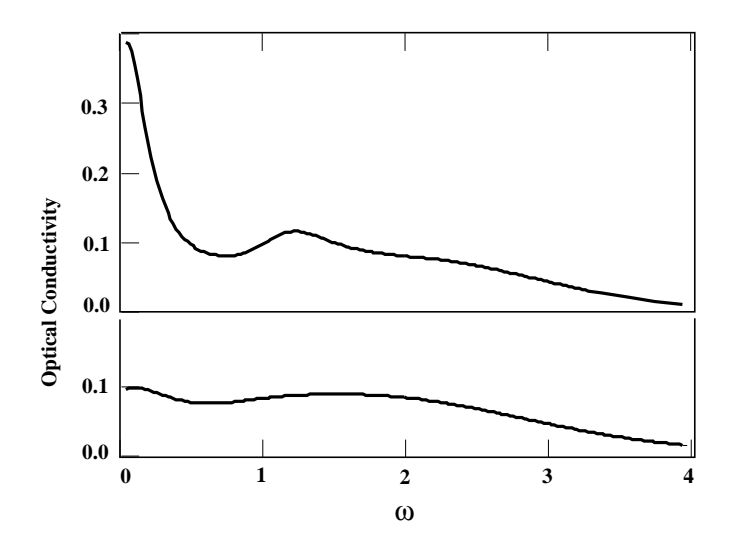


Figure 7.6: The optical conductivity from 2OPT for U=2.1D, and T=0.05D (top) and 0.083D (bottom). This values correspond to  $T\approx 170K$  and 300K by setting the half-bandwidth  $D\approx 0.3eV$ . A small  $\Gamma$  was included in the calculation to mimic a finite amount of disorder.

The lower and higher temperature spectra look rather featureless. However, upon considering their difference it becomes apparent an enhancement of the spectrum at frequencies of the order of 0.5eV, and more notably, the emergence of a low frequency feature that extends to  $\sim 0.15eV$ . We will argue below that this behavior can be accounted by the Hubbard model treated in mean field theory in the metallic state.

In figure 7.6 we present the results for the optical spectrum obtained from 20PT for two different values of the temperature. The repulsive interaction is set to U=2.1D that places the system in the correlated metallic state. The first feature that becomes clear from this figure is that, at least, the qualitative aspect of the physics is already captured. As the temperature is lowered, we observe both, the enhancement of the incoherent structures at frequencies of the order  $\frac{U}{2}$  to U, and the rapid emergence a feature at the lower end of the frequency spectrum. This behavior is consistent with the experimental data on  $V_2O_3$  shown in figure 7.5 [10].

The lower temperature optical spectrum displays various contributions: i) A narrow low frequency feature in the optical spectrum that is due to excitations within the many

body quasiparticle resonance. ii) At frequencies of order  $\frac{U}{2}$  and U, two broad incoherent features also emerge due to excitations between the Hubbard bands and the central resonance, and between the Hubbard bands respectively.

The interesting prediction of the model is the temperature dependence of the low frequency feature. We expect a transfer of spectral weight to the lower frequencies, as the temperature is decreased. This should occur at a scale  $T_{coh} \approx 200 K$  which we have introduced in chapter 5. It has the physical meaning of defining a temperature below which the Fermi liquid description applies, and the quasiparticle resonance in the density of states is formed.

As we have done previously for the insulator, we can consider the integrated spectral weight. We find a value  $W \approx 1100 \frac{ev}{\Omega cm}$  which is consistent with the experimental results, although somewhat lower. We believe that this is possibly due to the presence of higher energy bands that are not included in the present treatment.

To end the discussion of the metallic state we would like to briefly consider the question of the slope of the specific heat  $\gamma$ . The experiments show an unusually big value for this quantity. The need to account for this observation imposes further constraints for the model.  $\gamma$  is related to the Drude part of the conductivity since both quantities depend on the renormalized mass. The slope of the specific heat, within the present scheme, is given by  $\gamma = \frac{1}{zD} 3 \frac{mJeV}{molK^2}$ . Experimentally, it has been measured as function of different parameters and a remarkable high value is always found. For 0.08% Ti substitution  $\gamma \approx 40 \frac{mJ}{molK^2}$ , while for a pressure P = 25 Kbar in the stoichiometric compound  $\gamma \approx 30 \frac{mJ}{molK^2}$ , and with vanadium deficiency in a range of y = 0.013 to 0.033, the value is  $\gamma \approx 47 \frac{mJ}{molK^2}$  [20, 21, 22]. We find that the choice U = 2.1D above, corresponds to  $z \approx 0.3$  and gives  $\gamma \approx 30 \frac{mJ}{molK^2}$  which is in good agreement with the experimental findings.

Thus, it turns out that this framework naturally incorporates the physics of both the lower end of the optical conductivity spectrum, and the anomalously big values of the slope of the specific heat  $\gamma$ , as consequence of the appearance of a single small energy scale, the renormalized Fermi energy  $\epsilon_F^* = zD$ .

#### 7.4 Anderson lattice model

We would like now to turn to the second model, the Anderson lattice, and consider its results in the light of the recent experiments in Kondo insulators [11, 12]. In the non-interacting limit U=0, the effect of the localized orbital is to split the conduction band. The system becomes a hybridization band insulator, with a direct gap proportional to the magnitude of the hybridization V. In this limit, the optical conductivity exhibits a sharp gap followed by an incoherent absorption feature of width given also by V,  $\sigma(\omega) \approx \Theta(\omega - 2V)(\omega^2 - 4V^2)^{1/2}/\omega^4$ . This behavior is due to the crossing between the conduction p-band and the non-dispersive d or f-band.

As the interaction on the localized orbital is switched on, different approaches to this problem (e.g. perturbation theory, NCA, large N, etc. [23]) indicate that a low energy scale emerge due to the Kondo effect  $T_K \sim exp(-\frac{UD}{V^2})$ . The narrow band of quasiparticles, characterized by  $T_K$ , also opens a gap due to the hybridization. Thus, the physics remains basically identical to the non-interacting case, with the exception that the hybridization is renormalized to a smaller value  $V^*$  and  $\frac{V^{*2}}{D} \approx T_K$ .

The consequences for the optical conductivity, are that as the temperature becomes of the order of  $T_K \ll V^* \ll D$ , the Kondo quasiparticles are destroyed and the gap is filled by spectral weight which comes mainly from the higher frequency part of the incoherent spectrum. This picture is consistent with the experimental results [11, 12, 24].

The present mean field theory approach is in agreement with this basic picture but contains in addition the incoherent part of the excitation spectrum which cannot be described in terms of quasiparticles [14]. In addition it allows us to study quantitatively the evolution of the spectra as a function of temperature. Here we apply this method to the optical conductivity of heavy fermions.

In figure 7.7 we plot the results for the optical conductivity spectra of the Anderson lattice for different values of the interaction U, keeping the hybridization V fixed. We clearly observe how the optical gap is renormalized by the correlation effects in agreement with the previous discussion. The inset shows that the result  $\frac{V^{*2}}{D} \approx T_K$  is

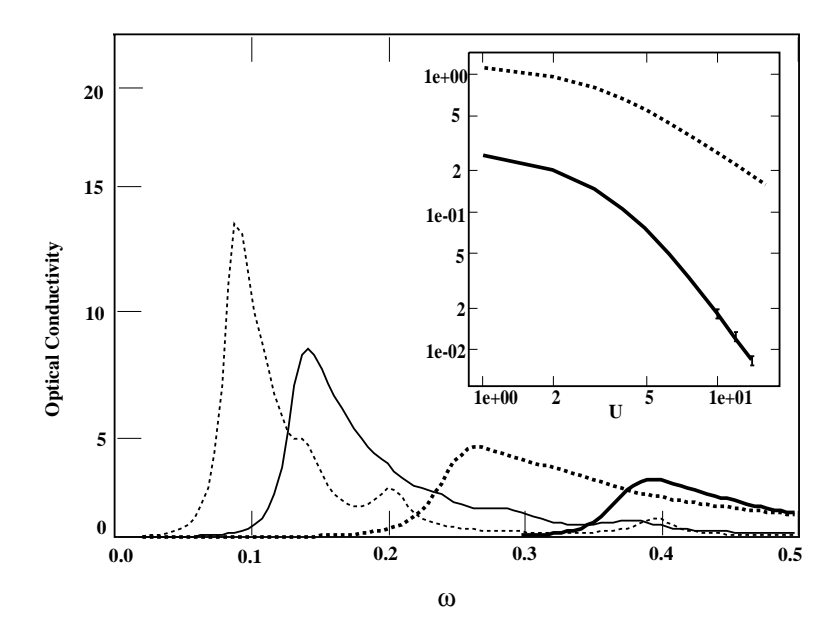


Figure 7.7: The optical conductivity spectra of the Anderson lattice for values of the interaction U=0.5,1,2,3 (right to left), keeping the hybridization V=0.25 fixed. The inset shows the gap  $\Delta_c \approx V^*$  and the indirect gap from the local density of states  $\sim T_K$  for V=0.6. The slopes of these curves give  $V^{*2}/D$   $\alpha$   $T_K$  in the strong correlation region.

indeed valid in the region where the correlations are strong. However, the exponential dependence of  $V^*$  and  $T_K$  with U, becomes power-law with exponents -1 and -2 respectively. The results are obtained at T=0 by the 2OPT calculation. As mentioned above this approximation reproduces remarkably well the essentially exact results of the ED method. A detailed comparison will be presented elsewhere.

A point worth mentioning is that the size of the gap  $\Delta_c$ , within the present approach, is basically given by  $V^*$  (the direct gap). This is in contradiction to the results that are expected in a large N calculation if contributions beyond the mean field are considered [25]. In that case, it is argued that higher order terms would produce optical excitations down to the scale of the indirect gap  $T_K$ . The argument follows from the assumption that the results for the metallic phase can be extended into the insulating one. The validity of this assumption is unclear. In the case considered here, however, the contributions to the spectral weight at the scale of the indirect gap seem to be

strongly suppressed.

We would like to consider now the effect of the temperature in the transfer of optical weight. In the experimental results for the optical conductivity on  $Ce_3Bi_4Pt_3$  and FeSi [11, 12] that we reproduce in figure 7.8, charge-gaps of size  $\Delta_c \approx 400K$  and 1500K are observed. However, they start to form at the much lower temperatures  $T_K \approx 100K$  and 200K respectively. They finally become depleted at  $T \approx 25K$  with most of the spectral weight being transferred to frequencies much bigger than  $\Delta_c$ . Thus, we see that in these materials,  $T_K$  is roughly five times smaller than  $\Delta_c$  and the temperature were the gap is depleted is roughly five times smaller that  $T_K$ .

Figure 7.9 show that the Anderson lattice in mean field theory can account for some aspects of the experimental observations. The results are obtained for U=3 and V=0.25. The charge-gap indeed starts to form at a temperature much lower than its size  $(\frac{\Delta_c}{T}\approx 4)$ , and it becomes depleted at an even much lower temperature  $(\frac{\Delta_c}{T}\approx 20)$ .

The only aspect that is not fully consistent with the observation is that this model shows that most of the spectral weight is being transfer to frequencies just of the order of the charge gap. In the experiments the transfer of weight to this energy range is smaller.

affected by surface defects, especially strain

To make a meaningful comparison with the experimental data we have added the effects of disorder by putting a lorentzian distributed random site energy on the conduction electron band with width  $\Gamma=0.05$ . The results are shown in the inset of figure 7.9. It is clear from the figure that the addition of disorder brings our results to a much closer agreement with the experimental results. It is also worth mentioning that we observe that increasing the disorder reduces the temperature  $T^*$ .

Although the dependence of the these results on the details of the density of states of the conduction band is a priori an important issue, our results seem to indicate that it is possibly a minor effect. This is mostly due to the observation that the shape of the optical spectra remain basically invariant (up to a rescaling) as the interaction U is increased, even to very high values. In that case the model approaches the atomic limit and the details of the shape of the conduction band should become irrelevant.

Figure 7.8: The optical conductivity spectra  $\sigma(\omega)$  in  $[\Omega^{-1}cm^{-1}]$  for the Kondo insulators  $Ce_3Bi_4Pt_3$  and FeSi. The higher figure corresponds to  $Ce_3Bi_4Pt_3$  at T=25,50,75,100,300K (from below). The lower figure corresponds to FeSi at T=20,100,150,200,250K (from below).

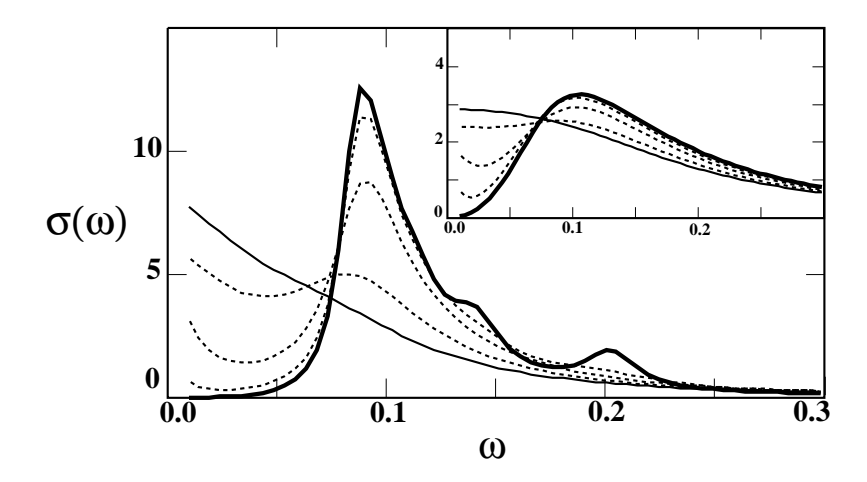


Figure 7.9: The optical conductivity for the Anderson model at T=0.001 (bold), 0.005, 0.01, 0.02 (dotted), 0.03 (thin). The interaction U=3 and V=0.25. Inset: The same quantity at T=0.001 (bold), 0.005, 0.01, 0.02 (dotted), 0.03 (thin) with lorentzian random site disorder of width  $\Gamma=0.005$ .

Finally we would like to consider a last but important issue, the magnetic response. Since the localized spins dynamics is solely controlled by the Kondo scale  $T_K$  and magnetic susceptibility data is available, it is interesting to consider it under the light of the results of the present approach. It is currently argued from experiments [24] that the fact that the spin and charge-gap are generally found to be of the same order of magnitude can be understood in terms of a simple hybridization band insulator with a single small energy scale  $T_K$ . However, a closer look to the experimental data indicates that the spin-gap is consistently smaller than the charge-gap. In particular, for the compounds that we are considering above we see that the charge-gap is at least two times bigger than the spin-gap in  $Ce_3Bi_4Pt_3$ , while for FeSi it differs by as much as approximately a factor of four [11, 24]. This observation may be an indication that the interpretation mentioned above is, perhaps, not correct.

The mean field results for the frequency dependent local spin-spin correlation function suggest a different interpretation of the energy scale controlling the optical gap. We find that the spin-gap is greater than the indirect charge gap (which is also controlled by  $T_K$ ), by a factor of order unity. The size of the indirect gap is obtained from the local

Green Functions, and the spin-gap is measured from the position of the lowest energy pole on the spin-spin correlation function obtained in the ED procedure. This result, when considered in regard to the observation made before, seems to be in conflict with the interpretation that the lowest frequency feature in the optical conductivity spectra is controlled by the Kondo scale (indirect gap). On the other hand, the experimental situation can be consistently accommodated within the present theory since the charge-gap in the optical spectra is given by the direct gap  $(\Delta_c \sim V^*, \ V^* > T_K).$ Figure 7.10 shows the local spin-spin and density-density correlation function of both the conduction and the localized electrons. As expected, the f-electron contribution to the magnetic response bigger and correspondingly will make up for most of the signal experimentally measured. The optical conductivity is also plotted for the same value of the parameters, this results should be compared to the corresponding in ref. [11]. In the inset we plot  $\Delta_s$ , the indirect gap  $\Delta_{ind}$  and  $\Delta_c$  as a function of the interaction U for a fixed value of the hybridization. The first corresponds to the position of the lowest pole of the correlation function and the second to the gap in the single particle spectrum, obtained from the ED calculation with 8 sites. The latter corresponds to the the frequency where the sharp edge in the optical spectrum calculated by 2OPT reaches half-height. We find that  $\Delta_c$  is consistently larger than  $\Delta_s$ , and that  $\Delta_s$  is somewhat smaller than  $\Delta_{ind}$ . As expected when  $U=0,\,\Delta_s=\Delta_{ind}$ , but as U increases  $\frac{\Delta_s}{\Delta_{ind}}$  becomes smaller than unity and approaches the value 0.5 at  $U \approx 2$ . We emphasize, once more, that both the indirect and direct gaps are small energy scales that go to zero as the interaction U is increased. They are correspondingly given by the Kondo scale  $T_K$  and  $V^*$ , and are related by  $T_K \sim \frac{{V^*}^2}{D}$ , thus they do not vanish in the same manner.

### 7.5 Conclusions

In this chapter we have illustrated how the mean field theory, that becomes exact in the limit of large dimensions, can be used to study the physics of systems where the local interactions are strong and play a major role. In particular we have demonstrated that the Hubbard and the Anderson lattice treated in the mean field approximation can

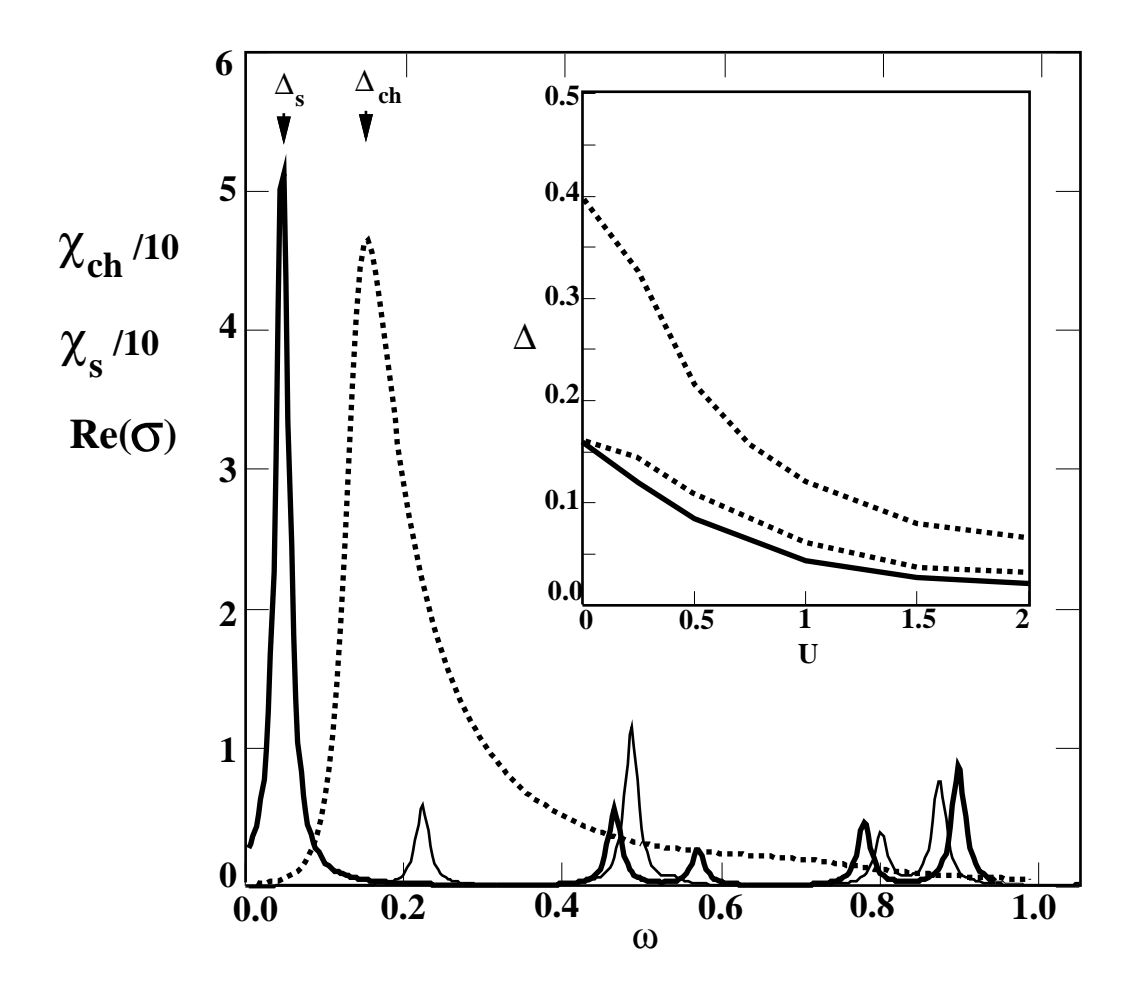


Figure 7.10: The local spin-spin (bold) and density-density (thin) susceptibility from 8 sites ED. The optical conductivity from 2OPT (dotted). The parameters are U=1 and V=0.2. The inset shows the direct gap as obtained form 2OPT (upper dotted line), the indirect gap (lower dotted line) and the spin gap (solid line) from 8 sites ED. The hybridization is V=0.2.

account for the main features of the temperature dependent transfer of spectral weight in the optical conductivity spectra. In the case of  $V_2O_3$  we found that the theory is able to account semi-quantitatively for the conductivity results in both the metallic and insulating states. In the latter, the theory seems to provide further insights in the role of the magnetic frustration. For the Kondo insulators, although the comparison was not carried to such detail, we have seen most of the qualitative features of the experimental results been naturally realized within the present approach. The remaining discrepancies would probably have to wait until a systematic expansion around the mean field theory is developed.

We also stress that this approach can easily incorporate more realistic band structure density of states and more complicated unit cells. This extensions would allow for a more precise quantitative description of the physical systems.

### References

- [1] W. Metzner and D. Vollhardt Phys. Rev. Lett. 62, 324 (1989).
- [2] A. Georges and G. Kotliar, Phys. Rev. B 45, 6479 (1992).
- [3] A. Georges, G. Kotliar and Q. Si Int. J. Mod. Phys. B 6, 705 (1992).
- [4] V. Janis, Z. Phys. B 83, 227 (1991). V. Janis and D. Vollhardt, Int. Journ. Mod. Phys. B, Vol. 6, Nos 5 & 6, 731 (1992).
- [5] M. Jarrell, Phys. Rev. Lett. 69, 168 (1992).
- [6] M. Rozenberg, X. Y. Zhang and G. Kotliar, Phys. Rev. Lett. 69, 1236 (1992).
- [7] A. Georges and W. Krauth, Phys. Rev. Lett. 69, 1240 (1992).
- [8] M. J. Rozenberg, G. Kotliar and X. Y. Zhang Phys. Rev. B 49, 10181 (1994).
- [9] G. Kotliar and M. J. Rozenberg, Proceedings of International Conference on Superconductivity and Strongly Correlated Electron Systems. Amalfi, Italy. (1992)
- [10] G. A. Thomas et al. Journ. Low Temp. Phys. 95, 33 (1994); and private communication.
- [11] B. Bucher, Z. Schlesinger, P. C. Canfield and Z. Fisk, Phys. Rev. Lett. 72, 522 (1994)
- [12] Z. Schlesinger, Z. Fisk, H. T. Zhang, M. B. Maple, J. F. DiTusa and G. Aeppli, Phys. Rev. Lett. 71, 1748, (1993)
- [13] X. Y. Zhang, M. J. Rozenberg and G. Kotliar, Phys. Rev. Lett. 70, 1666 (1993).
- [14] M. Jarrel, H. Akhlaghpour and Th. Pruschke, Phys. Rev. Lett. 70, 1670 (1993).
- [15] M. Caffarel and W. Krauth Phys. Rev. Lett. 72, 1545 (1994).
- [16] Q. Si, M. Rozenberg, G. Kotliar and A. Ruckenstein Phys. Rev. Lett. 72,2761 (1994). M. J. Rozenberg, G. Moeller, and G. Kotliar, Mod. Phys. Lett. B 8, 535 (1994).
- [17] K. Yamada, Prog. Theor. Phys. 53, 4, 970, (1975). K. Yosida and K. Yamada, ibid. 1286
- [18] W. Kohn, Phys. Rev. A171, 133 (1964).
- [19] J. H. Park, L. H. Tjeng, J. W Allen, P. Metcalf and C. T. Chen, AT&T Bell Labs Report, (1994).

- [20] D. Mc Whan et al. Phys. Rev. Lett. 27, 941 (1971).
- [21] D. Mc Whan et al. Phys. Rev. B 7, 3079 (1973).
- [22] S. A. Carter, T. F. Rosenbaum, P. Metcalf, J. M. Honig, and J. Spalek Phys. Rev. B 48, 16841 (1993).
- [23] A. C. Hewson, The Kondo Problem to Heavy Fermions (Cambridge University Press, 1993).
- [24] G. Aeppli and Z. Fisk, Comments Cond. Mat. Phys. 16, 155 (1992).
- [25] A. J. Millis, in *Physical Phenomena at High Magnetic Fields*, edited by E. Manousakis et al. (Addison-Wesley, Reading, MA, 1991); and references therein.

## Chapter 8

## **Conclusions**

In this thesis we have consider at length the behavior of systems of correlated electrons in the limit of large dimensionality. We have seen how the physics that results from the considered models not only retains most of the features commonly encounter in finite dimensional formulations, but has provided us with valuable new insights that were not possible to obtained before.

We have been able to take full advantage from the mapping to lattice models onto impurity problems to develop a set of powerful numerical tools that enabled us to solve the models in great detail.

We have combined the numerical results with analytic arguments to present a detailed solution of the Hubbard model and considered its relevance in regard of the experimental results on transition metal oxides. In particular, we have found that the model is able to capture some fundamental aspects of the physics observed in the compound  $V_2O_3$ , which is considered as a prototype of system with a Mott transition.

In chapters 3 and 4, we demonstrated the existence of a metal-insulator transition in the Hubbard model at an intermediate value of the interaction U in the half-filled case and in the absence of magnetic order. One most intersting aspect that the solution displayed is that it was able to make contact within a single framework with two important classical results for the model: the work of Hubbard that starts from the atomic limit, and the Brinkman Rice approach from the metallic side considering the Gutzwiller variational wavefunction. These traditional approaches hinted towards the existence of a Mott transition at an intermediate value of the Coulomb repulsion, which became fully realized in the large dimensional limit. From the mapping of the lattice model onto an

Anderson impurity model we obtained interesting insights on the nature of the transition. In particular, we showed that as the the interaction U reaches a critical value, the narrow quasiparticle feature at the Fermi energy that defined the metallic state disappears. This was due to a divergence in the inverse of the self-consistent Weiss field  $G_0$ , which translated into the vanishing of the effective hybridization of the impurity model. The Kondo model obtained from the Anderson model via the Schrieffer-Wolff transformation then flows to zero coupling at low energies, and the self-energy correspondingly develops a pole singularity at zero frequency. This has as a consequence the opening of a Mott-Hubbard gap in the one particle spectrum.

In chapter 5 and 6 we consider the solution of the Hubbard model in a greater perspective. Various early ideas could be put in perspective. In particular, for the frustrated lattice, we established the coexistence of a metallic and insulating solution in a finite region of the (U,T) plane. Within this region, there is a first order boundary where the two very different solutions cross in free energy, and several quantities experience a jump: the specific heat, the susceptibility, the number of doubly occupied sites, etc. The first order line has a negative slope indicating that the paramagnetic insulating phase has a higher entropy than the metallic phase. The line ends in an interesting second order critical point, above it there is a smooth crossover between a metallic and an insulating regime.

We also made more precise the connection between our approach and the Brinkman Rice scenario for the metal insulator transition, as well as with the complementary work of Hubbard.

In particular, regarding the first, we found similar behavior of the quasiparticle weight and the compressibility that vanish as  $(1 - \frac{U}{U_c})$  close to the transition. However, the study of the double occupation and the spin susceptibility revealed that the variational approached fails to produce non-singular corrections. In the actual solution, these quantities are finite and change smoothly at the metal-insulator transition.

In respect to the second, we found a natural scenario for the destruction of the insulating solution with the continuous narrowing of the gap of the insulator. This is a realization of the original Hubbard scenario for the metal insulator transition driven

by the closing of the upper and lower Hubbard bands.

The question of the magnetic phases was also considered. On non-frustrated, bipartite lattices, we found that the Néel temperature is much higher than the metal
insulator transition temperature, making the transition between small and large U continuous. In this case, the physics can be understood in terms of the magnetic long range
order and a smooth crossover within the broken symmetry phase. The Mott transition
is irrelevant, vindicating Slater's point of view of a transition driven by the doubling of
the lattice parameter.

Upon consideration of a partial degree of frustration, in addition, at low temperatures there is a first order line between an antiferromagnetic metal and an antiferromagnetic insulating phase. This is possibly relevant to the experimental results of Carter et al. [1]. In this case, the phase diagram has the same topology and even the same scale as the experimentally observed phase diagram of  $V_2O_3$  [2, 3, 1].

In the last chapter we consider the important issue of the optical conductivity. This subject has acquired renewed relevance in regard of the recent improvement of the quality of the experimental data in various strongly correlated systems [4] [5, 6]. We have demonstrated that the Hubbard and the Anderson lattice models, treated in the present mean field approximation, can account for the main features of the temperature dependent transfer of spectral weight in the optical conductivity spectra. In the case of  $V_2O_3$  we found that the theory is able to account semi-quantitatively for the conductivity results in both the metallic and insulating states. In the latter, the theory seems to provide further insights in the role of the magnetic frustration. For the Kondo insulators, although the comparison was not carried to such detail, we have seen most of the qualitative features of the experimental results been naturally realized within the our approach.

In closing we would like to point out that the mapping of lattice models onto impurity problems was a key ingredient in paving the way for the development of an arsenal of numerical tools. This, in combination with the ever increasing computational power of today's machines allowed for a new assault to the strongly correlated electron problem. As a result of our study we learned important lessons. The limit of large dimensionality

has revealed itself as a very physical one providing fresh new insights into relatively old questions. In particular, the results presented in this thesis lead us to conclude that the Hubbard model in this limit is able to account for some fundamental basic features that are experimentally observed in the  $V_2O_3$  system. A further degree of quantitative agreement will probably have to wait until a systematic expansion around the mean field theory is developed.

## References

- [1] S. A. Carter, T. F. Rosenbaum, J. M. Honig, and J. Spalek, *Phys. Rev. Lett.* **67**, 3440(1992).
- [2] D. B. McWhan, A. Menth, J. P. Remeika, W. F. Brinkman, and T. M. Rice Phys. Rev. B 7, 1920 (1973).
- [3] H. Kuwamoto, J. M. Honig, and J. Appel Phys. Rev. B 22, 2626 (1980).
- [4] G. Thomas et al. (preprint)
- [5] B. Bucher, Z. Schlesinger, P. C. Canfield and Z. Fisk, Phys. Rev. Lett. 72, 522 (1994)
- [6] Z. Schlesinger, Z. Fisk, H. T. Zhang, M. B. Maple, J. F. DiTusa and G. Aeppli, Phys. Rev. Lett. 71, 1748, (1993)

# Appendix A

#### Source codes

## A.1 Quantum Monte Carlo

```
c Quantum Monte Carlo simulation for the oo-d Hubbard
c Model on a Bethe lattice.
c This code accepts any chemical potential.
c Produces the local Green functions, the Selfenergy,
c and the local spin-spin correlation function.
c Has to be linked to IMSL
parameter(L=16384,LI=32)
       implicit real*8(a-h,o-z)
       double complex xi,d2,one,ome
       double complex fg0(2*L), fg0f(2*L), fg0b(2*L)
       double complex fg0t(2*L)
       double complex fgb(2*L),fgf(2*L),self(2*L),self0(2*L)
       double precision g0(-L:L),g(-L:L),dumg(2*L),dumg0(2*L)
       double precision dumg1(2*L),dumg01(2*L)
       double precision g00(-LI:LI),gtmp(-LI:LI)
c***** output data *******************************
c fort.10=G0 in imaginary time
c fort.11=G in imaginary time
c fort.30=Imaginary part of Selfenergy
c fort.31=Real part of Selfenergy
c fort.40=Imaginary part of GO
c fort.41=Real part of GO
c fort.60=Imaginary part of G
c fort.61=Real part of {\tt G}
c fort.90=particle occupation
c fort.91=local spin-spin correlation function
c fort.92=acceptance rate and number of negative determinants found
c***** input data (fort.50) ****************************
c LI=the number of time slices for the impurity subroutine
c dtauI=the imaginary time slice step for the impurity subroutine
c L=the number of time slices for the self-consistency part
c dtau=the imaginary time slice step for the self-consistency part
```

```
c u=interaction strength
c d=half-bandwidth
c nloop=number of iteration loops
c dmu=increment for the mu loop
c nmu=number of mu loops
c xmu0=initial mu (chemical potential, mu=0 at half-filling)
c NOTE: we introduce a thinner time discretization to improve the
c high frequency cut-off. dtau and L are defined such that:
c dtau*L=dtauI*LI=beta
c this is equivalent to the introduction of attenuation coefficients
c in the Fourier transforms.
c L must be multiple of LI
c if1=0 calculates the spin-spin correlation function
c if1=1 does not
       read(50,*)dtauI,u
       read(50,*)d,nloop,dmu,nmu,xmu0,if1
c******define some constants*****
       d2=d**2*(1.,0.)
       dtau=dtauI*float(LI)/float(L)
       pi=3.141592653589793
       xi=(0.,1.)
       one=(1.,0.)
       beta=dtau*float(L)
       plt=pi/float(L)/dtau
       dli=1.d0/float(L)/dtau
dth=dtau/2.d0
       do 301 i=1,2*L
         fg0(i)=(0.,0.)
301
      continue
c***** mu loop starts here ***********************
       do 432 imu=1,nmu
       xmu=xmu0+dmu*float(imu-1)
c***** here starts the iteration ********************
       do 103 iloop=1,nloop
C***************
c fg0(i) is g0 in Matsubara space
c fgf(i) is g in Matsubara space
c self(i) is the selfenergy in Matsubara space
C*****************
```

```
c**set a flag for the final loop for the impurity subroutine**
        if0=1
        if(iloop.eq.nloop)if0=0
c**in first loop gO is initialized**
   if(imu.eq.1.and.iloop.eq.1)then
c use mu=mu/4 to construct a seed with a non-zero particle number
c (is a trick to have a reasonable starting seed)
        do 101 i=1,L
           ome=xi*plt*(2.*float(i)-1.-float(L))
           ome=ome-xmu/4.
           sq=dimag(zsqrt((ome)**2-d**2))
           w=dimag(ome)
           sig=sq*w/dabs(sq*w)
           fg0(2*i)=2./(ome+sig*(zsqrt((ome)**2-d**2)))
 101
        continue
   else
        do 102 i=1,L
           ome=xi*plt*(2.*float(i)-1.-float(L))
           ome=ome-self(2*i)-xmu
           sq=dimag(zsqrt((ome)**2-d**2))
           w=dimag(ome)
           sig=w*sq/dabs(w*sq)
           fgf(2*i)=2./(ome+sig*(zsqrt((ome)**2-d**2)))
 102
        continue
        do 303 i=1,2*L
           fg0(i)=(0.,0.)
303
       continue
        do 104 i=1,L
           fg0(2*i)=one/(one/fgf(2*i)+self(2*i))
 104
        continue
   endif
        call dfftcb(2*L,fg0,fg0t)
        sg=-1.
        do 82 i=1,2*L
        sg=sg*(-1.)
           fg0t(i)=sg*dli*fg0t(i)
82
        continue
        do 83 i=1,L
           fg0b(i)=fg0t(i+L)
```

```
83
      continue
      do 84 i=L+1,2*L
        fg0b(i)=fg0t(i-L)
84
       continue
C***************
c fg0b(i) is g0 in time space
C************
c take the real part for the impurity subroutine input
      do 811 i=1,2*L
        g0(i-L-1)=real(fg0b(i))
811
       continue
C***************
c trick for the discontinuity in g(tau)
      g0(0)=g0(0)+.5
      g0(-L)=-g0(0)
C***************
c extract LI points from the L point GF
      call extract(g0,g00,L,LI)
C******************
c do the QMC impurity simulation
c g00 is the input non-interacting GF
c gtmp is the output interacting GF
      call impurity(g00,gtmp,dtauI,u,if0,if1,xmu)
c get the L point GF from the L point one by interpolation
      call interp(gtmp,g,L)
      call interp(g00,g0,L)
C***************
c "undoes" the trick for the discontinuity of g(tau)
     g(0)=g(0)-.5
     g0(0)=g0(0)-.5
     g(-L)=-g(0)
     g0(-L)=-g0(0)
C****************
```

```
C************
c fgb(i) is g in time space
C***********
       do 812 i=1,2*L
          fgb(i)=g(i-L-1)*(1.,0.)
          fg0b(i)=g0(i-L-1)*(1.,0.)
812
        continue
       call dfftcf(2*L,fg0b,fg0f)
       call dfftcf(2*L,fgb,fgf)
c** get the selfenergy **
       do 304 i=1,2*L
          self0(i)=(0.,0.)
304
       continue
       sg=-1.
       do 85 i=1,2*L
       sg = sg * (-1.)
          fg0f(i)=dth*sg*fg0f(i)
          fgf(i)=dth*sg*fgf(i)
          if(mod(i,2).eq.0)then
             self0(i)=one/(fg0f(i))-one/(fgf(i))
          end if
        continue
85
       do 409 i=1,L
          self(i)=self0(i+L)
          dumg(i)=dimag(fgf(i+L))
          dumg0(i)=dimag(fg0f(i+L))
          dumg1(i)=real(fgf(i+L))
          dumg01(i)=real(fg0f(i+L))
409
         continue
       do 410 i=L+1,2*L
          self(i)=self0(i-L)
          dumg(i)=dimag(fgf(i-L))
          dumg0(i)=dimag(fg0f(i-L))
          dumg1(i)=real(fgf(i-L))
          dumg01(i)=real(fg0f(i-L))
410
         continue
c*****print output********
       if(iloop.eq.nloop)then
c** g0, g, and selfenergy in Matsubara space **
          write(30,*)'"mu=',real(xmu),'"'
```

```
write(31,*)'"mu=',real(xmu),'"'
         write(40,*)'"mu=',real(xmu),'"'
         write(41,*)'"mu=',real(xmu),'"'
         write(60,*)'"mu=',real(xmu),'"'
         write(61,*)'"mu=',real(xmu),'"'
       do 106 i=L-LI*2,L+LI*2,2
          si=dimag(self(i))
          si1=real(self(i))
       xa=real(pi/beta*float(i-L-1))
         write(30,*)real(xa),real(si)
          write(31,*)real(xa),real(si1)
          write(40,*)real(xa),real(dumg0(i))
          write(41,*)real(xa),real(dumg01(i))
          write(60,*)real(xa),real(dumg(i))
          write(61,*)real(xa),real(dumg1(i))
106
         continue
         write(30,*)',
        write(31,*)' '
        write(40,*)', '
        write(41,*)' '
        write(60,*)' '
        write(61,*)', '
c** g0 and g in imaginary time **
         write(10,*)'"mu=',real(xmu),'"'
         write(11,*)'"mu=',real(xmu),'"'
       do 10 i=-LI,LI
          write(10,*)real(i*dtauI),real(g00(i))
          write(11,*)real(i*dtauI),real(gtmp(i))
10
       continue
        write(10,*)' '
        write(11,*)' '
c** occupation **
         write(90,*)real(xmu),real(-gtmp(0))+.5
       endif
c******close iteration loop**********************
103
       continue
c******close mu loop************************
432
       continue
       stop
       end
c this subroutine takes a GF in time with L points spaced
c at dtau, and extracts LI points spaced at dtauI for the
```

```
c impurity subroutine. Is the inverse of the subroutine
c interp
       subroutine extract(g0,g00,L,LI)
       implicit real*8(a-h,o-z)
       double precision g0(-L:L),g00(-LI:LI)
     g00(0)=g0(0)
     nrat=L/LI
     do 20 i=1,LI
        g00(i)=g0(i*nrat)
20
    continue
     do 21 i=1,LI
        g00(-i)=-g00(LI-i)
21
     continue
     return
     end
c this subroutine takes a GF in time with LI points spaced
c at dtauI, and interpolates to produce L points spaced at
c dtau. Is the inverse of the subroutine extract
     subroutine interp(gtmp,g,L)
     implicit real*8(a-h,o-z)
     parameter(LI=32,LI1=32+1)
     integer nintv
     double precision gtmp(-LI:LI),g(-L:L)
     double precision xa(LI1), ya(LI1)
     double precision break(LI1),cscoef(4,LI1)
     external dcsint,dcsval
C***LI1=LI+1*****
     do 10 i=1,LI1
        xa(i)=float(i-1)/float(LI)
        ya(i)=gtmp(i-1)
10
    continue
       call dcsint(LI1,xa,ya,break,cscoef)
c***assign g(i)****
       nintv=LI
       do 20 i=1,L
          x=float(i)/float(L)
          g(i)=dcsval(x,nintv,break,cscoef)
20
       continue
```

```
g(0)=gtmp(0)
       do 40 i=1,L
          g(-i)=-g(L-i)
40
       continue
       return
       end
c this subroutine takes a non-interacting GF and solves the
c impurity problem producing the interacting GF on output
     subroutine impurity(g0,g,dtau,u,if0,if1,xmu)
     implicit real*8(a-h,o-z)
     parameter(L=32)
     double precision gup(L,L),gdw(L,L),v(L)
     double precision g0(-L:L), del(L,L), g(-L:L)
     double precision gstup(L,L),gstdw(L,L)
     double precision xgu(-L:L),xgd(-L:L),xg(-L:L),xga(-L:L)
       dimension xs(0:L)
       dimension s(2*L,3000)
C*********************
     real rnunf
     external rnset, rnunf
c****parameters****
c nsweep=number of sweeps of the L spins
c ndirty=number of dirty updates (L**2 operations) between
c clean updates (L**3 operations)
c ncor=autocorrelation length
c nwarm=number of warm-up sweeps
c iseed=seed for the RNG
c polar= average polarization of the initial spins
C*******
     iseed=123457
     polar=.5
     nsweep=3500
     ndirty=50
     ncor=2
     nwarm=500
     do 11 i=1,L
        do 12 j=1,L
          del(i,j)=0.
12
       continue
        del(i,i)=1.
11
    continue
     do 800 i=1,L
        do 800 j=1,L
          gstup(i,j)=0.
          gstdw(i,j)=0.
```

```
800 continue
    z=dtau*u/2
     z=exp(z)
     xlam=log(z+sqrt(z**2-1.))
       if(u.eq.0.)u=.001
       xxx=1./(1.-exp(-dtau*u))
     call rnset(iseed)
     g0(-L)=-g0(0)
c**generates the initial spin configuration with**
c**average polarization = pol
     call initial(xlam, v, polar, L)
     call gnewclean(gup, v, g0, del, 1.d0)
     call gnewclean(gdw,v,g0,del,-1.d0)
c***parameters*********
c kx= counts # of measurements
c irr= counts # of accepted flips (after the warm-up)
c nrat= counts # of negative determinants encountered
     kx=0
     irr=0
     nrat=0
C*********
c******start measurement loop*****************
C*********
c does a total of nsweeps
c a clean update comes after
c ndirty dirty updates
C*********
     do 2 k=1,nsweep
        kk=mod(k,ndirty)
        kcor=mod(k,ncor)
        do 5 j=1,L
           dv=2.*v(j)
c****calculates the determinant ratio*******
           ratup=1.+(1.-gup(j,j))*(exp(-dv)-1.)
           ratdw=1.+(1.-gdw(j,j))*(exp(dv)-1.)
           rat=ratup*ratdw
           if(rat.lt.0.)then
             nrat=nrat+1
           end if
           rat=rat/(1.+rat)
```

```
r=rnunf()
           if(rat.gt.r)then
              if(k.gt.nwarm)then
                 irr=irr+1
              end if
              v(j) = -v(j)
              if(kk.eq.0)then
c makes a clean calculation of g
                 call gnewclean(gup, v, g0, del, 1.d0)
                 call gnewclean(gdw,v,g0,del,-1.d0)
                 goto 100
              endif
c makes a dirty calculation of g
              call gnew(gup,v,j,del,1.d0)
              call gnew(gdw,v,j,del,-1.d0)
           endif
 100
          continue
        continue
c*** store the measurements*********
       if(kcor.eq.0.and.k.gt.nwarm)then
       kx=kx+1
if(kx.ge.3000.and.if1.eq.0)then
print*,'increase the size of the spin measurement storage!!'
print*,'is the size of the matrix xs in the impurity routine'
stop
endif
c*****store the GF*****
       do 333 ix=1,L
          do 333 jx=1,L
             gstup(ix,jx)=gstup(ix,jx)+gup(ix,jx)
             gstdw(ix,jx)=gstdw(ix,jx)+gdw(ix,jx)
333
        continue
       if(if0.eq.0.and.if1.eq.0)then
c***store the Ising spins****
       do 557 iq=1,L
       s(iq,kx)=v(iq)/abs(v(iq))
       s(iq+L,kx)=s(iq,kx)
557
       continue
endif
       endif
C***************
c******end measurement loop*****************
     continue
```

```
c statistics for the acceptance rate
     write(92,*)'acc. rate:',real(float(irr)/float((nsweep-nwarm)*L))
c number of negative determinants
     write(92,*)'# of neg det:',nrat
c**** get g(-L:L) by wrapping-around and
c**** averaging the matrices up & dw (PM case) ******
     kxmax=kx
c*** normalize the sum of the matrices ***
       do 334 ix=1,L
          do 334 jx=1,L
             gstup(ix,jx)=gstup(ix,jx)/float(kxmax)
             gstdw(ix,jx)=gstdw(ix,jx)/float(kxmax)
334 continue
c**** wrap-around ******
       do 601 j=0,L-1
          xgd(-j)=0.
          xgu(-j)=0.
          do 602 i=1,L-j
                xgd(-j)=xgd(-j)+gstdw(i,i+j)
                xgu(-j)=xgu(-j)+gstup(i,i+j)
602
          continue
          xga(-j)=.5*(xgu(-j)+xgd(-j))
601
       continue
       do 604 j=1,L-1
          xgd(j)=0.
          xgu(j)=0.
          do 605 i=1,L-j
                xgd(j)=xgd(j)+gstdw(i+j,i)
                xgu(j)=xgu(j)+gstup(i+j,i)
605
          continue
          xga(j)=.5*(xgu(j)+xgd(j))
604
       continue
       do 606 i=1,L-1
          xg(i)=(xga(i)-xga(i-L))/float(L)
          xg(i-L)=-xg(i)
606
       continue
       xg(0)=xga(0)/float(L)
       xg(-L)=-xg(0)
c**the end point for the interpolation routine**
       xg(L)=1.-xg(0)
       g0(L)=1.-g0(0)
C***************
```

```
do 556 i=-L,L
         g(i)=xg(i)
556 continue
        if(if0.eq.0.and.if1.eq.0)then
c****get the spin susceptibility*********
c***from the ising fields****
      xsa=0.
      xs2=0.
      do 587 ii=0,L
      xs(ii)=0.
587
      continue
      do 558 iq=1,kxmax
      do 559 itq=0,L-1
      do 560 il=1,L
      itk=il+itq
      xs(itq)=xs(itq)+s(itk,iq)*s(il,iq)
      xsa=xsa+s(il,iq)
      xs2=xs2+s(il,iq)**2
560
      continue
559
      continue
      continue
558
write(91,*)'"xmu=',real(xmu),'"'
      do 561 ii=1,L-1
      xs(ii)=xxx*xs(ii)/float(kxmax*L)
      write(91,*)float(ii)/dtau/float(L),xs(ii)
561
      continue
write(91,*)' '
      endif
C*******************
      return
      end
c dirty update
c this subroutine calculates the new inverse matrix in L**2 operations
c using the Sherman-Morrison formula
```

```
subroutine gnew(g,v,j,del,xflag)
     implicit real*8(a-h,o-z)
     parameter(L=32)
     double precision g(L,L),v(L),del(L,L),d(L,L)
     do 1 i1=1.L
        do 2 i2=1,L
          dv=xflag*2.*v(j)
          a=1.+(1.-g(j,j))*(exp(dv)-1.)
          b=(g(i1,j)-del(i1,j))*(exp(dv)-1.)
          d(i1,i2)=g(i1,i2)+b/a*g(j,i2)
2
        continue
1
     continue
     do 3 i1=1,L
        do 4 i2=1,L
          g(i1,i2)=d(i1,i2)
       continue
3
     continue
     return
     end
c clean update
c this subroutine calculates the new inverse matrix in L**3 operations
c by standard method
     subroutine gnewclean(g,v,g0,del,xflag)
     implicit real*8(a-h,o-z)
     parameter(L=32)
     double precision g(L,L),v(L),b(L,L),binv(L,L)
     double precision g0(-L:L),del(L,L)
     do 1 i=1,L
        do 2 j=1,L
          dv=xflag*v(j)
          b(i,j)=del(i,j)-(g0(i-j)-del(i,j))*(exp(dv)-1.)
        continue
2
     continue
     call dlinrg(l,b,L,binv,L)
     do 3 i1=1,L
        do 4 i2=1,L
          xdum=0.
          do 5 i=1,L
             xdum=xdum+binv(i1,i)*g0(i-i2)
          continue
5
       g(i1,i2)=xdum
4
       continue
3
     continue
     return
     end
```

c this subroutine initialize the vector v of Ising fields

```
c with an average polarization given by polar
     subroutine initial(xlam, v, polar, L)
        implicit real*8(a-h,o-z)
     double precision v(L)
     real rnunf
     external rnset, rnunf
     iseed=765437
     call rnset(iseed)
     do 1 i=1,L
        s=1.
         r=rnunf()
        if(r.gt.polar) s=-1.
         v(i)=xlam*s
    continue
1
     return
```

end

#### A.2 2<sup>nd</sup> Order Perturbation Theory (Matsubara space)

```
c 2nd Order Perturbation Theory (a la Yamada Yosida)
c for the oo-d Hubard Model in Matsubara space.
c Produces the local Green function and the Selfenergy.
c Also calculates the kinetic T, potential V,
c and total E energies, and the double occupation.
c Has to be linked to IMSL
parameter(L=16384)
  implicit real*8(a-h,o-z)
 double complex xi,ep,om,om1,om2,d2,one,root
 double complex fg0(2*L),fg0b(2*L)
 double complex fg0t(2*L),fg(2*L)
 double complex sefb(2*L),seff(2*L),self(2*L)
c***** output data ******************************
c fort.30=Imaginary part of Selfenergy
c fort.60=Imaginary part of G
c fort.80=kinetic energy T as a function of temperature
c fort.81=potential energy V as a function of temperature
c fort.82=total energy E as a function of temperature
c fort.83=double occupation as a function of temperature
c fort.90=kinetic energy T as a function of U
c fort.91=potential energy V as a function of U
c fort.92=total energy E as a function of U
c fort.93=double occupation as a function of {\tt U}
c***** input data (fort.70) *********************************
c L=number of frequency points
c t0=initial temperature
c u0=initial interaction strength
c dt=step for the temperature loop
c du=step for the interaction loop
c nl=number of temperature/interaction loops
c d=half-bandwidth
c nloop=number of iteration loops
c nl0=number of final loops to be printed-out
c imet=selects initial seed (1=metallic, 0=insulating)
c isie=flag for computation of energies (isie=1 does it, isie=0 does not)
c itu=selects type of loop (itu=0 U loop, itu=1 temperature loop)
       read(70,*)t0,u0,dt,du,nl
       read(70,*)d,nloop,nl0,imet,isie,itu
c*****define some constants*****
```

```
ep=.0001*(1.,0.)
      d2=d*(1.,0.)
      d2=d2**2
      pi=3.141592653589793
xi=(0.,1.)
      one=(1.,0.)
u=u0
t=t0
do 301 i=1,2*L
  fg0(i)=(0.,0.)
  fg(i)=(0.,0.)
301 continue
c*****temperature/U loop starts here**************
do 222 il=1,nl
if(itu.eq.1)then
t=t0+dt*(float(il-1))
else
      u=u0+du*float(il-1)
endif
dtau=1./t/float(L)
binv=1./dtau/float(L)
do 103 iloop=1,nloop
c****g0 is the non interacting GF in real frequency space*****
c**on first loop compute a seed (imet=1 metallic, imet=0 insulating)
if(iloop*iu*it.eq.1)then
      do 101 i=1,L
         om=xi*(2.*float(i)-1.-float(L))*pi*binv
         fg0(2*i)=one/om
      if(imet.eq.1)then
         root=cdsqrt((om+ep)**2-d2)
         sig=1.
         if(dimag(om)*dimag(root).lt.0.)sig=-1.
         fg0(2*i)=2.*one/(om+(cdsqrt((om+ep)**2-d2)))
      endif
101
      continue
else
      do 102 i=1,L
```

```
om=xi*(2.*float(i)-1.-float(L))*pi*binv
           om1=om+self(2*i)
           om2=om-self(2*i)
     root=cdsqrt((om2+ep)**2-d2)
   sig=1.
     if(dimag(om)*dimag(root).lt.0.)sig=-1.
           fg0(2*i)=2.*one/(om1+sig*root)
   fg(2*i)=2.*one/(om2+sig*root)
       continue
 102
endif
c** fg0(i) is the non interacting GF in Matsubara space **
        call dfftcb(2*L,fg0,fg0t)
ex=-1.
        do 82 i=1,2*L
ex=-ex
           fg0t(i)=binv*fg0t(i)*ex
 82
         continue
do 83 i=1.L
           fg0b(i)=fg0t(i+L)
 83
         continue
do 84 i=L+1,2*L
           fg0b(i)=fg0t(i-L)
 84
         continue
c** fg0b(i) is the non interacting GF in time **
c***calculate the selfenergy in 20PT***********
do 520 i=1,L
 sefb(i+L)=u**2*fg0b(i+L)**3
520 continue
do 525 i=1,L
 sefb(L+1-i)=-sefb(i+L)
525 continue
        call dfftcf(2*L,sefb,seff)
ex=-1.
do 530 i=1,2*L
ex=-ex
           seff(i)=.5*dtau*ex*seff(i)
530
        continue
do 540 i=1,L
           self(i)=seff(i+L)
```

```
540
      continue
do 550 i=L+1,2*L
         self(i)=seff(i-L)
550
      continue
c***self is the self-energy in Matsubara space*****
x=pi/(L*dtau)
if(iloop.ge.nloop-nl0+1)then
 do 106 i=L-300,L+300,2
         si=dimag(self(i))
    g1=dimag(fg(i))
         write(30,*)real(x*(i-L-1)),real(si)
         write(60,*)real(x*(i-L-1)),real(g1)
106
        continue
 write(30,*)'
 write(60,*),
 endif
C********************
c*****close iteration loop*********************
103
      continue
c** E=tum,T=tuma,V=tum-tuma***
if(isie.eq.1)then
sum=0.
tum=0.
tuma=0.
do 111 i=1,L
         oma=(2.*float(i)-1.-float(L))*pi*binv
sg=1.
if(oma.lt.0.)sg=-1.
omb=oma*2.
 tum=tum+.5*dimag(fg(2*i))*dimag(self(2*i))
    $ -(dimag(fg(2*i))+2./(oma+sg*dsqrt(oma**2+d**2)))*oma
tuma=tuma+dimag(fg(2*i))*dimag(self(2*i))
    $ -(dimag(fg(2*i))+2./(oma+sg*dsqrt(oma**2+d**2)))*oma
111 continue
```

```
free=0.
e=-d
de=d/1000.
do 666 i=1,2000
  free=free+de*e*dsqrt(1.-(e/d)**2)/(dexp(e/t)+1.)
e=e+de
666 continue
free=free*2./(pi*d)
tum=t*tum+free
tuma=t*tuma+free
if(itu.eq.1)then
c***print-out energies as function of temperature***
c**kinetic**
 write(80,*)real(binv),real(tuma)
c**potential**
 write(81,*)real(binv),real(tum-tuma)
c**total**
write(82,*)real(binv),real(tum)
c**<Nup*Ndw>=<D> double ocupation**
 write(83,*)real(binv),real((tum-tuma)*2./u+.25)
else
c***print-out energies as function of U***
c**kinetic**
 write(90,*)real(u),real(tuma)
c**potential**
 write(91,*)real(u),real(tum-tuma)
c**total**
 write(92,*)real(u),real(tum)
c**<Nup*Ndw>=<D> double ocupation**
 write(93,*)real(u),real((tum-tuma)*2./u+.25)
endif
C**********************
endif
c*****close temperature/U loop************************
222 continue
```

stop end

#### A.3 $2^{nd}$ Order Perturbation Theory (Real space T=0)

```
c 2nd Order Perturbation Theory (a la Yamada Yosida)
c for the oo-d Hubard Model in real frequency space.
c Produces the local Green functions, the Selfenergy,
c and the local spin-spin correlation function.
c Has to be linked to IMSL
parameter(L=16384)
implicit real*8(a-h,o-z)
double complex one, xi, xs, sq, g
double complex g0(2*L),tg0(2*L),fg0(-L:L)
double complex sft2(2*L),sf2(2*L),sft(-L:L),sf(-L:L)
double precision dns(2*L)
C***** output data *******************************
c fort.10=Real part of GO
c fort.11=Imaginary part of GO
c fort.23=Real part of Selfenergy
c fort.24=Imaginary part of Selfenergy
c fort.25=Imaginary part of G (density of states)
c***** input data (fort.20) **************************
c L=number of frequency points
c f=frequency discretization step
c d0=half-bandwidth
c u0=initial interaction strength
c nloop=number of iteration loops
c du=step for the interaction loop
c nu=number of interaction loops
c i01=interval between points for output (from -imax1 to imax1)
c imax1=limit for low frequency printout
c iO2=interval between points for output (from -imax2 to -imax1)
     and (from imax1 to imax2)
c nl0=number of final loops to be printed-out
c imet=selects initial seed (1=metallic, 0=insulating)
read(20,*)f,d0,u0,nloop,du,nu
read(20,*)i01,imax1,i02,imax2,nl0,imet
c*****define some constants*****
       pi=3.141592653589793
dtau=2.*pi/f/dfloat(2*L)
f2=f**2
one=(1.,0.)
xi=(0.,1.)
XL=float(L)
epsilon=1./100000.
```

```
c****** U loop starts here *********************
do 121 iu=1,nu
u=u0+du*dfloat(iu-1)
xn=1./(u**2/pi/d0)
c***** the iteration loop starts here ****************
do 100 iloop=1,nloop
c****g0 is the non interacting GF in real frequency space*****
c****constructs gO using the continuity of the derivatives****
c****for choosing the correct brunch-cut***************
do 2 i=L+1,2*L
om=(float(i)-XL-1.)*f
sig=1.d0
ome=om*one
c***on first loop compute a seed (imet=1 metallic, imet=0 insulating)
if(iloop.eq.1)then
if(dabs(om).lt.1.d-9)then
 g0(i)=0.*one
else
 g0(i)=1./(ome+float(imet)*d0*xi/2.)
endif
else
xs=sf(i-L-1)
sq=cdsqrt((ome-xs)**2-d0**2*one)
sqim=dimag(sq)
sqre=real(sq)
if(i.le.L+5)then
c get the first 5 points right to define the branch-cut
if(sqre.gt.0..and.imet.eq.0)sig=-1.d0
else
```

```
benpr=real(2./(ome+xs+sq))
    benmr=real(2./(ome+xs-sq))
    benpi=dimag(2./(ome+xs+sq))
  benmi=dimag(2./(ome+xs-sq))
  xp=((benpr+benchr0-2.*benchr)**2
             +(benpi+benchi0-2.*benchi)**2)
  xm=((benmr+benchr0-2.*benchr)**2
             +(benmi+benchi0-2.*benchi)**2)
  if(xp.gt.xm)sig=-1.d0
       g=(2./(ome+xs+sq))
       d1=dimag(one/g)-dimag(sf(i-L-1))
       d2=real(one/g)-real(sf(i-L-1))
       d2=d2**2
       d3=d1**2
       dn=d1/(d2+d3)
       if(dn.lt.0)sig=-1.
end if
g0(i)=2./(ome+xs+sig*sq)
endif
benchr=real(g0(i))
benchi=dimag(g0(i))
benchr0=real(g0(i-1))
benchi0=dimag(g0(i-1))
2 continue
c**get the negative frequency part by symmetry**
do 222 i=1,L-1
g0(L+1-i)=-g0(L+1+i)
222 continue
g0(1)=g0(2)
g0(L+1)=0.*one
call dfftcb(2*L,g0,tg0)
ex=-1.
       do 3 i=1,2*L
ex=-ex
          tg0(i)=ex*f/2./pi*tg0(i)
3
       continue
       do 4 i=1,L
          fg0(i-1)=tg0(i)
4
       continue
       do 5 i=L+1,2*L
```

```
fg0(-2*L-1+i)=tg0(i)
 5
        continue
c***fg0 is the non interacting GF in real time*****
c***calculate the selfenergy in 20PT***********
do 7 i=-L+1,L-1
sft(i)=-u**2*fg0(i)**2*fg0(-i)
7 continue
sft(-L) = -u**2*fg0(-L)**2*fg0(L-1)
        do 24 i=-L,L-1
   sft2(i+L+1)=sft(i)
 24
    continue
call dfftcf(2*L,sft2,sf2)
ex=-1.
do 8 i=1,2*L
ex=-ex
sf2(i)=-ex*dtau*sf2(i)
8 continue
        do 34 i=1,L
           sf(i-1)=sf2(i)
34
       continue
        do 35 i=L+1,2*L
           sf(-2*L-1+i)=sf2(i)
35
        continue
c***sf is the self-energy in real frequency space*****
c**********print output********************
\verb|if(iloop.ge.nloop-nl0+1)| then|\\
c***get the final interacting GF***
do 111 i=1,2*L
if(i.eq.L+1)then
dns(i)=2./d0
else
d1=dimag(one/g0(i))-dimag(sf(i-L-1))
d2=real(one/g0(i))-real(sf(i-L-1))
d2=d2**2
```

```
d3=d1**2
dns(i)=d1/(d2+d3)
endif
111 continue
if(imet.eq.0)dns(L+1)=0.
do i=imax2,imax1,-i02
      write(25,*)-real(f*float(i)),real(dns(i+L+1))
enddo
      do i=imax1,0,-i01
      write(25,*)-real(f*float(i)),real(dns(i+L+1))
enddo
do 118 i=0,imax1,i01
 write(25,*)real(f*float(i)),real(dns(i+L+1))
 write(11,*)real(f*float(i)),real(real(g0(i+L+1)))
 write(12,*)real(f*float(i)),real(dimag(g0(i+L+1)))
 write(24,*)real(f*float(i)),real(dimag(sf(i)))
write(23,*)real(f*float(i)),real(real(sf(i)))
118 continue
 do 116 i=imax1,imax2,i02
 write(25,*)real(f*float(i)),real(dns(i+L+1))
 write(11,*)real(f*float(i)),real(real(g0(i+L+1)))
 write(12,*)real(f*float(i)),real(dimag(g0(i+L+1)))
 write(24,*)real(f*float(i)),real(dimag(sf(i)))
 write(23,*)real(f*float(i)),real(real(sf(i)))
116 continue
write(25,*)','
 write(11,*)''
 write(12,*)','
 write(24,*)','
write(23,*)','
endif
c*****close iteration loop*********************
100 continue
c*****close U loop*************************
121 continue
stop
end
```

#### A.4 Exact Diagonalization

```
c Exact diagonalization for the oo-d Anderson model
c on a Bethe lattice.
c This code accepts general values of the input parameters.
c Produces the local Green functions and the local
c spin-spin and charge-charge correlation functions.
c Note1: it may get trapped into cycles in the
c non particle-hole symmetric case.
c Note2: setting tpd and v to zero corresponds to the
c Hubbard model (with upp the Hubbard repulsion)
parameter(N=16,NN=2**N,NP=4900)
       parameter(1m=400)
       implicit real*8(a-h,o-z)
       double precision h(NN,2*N)
       double precision anr(0:NP),bnr(0:NP)
       double precision anl(0:NP),bnl(0:NP)
       double precision cnr(0:NP),dnr(0:NP)
       double precision cnl(0:NP),dnl(0:NP)
       double precision snr(0:NP),tnr(0:NP)
       double precision snl(0:NP),tnl(0:NP)
       double precision gs(NN)
       double precision cp(NN),cpdg(NN)
       double precision cd(NN),cddg(NN)
       dimension icp(NN),icpdg(NN)
       dimension icd(NN),icddg(NN)
       dimension ih(NN,2*N)
       double complex zr,zl,xi,xr,xl,gg(-lm:lm),gx(-lm:lm),s(-lm:lm)
       double complex zw,zy
       double complex dr,dl,ggd(-lm:lm),gxd(-lm:lm)
       double complex dw,dy
       double complex sr,sl,sch(-lm:lm),ssp(-lm:lm)
       dimension in0(N), is0(N)
c***** output data ******************************
c fort.7 a's of the Gpp> CF
c fort.8 a's of the Gpp< CF
c fort.17 b's of the Gpp> CF
c fort.18 b's of the Gpp< CF
c fort.27 a's of the Gdd> CF
c fort.28 a's of the Gdd< CF
c fort.37 b's of the Gdd> CF
c fort.38 b's of the Gdd< CF
c fort.60 Im(Gpp) Real frequency
c fort.61 Re(Gpp) Real frequency
c fort.70 Im(Gpp) Matsubara
c fort.71 Re(Gpp) Matsubara
c fort.80 Im(Gdd) Real frequency
c fort.81 Re(Gdd) Real frequency
```

```
c fort.90 Im(Gdd) Matsubara
c fort.91 Re(Gdd) Matsubara
c fort.92 spin-spin correlation function
c fort.93 charge-charge correlation function
c fort.96 poles & weights for spin and charge susceptibilities
c fort.97 poles & weights for d site
c fort.98 poles & weights for p site
c fort.99 poles & weights for effective bath
c***** input data (fort.50) **************************
c N=number of sites (impurity + chains)
c lm=size of the output files (2*lm)
c tem=spacing of Matsubara points (\delta\omega=\pi*tem)
c u0=initial interaction strength
c du=increment for the u loop
c nu=number of u loops
c tpd=hybridization between p & d sites
c v=charge repulsion between p & d sites
c ed0=atomic energy of d site
c upp=p site repulsion
c d=half-bandwidth
c xm0=initial chemical potential (=0 at the symmetrical point)
c nloop=number of iterations loops
c eps=broadening for the poles
c dmu=increment for the mu loop
c nmu=number of mu loops
c NB=number of poles to be evaluated in the last iteration (2NG+2)
c nlast=number of final iterations that are written on output
c iall=number of initial iterations where the gs is searched
       in all sectors
c ird=1 reads input parameters for Gpp (=0 generates new set)
c ifast=0 searches for gs in all sectors in the final (nloop-nlast)
        iterations (=1 does not)
        read(50,*)tem,u0,du,nu
        read(50,*)tpd,v,ed0,upp
        read(50,*)d,xmu0,nloop,eps,dmu,nmu
read(50,*)NB,nlast
read(50,*)iall,ird,ifast
c*****define some constants*****
u=u0
pi=3.141592653589793
        xi=(0.,1.)
xr=-eps*xi
xl=-eps*xi
        one=(1.,0.)
        pt=pi*tem
c 1=p site down
c 2=p site up
c iep=d site up
```

```
c ied=d site down
c NR =last site of up chain
c NR+1=first site of down chain
c NC =length of each side of the chains
NR = ((N-2)/2-1)/2+2
NC = NR - 2
nhalf=N/2
iep=N-1
ied=N
c**get creation and destruction operators in matrix form**
call getcp(cp,icp,cpdg,icpdg)
call getcd(cd,icd,cddg,icddg)
c*****constructs the initial seed*******
if(ird.eq.1)then
c reads-in parameters
do i=0,NC
read(7,*)x,anr(i)
read(17,*)x,bnr(i)
read(8,*)x,anl(i)
read(18,*)x,bnl(i)
enddo
close(7)
close(8)
close(17)
close(18)
else
c generates new parameters
 do 1 i=0,N
 anr(i)=d/2.d0
 bnr(i)=d**2/4.
1 continue
 do 2 i=0,N
 anl(i)=-d/2.d0
 bnl(i)=d**2/4.
2 continue
endif
egs=0.d0
```

```
c***** U loop starts here *********************
do 300 iu=1,nu
u=u0+du*dfloat(iu-1)
c***** mu loop starts here **********************
do 200 imu=1,nmu
xmu=xmu0+dmu*float(imu-1)
c***** here starts the iteration ******************
do 100 iloop=1,nloop
do 121 i=1,NN
gs(i)=0.d0
do 121 j=1,2*N
h(i,j)=0.d0
ih(i,j)=0
121 continue
c constructs the Hamiltonian h in the full hilbert space
c in compressed form. The matrix ih is the pointer
print*,'getting the new hamiltonian...'
  call geth(ih,h,d,u,xmu,ed0,v,tpd,upp,
    $
                 anr,bnr,anl,bnl,egs)
print*,'done!'
c iflag=0 searches in all sectors, iflag=1 doesn't
iflag=1
if(iloop.le.iall.or.iloop.ge.nloop-nlast) iflag=0
if(ifast.eq.1.and.iloop.ge.nloop-nlast) iflag=1
print*,'calculating the new gs...'
call getgs(ih,h,egs,gs,iloop,iflag,in0,is0,igs)
print*,'done!'
c** print the groundstate energy **
write(3,*)iloop,real(egs)
```

```
c adjust the size of the chains that need to be obtained
NG=NC
if(iloop.ge.nloop-nlast)NG=NB
print*,'getting Gpp...'
call getgf(h,ih,anr,bnr,anl,bnl,gs,igs,cp,icp,cpdg,icpdg,
     $
                  NG,in0,is0)
c renormalize the bn's, multiplying by t^2
c (up to here bnr(0)=yr, bnl(0)=yl)
yr=bnr(0)
yl=bnl(0)
bnr(0)=bnr(0)*d**2/4.
bnl(0)=bnl(0)*d**2/4.
c**in final loops get the Gdd continued fraction and**
c**the susceptibilities
\verb|if(iloop.ge.nloop-nlast|) then \\
print*,'getting Gdd...'
call getgf(h,ih,cnr,dnr,cnl,dnl,gs,igs,cd,icd,cddg,icddg,
                  NG,in0,is0)
print*,'getting susceptibilities...'
call getcorr(h,ih,snr,tnr,snl,tnl,gs,igs,NG,in0,is0)
endif
c***in last loop calculate the poles and the weights****
c iwr=1 writes output files (=0 does not)
  iwr=1
  if(iloop.ge.nloop)then
print*,'getting poles and weights...'
  call getpole(egs,snr,tnr,snl,tnl,NG,iwr,-1)
  call getpole(egs,cnr,dnr,cnl,dnl,NG,iwr,0)
  call getpole(egs,anr,bnr,anl,bnl,NG,iwr,1)
print*,'done!'
endif
```

```
c*****print output********
cut=2.d0*u
if(cut.1t.2.)cut=2.d0
if(cut.gt.4.)cut=u
if(iloop.ge.nloop-nlast)then
print*,'writting the output...'
c** Gpp, Gdd, and the susceptibilities***
do 24 i=-lm,lm
ome=pt*(2.*float(i)-1.)
if(dabs(ome).gt.cut)goto 24
zr=xr+ome+egs-anr(NG)
zl=xl+ome-egs-anl(NG)
zw=xi*ome-(anr(NG)-egs)
zy=xi*ome-(anl(NG)+egs)
dr=xr+ome+egs-cnr(NG)
dl=xl+ome-egs-cnl(NG)
dw=xi*ome+egs-cnr(NG)
dy=xi*ome-egs-cnl(NG)
sr=xr+ome+egs-snr(NG)
sl=xl+ome+egs-snl(NG)
if(NG.ge.1)then
do 25 in=NG,1,-1
zr=xr+ome+egs-anr(in-1)-bnr(in)/zr
zl=xl+ome-egs-anl(in-1)-bnl(in)/zl
zw=xi*ome+egs-anr(in-1)-bnr(in)/zw
zy=xi*ome-egs-anl(in-1)-bnl(in)/zy
dr=xr+ome+egs-cnr(in-1)-dnr(in)/dr
dl=xl+ome-egs-cnl(in-1)-dnl(in)/dl
dw=xi*ome+egs-cnr(in-1)-dnr(in)/dw
dy=xi*ome-egs-cnl(in-1)-dnl(in)/dy
sr=xr+ome+egs-snr(in-1)-tnr(in)/sr
sl=xl+ome+egs-snl(in-1)-tnl(in)/sl
25 continue
endif
gg(i)=yr/zr+yl/zl
gx(i)=yr/zw+yl/zy
ggd(i)=dnr(0)/dr+dnl(0)/dl
gxd(i)=dnr(0)/dw+dnl(0)/dy
s(i)=xi*ome-d**2/4.*gx(i)-1./gx(i)
```

```
ssp(i)=tnr(0)/sr
sch(i)=tnl(0)/sl
c**the minus sign is to match the QMC code convention**
write(60,*)real(ome),real(dimag(gg(i)))
  write(61,*)real(ome),real(real(gg(i)))
  write(70,*)real(ome),real(dimag(-gx(i)))
   write(71,*)real(ome),real(real(-gx(i)))
  write(80,*)real(ome),real(dimag(ggd(i)))
  write(81,*)real(ome),real(real(ggd(i)))
   write(90,*)real(ome),real(dimag(-gxd(i)))
   write(91,*)real(ome),real(real(-gxd(i)))
if(i.ge.0)then
   write(92,*)real(ome),real(dimag(ssp(i)))
   write(93,*)real(ome),real(dimag(sch(i)))
endif
24 continue
write(60,*)', '
  write(61,*)' '
write(70,*)' '
  write(71,*)' '
  write(80,*)', '
  write(81,*)' '
  write(90,*)' '
  write(91,*)' '
  write(92,*)' '
  write(93,*)' '
c** chopped Gpp to the size of the chains **
        do 28 i=-lm,lm
        ome=pt*(2.*float(i)-1.)
if(dabs(ome).gt.2.*u)goto 28
        zr=xr+ome+egs-anr(NC-1)
        zl=xl+ome-egs-anl(NC-1)
        zw=xi*ome-(anr(NC-1)-egs)
        zy=xi*ome-(anl(NC-1)+egs)
        if(NC-1.ge.1)then
        do 29 in=NC-1,1,-1
        zr=xr+ome+egs-anr(in-1)-bnr(in)/zr
        zl=xl+ome-egs-anl(in-1)-bnl(in)/zl
        zw=xi*ome+egs-anr(in-1)-bnr(in)/zw
        zy=xi*ome-egs-anl(in-1)-bnl(in)/zy
29
        continue
        endif
        gg(i)=yr/zr+yl/zl
        gx(i)=yr/zw+yl/zy
```

```
c**the minus sign is to match the QMC convention**
       write(160,*)real(ome),real(dimag(gg(i)))
       write(161,*)real(ome),real(real(gg(i)))
       write(170,*)real(ome),real(dimag(-gx(i)))
       write(171,*)real(ome),real(real(-gx(i)))
28
       continue
       write(160,*)' '
       write(161,*)' '
       write(170,*)' '
       write(171,*)' '
print*,'done!'
endif
if(iloop.ge.nloop-nlast)then
c**continued fraction parameters**
do 26 i=0,NG
write(7,*)i,(anr(i)-egs)
write(8,*)i,(anl(i)+egs)
write(27,*)i,(cnr(i)-egs)
write(28,*)i,(cnl(i)+egs)
26 continue
write(7,*),
write(8,*)' '
write(27,*)' '
write(28,*)' '
 do 27 i=0,NG
 write(17,*)i,(bnr(i))
 write(18,*)i,(bnl(i))
 write(37,*)i,(dnr(i))
 write(38,*)i,(dnl(i))
27 continue
 write(17,*)' '
 write(18,*)' '
 write(37,*)' '
 write(38,*)' '
endif
c*****close iteration loop*********************
100 continue
c******close mu loop************************
200 continue
```

```
c******close U loop************************
300 continue
end
c multiplication of H times a vector of size M
c used by the lanczos subroutine
      subroutine hxvl(h,ih,v,w,M)
      parameter(N=16,NP=4900)
      implicit real*8(a-h,o-z)
      double precision h(NP,2*N),v(NP),w(NP)
      double precision t(0:NP)
      dimension ih(NP,2*N)
      t(0)=0.d0
      do i=1,NP
      t(i)=v(i)
      enddo
      do 1 i=1,M
      w(i)=0.d0
      MM=ih(i,N)
      do 2 j=1,MM
      w(i)=w(i)+h(i,j)*t(ih(i,j))
2
      continue
      continue
      return
      end
c multiplication of H times a vector using the mask
c to avoid multiplication by 0
c used by the getcorr subroutine
      subroutine hxvm(h,ih,v,w,imk)
      parameter(N=16,NN=2**N)
      implicit real*8(a-h,o-z)
      double precision h(NN,2*N),v(NN),w(NN)
      double precision t(0:NN)
      dimension ih(NN,2*N)
      dimension imk(NN)
      t(0)=0.d0
      do i=1.NN
      t(i)=v(i)
      enddo
      do 1 i=1,NN
      w(i) = 0.d0
if(imk(i).eq.1)then
      MM=ih(i,N)
```

```
do 2 j=1,MM
       w(i)=w(i)+h(i,j)*t(ih(i,j))
2
       continue
endif
       continue
       return
       end
c action of operator c on a vector state v
c c is in compressed form and ic are the pointers
       subroutine cxv(c,ic,v,w)
       parameter(N=16,NN=2**N)
       implicit real*8(a-h,o-z)
       double precision c(NN), v(NN), w(NN)
       double precision t(0:NN)
       dimension ic(NN)
 t(0)=0.d0
 do i=1.NN
 t(i)=v(i)
 enddo
       do 1 i=1,NN
       w(i)=c(i)*v(ic(i))
С
       w(i)=c(i)*t(ic(i))
1
       continue
       return
       end
c calculates the recursive orthogonal basis for the
c continued fraction expansion
subroutine getfn(ih,h,f,f1,f2,a,b,imk)
parameter(N=16,NN=2**N)
       implicit real*8(a-h,o-z)
       double precision h(NN,2*N),f(NN),f1(NN),f2(NN)
       double precision x(NN)
dimension ih(NN,2*N)
dimension imk(NN)
call hxvm(h,ih,f1,x,imk)
do 1 i=1,NN
f(i)=0.d0
if(imk(i).eq.1)then
f(i)=x(i)-a*f1(i)-b*f2(i)
endif
1 continue
```

```
return
end
c calculates the recursive coefficients of the
c continued fraction expansion
subroutine getab(ih,h,f,f1,a,b,imk)
parameter(N=16,NN=2**N)
       implicit real*8(a-h,o-z)
       double precision h(NN,2*N),f(NN),f1(NN)
       double precision x(NN)
dimension ih(NN,2*N)
dimension imk(NN)
call hxvm(h,ih,f,x,imk)
a=0.
       y=0.
       z=0.
       do 5 i=1,NN
if(imk(i).eq.1)then
       a=a+f(i)*x(i)
       y=y+f(i)**2
       z=z+f1(i)**2
endif
       continue
if(y.ne.0.)then
       a=a/y
else
print*,'warning! the CF has ended unexpectedly'
print*,'but tried to continue anyway...'
a=.000001
endif
b=y/z
return
end
c input a state | i > and output a vector ib(N)
c with its binary decomposition
c (corresponds to the decomposition of the number i-1)
subroutine b2(i,ib)
parameter(N=16)
implicit real*8(a-h,o-z)
dimension ib(N)
do 1 ia=1,N
ib(ia)=0
1 continue
ii=i-1
j=1
10 continue
```

```
ib(j)=ii-int(ii/2)*2
ii=int(ii/2)
j=j+1
if(ii.gt.1)goto 10
ib(j)=ii
return
end
c input state |i> of the basis and calculates |j>=Cm|i>
c the sign of j has the phase convention
c m labels the sites
subroutine c(m,i,j)
parameter(N=16)
      implicit real*8(a-h,o-z)
      dimension ib(N)
c convention:
c + + + +
c C C C C | 0>
c 1 2 3 4
call b2(i,ib)
      if (ib(m).eq.0)then
       j=0
      else
if(m.eq.1)then
j=i-1
else
       km=0
       do 1 k=1, m-1
       km=km+ib(k)
1
       continue
       isg=(-1)**km
       j=isg*(i-2**(m-1))
endif
      endif
return
end
c input state |i\rangle of the basis and calculates |j\rangle=Cm+|i\rangle
c the sign of j has the phase convention
c m labels the sites
      subroutine cdg(m,i,j)
parameter(N=16)
      implicit real*8(a-h,o-z)
      dimension ib(N)
```

```
c convention:
c + + + +
c C C C C | 0>
c 1 2 3 4
       call b2(i,ib)
       if (ib(m).eq.1)then
j=0
else
if(m.eq.1)then
j=i+1
else
        km=0
        do 1 k=1, m-1
        km=km+ib(k)
1
        continue
        isg=(-1)**km
        j=isg*(i+2**(m-1))
endif
endif
       return
       end
c calculates the new effective Hamiltonian
c it is stored in matrix h in compressed form (compressed columns)
c the true column position is stored in ih (pointers)
       subroutine geth(ih,h,d,u,xmu,ed0,v,tpd,upp,
    $
                      anr,bnr,anl,bnl,egs)
       parameter(N=16,NN=2**N,NP=4900)
       implicit real*8(a-h,o-z)
       double precision h(NN,2*N),anr(0:NP),bnr(0:NP)
       double precision anl(0:NP),bnl(0:NP)
       dimension ib(N),ih(NN,2*N)
c NR =last site of up right chain
c NR+1=first site of up left chain
c NC =length of each side of the chains
       NR = ((N-2)/2-1)/2+2
       NC = NR - 2
c iep position of d site up spin
c ied position of d site down spin
iep=N-1
ied=N
c****diagonal entries*****
       do 1 k=1,NN
       call b2(k,ib)
       ec=0.
```

```
do 2 \text{ kp=3,NR}
        ec=ec+(anr(kp-3)-egs)*(dfloat(ib(kp)+ib(kp+2*NC)))
2
        continue
        do 10 kp=NR+1,NR+NC
        ec=ec+(anl(kp-NR-1)+egs)*(dfloat(ib(kp)+ib(kp+2*NC)))
10
        h(k,1)=(-xmu)*dfloat(ib(1))+(-xmu)*dfloat(ib(2))+
     $(-xmu+ed0)*dfloat(ib(iep))+(-xmu+ed0)*dfloat(ib(ied))
     $+ ec + u*(dfloat(ib(iep))-.5d0)*(dfloat(ib(ied))-.5d0)
     $+ v*dfloat(ib(iep)+ib(ied))*dfloat(ib(1)+ib(2))
     $+ upp*(dfloat(ib(1))-.5d0)*(dfloat(ib(2))-.5d0)
ih(k,1)=k
        continue
c start the big j loop
        do j=1,NN
c**index counts the number of non-zero entries of each row**
index=0
        index=index+1
c***hopping to the right chain
        do 4 \text{ m1=2,NR-1}
        call c(m1,j,k)
        if (k.eq.0) goto 6
        k1=abs(k)
        call cdg(m1+1,k1,i1)
        if (i1.eq.0) goto 6
        i=abs(i1)
        if(i.eq.0.or.k.eq.0)then
        print*,k,i
        endif
        sg=1.d0
        if(k.lt.0)sg=-1.d0
        if(i1.lt.0)sg=-sg
        tef=dsqrt(bnr(m1-2))
        index=index+1
        h(j,index)=tef*sg
ih(j,index)=i
        continue
4
        continue
        do 84 m1=2,NR-1
        call cdg(m1,j,k)
        if (k.eq.0) goto 86
        k1=abs(k)
        call c(m1+1,k1,i1)
        if (i1.eq.0) goto 86
        i=abs(i1)
```

```
if(i.eq.0.or.k.eq.0)then
        print*,k,i
        endif
        sg=1.d0
        if(k.lt.0)sg=-1.d0
        if(i1.lt.0)sg=-sg
        tef=dsqrt(bnr(m1-2))
        index=index+1
        h(j,index)=-tef*sg
        ih(j,index)=i
        continue
86
        continue
84
c*** note: the (-) comes from C+iCj + h.c. = C+iCj + (C+iCj)+ =
                               C+iCj + C+jCi = C+iCj - CiC+j
C***
c hopping from the p site to the first
c neighbour on the left side
c the left chain starts at NR+1 site
        call c(2,j,k)
        if (k.eq.0) goto 9
        k1=abs(k)
        call cdg(NR+1,k1,i1)
        if (i1.eq.0) goto 9
        i=abs(i1)
        if(i.eq.0.or.k.eq.0)then
        print*,k,i
        endif
        sg=1.d0
        if(k.lt.0)sg=-1.d0
        if(i1.lt.0)sg=-sg
        tef=dsqrt(bnl(0))
        index=index+1
       h(j,index)=tef*sg
ih(j,index)=i
        continue
        call cdg(2,j,k)
        if (k.eq.0) goto 89
        k1=abs(k)
        call c(NR+1,k1,i1)
        if (i1.eq.0) goto 89
        i=abs(i1)
        if(i.eq.0.or.k.eq.0)then
        print*,k,i
        endif
        sg=1.d0
        if(k.lt.0)sg=-1.d0
        if(i1.lt.0)sg=-sg
        tef=dsqrt(bnl(0))
        index=index+1
        h(j,index)=-tef*sg
```

```
ih(j,index)=i
89
        continue
c hopping to the rest of the left chain
if(NR+1.le.NR+NC-1)then
        do 7 m1=NR+1,NR+NC-1
        call c(m1,j,k)
        if (k.eq.0) goto 8
        k1=abs(k)
        call cdg(m1+1,k1,i1)
        if (i1.eq.0) goto 8
        i=abs(i1)
        if(i.eq.0.or.k.eq.0)then
        print*,k,i
        endif
        sg=1.d0
        if(k.lt.0)sg=-1.d0
        if(i1.lt.0)sg=-sg
        tef=dsqrt(bnl(m1-NR))
        index=index+1
        h(j,index)=tef*sg
ih(j,index)=i
        continue
7
        continue
        do 87 m1=NR+1,NR+NC-1
        call cdg(m1,j,k)
        if (k.eq.0) goto 88
        k1=abs(k)
        call c(m1+1,k1,i1)
        if (i1.eq.0) goto 88
        i=abs(i1)
        if(i.eq.0.or.k.eq.0)then
        print*,k,i
        endif
        sg=1.d0
        if(k.lt.0)sg=-1.d0
        if(i1.lt.0)sg=-sg
        tef=dsqrt(bnl(m1-NR))
        index=index+1
        h(j,index)=-tef*sg
        ih(j,index)=i
         continue
88
         continue
endif
c hopping to the d site of spin up
        call c(2,j,k)
        if (k.eq.0) goto 26
```

```
k1=abs(k)
        call cdg(iep,k1,i1)
        if (i1.eq.0) goto 26
        i=abs(i1)
        if(i.eq.0.or.k.eq.0)then
        print*,k,i
        endif
        sg=1.d0
        if(k.lt.0)sg=-1.d0
        if(i1.lt.0)sg=-sg
        tef=tpd
        index=index+1
        h(j,index)=tef*sg
        ih(j,index)=i
26
        continue
        call cdg(2,j,k)
        if (k.eq.0) goto 28
        k1=abs(k)
        call c(iep,k1,i1)
        if (i1.eq.0) goto 28
        i=abs(i1)
        if(i.eq.0.or.k.eq.0)then
        print*,k,i
        endif
        sg=1.d0
        if(k.lt.0)sg=-1.d0
        if(i1.lt.0)sg=-sg
        tef=tpd
        index=index+1
        h(j,index)=-tef*sg
        ih(j,index)=i
28
        continue
c****right down spin chain*****
c***hopping to the right down chain
c**the right down chain starts at NR+NC+1 site
c***hopping from the down site (1) to the first
c***neighbour on the right side
        call c(1,j,k)
        if (k.eq.0) goto 51
        k1=abs(k)
        call cdg(NR+NC+1,k1,i1)
        if (i1.eq.0) goto 51
        i=abs(i1)
        if(i.eq.0.or.k.eq.0)then
        print*,k,i
        endif
        sg=1.d0
        if(k.lt.0)sg=-1.d0
```

```
if(i1.lt.0)sg=-sg
        tef=dsqrt(bnr(0))
        index=index+1
        h(j,index)=tef*sg
ih(j,index)=i
        continue
        call cdg(1,j,k)
        if (k.eq.0) goto 71
        k1=abs(k)
        call c(NR+NC+1,k1,i1)
        if (i1.eq.0) goto 71
        i=abs(i1)
        if(i.eq.0.or.k.eq.0)then
        print*,k,i
        endif
        sg=1.d0
        if(k.lt.0)sg=-1.d0
        if(i1.lt.0)sg=-sg
        tef=dsqrt(bnr(0))
        index=index+1
        h(j,index)=-tef*sg
        ih(j,index)=i
71
        continue
c***hopping of the rest of the right down chain
        if(NR+NC+1.le.NR+2*NC-1)then
        do 52 m1=NR+NC+1, NR+2*NC-1
        call c(m1,j,k)
        if (k.eq.0) goto 53
        k1=abs(k)
        call cdg(m1+1,k1,i1)
        if (i1.eq.0) goto 53
        i=abs(i1)
        if(i.eq.0.or.k.eq.0)then
        print*,k,i
        endif
        sg=1.d0
        if(k.lt.0)sg=-1.d0
        if(i1.lt.0)sg=-sg
        tef=dsqrt(bnr(m1-NR-NC))
        index=index+1
        h(j,index)=tef*sg
ih(j,index)=i
53
        continue
52
        continue
        do 72 m1=NR+NC+1,NR+2*NC-1
        call cdg(m1,j,k)
        if (k.eq.0) goto 73
        k1=abs(k)
```

```
call c(m1+1,k1,i1)
        if (i1.eq.0) goto 73
        i=abs(i1)
        if(i.eq.0.or.k.eq.0)then
        print*,k,i
        endif
        sg=1.d0
        if(k.lt.0)sg=-1.d0
        if(i1.lt.0)sg=-sg
        tef=dsqrt(bnr(m1-NR-NC))
        index=index+1
        h(j,index)=-tef*sg
        ih(j,index)=i
73
        continue
72
        continue
        endif
c***left down spin chain******
c**the left down chain starts at NR+2*NC+1 site
c***hopping from the down site (1) to the first
c***neighbour on the left side
        call c(1,j,k)
        if (k.eq.0) goto 55
        k1=abs(k)
        call cdg(NR+2*NC+1,k1,i1)
        if (i1.eq.0) goto 55
        i=abs(i1)
        if(i.eq.0.or.k.eq.0)then
        print*,k,i
        endif
        sg=1.d0
        if(k.lt.0)sg=-1.d0
        if(i1.lt.0)sg=-sg
        tef=dsqrt(bnl(0))
        index=index+1
        h(j,index)=tef*sg
ih(j,index)=i
55
        continue
        call cdg(1,j,k)
        if (k.eq.0) goto 75
        k1=abs(k)
        call c(NR+2*NC+1,k1,i1)
        if (i1.eq.0) goto 75
        i=abs(i1)
        if(i.eq.0.or.k.eq.0)then
        print*,k,i
        endif
        sg=1.d0
        if(k.lt.0)sg=-1.d0
        if(i1.lt.0)sg=-sg
```

```
tef=dsqrt(bnl(0))
        index=index+1
        h(j,index)=-tef*sg
        ih(j,index)=i
75
        continue
c***hopping of the rest of the left down chain
        if(NR+2*NC+1.le.NR+3*NC-1)then
        do 56 m1=NR+2*NC+1,NR+3*NC-1
        call c(m1,j,k)
        if (k.eq.0) goto 57
        k1=abs(k)
        call cdg(m1+1,k1,i1)
        if (i1.eq.0) goto 57
        i=abs(i1)
        if(i.eq.0.or.k.eq.0)then
        print*,k,i
        endif
        sg=1.d0
        if(k.lt.0)sg=-1.d0
        if(i1.lt.0)sg=-sg
        tef=dsqrt(bnl(m1-NR-2*NC))
        index=index+1
        h(j,index)=tef*sg
ih(j,index)=i
57
       continue
        continue
56
        do 76 m1=NR+2*NC+1, NR+3*NC-1
        call cdg(m1,j,k)
        if (k.eq.0) goto 77
        k1=abs(k)
        call c(m1+1,k1,i1)
        if (i1.eq.0) goto 77
        i=abs(i1)
        if(i.eq.0.or.k.eq.0)then
        print*,k,i
        endif
        sg=1.d0
        if(k.lt.0)sg=-1.d0
        if(i1.lt.0)sg=-sg
        tef=dsqrt(bnl(m1-NR-2*NC))
        index=index+1
        h(j,index)=-tef*sg
        ih(j,index)=i
77
        continue
76
        continue
        endif
```

c hopping to the d site of spin down

```
call c(1,j,k)
       if (k.eq.0) goto 36
       k1=abs(k)
       call cdg(ied,k1,i1)
       if (i1.eq.0) goto 36
       i=abs(i1)
       if(i.eq.0.or.k.eq.0)then
       print*,k,i
       endif
       sg=1.d0
       if(k.lt.0)sg=-1.d0
       if(i1.lt.0)sg=-sg
       tef=tpd
       index=index+1
       h(j,index)=tef*sg
       ih(j,index)=i
       continue
36
       call cdg(1,j,k)
       if (k.eq.0) goto 38
       k1=abs(k)
       call c(ied,k1,i1)
       if (i1.eq.0) goto 38
       i=abs(i1)
       if(i.eq.0.or.k.eq.0)then
       print*,k,i
       endif
sg=1.d0
if(k.lt.0)sg=-1.d0
if(i1.lt.0)sg=-sg
       tef=tpd
       index=index+1
       h(j,index)=-tef*sg
       ih(j,index)=i
        continue
38
       if(index.ge.N)then
       print*,'need more room for h!!!'
       stop
       endif
       ih(j,N)=index
c close big j loop
enddo
       return
       end
c calculates the matrices cp and cp+ in compressed form
c icp has the pointers. Since they only connect one state of
c the basis to a unique other state, upon compression become
```

```
c matrices of size (NNx1). The matrix cp and cp+ has the
c information of the phase and icp and icp+ has which state is
c connected to which other
subroutine getcp(cp,icp,cpdg,icpdg)
       parameter(N=16,NN=2**N)
       implicit real*8(a-h,o-z)
       double precision cp(NN),cpdg(NN)
dimension icp(NN),icpdg(NN)
c calculates <j|Cp|i>
       do 2 j=1,NN
       call cdg(2,j,i1)
       if(i1.eq.0)goto 2
       i=abs(i1)
cp(j)=dfloat(i)/dfloat(i1)
icp(j)=i
       continue
c calculates <j|Cp+|i>
       do 3 j=1,NN
       call c(2,j,i1)
       if(i1.eq.0)goto 3
       i=abs(i1)
cpdg(j)=dfloat(i)/dfloat(i1)
icpdg(j)=i
       continue
return
end
c idem before (for cd)
       subroutine getcd(cd,icd,cddg,icddg)
       parameter(N=16,NN=2**N)
       implicit real*8(a-h,o-z)
       double precision cd(NN),cddg(NN)
       dimension icd(NN),icddg(NN)
iep=N-1
c calculates <j|Cd|i>
       do 2 j=1,NN
       call cdg(iep,j,i1)
       if(i1.eq.0)goto 2
       i=abs(i1)
       cd(j)=dfloat(i)/dfloat(i1)
       icd(j)=i
2
       continue
```

```
c calculates <j|Cd+|i>
       do 3 j=1,NN
       call c(iep,j,i1)
       if(i1.eq.0)goto 3
       i=abs(i1)
       cddg(j)=dfloat(i)/dfloat(i1)
       icddg(j)=i
3
       continue
       return
       end
c subroutine for determination of e-vectors and e-values
c from numerical recipes
     SUBROUTINE JACOBI(A,N,NP,D,V,NROT)
     implicit real*8(a-h,o-z)
     PARAMETER (NMAX=2500)
     double precision A(NP,NP),D(NP),V(NP,NP),B(NMAX),Z(NMAX)
     DO 12 IP=1,N
       DO 11 IQ=1, N
         V(IP,IQ)=0.
11
       CONTINUE
       V(IP,IP)=1.
12
     CONTINUE
     DO 13 IP=1,N
       B(IP)=A(IP,IP)
       D(IP)=B(IP)
       Z(IP)=0.
13
     CONTINUE
     NROT=0
     DO 24 I=1,50
       SM=0.
       DO 15 IP=1,N-1
         DO 14 IQ=IP+1,N
           SM=SM+ABS(A(IP,IQ))
14
         CONTINUE
15
       CONTINUE
       IF(SM.EQ.O.)RETURN
       IF(I.LT.4)THEN
         TRESH=0.2*SM/N**2
       ELSE
         TRESH=0.
       ENDIF
       DO 22 IP=1,N-1
         DO 21 IQ=IP+1,N
           G=100.*ABS(A(IP,IQ))
           IF((I.GT.4).AND.(ABS(D(IP))+G.EQ.ABS(D(IP)))
              .AND. (ABS(D(IQ))+G.EQ.ABS(D(IQ)))THEN
             A(IP,IQ)=0.
           ELSE IF(ABS(A(IP,IQ)).GT.TRESH)THEN
```

```
H=D(IQ)-D(IP)
              IF(ABS(H)+G.EQ.ABS(H))THEN
                T=A(IP,IQ)/H
              ELSE
                THETA=0.5*H/A(IP,IQ)
                T=1./(ABS(THETA)+SQRT(1.+THETA**2))
                IF(THETA.LT.O.)T=-T
              ENDIF
              C=1./SQRT(1+T**2)
              S=T*C
              TAU=S/(1.+C)
              H=T*A(IP,IQ)
              Z(IP)=Z(IP)-H
              Z(IQ)=Z(IQ)+H
              D(IP)=D(IP)-H
              D(IQ)=D(IQ)+H
              A(IP,IQ)=0.
              DO 16 J=1, IP-1
                G=A(J,IP)
                H=A(J,IQ)
                A(J,IP)=G-S*(H+G*TAU)
                A(J,IQ)=H+S*(G-H*TAU)
16
              CONTINUE
              DO 17 J=IP+1,IQ-1
                G=A(IP,J)
                H=A(J,IQ)
                A(IP,J)=G-S*(H+G*TAU)
                A(J,IQ)=H+S*(G-H*TAU)
17
              CONTINUE
              DO 18 J=IQ+1,N
                G=A(IP,J)
                H=A(IQ,J)
                A(IP,J)=G-S*(H+G*TAU)
                A(IQ,J)=H+S*(G-H*TAU)
18
              CONTINUE
              DO 19 J=1,N
                G=V(J,IP)
                H=V(J,IQ)
                V(J,IP)=G-S*(H+G*TAU)
                V(J,IQ)=H+S*(G-H*TAU)
19
              CONTINUE
              NROT=NROT+1
            ENDIF
21
          CONTINUE
22
        CONTINUE
        DO 23 IP=1,N
          B(IP)=B(IP)+Z(IP)
          D(IP)=B(IP)
          Z(IP)=0.
23
        CONTINUE
24
      CONTINUE
      PAUSE '50 iterations should never happen'
      RETURN
      END
```

```
c sorting subroutine for ordering e-values and e-vectors
c from numerical recipes
     SUBROUTINE EIGSRT(D, V, N, NP)
     implicit real*8(a-h,o-z)
     DIMENSION D(NP), V(NP, NP)
     DO 13 I=1,N-1
       K = I
       P=D(I)
       DO 11 J=I+1,N
        IF(D(J).GE.P)THEN
          K = J
          P=D(J)
         ENDIF
11
       CONTINUE
       IF(K.NE.I)THEN
        D(K)=D(I)
        D(I)=P
        DO 12 J=1,N
          P=V(J,I)
          V(J,I)=V(J,K)
          V(J,K)=P
12
         CONTINUE
       ENDIF
13
     CONTINUE
     RETURN
     END
c calculates the ground state of the effective Hamiltonian h
c can do search sector by sector
c constructs pointers to the sectors in and is
subroutine getgs(ih,h,egs,gs,iloop,iflag,in0,is0,igs)
       parameter (N=16, NN=2**N, NP=4900)
       implicit real*8(a-h,o-z)
       double precision h(NN,2*N),wh(NP,2*N)
       double precision gs(NN),gst(8,NN),esec(N,-N:N)
       double precision gsw1(NP)
       dimension ih(NN,2*N),iwh(NP,2*N)
       dimension isrt(NP),jsrt(NN)
       dimension in0(N), is0(N)
c 1=p site down
c 2=p site up
c iep=d site up
c ied=d site down
c NR =last site of up chain
c NR+1=first site of down chain
c NC =length of each side of the chains
       NR = ((N-2)/2-1)/2+2
       NC = NR - 2
```

```
nhalf=N/2
        iep=N-1
        ied=N
egs0=1.d4
if(iloop.eq.1.and.iflag.eq.1)then
in0(1)=nhalf
is0(1)=0
igs=1
print*,'considering the p-h symetric sector only!!!'
if(iflag.eq.0)then
c search all sectors
igs=1
c sweep all sectors
do ievod=0,1
c ievod=0 ==> even number of particles (and even spin)
c ievod=1 ==> odd number of particles (and odd spin)
do in= 2-ievod, N-ievod, 2
if(ilast.eq.1)then
write(100,*)'"N=',in,'"'
endif
ism=in
if(in.gt.nhalf)ism=N-in
do is= -ism,ism,2
c construct the pointers for sector (in,is)
call sector(in,is,idg,isrt,jsrt)
c construct wh = the hamiltonian in sector (in,is),
c and and iwh = the pointer of the hamiltonian
call gethns(idg,isrt,jsrt,h,ih,wh,iwh)
c diagonalize wh by modified Lanczos method
call lanczos(wh,gsw1,egs,iwh,idg,in,is)
esec(in,is)=egs
if(ilast.eq.1)then
write(100,*)is,real(egs)
endif
```

```
if(egs.lt.egs0+1.d-5)then
c found a new ground state vector (may be a degenerate one)
c check for degeneracy or new gs
\verb|if(dabs(egs-egs0).lt.1.d-5|| then||
   igs=igs+1
   in0(igs)=in
   is0(igs)=is
else
   igs=1
   egs0=egs
   in0(igs)=in
   is0(igs)=is
endif
c expand the new gs to full size and store it
do i=1,NN
gst(igs,i)=0.d0
enddo
        do i=1,idg
        ia=isrt(i)
        gst(igs,ia)=gsw1(i)
        enddo
endif
enddo
        if(ilast.eq.1)then
write(100,*),
        endif
enddo
enddo
else
c**** in inner loops skip the full search ****
do j=1,igs
in=in0(j)
is=isO(j)
c construct the pointers for sector (in,is)
call sector(in,is,idg,isrt,jsrt)
```

```
c construct wh = the hamiltonian in sector (in,is),
c and and iwh = the pointer of the hamiltonian
call gethns(idg,isrt,jsrt,h,ih,wh,iwh)
c diagonalize wh by modified Lanczos method
call lanczos(wh,gsw1,egs,iwh,idg)
   egs0=egs
c expand the new gs to full size and store it
do i=1,NN
gst(igs,i)=0.d0
enddo
        do i=1,idg
        ia=isrt(i)
        gst(igs,ia)=gsw1(i)
        enddo
enddo
endif
c copy the output
egs=egs0
do i=1,NN
gs(i)=0.d0
enddo
xnor=1.d0/dsqrt(dfloat(igs))
do j=1,igs
do i=1,NN
gs(i)=gs(i)+gst(j,i)*xnor
enddo
enddo
do i=1,igs
print*,'the gs sector is (N,Sz)=',in0(i),is0(i)
print*,'there are',igs,' degenerate gs'
if(iflag.eq.0)then
\verb|if(dabs(egs-esec(in0(1),is0(1))).gt.1d-5)then|\\
print*,'something is wrong...'
endif
endif
return
end
```

```
c extracts from the full hamiltonian the block corresponding
c to sector (n,s)
subroutine gethns(idg,isrt,jsrt,h,ih,wh,iwh)
       parameter(N=16,NN=2**N,NP=4900)
       implicit real*8(a-h,o-z)
       double precision h(NN,2*N),wh(NP,2*N)
       dimension ih(NN,2*N),iwh(NP,2*N)
       dimension isrt(NP), jsrt(NN)
c extract the rows of h and ih
do j=1,2*N
do i=1,NP
wh(i,j)=0.d0
iwh(i,j)=0
enddo
enddo
do i=1,idg
ia=isrt(i)
do k=1,2*N
wh(i,k)=h(ia,k)
iwh(i,k)=ih(ia,k)
enddo
enddo
c rewrite iwh to point inside the sector
       do 105 i=1,idg
MM=iwh(i,N)
       do 106 k=1,MM
jj=iwh(i,k)
if(jj.eq.0)goto 106
j=jsrt(jj)
iwh(i,k)=j
106
       continue
105
       continue
return
end
c constructs the pointers for the different sectors and
c the vectors isrt and jsrt with the corresponding
c ordering definition of the sub-basis within each sector
subroutine sector(in,is,idg,isrt,jsrt)
       parameter (N=16, NN=2**N, NP=4900)
       implicit real*8(a-h,o-z)
       dimension isrt(NP), jsrt(NN)
       dimension ib2(N)
```

```
c 1=p site down
c 2=p site up
c iep=d site up
c ied=d site down
c NR =last site of up chain
c NR+1=first site of down chain
c NC =length of each side of the chains
       NR = ((N-2)/2-1)/2+2
       NC = NR - 2
       nhalf=N/2
       iep=N-1
       ied=N
idg=0
do i=1,NN
jsrt(i)=0
enddo
do i=1,NP
isrt(i)=0
enddo
c construct idg and isrt. idg has the degeneracy of the
c sector (in,is). isrt has the list of vectors that belong
c to the sector (in,is). isrt defines the basis of the sector
c jsrt has the "inverse pointer" of isrt
       do i=1,NN
       call b2(i,ib2)
       ibs=0
       ibn=0
       ibs=ib2(2)-ib2(1)+ib2(iep)-ib2(ied)
       ibn=ib2(2)+ib2(1)+ib2(iep)+ib2(ied)
       do j=3,NR
       ibs=ibs+ib2(j)+ib2(j+NC)-ib2(j+2*NC)-ib2(j+3*NC)
       ibn=ibn+ib2(j)+ib2(j+NC)+ib2(j+2*NC)+ib2(j+3*NC)
       if(ibn.eq.in.and.ibs.eq.is)then
       idg=idg+1
       isrt(idg)=i
       jsrt(i)=idg
       endif
       enddo
return
end
c this routine calculates the position and strengh of the
c discrete poles of the Green function expressed in continued
```

c fraction form. It basically diagonalizes the tridiagonal

```
c matrix defined by the a's and the b's
subroutine getpole(egs,anr,bnr,anl,bnl,NG,iwr,ip)
        parameter(N=16,NN=2**N,NP=4900,NM=50)
        implicit real*8(a-h,o-z)
        double precision anr(0:NP),bnr(0:NP)
        double precision anl(0:NP),bnl(0:NP)
        double precision pr(NP), wr(NP)
        double precision prs(NP),wrs(NP)
        double precision pl(NP),wl(NP)
        double precision pls(NP),wls(NP)
double precision trdh(NM,NM),rot(NM,NM),ev(NM)
common/pw/pr,pl,wr,wl
common/pws/prs,pls,wrs,wls
common/size/NC,NL
common/par/tu
NL=NG
c NC=length of each side of the chains
        NR = ((N-2)/2-1)/2+2
        NC = NR - 2
do j=1,NM
do i=1,NM
trdh(j,i)=0.
enddo
enddo
c if ss (ip=-1) => skip the short chain
c if d site (ip=0) => skip the short chain
c if p site (ip=1) => do the short chain
c do the sign flip for "snl"
if(ip.eq.-1)then
do i=1,NG
anl(i-1)=-anl(i-1)
enddo
endif
if(ip.eq.1)then
c calculate the poles and weights for a short chain
c with one pole per effective bath site
c right side
do i=1,NC
trdh(i,i)=anr(i-1)-egs
trdh(i,i+1)=dsqrt(bnr(i))
trdh(i+1,i)=dsqrt(bnr(i))
enddo
```

```
call jacobi(trdh,NC,NM,ev,rot,irot)
        call eigsrt(ev,rot,NC,NM)
    do i=1,NC
   prs(i)=ev(i)
wrs(i)=rot(1,i)**2
    enddo
c left side
do i=1,NC
trdh(i,i)=-anl(i-1)-egs
        trdh(i,i+1)=dsqrt(bnl(i))
        trdh(i+1,i)=dsqrt(bnl(i))
enddo
        call jacobi(trdh,NC,NM,ev,rot,irot)
        call eigsrt(ev,rot,NC,NM)
   do i=1,NC
  pls(i)=ev(i)
wls(i)=rot(1,i)**2
   enddo
endif
c calculate the poles and weights for the full hamiltonian
c with a big number of poles
c right side
        do i=1,NG
        trdh(i,i)=anr(i-1)-egs
trdh(i,i+1)=dsqrt(bnr(i))
trdh(i+1,i)=dsqrt(bnr(i))
        enddo
call jacobi(trdh,NG,NM,ev,rot,irot)
        call eigsrt(ev,rot,NG,NM)
   do i=1,NG
   pr(i)=ev(i)
wr(i)=rot(1,i)**2
   enddo
c left side
        do i=1,NG
        trdh(i,i)=-anl(i-1)-egs
        trdh(i,i+1)=dsqrt(bnl(i))
        trdh(i+1,i)=dsqrt(bnl(i))
        enddo
```

```
call jacobi(trdh,NG,NM,ev,rot,irot)
        call eigsrt(ev,rot,NG,NM)
  do i=1,NG
  pl(i)=ev(i)
wl(i)=rot(1,i)**2
   enddo
c undo the sign flip for "snl"
if(ip.eq.-1)then
do i=1,NG
anl(i-1)=-anl(i-1)
enddo
endif
c***print out results****
if(iwr.eq.1)then
        if(ip.eq.-1)then
        write(96,*)'"poles & weigths suscept."'
        write(96,*)'"sp-sp"'
        do i=1,NG
        write(96,*)real(pr(i)),real(wr(i))
        enddo
        write(96,*)'
        write(96,*)'"ch-ch"'
        do i=1,NG
        write(96,*)real(pl(i)),real(wl(i))
        enddo
        write(96,*)' '
        endif
if(ip.eq.0)then
write(97,*)'"poles & weigths d site"'
write(97,*)'"right"'
  do i=1,NG
  write(97,*)real(pr(i)),real(wr(i))
enddo
write(97,*),
write(97,*)'"left"'
  do i=1,NG
   write(97,*)real(pl(i)),real(wl(i))
enddo
write(97,*)'
endif
if(ip.eq.1)then
        write(98,*)'"poles & weigths p site"'
        write(98,*)'"right"'
        do i=1,NG
        write(98,*)real(pr(i)),real(wr(i))
        enddo
```

```
write(98,*),
       write(98,*)'"left"'
       do i=1,NG
       write(98,*)real(pl(i)),real(wl(i))
       enddo
write(98,*),
write(99,*)'"poles & weigths p bath"'
write(99,*)'"right"'
  do i=1,NC
  write(99,*)real(prs(i)),real(wrs(i))
enddo
write(99,*),
write(99,*)'"left"'
  do i=1,NC
  write(99,*)real(pls(i)),real(wls(i))
write(99,*)' '
endif
endif
return
end
c This subroutine calculates the gs energy and
c the |gs> by the modified Lanczos method
c the Hamiltonian h has been compressed and ih has the pointers
c f0 is the seed on input and the |gs\rangle on output
       subroutine lanczos(h,f0,egs,ih,id,in,is)
       parameter(N=16, NP=4900, MP=15)
       implicit real*8(a-h,o-z)
       double precision h(NP,2*N)
       double precision fO(NP),f1(NP)
       double precision f2(NP),f3(NP)
       dimension ih(NP,2*N),zz(MP,MP),at(MP),bt(MP)
 dimension vect(MP,NP)
if(id.eq.1)then
egs=h(1,1)
do i=1,NP
f0(i)=0.d0
enddo
f0(1)=1.d0
goto 200
endif
```

```
e1=100.d0
        xx=0.d0
        do i=1,id
        xn=ran(2)
        f0(i)=xn
        xx=xx+f0(i)**2
        enddo
        xx=1.d0/dsqrt(xx)
        do i=1,id
        f0(i)=xx*f0(i)
        enddo
c does regular modified lanczos
  if(id.lt.3)then
        jloop=0
 100
        continue
        jloop=jloop+1
        e0=e1
        call hxvl(h,ih,f0,f1,id)
        call hxvl(h,ih,f1,f2,id)
        call hxvl(h,ih,f2,f3,id)
        ha=0.d0
        h2=0.d0
        h3 = 0.d0
        do i=1,id
           ha=ha+f0(i)*f1(i)
           h2=h2+f0(i)*f2(i)
           h3=h3+f0(i)*f3(i)
        enddo
hh=h2-ha**2
if(h2-ha**2.lt.0.d0)then
write(1,*)jloop,real(h2-ha**2)
hh=1.d-9
endif
        den=dsqrt(hh)
        do i=1,id
           f1(i)=(f1(i)-ha*f0(i))/den
        enddo
        den1=2.d0*(h2-ha**2)*den
        xnum=h3-3.d0*ha*h2+2.d0*ha**3
        f=xnum/den1
        alpha=f-dsqrt(f**2+1.d0)
        den2=dsqrt(1.d0+alpha**2)
```

```
do i=1,id
           f0(i)=(f0(i)+alpha*f1(i))/den2
        e1=ha+den*alpha
        if(dabs(e1-e0).gt.1.d-9)goto 100
        egs=e1
c print*,'regul lanczos egs:',egs
  else
c does tridiagonalization of MxM block
 300
        continue
        e0=e1
        do i=1,MP
at(i)=0.d0
bt(i)=0.d0
do j=1,NP
vect(i,j)=0.d0
enddo
enddo
        call hxvl(h,ih,f0,f1,id)
a=0.d0
b=0.d0
do i=1,id
a=a+f0(i)*f1(i)
enddo
at(1)=a
s=0.d0
do i=1,id
        f1(i)=f1(i)-a*f0(i)
        s=s+f1(i)*f1(i)
enddo
bt(2)=dsqrt(s)
s=1.d0/bt(2)
do i=1,id
f1(i)=s*f1(i)
vect(1,i)=f0(i)
vect(2,i)=f1(i)
        enddo
c check that the block for lanczos is not bigger than the
c size of the sector
M = MP
if(id.lt.M)M=id
do k=2,M
        call hxvl(h,ih,f1,f2,id)
```

```
b=bt(k)
        a=0.d0
        do i=1,id
        a=a+f1(i)*f2(i)
enddo
        at(k)=a
        s=0.d0
        do i=1,id
        f2(i)=f2(i)-a*f1(i)-b*f0(i)
        s=s+f2(i)*f2(i)
enddo
s=dsqrt(s)
if(k.le.M-1)then
bt(k+1)=s
s=1.d0/s
do i=1,id
        f2(i)=s*f2(i)
vect(k+1,i)=f2(i)
        enddo
endif
do i=1,id
f0(i)=f1(i)
f1(i)=f2(i)
enddo
enddo
do i=1,MP
do j=1,MP
zz(i,j)=0.d0
enddo
zz(i,i)=1.d0
enddo
         call tqli(at,bt,M,MP,zz)
         call eigsrt(at,zz,M,MP)
e1=at(M)
s=0.d0
do i=1,id
f0(i)=0.d0
do j=1,M
f0(i)=f0(i)+zz(j,M)*vect(j,i)
enddo
s=s+f0(i)*f0(i)
enddo
s=1.d0/dsqrt(s)
        do i=1,id
f0(i)=s*f0(i)
enddo
```

```
if(jloop.gt.1020)then
print*,'did not converge!!! (but continued anyway)'
goto 400
endif
if(dabs(e1-e0).gt.1.d-9)goto 300
400 continue
egs=e1
  endif
200 continue
       return
       end
c diagonalized a tridiagonal matrix
c from numerical recipes
     SUBROUTINE tqli(d,e,n,np,z)
     implicit real*8(a-h,o-z)
     INTEGER n,np
     double precision d(np),e(np)
     double precision z(np,np)
С
     USES pythag
     INTEGER i,iter,k,l,m
     double precision b,c,dd,f,g,p,r,s,pythag
     do i=2,n
        e(i-1)=e(i)
     enddo
     e(n)=0.d0
     do 15 l=1,n
        iter=0
1
        do m=1, n-1
           dd=dabs(d(m))+dabs(d(m+1))
           if (dabs(e(m))+dd.eq.dd) goto 2
        enddo
        m=n
        if (m.ne.1) then
           if(iter.eq.30)pause 'too many iterations in tqli'
           iter=iter+1
           g=(d(1+1)-d(1))/(2.d0*e(1))
           r=pythag(g,1.d0)
           g=d(m)-d(1)+e(1)/(g+dsign(r,g))
           s=1.d0
           c=1.d0
           p=0.d0
           do 14 i=m-1,1,-1
              f=s*e(i)
              b=c*e(i)
              r=pythag(f,g)
              e(i+1)=r
              if(r.eq.0.d0)then
```

```
d(i+1)=d(i+1)-p
                e(m) = 0.d0
                goto 1
             endif
             s=f/r
             c=g/r
             g=d(i+1)-p
             r=(d(i)-g)*s+2.d0*c*b
             p=s*r
             d(i+1)=g+p
             g=c*r-b
     Omit lines from here ...
С
             do 13 k=1,n
                f=z(k,i+1)
                z(k,i+1)=s*z(k,i)+c*f
                z(k,i)=c*z(k,i)-s*f
13
             continue
C
     ... to here when finding only eigenvalues.
14
          continue
          d(1)=d(1)-p
          e(1)=g
          e(m)=0.d0
          goto 1
        endif
15
     continue
С
     return
     END
c used by tqli
c from numerical recipes
     double precision FUNCTION pythag(a,b)
     implicit real *8(a-h,o-z)
     double precision a,b,pythag
     double precision absa, absb
     absa=dabs(a)
     absb=dabs(b)
     if(absa.gt.absb)then
       pythag=absa*dsqrt(1.+(absb/absa)**2)
     else
       if(absb.eq.0.)then
        pythag=0.
       else
        pythag=absb*dsqrt(1.+(absa/absb)**2)
       endif
     endif
     return
     END
c constructs a mask of 1 and 0's to avoid multiplication by 0's
c in the operation of h times a state.
c it takes a state from a sector (n0,s0) and depending
```

```
c on how the operator that acts changes the spin and particle
c number, it constructs the appropiate mask.
subroutine mask(in0,is0,igs,imk,imc)
parameter(N=16,NN=2**N,NP=4900)
implicit real*8(a-h,o-z)
dimension in0(N),is0(N),imk(NN)
       dimension isrt(NP),jsrt(NN)
c the GF are spin up by convention
c imc is 0 for the C C | 0> sector (does not change)
c imc is +1 for the C | 0> sector
c imc is -1 for the C \mid 0> sector (N-1, S-1)
do i=1,NN
imk(i)=0
enddo
do i=1,igs
in=in0(i)+imc
is=is0(i)+imc
c construct the pointers for sector (in,is)
call sector(in,is,idg,isrt,jsrt)
do j=1,idg
jj=isrt(j)
imk(jj)=1
isrt(j)=0
enddo
enddo
return
end
c This subroutine calculates a Green function in terms of
c a continued fraction
subroutine getgf(h,ih,anr,bnr,anl,bnl,gs,igs,cp,icp,cpdg,icpdg,
                  NG, in0, is0)
       parameter(N=16,NN=2**N,NP=4900)
```

implicit real\*8(a-h,o-z)

```
double precision h(NN,2*N)
        double precision anr(0:NP),bnr(0:NP)
        double precision anl(0:NP),bnl(0:NP)
        double precision xa(NN)
        double precision f0(NN),f1(NN),f2(NN),f(NN)
        double precision gs(NN)
        double precision cp(NN),cpdg(NN)
        dimension icp(NN),icpdg(NN)
        dimension ih(NN,2*N)
        dimension inO(N), isO(N), imk(NN)
c construct the mask
call mask(in0,is0,igs,imk,1)
c***starts the tridiagonalization****
c right chain
call cxv(cpdg,icpdg,gs,f0)
c get an(0) and bn(0)
call hxvm(h,ih,f0,xa,imk)
anr(0)=0.
yr=0.
do 11 i=1,NN
anr(0)=anr(0)+f0(i)*xa(i)
yr=yr+f0(i)**2
11 continue
anr(0)=anr(0)/yr
bnr(0)=yr
c get the an(i) and bn(i)
c f1=f(n-1), f2=f(n-2)
a=anr(0)
b=0.
do 13 i=1,NN
f1(i)=f0(i)
f2(i)=0.
13 continue
do 14 in=1,NG
call getfn(ih,h,f,f1,f2,a,b,imk)
call getab(ih,h,f,f1,a,b,imk)
anr(in)=a
bnr(in)=b
do 15 i=1,NN
```

```
f2(i)=f1(i)
 f1(i)=f(i)
15 continue
14 continue
c construct the mask
call mask(in0,is0,igs,imk,-1)
c left chain
c***cp(j,i)=cp+(i,j)***
c**change the sign of H to calculate the hole excitations**
do 102 j=1,2*N
do 102 i=1,NN
h(i,j)=-h(i,j)
102 continue
call cxv(cp,icp,gs,f0)
c get an(0) and bn(0)
call hxvm(h,ih,f0,xa,imk)
        anl(0)=0.
        yl=0.
        do 19 i=1,NN
        anl(0)=anl(0)+f0(i)*xa(i)
        yl=yl+f0(i)**2
19
        continue
        anl(0)=anl(0)/yl
        bnl(0)=yl
c get the an(i) and bn(i)
c f1=f(n-1), f2=f(n-2)
        a=an1(0)
        b=0.
        do 21 i=1,NN
        f1(i)=f0(i)
        f2(i)=0.
21
        continue
        do 22 in=1,NG
        call getfn(ih,h,f,f1,f2,a,b,imk)
        call getab(ih,h,f,f1,a,b,imk)
        anl(in)=a
        bnl(in)=b
```

```
do 23 i=1,NN
         f2(i)=f1(i)
         f1(i)=f(i)
23
      continue
22
       continue
c**restore the sign of H**
do 103 j=1,2*N
do 103 i=1,NN
h(i,j)=-h(i,j)
103 continue
print*,'done!'
return
end
c This subroutine calculates the spin-spin and charge-charge
c correlation function in terms of a continued fraction
subroutine getcorr(h,ih,snr,tnr,snl,tnl,gs,igs,NG,in0,is0)
       parameter(N=16,NN=2**N,NP=4900)
       implicit real*8(a-h,o-z)
       double precision h(NN,2*N)
       double precision snr(0:NP),tnr(0:NP)
       double precision snl(0:NP),tnl(0:NP)
       double precision xa(NN)
       double precision fO(NN),f1(NN),f2(NN),f(NN)
       double precision gs(NN)
       dimension ih(NN,2*N)
       dimension ib2(N)
       dimension inO(N), isO(N), imk(NN)
c 1=p site down
c 2=p site up
c iep=d site up
c ied=d site down
c NR =last site of up chain
c NR+1=first site of down chain
c NC =length of each side of the chains
       NR = ((N-2)/2-1)/2+2
       NC = NR - 2
       nhalf=N/2
       iep=N-1
       ied=N
c calculates the <sp-sp> continued fraction
c construct the mask
call mask(in0,is0,igs,imk,0)
```

```
c***starts the tridiagonalization****
c right chain
        xnp=0.d0
        xnd=0.d0
        do i=1,NN
        call b2(i,ib2)
        xnp=xnp+gs(i)*gs(i)*ib2(2)
        xnp=xnp+gs(i)*gs(i)*ib2(1)
        xnd=xnd+gs(i)*gs(i)*ib2(iep)
        xnd=xnd+gs(i)*gs(i)*ib2(ied)
        \texttt{f0(i)} = \texttt{dfloat(ib2(2)} - \texttt{ib2(1)} + \texttt{ib2(iep)} - \texttt{ib2(ied)}) * \texttt{gs(i)}
        enddo
        print*,'Np:',real(xnp)
        print*,'Nd:',real(xnd)
c get cn(0) and dn(0)
        call hxvm(h,ih,f0,xa,imk)
        snr(0)=0.
        srd=0.
        do 311 i=1,NN
        snr(0)=snr(0)+f0(i)*xa(i)
        srd=srd+f0(i)**2
311
        continue
        snr(0)=snr(0)/srd
        tnr(0)=srd
c get the cn(i) and dn(i)
        c=snr(0)
        dd=0.
        do 313 i=1,NN
        f1(i)=f0(i)
        f2(i)=0.
313
         continue
        do 314 in=1,NG
        call getfn(ih,h,f,f1,f2,c,dd,imk)
        call getab(ih,h,f,f1,c,dd,imk)
        snr(in)=c
        tnr(in)=dd
        do 315 i=1,NN
          f2(i)=f1(i)
          f1(i)=f(i)
315
        continue
```

```
314 continue
c use left chain for the <ch-ch>
c can use the same mask
c construct f0
        xnp=0.d0
        xnd=0.d0
        do i=1,NN
        call b2(i,ib2)
idnp=ib2(2)+ib2(1)-1
idnd=ib2(iep)+ib2(ied)-1
        f0(i)=dfloat(idnp+idnd)*gs(i)
        enddo
c get cn(0) and dn(0)
        call hxvm(h,ih,f0,xa,imk)
        snl(0)=0.
        sld=0.
        do 319 i=1,NN
        snl(0)=snl(0)+f0(i)*xa(i)
        sld=sld+f0(i)**2
319
        continue
        snl(0)=snl(0)/sld
        tnl(0)=sld
c get the cn(i) and dn(i)
        c=sn1(0)
        dd=0.
        do 325 i=1,NN
        f1(i)=f0(i)
        f2(i)=0.
325
        continue
        do 322 in=1,NG
        do 322 in=1,10
        call getfn(ih,h,f,f1,f2,c,dd,imk)
        call getab(ih,h,f,f1,c,dd,imk)
        snl(in)=c
        tnl(in)=dd
        do 323 i=1,NN
          f2(i)=f1(i)
```

f1(i)=f(i)

323 continue 322 continue print\*,'done!'

return end

## Vita

## Marcelo J. Rozenberg

- 1982-89 Attended University of Buenos Aires, Buenos Aires, Argentina. Majored in Physics.
- 1986-89 Teaching Assistant, Department of Physics, University of Buenos Aires, Buenos Aires, Argentina.
- 1989 Licenciatura in Physics, University of Buenos Aires, Buenos Aires, Argentina.
- 1989-90 Graduate work in Physics, Hunter College, The City University of New York, New York, New York.
- 1989-90 Teaching Assistant, Department of Physics and Astronomy, Hunter College, The City University of New York, New York, New York.
- 1990-94 Graduate work in Physics, Rutgers, The State University of New Jersey, New Brunswick, New Jersey.
- 1990-91 Teaching Assistant, Department of Physics and Astronomy.
- 1990-94 Research Assistant, Department of Physics and Astronomy.
- 1994 Teaching Assistant, Department of Physics and Astronomy.
- Dussel, G.G., and M.J. Rozenberg, Comparison between the exact solution and the thermal description of the pairing interaction in <sup>114</sup>Sn. Phys. Rev. C, Rapid Comm., 40:1114.
- Rozenberg, M.J., X.Y. Zhang, and G. Kotliar, The Mott Hubbard Transition in Infinite Dimensions. *Phys. Rev. Lett.*, 69:1236.
- Castellani, C., G. Kotliar, R. Raimondi, M. Grilli, Z. Wang, and M.J. Rozenberg, Collective excitations, photoemisson spectra, and optical gaps in strongly correlated fermi systems. *Phys. Rev. Lett.*, 69:2009.
- Zhang, X.Y., M.J. Rozenberg, and G. Kotliar, Mott transition in the  $d = \infty$  Hubbard model at zero temperature. Phys. Rev. Lett., 70:1666.
- Si, Q., M.J. Rozenberg, G. Kotliar, and A. Ruckenstein, Correlation Induced Insulator to Metal Transitions. *Phys. Rev. Lett.*, 72:2761.
- Rozenberg, M.J., G. Kotliar, and X.Y. Zhang, The Mott Hubbard transition in infinite dimensions II. *Phys. Rev. B*, 49:10181.

- Rozenberg, M.J., G. Moeller, and G. Kotliar, Mott-Hubbard transition at zero temperature II. *Mod. Phys. Lett. B*, 8:535.
- 1994 Kotliar, G., and M.J. Rozenberg, Proceedings of the International Conference on Superconductivity and Strongly Correlated Electron Systems. Amalfi, Italy.
- Kotliar, G., and M.J. Rozenberg, Proceedings of the Conference "The Physics and the Mathematical Physics of The Hubbard Model". San Sebastian.
- Moeller, G., Q. Si, G. Kotliar, M.J. Rozenberg, and D. Fisher, Critical behavior near the Mott transition in the Hubbard model. Rutgers University preprint.
- Rozenberg, M.J., G. Kotliar, and H. Kajueter, Optical conductivity in correlated electron systems. Rutgers University preprint.
- 1994 Ph.D. in Physics.